NTNU – Trondheim
Norwegian University of
Science and Technology

The effect of Zr and V on the structural and mechanical properties of the 2618 Al alloy

Eleonora Zappi

Master's Thesis
Submission date: November 2014
Supervisor: Marisa Di Sabatino, IMTE
Co-supervisor: Lars Arnberg, IMT
Lorella Ceschini, Alma Mater Studiorum - Università di Bologna

Norwegian University of Science and Technology
Department of Materials Science and Engineering

ABSTRACT

During the last decades, the use of aluminium components for automotive applications has continuously increased. The main reason for this success is the high strength-to-weight ratio which characterizes these alloys, and which allows to reduce the vehicles weight. In fact, weight reduction is critically important to meet the strict regulations concerning fuel-economy and reduction of exhaust gas emissions.

In order to take more advantage of the benefits brought by weight reduction, the trend is to use aluminium alloys even for critical component, such as cylinder blocks and pistons. These components, however, operate at elevated temperatures, and the demand for high-performance engines is raising these temperatures even more.

This situation represents an issue for the use of aluminium alloys for engine components. Heat treated aluminium alloys are subjected to a decrease in their mechanical properties after exposure at elevated temperature, this decrease being faster when temperature is higher. This problem has been extensively studied, and many developments in high temperature mechanical properties of aluminium alloys have been achieved. Nevertheless, at the moment there are no aluminium alloys that could be used at temperature higher than 300 °C, as required by latest developments in modern engines. A further improvement, however, seems possible: additions of small amounts of transition metals (in particular Sc, Zr, Ti and V) have the potential to enhance the thermal stability of aluminium alloys.

The experimental work of this thesis investigated an Al-Cu-Mg-Si-Fe-Ni aluminium alloys used for the production of forged pistons for high-performance engine, namely AA 2618.

In the first part of the work, the heat treatment of AA 2618 was optimized in order to achieve high mechanical properties. It was found that the optimum condition is achieved when ageing treatment is carried out at 200 °C for 20 h. Then, the thermal stability of peak-aged AA 2618 was examined, for exposure temperatures in the range 200-305 °C, and tensile tests were carried out after high temperature exposure. As expected, tensile tests confirmed that UTS and YS both decrease with decreasing the residual hardness, while ductility increases in the opposite direction. SEM micrographs showed that the coarsening of the precipitate phase during thermal exposure and the consequent appearance of PFZ are responsible for the decrease in mechanical properties.

The experimental work concerning AA 2618 clearly showed that this alloy, in T6 condition, presents a suitable thermal stability for temperatures up to 230 °C, but when

exposed at higher temperatures the decrease in hardness is quite fast. As a consequence, despite AA 2618 can be used at higher temperatures than the majority of other commercial aluminium alloys, its thermal stability is not high enough for applications in modern high-performance engines.

In order to overcome this problem, the second part of the work is concerned with addition of Zr and V. Two modified alloys were produced, one containing a higher Zr amount compared to the base material, and another containing a small amount of V in addition to the higher content of Zr. This preliminary investigation mainly dealt with the production of the modified alloys, the plastic deformation of the material in order to simulate the hot forging industrial process, and a microstructural investigation.

TABLE OF CONTENTS

Chapter 1

Theoretical Background

Chapter 2

Experimental

Chapter 3

Results and Discussion

INTRODUCTION

Heat-treatable aluminium alloys are regarded as one of the most suitable materials for the production of structural components for automotive applications. This is due to their excellent response to plastic deformation and casting processes, good corrosion resistance and, first of all, high strength-to-weight ratio. In fact, such properties meet the modern industrial need for producing light vehicles with increasingly high specific power engines, in order to provide high performance together with reduced fuel consumption and low polluting emissions. Weight reduction is indeed the most effective method to reduce transportation costs and to satisfy the more and more stringent requirements of reducing CO_2 emissions. In order to achieve this aim, a rise in the use of aluminium alloys, even for critical parts such as engine blocks and pistons, is a well-established trend.

However, the use of heat-treatable aluminium alloys at elevated temperatures represents a serious issue. In fact, it is well known that when using a T6 heat-treated Al alloy at temperatures higher than the aging one, a loss in the mechanical properties will take place, which is a function of both exposure time and temperature.

In recent years several studies were carried out with the aim of overcoming the problems linked to high working temperatures. Most of these works deal with the addition of small amount of transition metals (such as Zr, Hf, Sc, Ti, V) to the aluminium alloys, in order to form more stable intermetallic compounds, which should enhance the mechanical properties of the alloys both at room and elevated temperatures. However, the picture is still not completely clear and the data available is fragmentary and incomplete. The present study intends to supply further knowledge in this direction.

This experimental work is concerned with the study of a commercial Al-Cu wrought alloy - AA 2618 - that is currently used for the production of pistons for high-performance engines. The interest in producing engines with ever higher performance results in the need for the pistons to stand temperatures equal to or higher than 300 °C. At these temperatures, the mechanical properties of AA 2618 drastically decrease, and the idea was to chemically modify the standard alloy by proper addition of elements suitable to form more stable strengthening intermetallic compounds.

The present work consists of two parts: first of all, the advantages and issues with the use of aluminium alloys as piston material are described, and a state-of-the-art in development of new aluminium piston alloys is presented. A literature review was also carried out to study the effect of the addition of transition metals to aluminium and aluminium alloys on high temperature mechanical properties. This study was the premise for the choice of the elements and corresponding amounts to add to AA 2618 alloy in order to produce a modified heat-resistant alloy.

The second part is concerned with the experimental work. First, heat treatment and thermal stability of unmodified AA2618 alloy were studied, mainly through hardness measurements and microstructural investigation. Then, in order to increase thermal stability of AA2618, transitional metals were added to this alloy. The modified alloy was cast and hot rolled, in order to simulate the forging process generally used to produce the pistons. Microstructural and mechanical characterizations were carried out, both on the as-cast and hot rolled modified alloy, in order to determine the effect of the added elements.

The research work was carried out both at the Department of Industrial Engineering (DIN) of Alma Mater Studiorum - University of Bologna and at the Department of Material Science and Engineering (IMT) of NTNU - Norwegian University of Science and Technology. The study was coordinated by Professor Lorella Ceschini, Professor Alessandro Morri and PhD Andrea Morri (from DIN - Department of Industrial Engineering of the University of Bologna), and by Professor Lars Arnberg and Professor Marisa Di Sabatino (from the Department of Material Science and Engineering (IMT) of NTNU.

CHAPTER 1

Theoretical Background

INTRODUCTION

This work dealt with an Al-Cu alloy (AA 2618), typically used for the production of forged pistons for high-performance engines. In particular, the study focused on high temperature behaviour of this alloy and possible ways to improve it, especially through the addition of transitional metals in small amounts.

Aluminium alloys can bring several advantages if used for engine components, but operating temperatures represent a strong limitation in this respect. In last decades, the strong need for light materials in the automotive field has been a driving force to try and produce new heat-resistant aluminium alloys that can be used for pistons and other engine components. This chapter is first of all intended to give an overview of this situation, which encouraged the undertaking of the project presented in this work.

Then, a thorough description of the main characteristics and precipitation strengthening of AA 2618 aluminium alloys are presented.

Finally, a review of the scientific literature concerning addition of transition metals for the production of high temperature resistant aluminium alloys is provided.

1.1 ALUMINIUM PISTON ALLOYS

In this paragraph, piston operating conditions and resulting requirements for piston materials are described. In particular, the focus is on the use of aluminium alloys as piston material, with related advantages and limitations.

Then, an account is given of the progress made during last decades in the development of aluminium alloys for high temperature applications.

1.1.1 Piston operating conditions and related requirements for piston materials

Modern engines take advantage of high technology in the materials field in order to achieve ever better performance. Clearly, the materials to be used and their characteristics are determined by the function of a component, that is dictated by the engine operating conditions. Therefore, in order to choose suitable materials - with related manufacturing processes and treatments - for pistons, it is necessary to understand their role in the engine, which defines the operating conditions they are subjected to.

Figure 1.1 shows a four-stroke cycle diesel engine with its various parts indicated and the position of piston highlighted. In a reciprocating engine like the one in Figure 1.1, a mixture of fuel and air burns explosively in a narrow container - the combustion chamber - limited by piston and cylinder. Air is let into the chamber by a valve, through the inlet manifold, while fuel is introduced into the chamber by a fuel injector. The compression due to piston movement into the cylinder ignites the fuel and air mixture; the piston then receives the combustion pressure, and the connecting rod and crankshaft mechanism converts this pressure into rotation. Finally, when combustion is over and the piston is at his BDC, another valve opens to evacuate exhaust gas through the exhaust manifold [1], then a new cycle can start. Petrol engines work in a slightly different way, the main difference being the combustion ignition, that in petrol engine is not due to gas compression but is controlled by a spark plug.

When it comes to pistons, however, their working principles are the same in both petrol and diesel engine, so it is possible to make a general discussion for both the engine types. The different elements of the piston system are indicated in the schematic drawing shown in Figure 1.2.

Piston functions are several: the main one is to transmit the gas forces via the connecting rod to the crankshaft, thus converting the thermal energy into mechanical energy. In addition, pistons must fulfil other functions that are crucial for engines operation: they are required to seal - in conjunction with the piston rings - the combustion chamber against gas leakage and infiltration of oil from the crankcase, and to dissipate the absorbed combustion heat to the cylinder liner and the cooling oil.

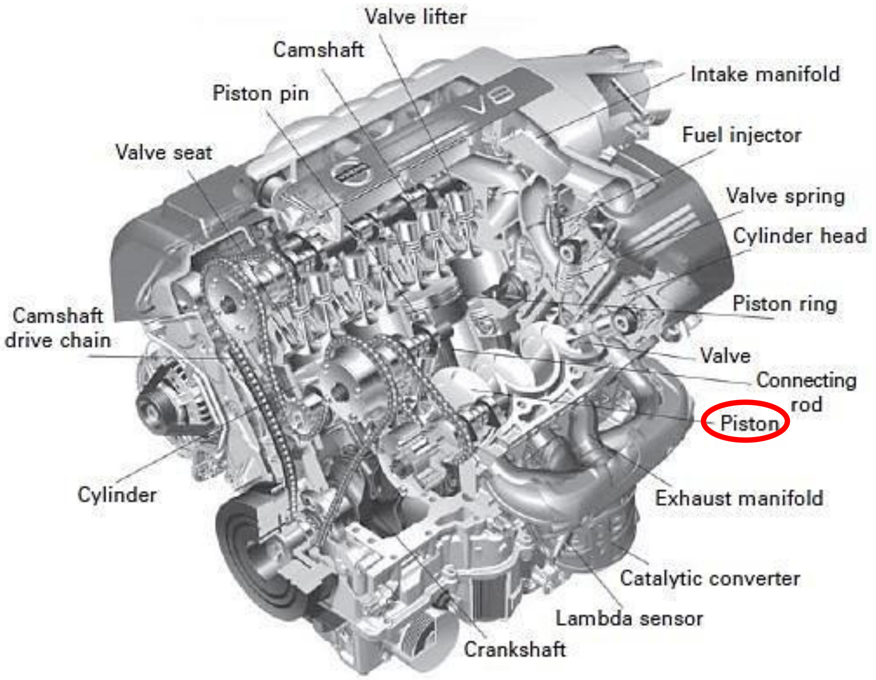

Fig. 1.1 - Cutaway of four-stroke cycle diesel engine with various parts indicated. [1]

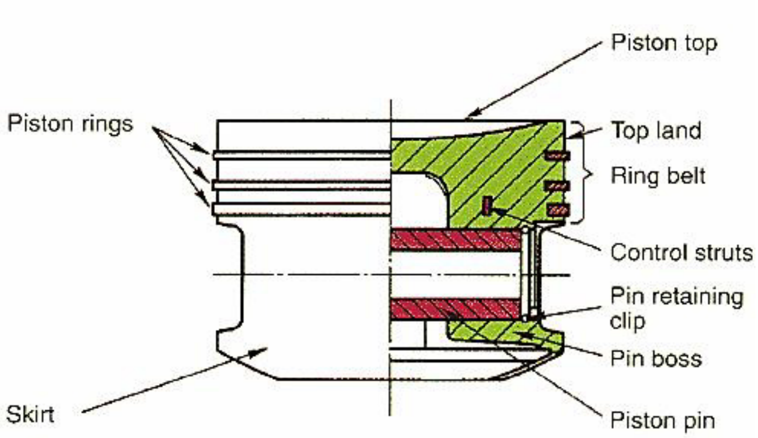

Fig. 1.2 – Schematics representation of a piston with its main parts indicated. [2]

That being said, it is easy to understand that pistons are subjected to high mechanical and thermal loads.

The mechanical loads on pistons result from extreme pressure cycles with pressure peaks up to 200 bar in the combustion chamber and huge forces of inertia caused the by extremely high acceleration during the reciprocating motion of pistons.

To make the situation more critical, these mechanical loads are superimposed by thermal stresses, which are primarily generated by the high temperature gradients on the piston top, due to thermal loads. Thermal loads result from the combustion process, that produces gas temperature peaks in the combustion chamber between 1800 °C and 2600 °C, depending on a number of factors such as engine type, fuel, gas exchange, compression, and air-fuel ratio. Moreover, the thermal loads on pistons rose significantly during last years as a result of higher power and performance demands, making pistons resistance requirements more demanding.

Thermal stresses on pistons have their origin in the quite complex temperature gradient which results as a consequence of heat transfer processes which dissipates combustion heat. Combustion heat is transferred to the chamber walls and piston top primarily by convection; the heat is then dissipated by the water cooling of the chamber walls and by the oil cooling of the piston. A large share of the heat absorbed by the piston top is transferred by the piston ring belt area; the remainder is essentially removed by the oil lubricant impinging on the underside of the piston. The head and top-land areas reach the highest temperature because they directly contact with combustion gas; other areas of the piston presents lower temperatures. The result of this heat exchange process is a complex temperature profile within the piston, as schematically outlined in Figure 1.3. It can be seen that in a piston for petrol (gasoline) engine temperatures range from 100 °C to more than 300 °C, while in diesel engines they can be even higher.

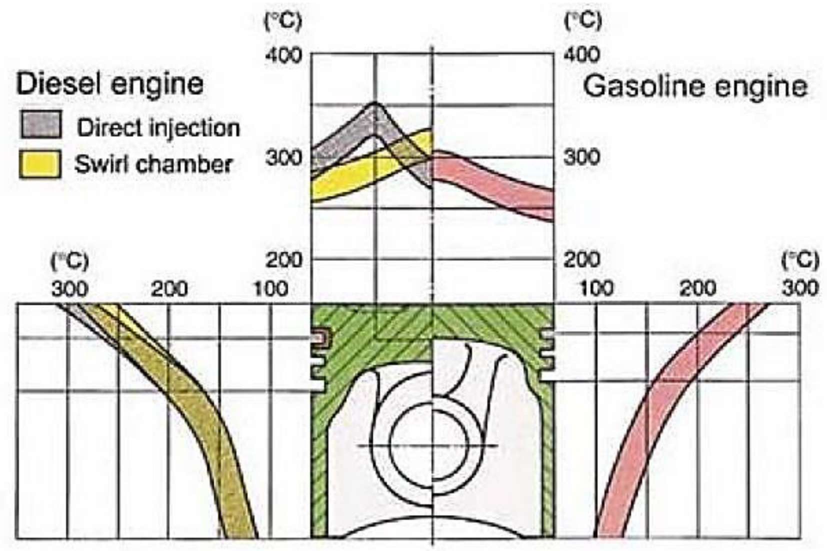

Fig. 1.3 - Operating temperatures distribution within the piston in automotive diesel and gasoline engines under full load. It can be seen that in a piston for gasoline engine temperatures range from 100 °C to more than 300 °C. [2]

That being said, it is easy to understand that proper piston materials must exhibit suitable strength to bear high mechanical and thermal stresses, and must retain this strength up to temperatures higher than 300 °C. In particular, high creep resistance and high fatigue strength at elevated temperature are required, to sustain high stresses at elevated temperatures for a high number of cycles.

Besides obvious resistance requirements, there are other important characteristics to be taken into account when choosing piston materials. One of this it the strength-to-weight ratio, which determinate the piston weight and thus has an influence on fuel consumption, as it will be extensively discussed later.

Moreover, a suitable wear resistance is required to sustain the high contact pressure exerted by the piston pin and avoid abrasive wear of the boss.

As the engine starts, the piston head heats up rapidly and expands in diameter, while the cylinder block heats up more slowly because of its large heat capacity and water-cooling system. If the running clearance between the piston and the cylinder bore is too narrow, then the expanded piston will touch the bore wall instantly, while, if the clearance is too wide, it will cause leakage of the combustion gas when the block warms up. Hence, to avoid these problems, the piston material should have a low thermal expansion coefficient, in addition to the other characteristics listed before. It should also present a low friction coefficient with the cylinder material, in order to reduce the energy loss and avoid scuffing.

High thermal conductivity is also required, in order to easily dissipate the combustion heat.

Finally, for the economic feasibility, piston materials should be easily casted and cost-effective. Therefore, material should exhibit low melting temperature and high fluidity, good machinability and a low cost.

1.1.2 Use of aluminium alloys for pistons

Recently, light aluminium alloys became the most widely used material for pistons production. The reason for the success of aluminium alloys as piston material in both gasoline and diesel engines lies in their specific characteristics: high strength-to-weight ratio, high thermal conductivity, simple fabrication techniques, easy machinability, high reliability and very good recycling characteristics. The high strength-to-weight ratio is a particularly attractive characteristic. In fact, it makes aluminium alloys effective in reducing the mass of components, and thus makes it easier to meet the ever stricter requirements concerning reduction of fuel consumption and exhaust gas emissions.

Most of the aluminium pistons are produced from cast, high-temperature resistant aluminium-silicon alloys, which can satisfy most of the requirements described in §1.1.1. Al-Si alloys are widely used for the production of pistons since alloying with Si brings several advantages. In fact, Si can reduce the thermal expansion coefficient, lower the alloy's density and thus decrease the piston weight, raise pistons wear resistance and effectively prevent seizure of the piston ring to the ring groove, thanks to a Vickers hardness value in the range of 870 to 1350 HV.

To achieve a combination of high strength and good ductility, necessary to resist to the high piston loads, the application of the appropriate heat treatment is of primary importance in heat-treatable aluminium alloys, such as the alloys from the Al-Si-Mg system. The heat treatment of aluminium alloys, which is able to dramatically increase the mechanical properties, consists of three steps, each of which must be carefully controlled in order to achieve the desired properties. The first step is solutionising, which is carried out at a temperature close to the solidus temperature of the alloy, in order to dissolve primary phases and obtain a solid solution. Solutionising must be quickly followed by quenching in cold (<30 °C) or hot (up to 90 °C) water, depending on the alloy, to block the atoms of alloying elements in solid solution and obtain a supersaturated solid solution at room temperature. To attain peak hardness (T6 condition), the alloy must be artificially aged at high temperature (150 - 200 °C depending on the alloy) soon after quenching. This heating allows the precipitation of strengthening phases from the supersaturated solid solution. The holding time at high temperature must be carefully controlled in order to avoid overageing conditions, that would lead to a reduction in hardness and strength.

Heat treatment of aluminium alloys has a crucial role. In fact, mechanical properties of Al-based alloys vary not just depending on chemical composition, but largely depend on the heat treatment [4,5]. Characteristics of heat treatment (heating temperature, holding time at this temperature and cooling rate) play a vital role for a good combination of microstructure and mechanical properties [4]. Several studies have been carried out to define the effect of heat-treatment parameters on microstructure and properties of Al-Si piston alloys and optimize them [4,5]. Manasijevic *et al.* [4], for example, highlighted the importance to determine the optimum times and temperatures of solution and ageing heat treatments, to obtain a satisfactory structure and the required mechanical properties of castings.

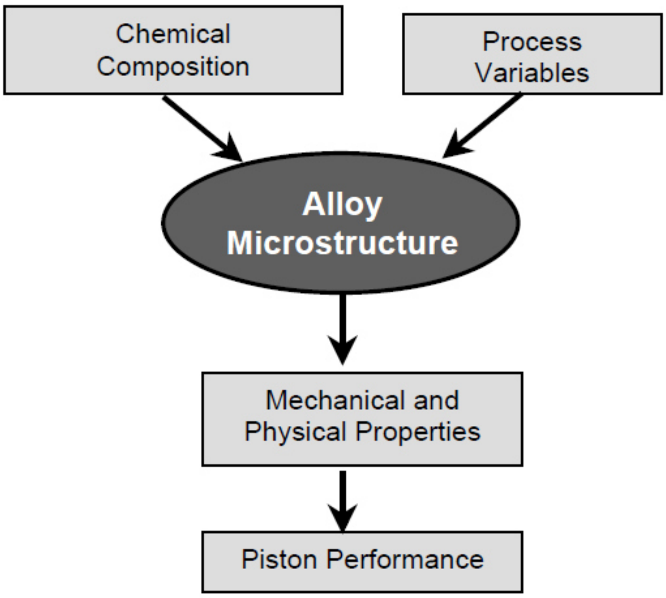

Fig. 1.4 – Schematic representation of factors affecting piston performance. [6]

The scheme reported in Figure 1.4 summarize what have been said. The key to the performance of a piston in the engine is the mechanical and physical properties of the piston material, which are themselves controlled by the microstructure of the cast piston. These microstructural factors, however, would themselves be expected to be determined by both chemical composition and process parameters, such as solidification rate and heat treatment. This parameters must be carefully controlled in order to obtain the desired properties.

However, when using heat-treatable aluminium alloys, operation at elevated temperatures represents a serious issue and must be taken into account. In fact, it is well known that when using a T6 heat-treated casting or wrought alloy at temperatures higher than the aging temperature, a decline in the mechanical properties will take place, this decline being function of both exposure time and temperature. This means that that the properties of the alloy obtained after heat treatment will change during high temperature operation.

Therefore, the main obstacle to the use of aluminium alloys for the production of pistons is represented by temperatures reached during engine operation. As shown in Figure 1.3, pistons are subject to a complicated temperature distribution from their head to skirt, the temperature at the piston head being high (about 300-350 °C), whilst that of the skirt being low (about 150 °C). However, a piston operated above 150 °C is gradually subject to age softening in the long term, so that the hardness obtained after T6 treatment is not kept constant during engine operation. It is generally accepted that the higher the holding temperature, the faster the softening; this is because softening is controlled by atomic diffusion.

Furthermore, the continuous development of engines is setting new challenges. In particular, ever rising demands regarding power density as well as the need for reduced emissions, low noise and more efficient fuel and oil consumption have resulted in steep increases in both specific powers and maximum cylinder pressures; this, in turn, lead to higher temperatures and pressures being felt by the pistons. For the future, pistons are going to reach temperatures as high as 400 °C and pressures higher than 20 MPa [6].

The increasing temperatures and pressures cause service durability problems, particularly in three main areas of the piston: the top ring groove, upper pin boss region and the combustion bowl edge, where the concurrent action of high temperature and stresses are likely to lead to failure.

The top ring groove region is subjected to considerable wear as a result of gas, inertia and frictional forces together with the rotation of the top ring.

The upper pin boss region is one of the most highly loaded areas of the piston. The material in this region is subjected to a high cyclic stress whilst running at a temperature of around 200°C. Fatigue cracks can initiate at the pin bore and propagate through the pin boss region under the action of these stresses.

The combustion bowl edge region is directly exposed to the hot combustion gases and thus reaches very high temperatures. Peaks in excess of 400°C can now be reached at the bowl rim in some applications. The load from the combustion pressure results in high mechanical stresses on the bowl rim. This region is also subjected to significant thermal strains as a result of the expansion and contraction of the bowl rim which occurs during engine operation. These stresses and strains can lead to fatigue cracks emanating from the bowl rim after prolonged exposure.

Considerable development work has been required over the past 20 years to increase durability in these piston areas to cope with the increases in cylinder pressure and crown thermal loading.

1.1.3 Evolution of casting aluminium alloys to increase heat resistance

The continuing development of modern engines leads to specific objectives for further piston development: reduction of piston weight, increase of mechanical and thermal load capacity, lower friction and thus improved scuffing resistance, etc. These goals can be achieved by a targeted combination of high performance aluminium piston materials, novel piston designs and the application of innovative coating technologies. This paragraph is focused on enhancements in aluminium alloys achieved during the last decades, which allowed to improve engines efficiency.

As explained in the previous paragraph, precipitation hardening treatment can strengthen aluminium piston alloys, but the strength is kept only at lower temperature parts of the piston, while it disappears in higher temperature areas, particularly at the centre of the head. Clearly, age hardening cannot guarantee strength in these conditions.

The trend to raise piston temperatures even more, demand an aluminium alloy with higher strength at elevated temperatures. In the temperature range where the age hardening effect disappears, the base strength of the alloy becomes important. It is generally known that strength at high temperatures depends on the distribution as well as the quantity of dispersed intermetallic compounds [1]. At elevated temperatures, thermally stable intermetallics should prevent or retard the movement of dislocations, and thus increase the mechanical properties of the alloy. The strengthening effect of such intermetallics depends on their stability at elevated temperatures. More thermally stable intermetallics achieve a better strengthening effect: generally, the higher the quantity of intermetallic compounds, the higher the strength [4]. However, it is difficult to increase the content above a certain limited amount because the increased content coarsens the intermetallic compound, which in turn makes the material brittle [1].

From the metallurgical point of view, the obvious compositional additions to produce thermally stable intermetallics and increase high temperature strength of the Al-Si-(Mg) piston alloys are copper and nickel.

Copper is added to increase the strength and fatigue resistance without loss of castability. Increasing the amount of copper, in fact, increases the amount of the age hardening precipitate $CuAl_2$, and thus the hardening effect of heat treatment. Jayamathy and Vasanth [7] proved that increasing copper to 3.4 wt.% in a Al-Si eutectic alloy can retard age softening and improve durability of pistons.

Stadler *et al.* [3] confirmed that an increase in Cu concentration results in a significant improvement of the high temperature strength. Exposure to temperatures greater than 250 °C for an extended period, however, results in severe coarsening of Al_2Cu precipitates due to Ostwald ripening [8]. These coarser precipitates are ineffective for strengthening purposes and could even provide sites for fatigue crack initiation.

When it comes to nickel, Stadler *et al.* [3] showed that both yield and tensile strengths increase upon the addition of Ni, but only in the range below 1-2 wt.% Ni. The result found by the authors are displayed in Figure 1.5.

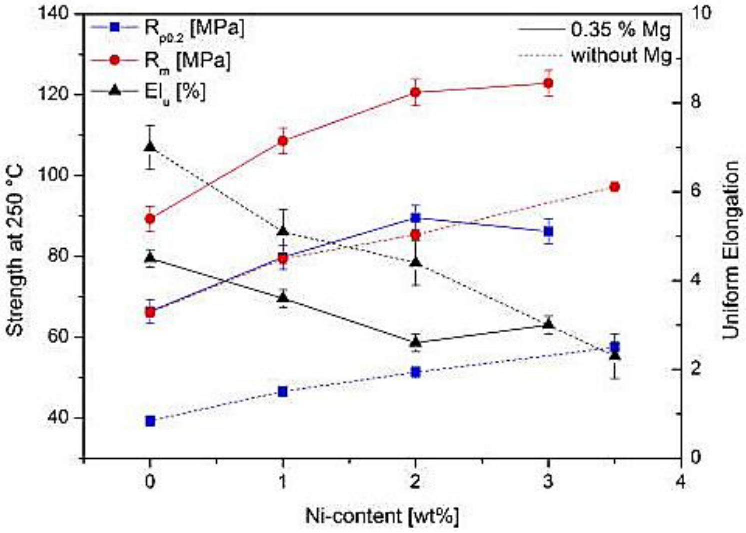

Fig. 1.5 - Mechanical properties as a function of Ni content in near eutectic Al-12Si-0.44Fe-0.30Mn alloys: full lines represent alloys containing 0.35%Mg, and dashed lines illustrate Mg free alloys; all alloys were tested at 250 °C after solutionising at 495 °C for 8 h and long term exposure to 250 °C for 100 h. [3]

However, Ni is often added not alone but in combination with Cu. The simultaneous addition of Cu and Ni results in the formation of thermally stable AlCuNi intermetallics, which, although initially much coarser than $CuAl_2$, do not coarsen rapidly at the elevated temperatures experienced in the piston crown and thus improve the strength of the piston alloy at 350°C. Increasing the Ni content also results in the formation of FeNiAl intermetallic phases that are also stable at 350 °C, providing further strengthening at crown operating temperatures [6]. Mielke *et al.* [8] found that adding 4 wt.% Cu, 2 wt.% Ni and 0.8 wt. % Mg to a Al-12Si alloy results in improvements in fatigue strength and creep resistance at temperatures up to 340 °C. The authors [8] report that Ni positively influences the alloy kinetics because it is almost insoluble in the Al-matrix even at higher temperatures, and thus is able to avoid the formation of coarse Al_2Cu particles. The Ni-containing precipitates are of the type $Al_3(Ni,Cu)_2$ and result stationary during ageing at higher temperatures; therefore can be regarded as "anchorage" for Cu, avoiding the formation of coarse Al_2Cu particles. The study conducted by Jeong [9] on Al-12Si wt% casting alloys for piston proved that the room and high temperature (up to 400 °C) hardness and tensile strength are increased with Ni and Cu content, whereas the elongation is increased in the reverse case. These results are shown in the graph in Figure 1.6. Jeong [9] also found that the creep properties were significantly improved and softening behaviour during high temperature fatigue was reduced as the alloying elements were increased. In conclusion, these results confirm that the rise of Cu and Ni content contributes to high temperature stability.

Although additions of copper and nickel provide beneficial strengthening phases, the levels of additions need to be tightly controlled to avoid the formation of large intermetallic clusters that can act as fatigue crack initiators [6].

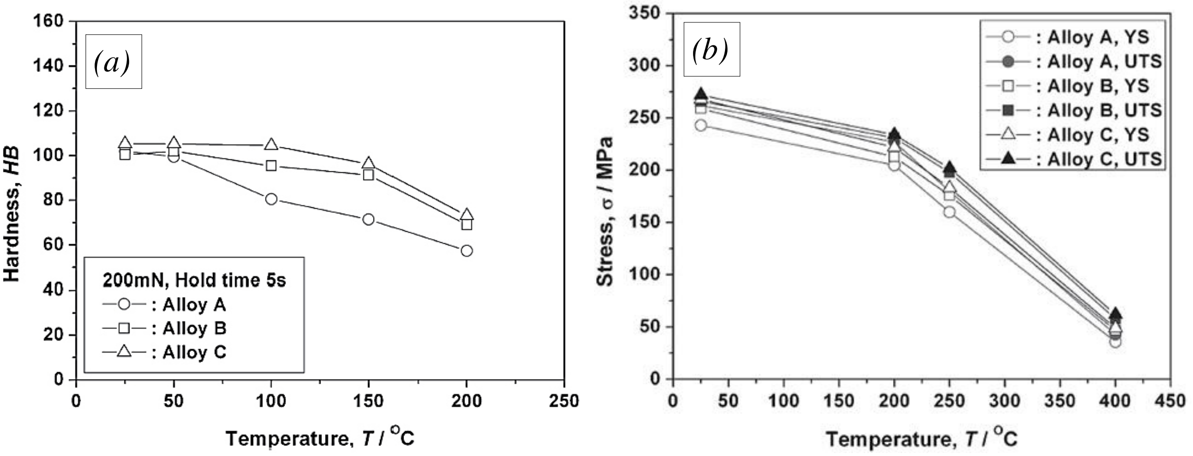

Fig. 1.6 – Variation of hardness (a) and strength (b) with temperature in three Al-12Si-0.8Mg alloys containing 1.0 wt.% Cu and 1.2 wt.% Ni (Alloy A), 2.8 wt.% Cu and 2.6 wt.% Ni (Alloy B), 4.9 wt.% Cu and 2.8 wt.% Ni (Alloy C). The graphs show that increasing Cu and/or Ni amounts result in higher resistance both at room and high temperatures (up to 400 °C). [9]

In addition to Cu, Ni and Mg, more novel alloying additions which could have an effect on the elevated temperature fatigue strength of Al-Si piston alloys were examined over the past years. The transition metals (same group of the periodic table as Cu, Ni and Fe) are of most interest in this respect. Combinations of Cu, Ni, Fe, Mn, Mo, Co, Zn and Cr were examined in detail, and some combinations of these elements were found to have the capacity to increase both 200 °C and 350 °C fatigue strength. The additions of this element did, however, have to be tightly controlled in the same way as Ni to avoid the formation of large brittle intermetallics [6].

The different alloy modifications studied during the past 20 years have given significant improvement in the fatigue strength of piston alloys, particularly at 350 °C [6]. That is of most interest, since the aim of the development of new heat resistant alloys has been to achieve the maximum performance at 350 °C and above, whilst not losing too much fatigue resistance at lower test temperatures (200 °C). This has been the biggest challenge since the mechanisms for increasing fatigue performance at very high temperatures tend to involve having greater numbers of brittle intermetallic particles in the piston alloy microstructure, which can initiate fatigue cracks under the action of high mechanical loads at lower temperatures if their shape, size or distribution is not controlled. Alloying additions and process route changes which affect the size, shape and segregation of intermetallic phases have, therefore, become very important in the development of further aluminium based casting alloys [6].

Nowadays, in cast aluminium alloys for pistons there are at least six major alloying elements: Al, Si, Cu, Ni, Mg and Fe, which have a significant impact on the physical and mechanical properties of these alloys. Usual grades of piston alloys contain 11–23 wt.% Si, 0.5–3 wt.% Ni, 0.5–5.5% Cu, 0.6–1.3 wt.% Mg, up to 1 wt.% Fe , and up to 1% Mn [4,5]. In these alloys, Fe is usually an impurity and there is a need to keep its amount at low levels, since Fe forms undesired intermetallics dangerous for fatigue resistance. To control the shape of the Fe-rich intermetallics it is common foundry practice to add a small amount of Mn [8].

1.2 AA 2618 ALUMINIUM ALLOY

AA 2618 is a Al-Cu aluminium alloys used for high-temperature applications. In this paragraph are reported its characteristic and mechanical properties, which make this alloy particularly suitable for applications in high-performance engines.

An analysis of the microstructural features which make this alloy able to stand elevated temperatures is also presented.

Finally, a detailed description of heat treatment, and in particular of precipitation during ageing treatment, is provided.

1.2.1 Generalities and mechanical properties

AA 2618 is an aluminium alloy from the 2xxx series. 2xxx series, whose principal alloying element is copper (Cu), is a class of heat treatable wrought aluminium alloys, used in many applications for their particular combinations of strength and corrosion resistance. In aerospace and automobile industries, the high strength-to-weight ratio, which is particularly important in the design of structural components, makes these alloys a very attractive class of materials. For this reason, aluminium-copper alloys containing 2 to 10 % Cu, generally with other additions, form an important family of alloys. One of the most common addition is Mg, which enhance the behaviour of Al-Cu alloys to precipitation hardening, increasing strength after ageing treatment [10].

Among the Al-Cu-Mg system, alloy 2014 (Al-4.4Cu-0.8Si-0.8Mn-0.5Mg) and 2024 (Al-4.4Cu-1.5Mg-0.6Mn-0.5Si-0.5Fe) are widely used in aircraft structures, rivet hardware, truck wheels, screw machine products, and other miscellaneous structural applications because of their good performance below 100 °C.

However, the mechanical properties of these alloys decrease significantly when they are exposed at temperature more than 100 °C [11].

An improvement in heat resistance was achieved with AA 2618 alloy, also known as RR58 and EN AW-2618A. Aluminium based alloy AA 2618 is an Al-Cu-Mg-Fe-Ni forging alloy developed for aircraft engine components and presents a good elevated-temperature strength up to 240 °C [12].

AA 2618 aluminium alloy is a heat treatable Al–Cu–Mg alloy with Fe, Ni and Si additions to form intermetallic phases. This alloy is designed for parts operating at elevated temperatures which are manufactured mainly by plastic deformation, as forging, extrusion and rolling [13]. This alloy draws its strength from a combination of precipitation and dispersion hardening [14].

A peculiar characteristic of AA 2618 is its quite high content of Fe and Ni; its chemical composition, according to European and American standards, is listed in Table 1.1.

Chemical composition [wt%] of EN AW-2618A											
Cu	**Mg**	**Ni**	**Fe**	**Si**	**Ti**	**Mn**	**Zn**	**Zr + Ti**	**Others each**	**Others total**	**Al**
1.8 2.7	1.2 1.8	0.8 1.4	0.9 1.4	0.15 0.25	max 0.20	max 0.25	max 0.15	max 0.25	max 0.05	max 0.15	balance

(a)

Chemical composition [wt%] of AA 2618										
Cu	**Mg**	**Ni**	**Fe**	**Si**	**Ti**	**Mn**	**Zn**	**Others each**	**Others total**	**Al**
1.9 2.7	1.3 1.8	0.9 1.2	0.9 1.3	0.10 0.25	0.04 0.20	max 0.25	max 0.10	max 0.05	max 0.15	balance

(b)

Tab. 1.1 – Limits for alloying elements in aluminium alloy 2618 according to European Standard EN 563-3 (a) and to The Aluminum Association USA (b)

The addition of Fe and Ni to this alloy was found to improve its performance in applications involving high temperature exposures up to 300 °C, making this alloy suitable for the production of engines components for both automotive and aircraft applications. In fact, AA 2618 is frequently used for high temperature applications in automotive and aerospace industries and has been successfully used as the primary structure of the supersonic Concorde airplane [15].

Figure 1.7 shows a comparison between the mechanical properties of aluminium alloy AA 2618 and other two main alloys of the Al-Cu-Mg system, AA 2014 and AA 2024, after high temperature exposure for 1000 h. While AA 2014 and AA 2024 are subjected to a sharp decrease in yield strength after exposure at temperature higher than 100 °C, AA 2618 shows good mechanical properties at temperatures as high as 200 °C. In other words, AA 2618 presents a higher heat resistance than AA 2014 and AA 2024 alloy.

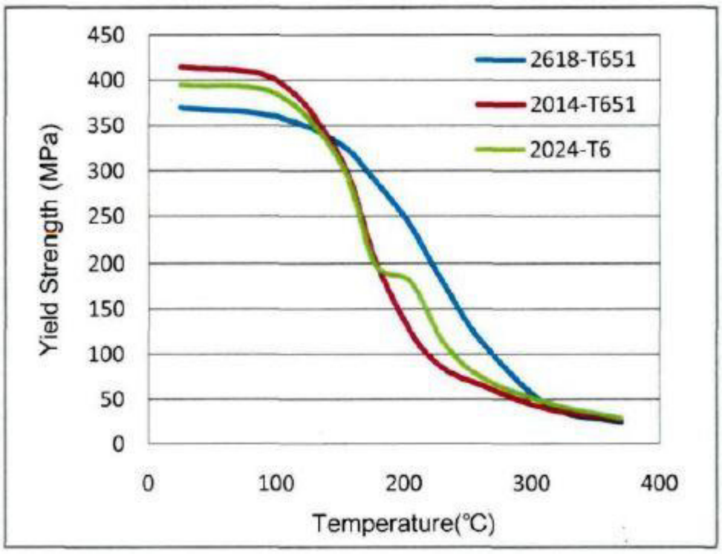

Fig. 1.7 - Values of 0.2% yield strength of three Al-Cu-Mg aluminium alloys as a function of temperature after exposure for1000 h. [15]

Table 1.2 shows the mechanical properties (ultimate tensile strength, yield strength and elongation) of AA 2618 in peak-ageing T61 condition after thermal exposure at temperature from 100 °C to 370 °C and for times to 0.5 to 10000 h. The data show that at temperature lower than 200 °C the alloy is quite stable, while for higher temperatures the decrease in UTS and YS is quite fast. For example, after 0.5 h at 260 °C the values of ultimate tensile strength and yield strength are little more than the half of the values at room temperature. As expected, the reduction in strength is accompanied by an increase in elongation.

Figure 1.8 [11] shows the influence of the exposure at elevated temperatures for times ranging from 0.5 h to 1000 h on the tensile properties of AA 2618 in peak-aged T61 condition. The properties are determined at the exposure temperature, after holding for the indicated time under no load. Tensile and yield strengths are plotted as percentage of the corresponding room-temperature value, while elongation is plotted as value determined at temperature. Figure 1.8 shows that for temperatures up to 100-150 °C the length of time of exposure at high temperature has a negligible effect. In fact, there is no consistent difference in the mechanical properties of material exposed for 0.5 and 1000 hours. Not even the effect of test temperature has a great effect, with mechanical properties at 150 °C being approximately 90% of the values at room temperature. In contrast, when temperature is increased over 150 °C the loss of strength is quite fast, and the effect of exposure time become increasingly important.

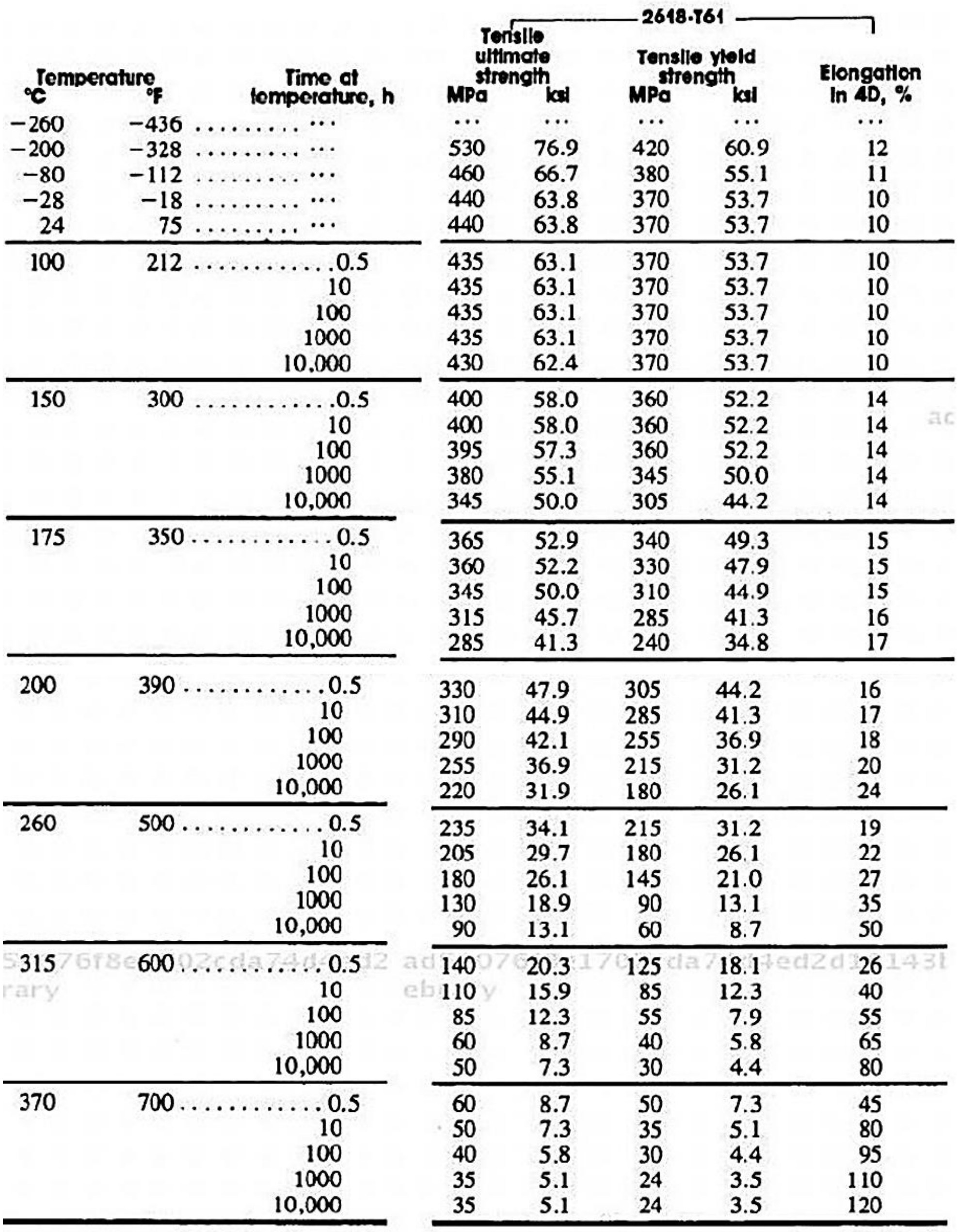

Temperature		Time at temperature, h	2618-T61				
			Tensile ultimate strength		Tensile yield strength		Elongation in 4D, %
°C	°F		MPa	ksi	MPa	ksi	
−260	−436	···	···	···	···	···	···
−200	−328	···	530	76.9	420	60.9	12
−80	−112	···	460	66.7	380	55.1	11
−28	−18	···	440	63.8	370	53.7	10
24	75	···	440	63.8	370	53.7	10
100	212	0.5	435	63.1	370	53.7	10
		10	435	63.1	370	53.7	10
		100	435	63.1	370	53.7	10
		1000	435	63.1	370	53.7	10
		10,000	430	62.4	370	53.7	10
150	300	0.5	400	58.0	360	52.2	14
		10	400	58.0	360	52.2	14
		100	395	57.3	360	52.2	14
		1000	380	55.1	345	50.0	14
		10,000	345	50.0	305	44.2	14
175	350	0.5	365	52.9	340	49.3	15
		10	360	52.2	330	47.9	15
		100	345	50.0	310	44.9	15
		1000	315	45.7	285	41.3	16
		10,000	285	41.3	240	34.8	17
200	390	0.5	330	47.9	305	44.2	16
		10	310	44.9	285	41.3	17
		100	290	42.1	255	36.9	18
		1000	255	36.9	215	31.2	20
		10,000	220	31.9	180	26.1	24
260	500	0.5	235	34.1	215	31.2	19
		10	205	29.7	180	26.1	22
		100	180	26.1	145	21.0	27
		1000	130	18.9	90	13.1	35
		10,000	90	13.1	60	8.7	50
315	600	0.5	140	20.3	125	18.1	26
		10	110	15.9	85	12.3	40
		100	85	12.3	55	7.9	55
		1000	60	8.7	40	5.8	65
		10,000	50	7.3	30	4.4	80
370	700	0.5	60	8.7	50	7.3	45
		10	50	7.3	35	5.1	80
		100	40	5.8	30	4.4	95
		1000	35	5.1	24	3.5	110
		10,000	35	5.1	24	3.5	120

Tab. 1.2 – Typical mechanical properties (ultimate tensile strength, yield strength and percent elongation) of AA 2618 in peak-aging condition at various temperatures after exposure for times from 0.5 h to 10000 h. [10]

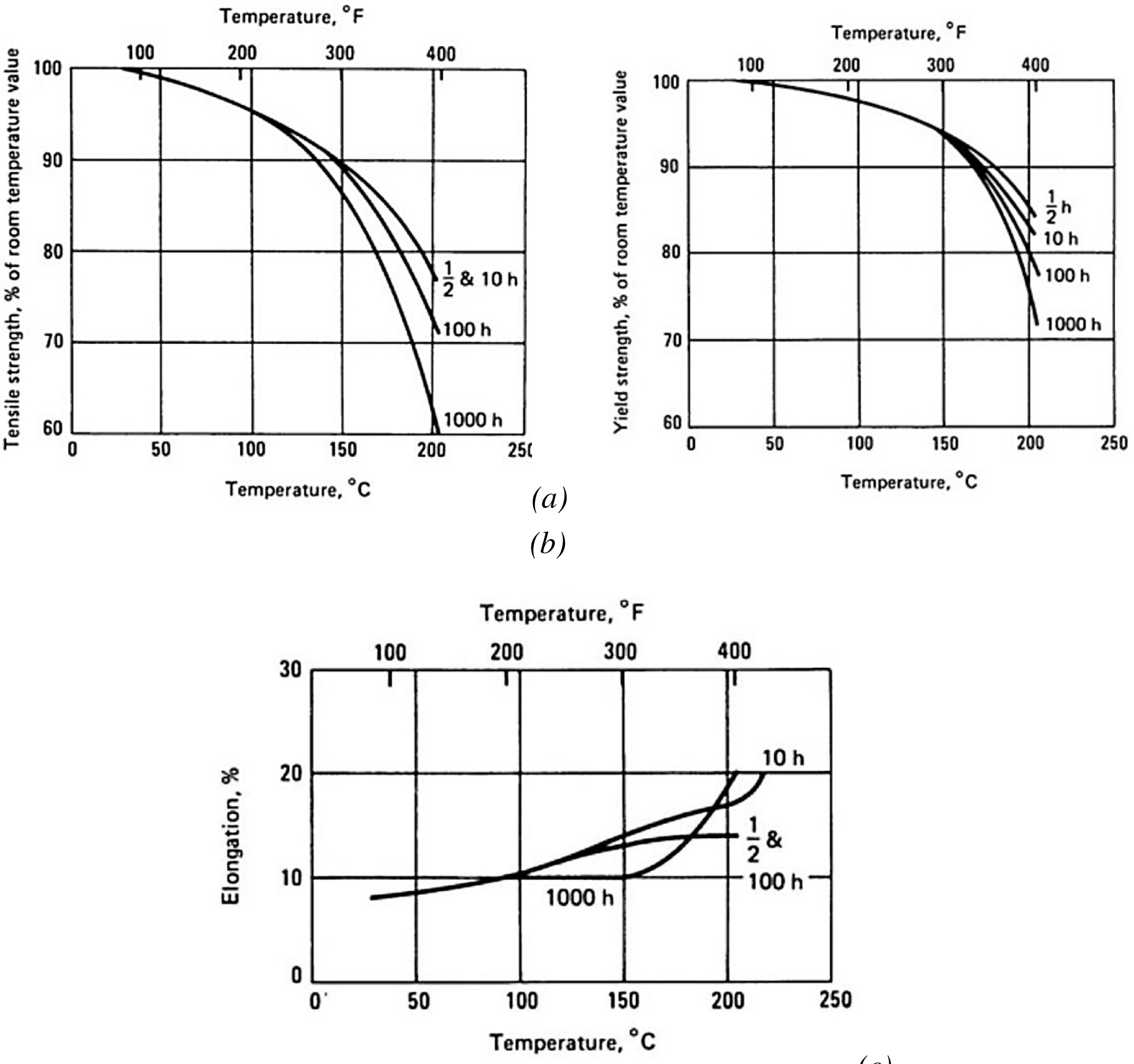

(a)

(b)

(c)

Fig. 1.8 - Influence of prolonged holding at elevated temperature on tensile properties of alloy 2618-T61 hand-forged billets: tensile strength (a), yield strength (b) and elongation to failure (c). Properties determined at temperature after holding for the indicated time under no load. Tensile and yield strengths plotted as percentage of corresponding room-temperature value. Elongation plotted as value determined at temperature. [11]

1.2.2 Effects of combined additions of Ni and Fe

Wilson and Forsyth [17] found that when 1.0 wt.% Ni and 1.0 wt.% Fe were added together into the Al-Cu-Mg alloy, the age-hardening behaviour at both room and elevated temperature restored to that of the ternary Al-2.5Cu-1.2Mg alloy, as shown in Figure 1.9.

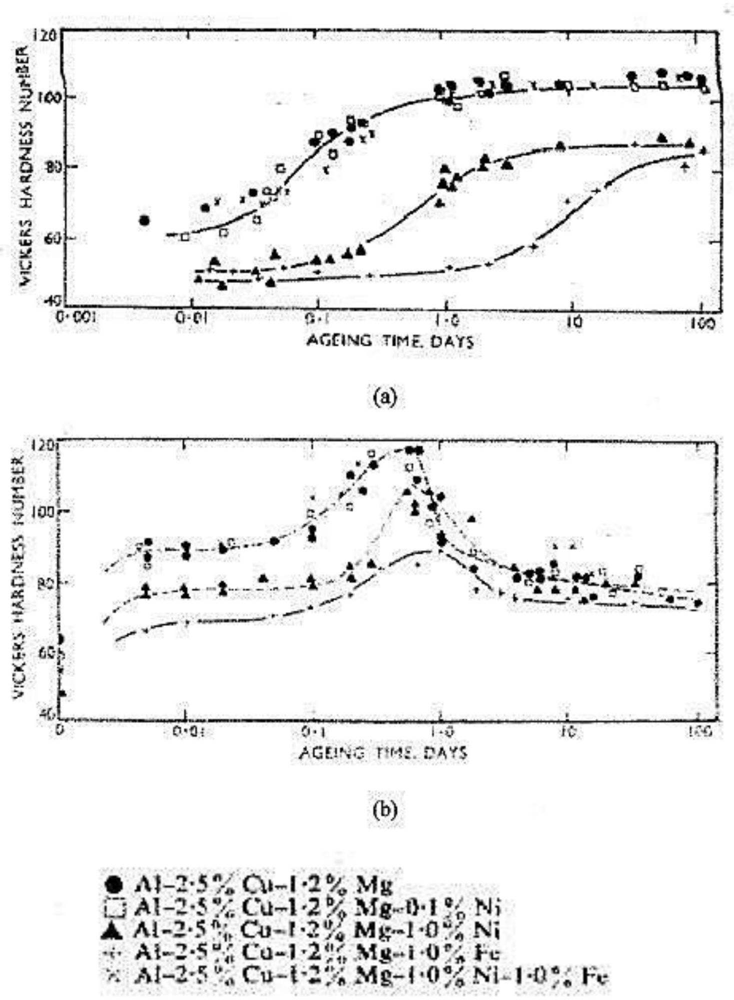

(a)

(b)

Fig. 1.9 - Effects of Fe and Ni on the age hardening of an Al-2.5Cu-1.2Mg alloy at: (a) room-temperature and (b) 190 °C. [17]

This observation can be explained in terms of the fact that the combined addition of Ni and Fe forms the low Cu content Al_9FeNi intermetallic phase and therefore allows the full Cu content of the alloy to enter into solid solution, which in turn improve the age-hardening process. This phase also provides insoluble particles which stabilize the grain size by pinning the grain boundaries, and as a result the grain growth is restricted during solution-treatment and high temperature applications [17].

Oguocha *et al.* [18] reported the Al_xFeNi phase in cast AA 2618 alloy has a C-centred monoclinic structure and the structural formula of this phase varies from particle to particle, according to the aluminium content.

Moreau *et al.* [19] studied a Al-4.4Cu-1.5Mg-0.2Sn (wt.%) PM alloy with and without addition of 1.0 wt.% Fe and 1.0 wt.% Ni, heat treated to peak-aged conditions. A significantly higher concentration of secondary phases (Al_9FeNi, Al_7Cu_2Fe, Al_7Cu_4Ni) was found when the material was modified with Fe and Ni. Isochronal exposure trials (100 h) revealed that the modified material was microstructurally and mechanically stable at temperatures as high as 160 °C, while under the same conditions, the unmodified alloy experienced measurable degradation. DSC data confirmed that precipitates in the modified material offered enhanced thermal stability at temperatures ≤160 °C. DSC analysis after isothermal aging at 120 °C for 1000 h showed that the precipitates in the modified alloy are more resistant to overaging effect. At higher temperature (>200 °C) the Fe/Ni additions were less effective and both alloys exhibited comparable level of strength degradation, while at 280 °C both alloys resulted highly over-aged [19]. In conclusion, according to Moreau *at al.* [19], adding Fe and Ni in effective to retard age-softening at temperature lower than 200 °C.

No effects were observed on the nucleation of the strengthening precipitates that form during heat treatment. The grow rate and the general distribution of these precipitates are little affected by the addition of 1.0 wt.% Fe and 1.0 wt.% Ni [17].

1.3 HEAT TREATMENT AND PRECIPITATION PROCESSES

Precipitation hardening (or age hardening) represents the most important heat treatment for aluminium alloys. It is composed by three different phases: solutionizing, quenching and ageing. Each of these phases is fundamental and must be carefully controlled in order to attain the desired properties.

It’s well known that age hardening is a very effective way to enhance the mechanical properties of heat-treatable aluminium alloys. The purpose of age hardening is to induce the formation and precipitation of fine particles of alloying atoms within the matrix. These precipitates will cause a deformation in the matrix that will obstruct the movement of dislocations, and therefore improve the mechanical properties of materials. Strengthening mechanism is strongly conditioned by precipitates size and type.

The heat treatment procedures of AA 2618 alloy are similar to that of other 2xxx series alloys and are discussed in this paragraph. First, a brief description of solutionizing and quenching is given. Then, an investigation on precipitation processes during ageing treatment is presented. A brief description of modification during overageing is also reported.

1.3.1 Solution heat treatment, quenching and ageing

The purpose of solution heat treatment is to obtain a solid solution at high temperature, containing the maximum possible concentration of the hardening alloying elements, which mainly are Cu and Mg in AA 2618 alloy.

The rate of solution increases with temperature, because of increased diffusion rate. At low temperatures, alloying elements are not completely dissolved into the matrix, and this condition may reduce the strengthening effect after ageing treatment. On the other hand, high solution treatment temperatures could cause incipient melting of eutectic phases leading to a decrease in both strength and ductility.

Usually, the nominal temperatures specified for commercial solution heat treatments of many alloys are only 10-15 °C below the eutectic temperature, in order to achieve the highest solution rate without compromise the material. In these conditions, good control and uniformity of temperature within furnaces are essential to avoid incipient melting [16].

Phase diagram for AA 2618 alloy is not available, since the complex chemical composition of the alloy makes its construction very difficult. Therefore, in order to choose the optimal solution temperature for this alloy, it is necessary to refer to industrial practice, or to use techniques such as DSC in order to verify the solidus temperature. ASM Handbook [20] indicates 530 °C as typical solution temperature for this alloy.

The holding time at the nominal solution heat-treating temperature (soak time) must be long enough to realise a satisfactory degree of solution of the undissolved or precipitated soluble phases and to achieve good homogeneity of the solid solution. The optimum soak time is a function of temperature and of microstructure before heat treatment; however, compared to the solution temperature, the solution holding time has less effect on microstructure and mechanical properties of heat-treated material [20].

Quenching after solution treatment is a very critical step in the sequence of heat treatment practice. The objective of quenching is to preserve as nearly intact as possible the solid solution formed at the solution heat treating temperature, by rapid cooling to lower temperatures, usually near to room temperature.

Cooling rate during quenching has a significant impact on precipitation strengthening. In fact, when cooling rate is lower than about 50 °C/s, the tensile strength obtained after ageing rapidly decreases. The reduction in strength for a specific decrease in cooling rate differs from one alloy composition to another [20]. Figure 1.10 shows the relation between cooling rate in the range from 400 to 290 °C and ultimate tensile strength after ageing for eight wrought aluminium alloys [20]. All the alloys exhibit a sharp decrease in tensile strength when cooling rate becomes lower than 50-100 °C/s, confirming the important influence of quenching on mechanical properties of heat-treated materials. This sensitivity to the quench path is attributed primarily to loss of solute by heterogeneous nucleation and growth of quench precipitates which do not provide strengthening during following ageing treatment [21].

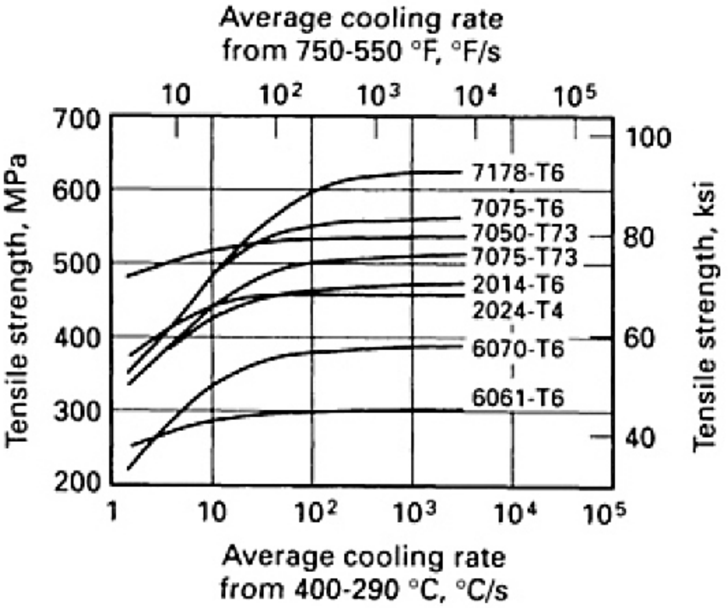

Fig. 1.10 – Ultimate tensile strength of eight wrought aluminium alloys obtained after ageing, as a function of average quench rate in the range from 400 to 290 °C. [20]

When quenching medium is concerned, water is not only the most widely used medium but also the most effective. Moreover, in water quenching, cooling rates can be reduced by increasing water temperature.

AA 2618 alloy is a quench sensitive alloy, therefore cooling rate is a very important factor in the manufacturing and post-fabrication processes of this alloy. In particular, it equally affects the as-quenched and aged properties of this alloy, but it does not alter the precipitation sequence of during ageing treatment [22].

After solution treatment and quenching, a supersaturated solid solution is obtained at room temperature. If the material in these conditions is exposed at room or higher temperature, some of the solute atoms will react with some of the solvent atoms to form precipitate particles, since the solute content is higher than the solubility limit at that temperature. These fine precipitates will obstruct the movement of dislocations and therefore improve the mechanical properties of the material. The precipitation process is known as ageing, and it is called “natural” if it takes place at room temperature, while it is called “artificial” if it takes place at higher temperatures (typically in the range 150-200 °C).

During natural ageing, proper precipitates are not formed, but just a clustering or a short-range ordering of solute atoms occurs, therefore the resulting strengthening effect is low. These clusters are called GP zones, after the scientists Gunier and Preston who first were able to observe these zones with x-ray diffraction techniques. On the contrary, when aluminium alloys are artificially aged, precipitation of various metastable phases occurs, providing a much higher strengthening effect.

The strengthening effect attained due to precipitation hardening depends on shape, size, type and amount of precipitates formed during ageing, which in turn are a function of ageing temperature and time (for a given chemical composition and microstructure obtained after solutionizing and quenching). Depending on the chemical composition of the alloy, different metastable phases are formed. Precipitates formed during the first stage of ageing treatment are too fine to realise an effective strengthening of the alloy. These precipitates then grow in size and develop due to the effect of soaking time and temperature. Particular combinations of time and temperature result in a critical precipitate size, which lead to optimum strengthening effect. At the end of the precipitation sequence the equilibrium phases are formed, with resulting loss in mechanical properties.

In the next paragraphs, a discussion about precipitations sequence in AA 2618 is presented. Since AA 2618 alloy has a quite complex chemical composition, its precipitation sequence is complex too. In order to understand it, precipitation behaviour in Al-Cu and Al-Cu-Mg alloys is described first.

1.3.2 Precipitation sequence in Al-Cu and Al-Cu-Mg alloys

On the basis of what explained above, it is clear that aluminium alloys must exhibit two fundamental characteristics to make precipitation treatment possible: solute atoms must present sharp reduction of solubility in the aluminium matrix with decreasing temperature, and must form fine metastable precipitates before reaching the equilibrium condition.

Clearly, not all aluminium alloys are suitable for heat treatment, but Al-Cu alloys show good characteristics in these respect. Additions of other alloying elements, such as Mg and Si as in AA 2618 alloy, can improve the precipitation hardening behaviour in this alloy system. Al-Cu phase diagram is reported in Figure 1.11, with temperature ranges indicated for heat treating of these alloys.

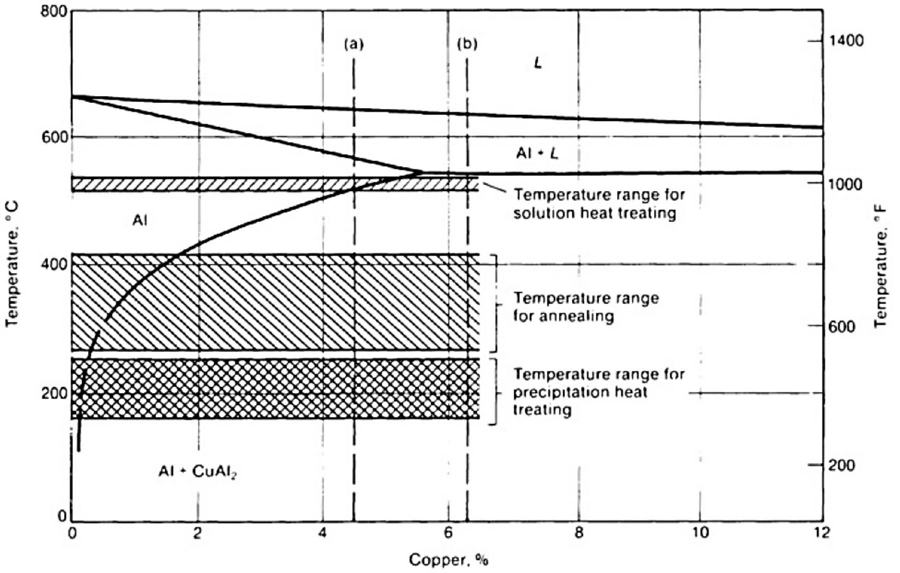

Fig. 1.11 – Portion of A-Cu binary phase diagram. The sharp slope of the solvus curve at the Al-rich corner makes Al-Cu alloys suitable for precipitation hardening. Temperature ranges for annealing, precipitation heat treating, and solution heat treating are indicated. [20]

Hardy [23] examined the ageing behaviour of an Al-4Cu alloy solution heat treated for at least 48 h at 520 °C and water quenched to 20 °C. The hardness was measured as a function of ageing time at various temperatures, as shown in Figure 1.12. This graph shows some important features of aluminium alloys behaviour during ageing treatment.

An important characteristic is that the hardness curves pass through a maximum value, and are quite temperature dependent. The maximum hardness, which is known as the peak ageing point or T6 temper, is associated with precipitates attaining a critical size and distribution.

When the precipitates become coarser, they are too dispersed to be effective in retarding dislocation motion, therefor hardness decreases. The formation of the precipitates to an optimum size and distribution is more rapid at higher temperature, so that the peak hardness occurs at shorter time as the ageing temperature increases. However, the number of formed precipitates decreases with increasing temperature because the degree of supersaturation decreases, and the magnitude of the peak hardness decreases too.

Moreover, it is expected that at a given ageing temperature, the higher the solute content, the faster the peak hardness will be attained, because the supersaturation will be greater, and therefore diffusion will be faster. Harden also increases at higher solute content, because more precipitates form.

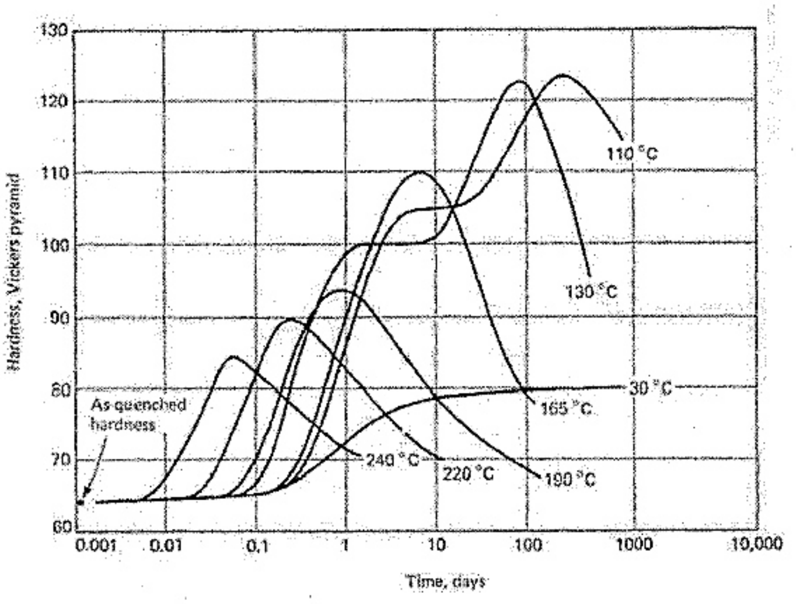

Fig. 1.12 – Hardness as a function of ageing time for an Al-4Cu alloy after solutionizing (520 °C for 48 h) and quenching to room temperature. [23]

In Al-Cu alloys it has been proposed [24] that the decomposition sequence contains one or more of the following processes:

$$\alpha\text{-Al(sss)} \rightarrow \text{GP zones} \rightarrow \theta'' \rightarrow \theta' \rightarrow \theta\ (\text{CuAl}_2)$$

where α-Al(sss) represents the supersaturated solid solution, θ'' and θ' are metastable semi-coherent precipitates and θ is the equilibrium incoherent precipitate represented by the formula $CuAl_2$. Furthermore, Ringer and Hono [24] suggested that GP zones formation is preceded by solute clusters that cannot be observed with TEM techniques. According to the authors [24], GP zones may be regarded as fully coherent metastable precipitates. Various steps in this process may be suppressed by ageing at temperatures close to or above the solvus temperatures of intermediate precipitates.

One of the most important heat treatable aluminium alloy systems is represented by Al-Cu-Mg system, which includes, among the others, AA 2618 alloy. Addition of Mg to Al-Cu binary alloys lead to a variety of microstructures and phases highly dependent on alloy composition, as shown by the Al-Cu-Mg phase diagram in Figure 1.13 [24]. According to Ringer and Hono [24], the addition of Mg to Al-Cu alloys in the composition range of AA 2618 alloy, lead to precipitation of another phase, called S, whose equilibrium composition is represented by the formula Al_2CuMg.

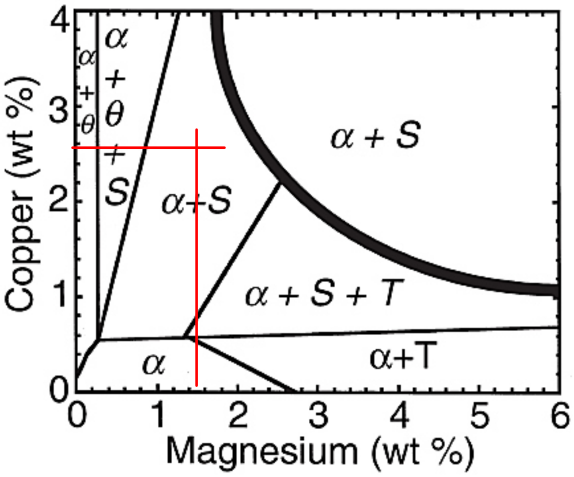

Fig. 1.13 - Al–Cu–Mg phase diagram showing phase fields at 190 °C. The thick solid line defines the α/α+S phase boundary at 500 °C. The red lines represent the chemical composition of AA 2618 aluminium alloy. [24]

Isothermal ageing of Al-Cu-Mg alloys and their commercial counterparts such as AA 2618 reveals several interesting features (Figure 1.14):

(i) hardening occurs in two distinct stages separated by a plateau during which time the hardness remains constant for many hours;

(ii) the first stage of hardening occurs very rapidly;

(iii) some 60% of the total hardening during ageing (calculated as peak hardness minus the as-quenched hardness value) occurs during this rapid first stage.

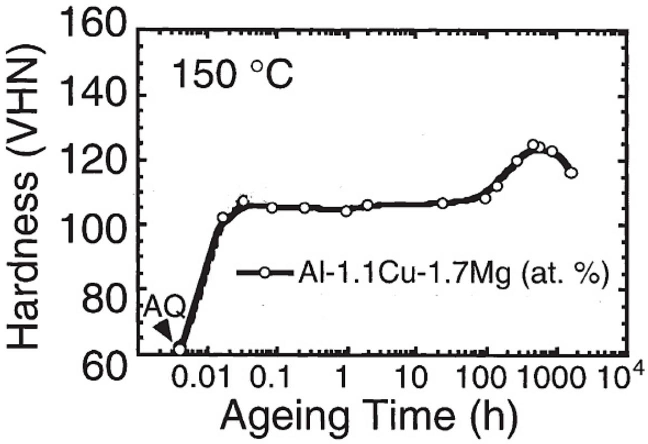

Fig. 1.14 - Hardness–time plots for the Al–1.1Cu–1.7Mg at.% alloy aged at 150 °C. [24]

The precipitation sequence in Al-Cu-Mg alloys is quite complex and still in dispute. Bagaryatsky [25] first proposed the precipitation sequence during the artificial ageing of Al-Cu-Mg alloys as:

$$\alpha\text{-Al(sss)} \rightarrow \text{GPB zones} \rightarrow \text{S''} \rightarrow \text{S'} \rightarrow \text{S } (Al_2CuMg)$$

The zones, which are coherent with the matrix and enriched with Cu and Mg, were named as the Guinier-Preston-Bagaryatsky (GPB) zones by Silcock [26], who showed that they possess a rod-shaped morphology. Bagaryatsky [25] considered the GPB zone as a short-range ordering of Cu and Mg solute atoms. Some authors [24] reported that their formation is preceded by the formation of more diffuse Cu-Mg cocluster.

The structure of S'' has not been clearly confirmed. Despite some authors as Bagaryatsky [25] reported its presence, other authors such as Silcock [26] were unable to confirm it. Other authors such as Wang *et al.* [27] and Shih *et al.* [28] designated GPB2/S'' for the intermediate phase between GPB zones and S'. GPB2/S'' and S' phases are proposed to be precursors to the equilibrium S phase, and are semi-coherent with the matrix.

As the S' phase possesses the same structure as the S phase with slightly difference in lattice parameters, it is now regarded that there is no distinction between the S' and S phases [27,28]. They occur as lath-shaped precipitates.

The ternary S phase with a composition of Al_2CuMg has been determined as an orthorhombic structure with lattice parameters a = 0.400 nm, b = 0.923 nm, c = 0.714 nm by Perlitz and Westgren [29] on the basis of X-ray diffraction (XRD) work. This model for S-phase, called P-W model, is the most generally accepted.

On the basis of a DSC study, Shih *et al.* [28] proposed a more detailed precipitation sequence for the ageing of an Al-2.6 Cu-1.4Mg wt.% alloy at 190 °C:

$$\alpha\text{-Al(sss)} \rightarrow \text{GPB} \rightarrow \text{GPB + GPB2} \rightarrow \text{GPB + GPB2 + S'} \rightarrow \text{GPB2 + S' + S} \rightarrow \text{S' + S} \rightarrow \text{S}$$

However, they did not find definite peaks for the precipitation of GPB2 zones or the S phase, and deduced that the transformation of GPB zones to GPB2 zones and of the S' to S phase were both in situ.

The relation between hardness stage and the phases present at that stage is even more confused. The first stage of hardening (plateau) in Al–Cu–Mg alloys has generally been attributed to the formation of GPB zones, while the second stage of hardening (peak hardness) has been attributed to the formation of the S' or S phase [26].

Other works, however, suggested different interpretations of the origins of hardening in these alloys. Ringer *et al.* [24] proposed that Cu-Mg coclusters are responsible for the early hardness plateau, while GPB zones start forming at the end of the plateau and are responsible for second-stage hardening (peak). According to the authors [24], S-phase appears later in the softening stage.

On the contrary, Wang *et al.* [27] found that the peak ageing in Al-Cu-Mg alloys is dominated by the formation of S precipitates with no significant amounts of other phases or zones present, while the orthorhombic S'' phase or GPB2 zone is present in the latter stages of the plateau stage.

1.3.3 Precipitation hardening of AA2618

As said before, AA 2618 has a very complex chemical composition, which makes it difficult to draw a phase diagram for this alloy and to forecast, on the basis of thermodynamic considerations, the precipitates formed during ageing. When studying the heat treatment, AA 2618 can be considers as an Al-Cu-Mg-Si alloy, since it has been proved that the effect of Fe and Ni in this respect is negligible. The Al-Cu-Mg phase diagram in Figure 1.13 shows that AA 2618 is situated in the (α + S) phase field, taking into account the amounts of Cu and Mg. However, Si addition is likely to cause the precipitation of other phases during ageing treatment, such as θ' and β''. Moreover, due to the presence of insoluble phases, the supersaturated solid solution composition is different from the nominal chemical composition, and this make the use of phase diagrams dangerous [30]. Therefore, in order to analyse the precipitation processes of AA 2618 alloy, it is more reliable to examine experimental data than basing on thermodynamic studies. According to research works [13,31], however, the main strengthening phase in AA 2618 alloy is S phase in agreement with the Al-Cu-Mg phase diagram.

Novy *et al.* [13] examined a forged AA 2618 alloy, and found that in the peak aged condition the main strengthening S-Al_2CuMg phase was distributed uniformly in the form of tiny plate-like precipitates (GPB2 zones) of the approximate size of 50 nm in grain interior. The Al_9FeNi, Al_2CuMg, Mg_2Si, AlCuNi and Al_7Cu_2Fe intermetallic phases were also identified in the microstructure; the majority of the intermetallic phases found, however, belonged to the phase Al_9FeNi.

In contrast with the results by Novy *et al.* [13], Oguocha *et al.* [12] found only Al_9FeNi and Mg_2Si as insoluble phases in the microstructure of an extruded AA 2618 after solutionizing. Probably this difference is ascribable to the different plastic deformation processes used in the two studies. In peak ageing conditions, the authors [12] found S' precipitates distributed in the matrix, at grain boundaries and in the vicinity of the Al_9FeNi particles. In addition, the authors [12] observed plate-like precipitates of a unidentified X phase (containing Al, Cu and Mg) in samples naturally aged, and the θ ($A1_2Cu$) phases in the overaged specimens. The presence of θ phases is probably due to the fact that, with the number of Mg atoms being about twice that of Cu, the diffusion of copper atoms for the formation of Al_2CuMg phases is retarded, thereby allowing some copper atoms to precipitate as Al_2Cu phases [12].

Lu *et al.* [32], however, studying an extruded, hot forged and solutionized AA 2618 alloy, detected only the presence of S phase and its precursors during ageing treatment, in agreement with Novy *et al.* [13]; no evidence was found for the presence of θ, β',or X reported by Oguocha *et al.* [12]. The strengthening occurring during natural ageing was attributed to Cu-Mg coclusters, probably enriched with Si, while, on the basis of DSC analyses, the modifications during artificial ageing at 200 °C were interpreted as follows: after few minutes of ageing, GPB and GPB2 zones are already present; some of the GPB/GPB2 zones that formed during the early stages of ageing are replaced with S'/S at later times, between 5 and 20 hours [32]. These structures coexist in the peak aged specimens, as observed also by Silcock [26]. In the specimen treated for 48 and 80 hours (overaged), the S phase had almost fully precipitated, replacing GPB/GPB2 zones and S' precipitates.

In contrast with previous results [12,13,32], Shen *et al.* [33], based on electrical conductivity measurement and DSC analysis, suggested that under artificial ageing the main strengthening phase of an undeformed AA2618 DC cast alloy at peak hardness condition (195°C for 10 h) is S phase, as reported by Wang *et al.* [27] for Al-Cu-Mg alloys. On the other hand, the strengthening effect caused by natural ageing was mainly attributed to the formation of Cu-Mg co-clusters and/or GPB zones [33].

However, a more recent study carried out by Elgallad *et al.* [34] on the same DC cast and undeformed AA 2618 alloy, lead to different results. The use of TEM imaging showed the presence of fine, dark dots and uniformly distributed needle-like precipitates in the sample peak-aged at 175 °C for 36 h, indicating the GPB zones and S' phase (Figure 1.15 (a)). All needlelike precipitates (mostly S' phase) were aligned along $\{100\}_\alpha$ planes and were often oriented parallel and perpendicular to each other in the microstructure; the length of these precipitates ranged from 50 to 150 nm. TEM images of the sample peak-aged at 195 °C for 10 h, however, showed a quite different microstructure, dominated by large and coarsened S' precipitates with a length ranging from 250 to 400 nm (Figure 1.15 (b)).

The precipitation sequence under the peak-ageing condition of 195 °C/10 h was about to complete the stage controlled by the combination of GPB zones and S' phase to transfer to the next stage controlled by the combination of S' and S phases, leading to the subsequent overageing. On the other hand, under the peak-ageing condition at lower temperature (175 °C for 36 h), the combined precipitation of GPB zones and S' phase was still in progress, resulting in a much finer and denser precipitate microstructure and consequently producing higher peak-aged mechanical properties [34].

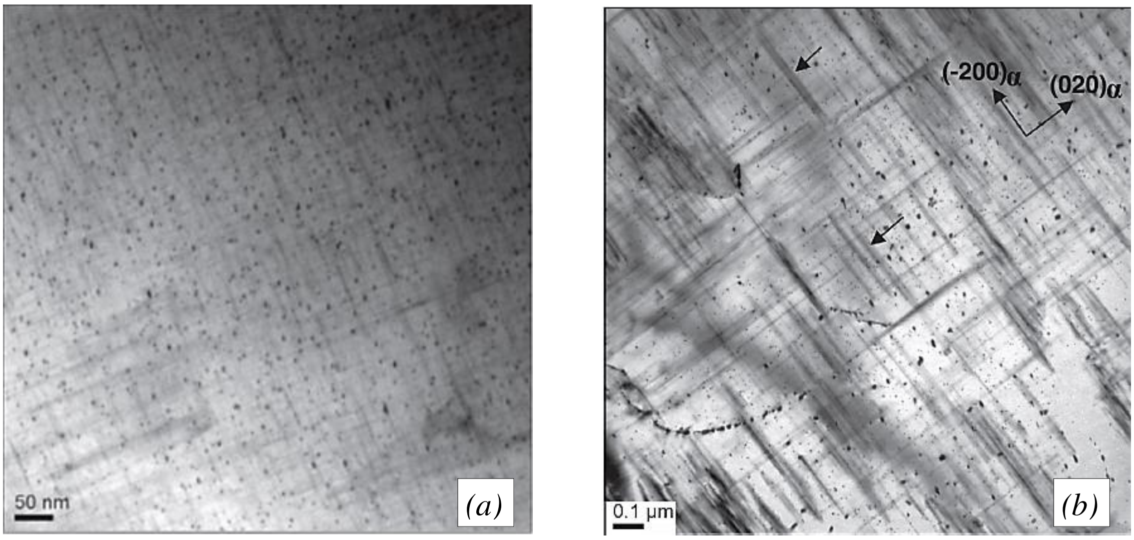

Fig. 1.15 - TEM bright-field images obtained near the [001]$_\alpha$ zone axis from a sample peak-aged at 175 °C for 36 h (a) and from the sample peak-aged at 195 °C for 10 h. The arrows indicate coarsened S' needles. [34]

To sum up, most of literature studies on precipitation in AA 2618 alloy indicate S-type precipitates as the only strengthening phases formed during heat treatment [13,32-34], even if some works highlight a smaller presence of other phases [12]. However, S-type precipitates are indicated as the most important phases in every work.

Comparing the studies presented in this paragraph, it appears that there is some confusion about the form of S-type precipitates which can confer peak-hardness to the alloy. This confusion, however, has already been discussed for Al-Cu-Mg alloys (§1.3.2). In addition, the study carried out by Elgallad *et al.* [34] suggests that even ageing temperature can have an influence on peak-hardness microstructure.

1.3.4 Overageing

When aluminium alloys, heat treated to peak hardness condition, operate at elevated temperatures, their microstructure is bound to undergo modifications and consequently mechanical properties will deteriorate. In this paragraph are discussed the microstructural modifications in AA 2618 due to thermal exposure or creep.

The microstructure of AA 2618, after hot forging and heat treatment to T6 condition, is composed by α-Al matrix and very fine coherent plate-like precipitates of S-phase (GPB zones), homogeneously distributed in the matrix [13]. After creep test at 270 °C for 24 h, with a load of 140 MPa, the coherent precipitates transformed into partially coherent precipitates of S'-phase. However, for longer test duration or temperatures exceeding 300 °C, the S'-phase is transformed into the equilibrium S-phase. The transformation of S‘ precipitates in stable S phase is more significant at the grain boundaries, where occurs with larger precipitates.

Novy *et al.* [13] also observed in the microstructure of the crept alloy the presence of denuded precipitation free zones (PFZ) of the width of 0.5–1.0 μm along grain boundaries, Figure 1.16. These zones negatively influence many mechanical properties of the alloy, such as strength, ductility, creep and fatigue resistance. PFZs are formed since, at high temperatures, a great amount of solute elements is consumed for the growing and coarsening of S-phase, resulting in the depletion of solutes in the matrix near large particles of S-phase. As a consequence, the growth of S-phase during creep test accompanied by the gradual dissolution of metastable S'-phase near grain boundary results in the growth of the width of PFZs.

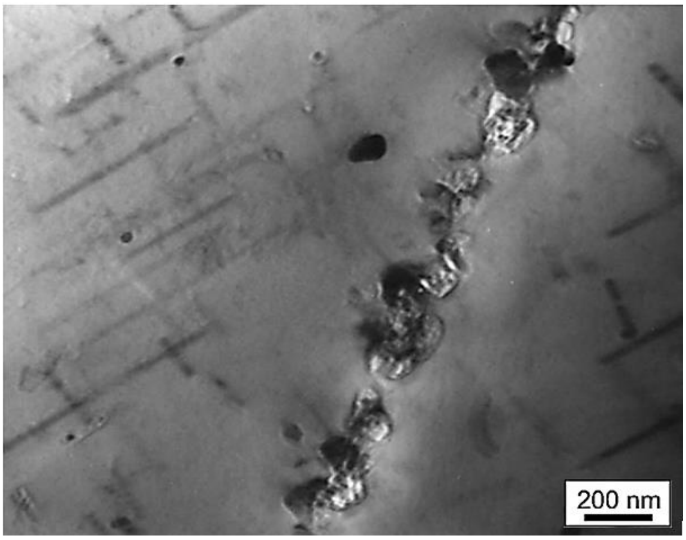

Fig.1.16 - Irregular S precipitates at the grain boundaries surrounded by a precipitate depleted zone (PFZ) in a crept AA 2618 alloy. [13]

Du *et al.* [14] confirmed that after creep test of AA 2618 (extruded and peak aged), precipitates become coarser. The transformation of GPB zones/co-clusters and S'', present in the peak-hardness condition, to S phase takes place during creep. A large number of GPB zones/co-clusters as those in ageing state exist after 180 °C/100 h creep which possibly dynamically precipitates during the creep process. After the 240 °C/100 h creep, however, most of the precipitates are S variants and most precipitates have become coarse.

Majimel *et al.* [35], showed that in a 2650-T8 aluminium alloy (Al-2.68Cu-1.86Mg-0.21Fe-0.21Si-0.34Mn-0.24Ni), the initial homogeneous precipitation of GPB fine needles and S'' precipitates tend to disappear during thermal exposure presumably because it is consumed by the formation of S' precipitates, causing the softening of the alloy.

In creep conditions, this dissolution is accelerated probably in relation to the enhancement of diffusion, leading to an increase in softening effect and loss of mechanical properties.

Moreau *et al.* [19] studied thermal exposure of an Al–4.5Cu–1.5Mg-1.0Fe-1.0Ni wt.% powder metallurgy alloy. The microstructure of the specimens after exposure at 120 °C for 1000 h resulted similar to the microstructure of the peak aged material, with a fine dispersion of Cu-Mg co-clusters and S'' precipitates; most notably, the α-Al grains still appeared to be largely featureless and there were no obvious signs of precipitate formation detectable via SEM imaging (Figure 1.17 (a)). This differed substantially from the microstructure of the specimens after 280 °C exposure for 1000 h. Here, regular arrays of what appeared to be lathe-like precipitates were clearly present in the grains (Figure 1.17 (b)). Owing to the size and shape of the precipitates, the authors [19] were not able to acquire any meaningful EDS chemical assays, but the apparent habitual crystallographic arrangement of the lathes appear typical of S precipitates. This means that precipitates in the alloy exposed to 280 °C had fully overaged to the point of forming the equilibrium variant of the S phase.

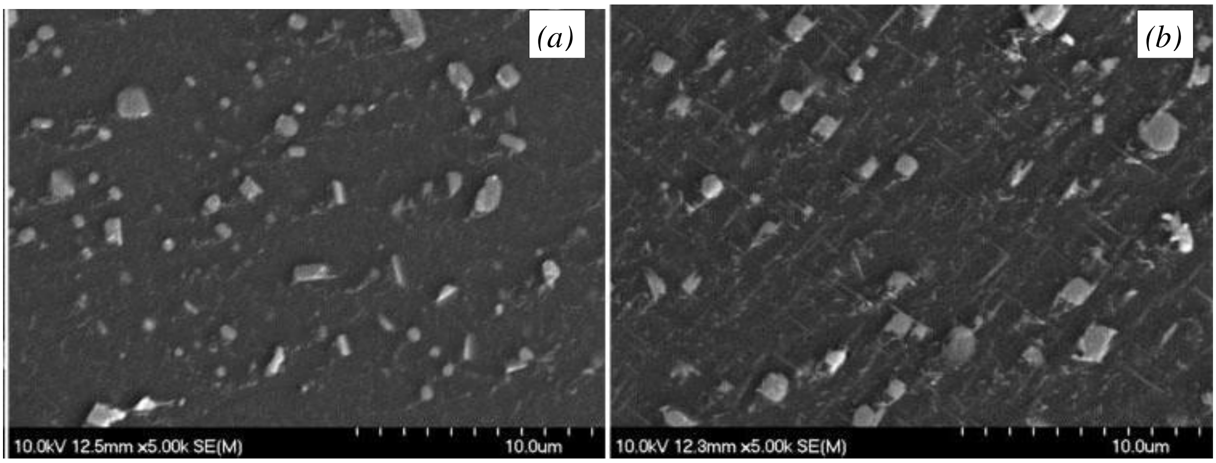

Fig. 1.17 - SEM images of microstructures of Al–4.5Cu–1.5Mg-1.0Fe-1.0Ni wt.% powder metallurgy alloy observed in samples T6 heat treated and further thermally exposed at 120°C for 1000 h (a) and at 280°C for 1000 h (b). [19]

1.4 TRANSITION METALS ADDITIONS FOR HIGH-TEMPERATURE RESISTANCE IN ALUMINIUM AND ALUMINIUM ALLOYS

As explained in §1.1.1, the need for light and high-temperature resistant materials is increasingly felt in the automotive field. Aluminium alloys have peculiar characteristics which made them extremely good candidates to meet this need. However, they generally cannot be used for applications at temperatures higher than 200 °C, because at these temperatures traditional aluminium alloys are subjected to a sharp decrease in mechanical properties.

In order to overcome this problem, in last decades many studies have been carried out and many developments have been attained, resulting in an increase of aluminium alloys operating temperatures up to 300 °C (§1.13). More recently, in an effort to produce aluminium alloys that can stand temperatures higher than 300-350 °C, it was found that adding small amounts of transition metals is very promising in this respect.

In this paragraph is presented a literature review concerning the effects of transition metals additions to pure aluminium and aluminium alloys, with particular attention to AA 2618 alloy. The effects of Sc and Zr additions on high-temperature resistance are mainly analysed, since they seems to be the most suitable elements to attain advantageous properties.

1.4.1 Selection of transition elements additions

Knipling *et al.* [36] studied the selection of alloying elements capable of producing castable, precipitation strengthened Al alloys with high-temperature stability and strength; they established that alloying elements, to be effective, must satisfy four criteria:

(i) be capable of forming a suitable strengthening phase;
(ii) show a shallow α-Al solvus curve and the concomitant low solid solubility in Al at the ageing temperature;
(iii) show low diffusivity in Al;
(iv) retain the ability for the alloy to be conventionally solidified.

To satisfy criterion (i), the strengthening phase must be able to supply a suitable strengthening effect, in order to attain high mechanical properties. Strengthening effect of precipitates increases with increasing their volume fraction or with decreasing their size. Because of low solubility of other elements in aluminium, only low precipitate volume fractions can be obtained in Al-based alloys. Therefore, in order to attain a high strengthening effect, it is critical that the dispersed phased are small (of the order of 10 nm or less) and remain small throughout thermal exposure during operation, that is, they must resist coarsening. With regard to criterion (i), the authors [36] consider systems forming Al_3M

trialuminide compounds with a cubic $L1_2$ crystal structure, which are chemically and structurally analogous to Ni_3Al in the Ni-based superalloys. Ni-based superalloys, in fact, are able to operate for thousands of hours at temperatures as high as 75% of their melting temperature, and they achieve this extraordinary creep resistance primarily due to the precipitation of Ni_3Al trialuminides. Moreover, trialuminide compounds of the type Al_3M have particularly attractive characteristics that include low density (they are nominally 75% Al on an atom basis), high specific strength, good thermal stability (they have generally very high melting points), and excellent oxidation resistance (again, mostly due to the high Al content). It is desirable that these dispersed trialuminide precipitates have the cubic $L1_2$ structure, since the similarity in crystal structure with a low lattice parameters mismatch between the aluminium matrix and the precipitated phases allows for a coherent interface between the two phases. The presence of a coherent interface, in turn, maximizes the strengthening efficacy of the dispersed phase. Furthermore, coherency minimizes the surface energy per unit area of the hetero-phase interface, conferring stability at high temperatures by reducing the driving force for precipitate coarsening. However, precipitation of an Al_3M trialuminide phase from solid solution requires that Al_3M is the most Al-rich intermetallic compound in the system, that is, Al_3M exist in equilibrium with the terminal α-Al solid solution.

To obtain a higher strengthening effect, it is necessary to have a high potential for obtaining large volume fraction of dispersed phase, which scales with the maximum solubility. A large maximum solubility is essential for solutionizing the alloy in the single phase α-Al solid solution prior to precipitation ageing. A low equilibrium solid solubility at the intended service temperature, on the other hand, is necessary to retard volume diffusion-controlled coarsening and prevent dissolution of the precipitated phases.

Limited diffusivity of the solutes in the Al matrix (criterion iii) should also stifle volume diffusion-controlled coarsening, allowing the precipitates to remain effective barriers to dislocation motion at elevated temperatures. This requirement is especially true for any Al-based system due to the intrinsically low volume fraction of dispersed phases and the concomitant necessity for fine precipitates with exceptionally coarsening resistance.

The request for the alloy to be conventionally solidified (criterion iv) meets the need for a cost-effective industrial production. In particular, it is required that solid-liquid partition coefficient (k_0) is near unit, to minimize segregation and accommodate conventional solidification. In a dilute eutectic system, the first solid to form is solute-poor α-Al, whereas for the peritectics the first solid to form can be the solute rich primary Al_3M phase. Consequently in the peritectic systems there is a strong tendency to lose a significant amount of solute to this primary phase; moreover, there is a significant increase in melting temperature. To limit these harmful effects, a shallow Al_3M liquidus boundary is desirable in the peritectic systems for minimizing the casting temperature and suppressing Al_3M primary precipitation during solidification.

Now the criteria have been defined, it is necessary to find which elements can satisfy all these characteristics. With regard to criterion (i), a number of alloying additions crystallise to form stable Al_3M trialuminides. The high symmetry $L1_2$ structure and related tetragonal $D0_{22}$ and $D0_{23}$ structures are prevalent among transition elements and rare earths. Unfortunately, however, the low-symmetry tetragonal structure ($D0_{22}$ and $D0_{23}$) makes the precipitates intrinsically brittle. Moreover, the cubic L12-structured trialuminides are especially attractive since these ordered fcc structures are commensurate with Al. $L1_2$, $D0_{22}$ and $D0_{23}$ structure are schematically illustrate in Figure 1.18. While 31 elements form trialuminides when alloyed with Al, only six elements – Sc, Er, Tm, Yb, Lu, U and Np - form thermodynamically stable cubic $L1_2$ Al_3M structures. Several metastable $L1_2$ structures exist, most notably among Group 4 and Group 5 elements. The Group 4 elements (Ti, Zr, Hf) are especially attractive since the degree of metastability of the cubic $L1_2$ trialuminide is very slight. That means that hundreds of hours at high temperatures are required before attain the equilibrium tetragonal structure. Furthermore, the cubic metastable structure can be stabilized through ternary or quaternary additions.

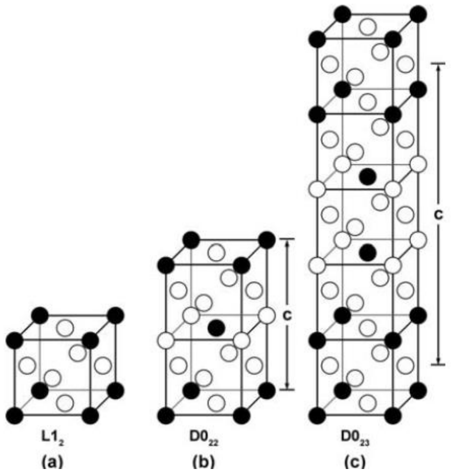

Fig. 1.18 – The $L1_2$ (a), $D0_{22}$ (b) and $D0_{23}$ (c) structures. [36]

Eight elements, clustered in the same region of the period table, fulfil criterion (i), forming stable or slight metastable $L1_2$ trialuminides in equilibrium with their respective α-Al solid solutions: the first Group 3 transition metal (Sc), the three Group 4 transition metals (Ti, Zr, Hf) and the four latest lanthanides elements (Er, Tm, Yb, Lu). Among these elements, Sc and Zr stand out for the following reasons:

- the Al-Sc system exhibits a unique combination of a shallow solvus curve conducive to precipitation strengthening, an eutectic phase equilibrium favouring conventional solidification, and thermodynamically stable Al_3Sc with the $L1_2$ structure. Sc is, however, the fastest diffuser in Al and the priciest of the above eight elements;

- the Al-Zr system is characterized by one of the lowest diffusion rates and lattice parameter mismatch between Al_3M and Al, as well as price among the eight candidates. The $L1_2$ structure of Al_3Zr, however, is metastable. Furthermore, the Al-Zr system is peritectic, which limits the concentration of Zr retained in solid solution after conventional solidification, ultimately limiting the strength attainable by precipitation strengthening. Unlike the other Group 4 systems (Al-Ti and Al-Hf), the solid solubility of Zr in Al at temperatures of interest for post-solidification aging is negligible, both maximizing the volume fraction of the precipitated Al_3Zr phase as well as improving its resistance to coarsening. Consequently, precipitation strengthening can be obtained in conventionally cast alloys. The steep α-Al solvus, however, limits the possibility of post-solidification homogenization.

Generally, Sc is more effective than Zr to enhance mechanical property of pure aluminium and aluminium alloys. However, metallic Sc is excessively expensive, which is due to both the scarceness of ores and a complicated extraction process. Despite the good results on high temperature resistance attained due to Sc additions, the high price of these element is prohibitive for extended commercial applications of Sc-containing aluminium alloys. At present, the use is limited to sporting equipment and to a few aerospace applications [38].

The Al-Sc and Al-Zr phase diagrams with low solute concentration (< 1 at.%) are reported in Figure 1.19. The aluminium-rich side of the Al-Sc phase diagram (Figure 1.19 (a)) shows an eutectic point at 660°C. The system has also a very narrow freezing range. The maximum equilibrium solubility of Sc in aluminium is 0.35-0.4 wt.% (0.23 at.%). With cooling rates in solidification corresponding to the continuous casting of ingots, a supersaturated solution of Sc (up to 0.6 wt.%) with aluminium is obtained [37].

The aluminium-rich side of Al-Zr phase diagram (Figure 1.19 (b)), on the other hand, shows a peritectic point at around 660 °C. As said before, because of the presence of a peritectic reaction, the first solid to form in equilibrium condition is Al_3Zr trialuminide (for concentration of Zr higher than 0.1 wt.%). This can be a problem since the amount of Zr retained in solid solution decreases due to primary precipitation. The maximum equilibrium solubility of Zr in aluminium at the peritectic temperature is 0.083 at.% (corresponding to ~ 0.28 wt.%).

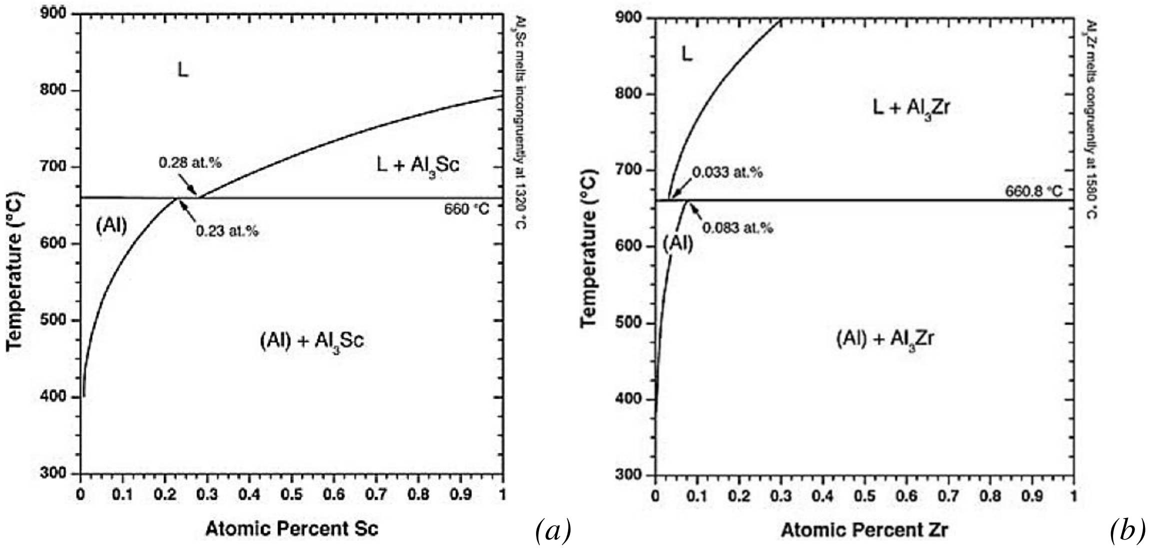

(a) *(b)*

Fig. 1.19 – Reported binary phase diagrams for diluted (< 1 at.%, corresponding to 1.7 wt.% for Sc and 3.3 wt.% for Zr) additions of Sc (a) and Zr (b) alloyed with Al. [36]

1.4.2 Zirconium-reinforced aluminium and aluminium alloys

After Sc, that has no commercial applications because of its high cost, Zr is the best candidate for enhancing high temperature behaviour of aluminium alloys when alloyed in small amounts. Compared to Sc, Zr is a much slower diffuser in α-Al, and therefore Zr precipitates show a higher resistance to Ostwald ripening. On the other hand, the $L1_2$ structure of Al_3Zr is thermodynamically metastable; nevertheless, the precipitates are kinetically stable up to 475 °C, above which the metastable $L1_2$ Al_3Zr precipitates coarsen and transform to their equilibrium $D0_{23}$ structures. These Al_3Zr precipitates are, however, heterogeneously distributed because of the dendritic microsegregation of Zr atoms during solidification, and the resulting precipitate-free interdendritic channels have a deleterious effect on the mechanical properties at ambient temperature and during creep [39].

Knipling *et al.* [40,41], examined the precipitation behaviour of an Al-0.1Zr at.% (corresponding to an Al-0.34 wt.% alloy), and an Al-0.2Zr at.% (corresponding to an Al-0.67 wt.% alloy), solidified with a quite high cooling rate (of the order of 10-100 °C/s). They found that the relative sizes of the columnar and equiaxed zones in the as-cast Al-0.2Zr at.% was strongly dependent on the extent of properitectic Al_3Zr precipitation, because these primary phases are potent grain refiners. The primary precipitates were 10 to 20 μm in diameter and exhibited a morphology characteristic of the metastable $L1_2$ Al_3Zr phase. This observation showed that for the investigated casting conditions, exceeding 0.2 at.% solute (Zr) results in primary precipitation of the properitectic trialuminide and hence decreases the amount of solute retained in solid solution [40,41].

The as-cast alloys were isothermally aged at 375 °C or 425 °C, as shown in Figure 1.20. The Al-0.2Zr exhibited significant precipitation hardening response, which commenced at times as short as 6 minutes at 425 °C and achieved peak strength within 25 hours at both 375 °C and 425 °C. The pronounced strengthening is due to precipitation of small (<10 nm) coherent Al_3Zr ($L1_2$) precipitates [40]. For all alloys investigated, the peak hardness decreased with increasing aging temperature, attributable to the reduction in volume fraction of the dispersed phase due to the temperature dependence of solute solid solubility. There is a particularly pronounced drop in plateau hardness between aging at 400 and 425 °C in the alloys containing 0.1 at.% Zr [41]. Obviously, increasing the Zr content resulted in much higher hardness values because of an higher volume fraction of Al_3Zr precipitates.

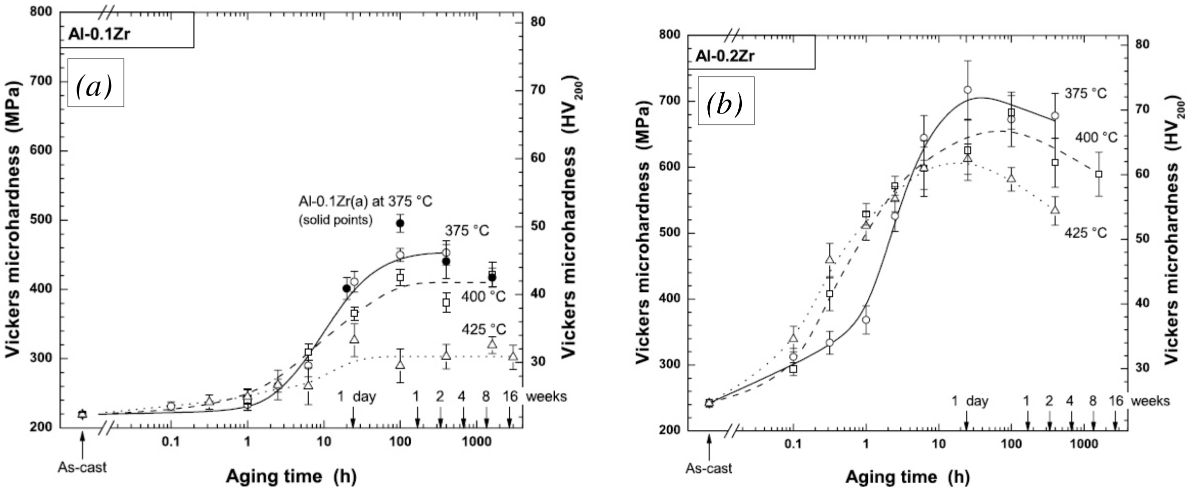

Fig. 1.20 - Vickers microhardness as a function of aging time at 375, 400 or 425 °C for: Al–0.1 Zr at.% (a) and Al–0.2 Zr at.% (b). [41]

The alloys exhibited precipitate-rich and precipitate-free regions associated with the initial dendritic Zr distribution (Figure 1.21). Within the centre of the dendrites, with a largest solute supersaturation, Al_3Zr precipitates resulted small (<R> = 6.7 ± 1.7 nm), with the metastable cubic $L1_2$ structure coherent with α-Al and homogeneously distributed in high number densities. In lateral position from the dendrite centres, where the supersaturation decays, the precipitates resulted progressively larger and occurred in smaller number densities. Moreover, the interdendritic regions contained insufficient solute to effect homogeneous nucleation, so these regions appeared largely precipitate-free. However, small (R <10 nm) spheroidal $L1_2$ precipitates within the dendritic cells was the most prevalent precipitate morphology in the examined Al-Zr alloys [41]. Obviously, it is the small, coherent, high number density Al_3Zr ($L1_2$) precipitates within the dendrites that are responsible for the marked precipitation-hardening response [40,41].

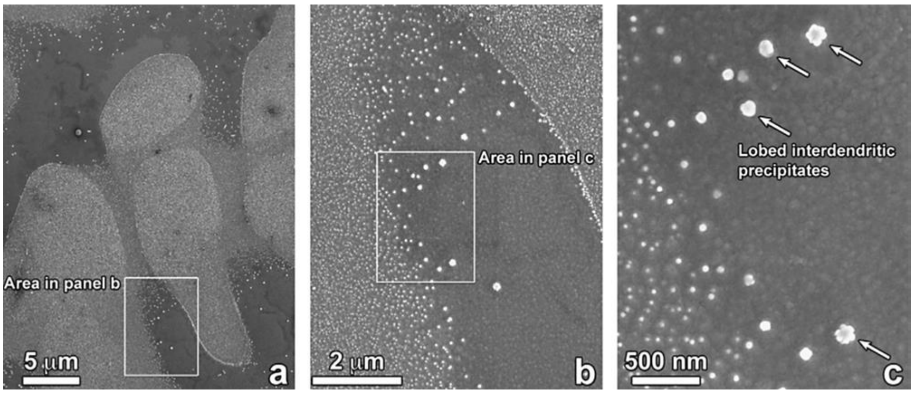

Fig. 1.21 - SEM micrographs of Al_3Zr ($L1_2$) precipitates in Al-0.2Zr at.% aged at 425 °C for 400 h, showing a inhomogeneous distribution of Al_3Zr precipitates within the dendrites. [41]

Knipling *et al.* [40,41] reported that, despite extended aging times (3200 h) at 425 °C (0.75 Tm), precipitates with the equilibrium $D0_{23}$ structure were not observed, indicating that metastable Al_3Zr (L_{12}) precipitates are kinetically stable to high homologous temperatures. This is in agreement with the results reported in [42], which shows that fine $L1_2$ Al_3Zr precipitates exhibit excellent coarsening resistance after aging at 500 °C for 100 h (preceded by aging at 375 °C for 100 h).

However, Al-Zr alloys were subject to overageing after longer exposure at 500 °C, due to dissolution of the small Al_3Zr ($L1_2$) precipitates, that re-precipitate forming extensive arrays of heterogeneously nucleated equilibrium $D0_{23}$-structured precipitates. Because of their large size (ca. 200 nm in diameter), the equilibrium precipitates are semi-coherent with the α-Al matrix, leading to a decrease in strengthening effect [42]. Therefore, the $L1_2 \rightarrow D0_{23}$ structural transformation occurs at approximately 500 °C, which corresponds also to the onset of significant overaging as observed by Vickers microhardness [42].

The high thermal stability of Al-Zr alloys was also reported by Nes [43], who found that in an Al-0.18Zr wt.% alloy annealed at 460 °C the metastable $L1_2$ Al_3Zr precipitates was stable within the investigated time ranges (up to 700 h).

Numerous studies have been carried out concerning Al-Zr alloys. However, as for Sc, when Zr is added to commercial aluminium alloys, more investigations are required. In fact, the presence of other main alloying elements can modify precipitation behaviour of Zr.

Robson and Prangnell [44], for example, utilized a multicomponent Scheil-Gulliver simulation to calculate the effect of Zr addition to a 7xxx series alloy. The simulation predicted that Cu, Mg and Zc additions all accelerate the Al_3Zr precipitation kinetics compared to those in a binary Al-Zr alloy; changes in the Mg concentration were predicted to have the greatest effect on the dispersoid precipitation.

Moreover, alloying elements shift the $L1_2$ Al_3Zr solvus to lower Zr concentrations, so that less Zr is required for precipitation. As the solute concentration is increased, the mean particle radius is reduced and the particle number density rises.

The presence of Cu, Mg and Zn is also predicted to have a significant effect on the distribution of dispersoids across the dendrites after homogenization. In particular, the initial high concentrations of the solute elements at the dendrite edges is predicted to promote dispersoid formation in these regions, leading to a substantial reduction in the width of the dispersoids free zone [44].

A number of experimental works have been carried out on addition of small a mounts of Zr to different types of aluminium alloys. Yin *et al.* [45], for example, investigated a Al-5Mg wt.% alloy with addition of 0.1 Zr wt.%. They found that the addition of such a small amount of Zr can reduce the degree of recrystallization after hot rolling, thus leading to strength increase in the hot deformed alloy.

Robinson *et al.* [46] studied a commercial 2025 alloy (4.51Cu-0.78Si-0.2Fe-0.[48]Mn-0.02Ni-0.01Zn wt.%) with 0.12 Zr wt.% addition. The addition of Zr to 2025 was intended to modify the materials response to hot working, producing a refined fully recrystallized microstructure for a wider range of forging temperatures. However, this did not prove to be the case here, and the microstructural differences between the modified and unmodified alloys were minor. This is in contrast with the results reported by Yin *et al.* [45]; this discrepancy can maybe be attributed to the different homogenization treatments used in the two works (Yin *et al.* [45] soaked the material at 460 °C for 13 h, while Robinson *et al.* [46] at 495 °C for 24 h) or to different solidification conditions. Robinson *et al.* [46] indicated the presence of tetragonal $D0_{23}$ form of Al_3Zr. There is the possibility that the Zr reacted with the other alloying elements in AA 2025 to form the coarse Zr rich phase during solidification [46]. The reduction in the Zr concentration in solid solution prior to homogenization through the formation of the coarse Zr particles prevents sufficient Al_3Zr dispersoids being formed to significantly influence the microstructure.

Wong *et al.* [47], on the other hand, investigated an Al-1.2Si-0.5Mg-0.25Fe alloy homogenized at 550 °C for 24 h, hot and cold rolled, solutionized at 550 °C for 0.5 h, natural aged for 2 weeks and heat treated at 180 °C for 0.5 or 11 h (latter condition corresponds to peak hardness). They found that adding 0.02-0.30 wt.% Zr to this alloy, both microhardness and ultimate tensile strength (UTS) increased for heat-treatments of 0.5 and 11 h; increasing Zr content resulted in better mechanical properties (Figure 1.22). For additions of Zr above 0.15 wt.%, both microhardness and UTS for the alloys heat-treated for 0.5 h were higher than the values of Al-1.2Si-0.5Mg-0.25Fe without Zr addition heat-treated to peak-hardness condition (11 h), as shown by the red line, representing UTS of peak-aged unmodified alloy, in Figure 1.22.

Zr-containing precipitates are believed by the authors [47] to be Al_3Zr phase and to have contributed to this increase in mechanical properties. Besides the formation of precipitates, the grain sizes resulted obviously refined with the addition of Zr.

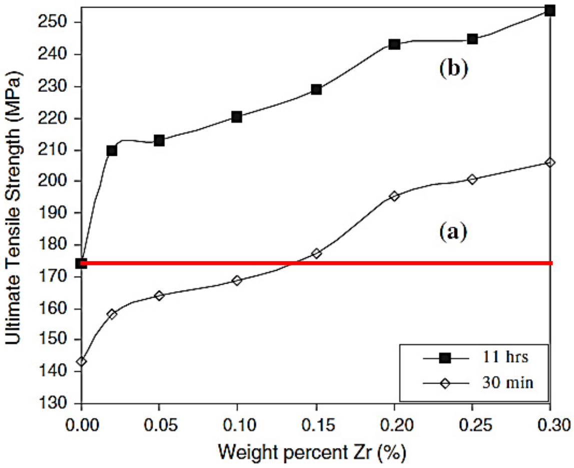

Fig. 1.22 - Ultimate tensile strength (UTS) of Al-1.2Si-0.5Mg-0.25Fe as a function of Zr additions: (a) natural aging for 14 days, followed by heat-treatment at 180 °C for 30 min, and (b) natural aging for 14 days, followed by heat-treatment at 180 °C for 11 h. The red line represents UTS of unmodified alloy in peak hardness condition. [47]

There are also numerous studies concerning Zr addition to AA 2618. Zeng *et al.* [48], for example, modified an AA 2618 alloy by adding 1.0% excess Cu, 0.24% Mn, and 0.16% Zr to the standard composition. They found that, after homogenization and hot extrusion at 450 °C, the modified alloy exhibited a reduction in the grain size in the transverse and normal directions from 50-200 µm to 5-500 µm, mainly attributed to the presence of Mn and Zr. Considering the different sizes of the grains and the well-known Hall-Petch relation, it can be deduced that the modified alloy had higher yield strength.

Moreover, by comparing the fatigue strength property of the two alloys, it was found that the modified alloy showed evidently higher ratios between the endurance limit and the yield strength in the two directions, indicating that it had excellent fatigue strength.

Kotov *et al.* [49], similar to Zeng *et al.* [48], modified an AA 2618 alloy by adding 1.0% excess Cu, 0.8% Mn, and 0.25% Zr and found that, after a two steps homogenization (430 °C 3 h and 480 °C 5 h) and hot and cold rolling, the modified alloy showed the smallest grain size due to the presence of Zr. The authors [49] suggest that the equiaxed fine-grained structure induced by Zr addition makes the material suitable for superplastic deformation.

Wang *et al.* [50] examined the effect of adding 0.22 wt.% Zr to AA 2618 alloy together with the effect of over-heating the alloy to 960 °C for 20 min before casting. The alloys were homogenized and hot rolled at 480 °C, and then T6 heat treated using typical parameters of AA 2618 alloy. The authors confirmed that grain size of AA 2618 alloy with Zr after extrusion was very small due to the formation of dispersed Al_3Zr particles, as reported in [48,49]. Wang *et al.* [50] suggest that these particles could enhance alloy's recrystallization temperature and restrain the growth of recrystallized grains so as to attain small grain microstructure.

Tensile test results (Table 1.3) showed that strength and elongation at room temperature and at 250 °C of the unmodified alloy over-heated at 960 °C were apparently improved. The tensile property of the modified and over-heated alloy, however, was higher due to the addition of Zr (Table 1.3), showing that Zr is effective in enhancing mechanical properties at both room and elevated (250 °C) temperatures.

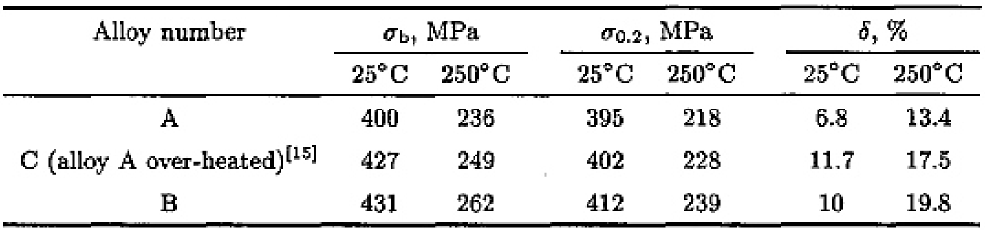

Alloy number	σ_b, MPa		$\sigma_{0.2}$, MPa		δ, %	
	25°C	250°C	25°C	250°C	25°C	250°C
A	400	236	395	218	6.8	13.4
C (alloy A over-heated)[15]	427	249	402	228	11.7	17.5
B	431	262	412	239	10	19.8

Tab. 1.3 – Ultimate tensile strength (σ_b), yield strength ($\sigma_{0.2}$) and elongation to failure (δ) at room temperature and 250 °C for conventional AA 2618 alloy (A), over-heated AA 2618 alloy (C), over-heated and Zr modified alloy (B). [50]

The improvement of recovery resistance of AA 2618 alloy due to Zr addition in the range 0.08-0.24 wt.% was extensively studied by Jaukovic *et al.* [51,52]. The authors claim that obstacles to recovery process mean obstacles to creep process, thus enhancing heat resistance of the alloy. In this way, the recovery resistance can be increased and creep velocity decreased, which leads to high values of hardness parameters at raised working temperatures [51,52].

Jaukovic and Perovic [51] showed that activation energy of the recovery process at a given temperature is directly proportional to the quantity of Zr content. Zr additions lead to a decrease in the recovery rate, and therefore delay creep process. As a result, mechanical properties at elevated working temperatures are increased [51].

In a following study, Jaukovic and Lalovic [52] defined the relative degree of recovery with the following equation:

$$R = \frac{H_d - H}{H_0 - H_d}$$

where H_0 is the microhardness of the material before deformation, H_d is the microhardness of deformed material and H is the microhardness of recovered material. They showed that, for given deformation condition and annealing temperature, the relative degree of recovery was retarded by increase of Zr content from 0.08 wt.% to 0.24 wt.%. The results for AA 2618 with different Zr contents (0.00, 0.08, 0.18 and 0.024 wt.%) are reported in Figure 1.23 (a) and (b) for alloys annealed at 200 °C and 300 °C, respectively. At lower temperatures (150-250 °C) Zr exhibited stronger effect than at higher temperatures (300-350 °C). However, results from Jaukovic et al. [51,52] showed that Zr can impede the recovery process and consequently cause an increase in creep resistance of AA 2618 alloy.

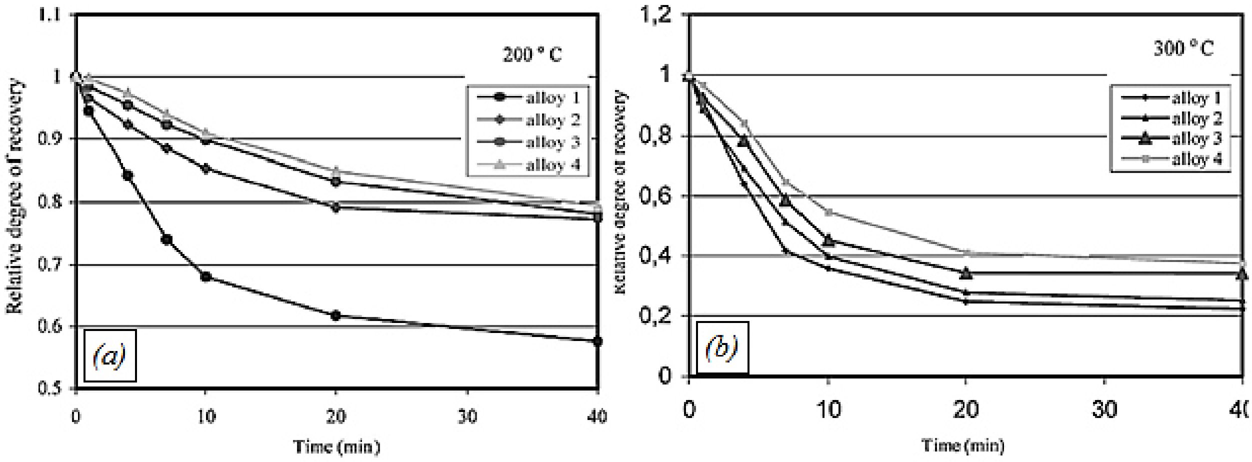

Fig. 1.23 – Influence of Zr content in AA 2618 alloy on the relative degree of recovery at 200 °C (a) and at 300 °C (b). AA 2618 alloy with addition of 0.0 (alloy 1), 0.08 (alloy 2), 0.18 (alloy 3) and 0.24 (alloy 4) Zr wt.%. [52]

To sum up, an analysis of the studies presented in this section [45-52] shows that addition of small amounts of Zr to commercial aluminium alloys are effective to reduce grain size and improve recrystallization resistance; as a consequence, the alloys with Zr addition present higher mechanical properties at room and elevated temperatures, and have improved creep resistance.

As will be explained in the next section, however, it is suggest that even better characteristic can be obtained by addition of other transition metals (such as Ti and V) together with Zr.

1.4.3 Effects of simultaneous addition of Ti/V and Zr

The Al-Zr system is particularly promising for developing thermally stable, precipitation-strengthened Al alloys. However, it has been proposed that even greater stability can be achieved by decreasing the lattice parameter mismatch between Al_3Zr and the α-Al solid solution by additions of Ti, Hf or V [41]. The Al-Zr-V system, in particular, has been extensively studied. The reduced lattice parameters mismatch was observed to decrease the rate of Ostwald ripening for both metastable cubic $L1_2$ and the equilibrium tetragonal $D0_{23}$ phases [36]. The formation, however, of an additional $Al_{10}V$ phase, particularly at grain boundaries, can occur, with an adverse effect on the mechanical properties [41].

Chen *et al.* [53,54] examined three Al-Zr-V alloys with different Zr and V contents (Al-3.12Zr-0.66V, Al-2.14Zr-1.24V and Al-1.13Zr-1.82V wt.%) . All alloys were designed to present about 5 vol.% of metastable $L1_2$ $Al_3(Zr_xV_{1-x})$ phase after aging, and were rapidly solidified by melt spinning process.

The metastable $L1_2$ phase were found to precipitate initially instead of the equilibrium phases, $Al_{10}V$ and $A1_3Zr$ ($D0_{23}$). The precipitation mechanism of the $L1_2$ phase depends on alloy composition and aging temperature. The as-melt spun microstructures show precipitation has occurred in the alloys with higher Zr concentration. In the alloys with a Zr/V ratio equal to 3 or 1, a cellular $L1_2$ phase forms by discontinuous precipitation immediately after solidification. However, a supersaturated solid solution is obtained in an alloy with a Zr/V ratio equal to 1/3. In the latter, both spherical and cellular $L1_2$ structured precipitates form during aging. A higher aging temperature suppresses the cellular and favours the spherical $L1_2$ precipitates [53,54].

A slow volumetric particle coarsening rate at 425 °C was measured for the $L1_2$ structured $Al_3(Zr_xV_{1-x})$ precipitate, and the coarsening kinetics of the $L1_2$ particles were controlled by volume diffusion of Zr. Partial substitution of V for Zr in the precipitate increases the thermal stability of the metastable $L1_2$ phase in very dilute alloys and also slows down the particle coarsening rate at 425 °C. The alloy with the higher concentration of Zr is weaker at 425°C due to the lower thermal stability of $Al_3(Zr_xV_{1-x})$ with high Zr/V ratio and due to its inhomogeneity [54]. The good resistance at 425°C of $L1_2$ structured $Al_3(Zr_xV_{1-x})$ both to transformation to the stable $D0_{23}$ form and to Ostwald ripening suggests that it is a promising dispersoid for high temperature aluminium alloys. Preliminary creep results support this suggestion. The present results confirm that reducing the misfit between dispersed particles and matrix, and adding alloying elements which have low volume diffusion rates to the precipitate, slow the rate of Ostwald ripening and lead to better creep resistance in Al base alloys [53].

On aging at 500 °C for 1 h, $Al_{10}V$ and $D0_{23}$-structured $A1_3Zr$ particles formed on the grain boundaries. Because of the growth of grain boundary $Al_{10}V$ equilibrium phase particles during aging, precipitate free zones (PFZs) form adjacent to the grain boundaries, with a consequent negative effect on mechanical properties [53].

Zedalis and Fine [55], on the other hand, studied three more dilute rapidly solidified Al-Zr-V alloys (Al-0.79Zr, Al-0.10Zr-0.35V and Al-0.23Zr-0.34V wt.%), designed to present about

1 vol.% of metastable L1$_2$ $Al_3(Zr_xV_{1-x})$ precipitate phase. In the three alloys, depending on the Zr/V ratio, Al_3Zr, $A1_3(V_{0.725}Zr_{0.275})$ and $A1_3(V_{0.875}Zr_{0.125})$ precipitates are formed, respectively. The overall sequence of decomposition in an Al-V-Zr alloy containing $A1_3(V_{0.875}Zr_{0.125})$ was identical to that observed for the unalloyed $A1_3Zr$ phase, but the kinetics were appreciably more sluggish. For the cubic $A1_3(V_{0.875}Zr_{0.125})$ phase, coalescence and formation of coarse precipitates was not observed until after 20 hours of aging at 450 °C, in comparison to 13.5 hours of aging for the binary A1-Zr alloy, while the tetragonal phase was not observed until after 100 hours of aging, compared to 15 hours for the binary alloy. The present results thus confirm that reducing the lattice disregistry decreases the decomposition kinetics (or increases the stability) of cubic L1$_2$ particles, as also observed by Chen *et al.* [53,54]. For the cubic Al_3Zr particles, the average particle radius approaches 16 nm prior to the initial observance of the tetragonal phase; however, this average radius is approximately 20 nm for the $A1_3(V_{0.875}Zr_{0.125})$ particles. Since the growth rate of the latter is slower, this corresponds to a much longer transformation initiation time [55].

The coarsening kinetics of the tetragonal (D0$_{23}$) $A1_3Zr$ and $A1_3(V_{0.875}Zr_{0.125})$ precipitates isothermally aged at 425 °C after cold working and pre-aging at 600 °C are shown in Figure 1.24; the larger initial particles size for the $A1_3(V_{0.875}Zr_{0.125})$ phase was the result of the double pre-aging treatment employed to obtain a homogeneous dispersion of tetragonal precipitates. The tetragonal (D0$_{23}$) $A1_3(V_{0.875}Zr_{0.125})$ particles coarsened in volume one-third slower at 425 °C than the (D0$_{23}$) $A1_3Zr$ particles. This is most likely due to a reduction in overall mismatch from 2.8 to 2.4% with a resulting reduction in the average interfacial energy of the particles. At 425 °C the tetragonal (D0$_{23}$) $A1_3Zr$ phase coarsened in volume 16 times faster than cubic (L1$_2$) $A1_3Zr$ phase in keeping with the fact that the latter is coherent and coplanar with the matrix while the former forms a semicoherent interface with the matrix. On the other hand, tetragonal $A1_3(V_{0.875}Zr_{0.125})$ phase coarsened 8 times faster than cubic $A1_3(V_{0.875}Zr_{0.125})$ phase. These differences between the cubic (L1$_2$) and tetragonal (D0$_{23}$) particle coarsening rates are most certainly related to the higher average interfacial energies for the tetragonal particles. However, partial substitution of V for Zr reduced the precipitate-matrix mismatch for both phases and slowed both coarsening rates as well as retarded the cubic to tetragonal transformation.

Also Park [56] examined three rapidly solidified (10^6 °C/s) Al-Zr-V alloys, whit the following chemical compositions: Al-2.12Zr, Al-1.83Zr-0.45V and Al-0.51Zr-2.23V wt.%. Microhardness of the as-cast materials proved an enhanced thermal stability of the Al-Zr-V alloys compared to the binary Al-Zr alloy during thermal exposure at 400 °C (Figure 1.25). The enhanced age hardening and improved thermal stability in the Al-Zr-V alloys appeared to have been caused by the formation of the metastable L1$_2$-$Al_3(Zr,V)$ phase, having a reduced misfit with the Al matrix. Discontinuous precipitation, which has harmful effects on mechanical properties and thermal stability, was suppressed by the addition of V, because of a reduced misfit between the Al matrix and $L1_2$-$Al_3(Zr,V)$ phase.

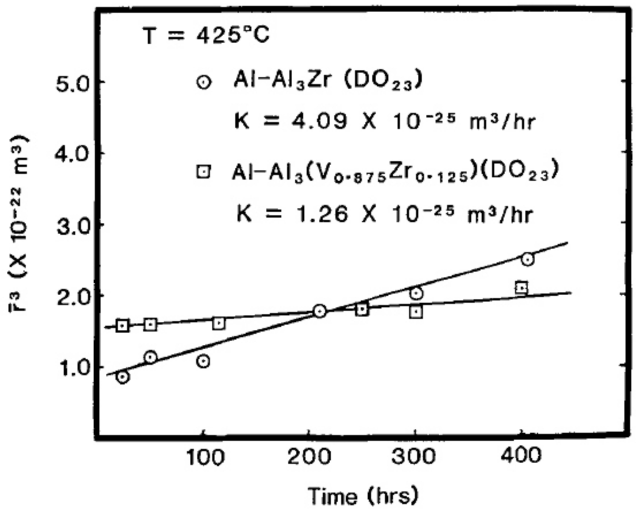

Fig. 1.24 – Comparison of volumetric coarsening rate (particle size) of tetragonal $D0_{23}$ $Al_3(V_{0.875}Zr_{0.125})$ *and* Al_3Zr *during isothermal aging at 425 °C. The Al-Zr alloy was cold rolled 90% and pre-aged 50 h at 600 °C; the Al-V-Zr alloy was cold rolled an additional 5% and annealed additional 50 h at 600 °C to convert the cubic precipitates to the* $D0_{23}$ *phase, thus the short times particle size is much larger for the ternary alloy.* [55]

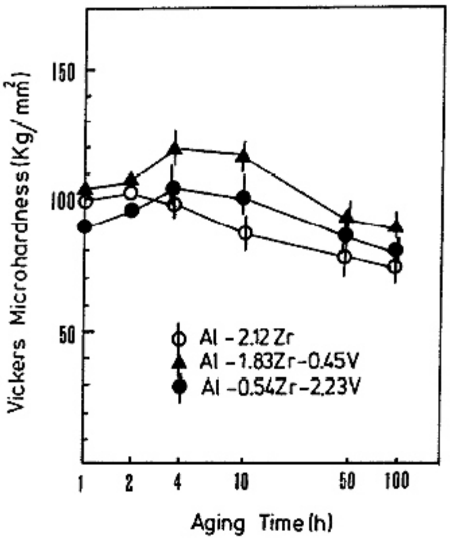

Fig. 1.25 – Effect of isothermal aging at 400°C on microhardness changes of the rapidly solidified Al-Zr and Al-Zr-V alloys with different Zr/V ratios. [56]

However, despite the fact that a small amount of V was contained in the Al-1 .83Zr-0.45V alloy, some large precipitates were identified as the $Al_{10}V$ phase. It is recommended that the amount of V in the Al-Zr-V base alloys should be controlled within the extended solid solubility limit of V in the Al matrix and $Al_3(Zr,V)$ phase - which depends on the cooling rate of the molten metal - to avoid the primary precipitation of $Al_{10}V$ [56].

To sum up, additions of V to rapidly solidified Al-Zr alloy seem to have a beneficial effect on thermal stability and ageing propertied of $Al_3(Zr,V)$ phase, but is important to avoid the formation of the brittle $Al_{10}V$ equilibrium phase. However, besides V, also Ti additions were taken into account during last years. In fact, Knipling *et al.* [36,41] reported that Ti, as V, reduces the lattice parameter mismatch of Al_3Zr ($L1_2$) with α-Al and. Moreover, since Al_3Ti is the terminal intermetallic in the Al-Ti system, the problem of additional brittle intermetallics is avoided [41].

Knipling et al. [41,42] compared two binary Al-Zr alloys (Al-0.1Zr and Al-0.2Zr at.%) and two ternary Al-Zr-V alloys (Al-0.1Zr-0.1Ti and Al-0.2Zr-0.2Ti at.%). Vickers microhardness of the as-cast Al-Zr and Al-Zr-Ti alloys as a function of aging time at 375, 400 or 425 °C showed, in most cases, no significant hardness difference between the Al-Zr and Al-Zr-Ti alloys for a given Zr concentration (0.1 or 0.2 at.%) and aging temperature. However, at 425 °C, Al-0.1Zr-0.1Ti alloy showed a significantly lower decrease in hardness and noticeable increase in peak strength compared to the Al-0.1Zr alloy.

In addition to the noticeable increase in peak strength at 425 °C, Ti additions appear also to accelerate the onset of precipitation hardening in the more dilute alloys containing 0.1 at.% Zr. This effect may be interpreted in terms of solute supersaturation influencing the incubation time for nucleation and the volume fraction of precipitate-rich dendritic regions, and is not an effect of precipitate radius or coarsening resistance. In fact, the alloys overaged sluggishly, even after 3200 h at 425 °C, but with no benefit from Ti additions in delaying overaging [41].

Moreover, both Al-0.1Zr and Al-0.1Zr-0.1Ti alloys after aging at 375 °C for 100 h, overaged at the same rate when exposed at 500 °C, with no improved coarsening resistance of $Al_3(Zr_{1-x}Ti_x)$ ($L1_2$) as compared to Al_3Zr ($L1_2$) [42].

As said before, improving the coarsening resistance of Al_3Zr with ternary or quaternary additions of V and/or Ti has generated considerable interest in the scientific literature. Some of these studies are summarized in Figure 1.26, which indicates the alloy compositions, nominal volume fractions of $L1_2$-structured $Al_3(Zr_{1-x}M_x)$ (M = V and/or Ti) precipitates, and their measured precipitate radii as a function of aging time at 425 °C. Note that the extension of solid solubility by rapid solidification processes like melt spinning lead to smaller precipitate radii because of the larger achievable supersaturation of solutes, thus explaining the smaller precipitate radii produced in the melt-spun alloys as compared with those that are arc melted. Data collected in Figure 1.26 suggest that, despite the confirmed partitioning of Ti to the $Al_3(Zr_{1-x}Ti_x)$, there is no benefit in terms of coarsening resistance of the small dendritic $Al_3(Zr_{1-x}M_x)$ (L12), as compared with Al_3Zr ($L1_2$) precipitates during extended isothermal aging at 425 °C, consistent also with the similar overaging behaviour observed by Vickers microhardness [41].

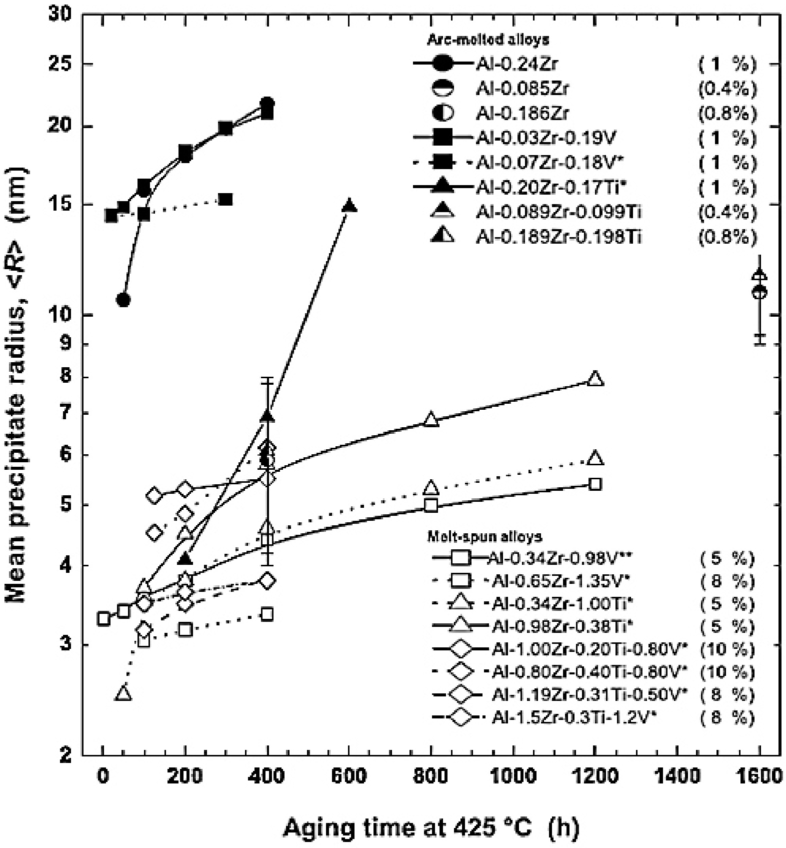

Fig. 1.26 - Comparison of L1$_2$*-structured Al*$_3$*(Zr*$_{1-x}$*M*$_x$*) (M = V and/or Ti) with <R> in nm for different aging times at 425 °C. Shaded symbols represent prior studies on arc-melted alloys, open symbols represent prior studies on melt-spun alloys, and half-shaded symbols are from the study on arc-melted alloys carried out by Knipling et al. [41]. Alloy compositions (at.%) and reported volume fractions of the L12 precipitates are also indicated. *Specimens pre-aged at 500 °C for 1 h; **specimens pre-aged at 500 °C for 2.5 h.* [41]

However, scientific literature concerning combined additions of Zr together with V and/or Ti to commercial aluminium alloys is quite poor. Jia *et al.* [57] examined an Al-5.0Cu wt.% alloy with addition of 0.2Zr wt.% and 0.2Zr-0.1Ti-0.2V wt.%. The precipitate in the Al-Cu-Zn-Ti-V alloy was composed of Al, Zr, Ti and V. In this alloy, after heat treatment at 500 °C for 5 h, the precipitates were spherical, small and had a high density in dendrites, while they were relative big and had a low density in interdendritic region. This observation shows that additions of Ti and V have no effect on the not homogenous distribution of Zr precipitates. All precipitates at this treatment condition were coherent with the Al matrix.

As reported by Knipling *et al.* [41,42], addition of Ti was confirmed not to influence the size of the Al_3Zr precipitate although it substitutes Zr partly in the precipitates, while addition of V was shown to reduce the coarsening rate of Al_3Zr precipitate but did not seem to affect the size of the Al_3Zr precipitates [57].

The presence in the alloy of other elements, however, can modify the precipitation behaviour of Zr, Ti and V. Jia *et al.* [57] observed that addition of Cu can reduce the metastable Zr solubility and that this effect increases with increasing Cu content. Although the added Zr amount (0.2%) in the examined alloy is lower than that in the Al-Zr-Ti alloy examined by Knipling *et al.* [42] (0.34%), a similar supersaturation of Zr was reached by the addition of Cu. Moreover, Jia *et al.* [57] reported that addition of Cu seemed to promote the $L1_2 \rightarrow D0_{23}$ structural transformation of the Al_3Zr precipitate. The phase transformation from metastable $L1_2$ to $D0_{23}$ structure was detected in the Al-5Cu-0.2Zr-0.1Ti-0.2V wt.% after thermal exposure at 500 °C for 20 h.

Elgallad *et al.* [58] examined an Al-2.0Cu-1.0Si-0.4Mg-0.6Fe-0.6Mn wt.% alloy, with and without concomitant additions of 0.2 Zr and 0.15 Ti wt.%, intended for automotive applications. They found that the addition of Zr produced a significant improvement in the tensile properties as a result of its grain refining action. The Zr-Ti particles, in fact, acted as nucleation sites for small equiaxed grains of α-Al, and therefore the combined addition of Zr and Ti caused a decrease in the grain size from 500 µm to 160 µm.

The Zr- and Ti-containing alloy showed the highest values for tensile properties. This alloy displayed significant increases in the YS and UTS along with a higher level of ductility in both the as-cast and heat treated (T6) conditions. There is a distinct possibility that the higher strength increment may be attributed to the strengthening mechanism stimulated by the grain-refining effect of Zr [58].

Kasprzak *et al.* [59,60] analysed an Al-7.0Si-1.0Cu-0.5Mg-0.1Fe wt.% alloy containing additions of 0.15 wt.% Zr, 0.28 wt.% V and 0.18 wt.% Ti, solidified with the average cooling rate of approximately 20 °C/s. The authors [59] reported that additions of Zr, V and Ti resulted in the formation of complex phases with Al, Si, Cu, Mg and Fe in both the as-cast and T6 microstructure.

However, the analysis of modified T6 treated material revealed a primary GP zones, S-phase (Al_2CuMg) precipitates, $Al_3(Zr,V,Ti)$ $L1_2$ nanoprecipitates with average size below 50 nm and $Al_3(Zr,V,Ti)$ $D0_{23}$ rod-shaped precipitates with average size of 230 nm covered with Si-rich nanoparticles and Cu-rich particles. The $Al_3(Zr,V,Ti)$ secondary precipitates presented varied concentration ratios of Zi, V and Ti [59].

High-temperature tensile testing showed a significant drop in strength of the modified alloy above the over-aging temperature interval of 250-300 °C accompanied by a transitional increase in strain at the break. Similar results were obtained in hardness measurements, indicating that 250 °C is a critical aging temperature for the given alloy's chemistry and heat treatment conditions. This critical temperature is related to stability of Cu–Mg based precipitates. Long temperature exposure at 475 °C for 128 h for the modified alloy in T6 condition, resulted in improved hardness retention and most likely is associated with further precipitation of $Al_3(Zr,V,Ti)$ phase, and precipitation and subsequent dissolution of lath shaped Q' type precipitates. These reactions take place between 440 and 460 °C [59]. Elevated temperature tensile testing carried out from 25 to 400 °C revealed similar values of tensile stress (σ) up to 150 °C for both alloys, while between 200 and 400 °C the strength was marginally higher for modified alloy with additions of Zr, V and Ti (for example 260 vs. 247 MPa at 200 °C) These results are shown in Figure 1.27.

In comparison to the base Al-7Si-1Cu-0.5Mg alloy, the modified alloy containing Zr, V and Ti showed improved yield strength and cyclic yield strength, but lower ductility. The modified alloy exhibits also slightly higher hardness between 150 to 250 °C and 350 to 450 °C, but not accompanied by significant improvement of tensile strength [59].

Further studies are required to optimize the concentration of Zr, V and Ti together with liquid metal processing and heat treatment in order to maximize their effect on mechanical properties at elevated temperatures [59].

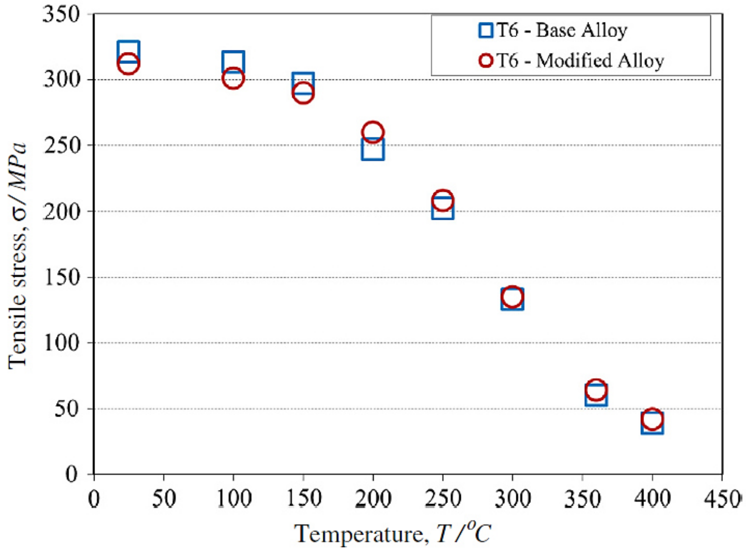

Fig. 1.27 - Comparison of tensile strength for the base and Zr-Ti-V modified alloys in the T6 condition as a function of test temperature. [59]

From the analysis of the experimental results summarized in this section, it appears that the behaviour of commercial aluminium alloys modified with combined additions of Zr, V and/or Ti is not fully understood. Moreover, it is worth noticing that no scientific literature was found concerning combined addition of these elements to wrought aluminium alloys. In fact, all the experimental work reviewed in this section deal with undeformed material (as-cast or heat treatment).

In conclusion, there is a need for further experimental work concerning binary or ternary additions of Zr and Ti/V to commercial wrought aluminium alloys. These additions, and in particular combined additions of Zr and V, proved to be highly effective in enhancing thermal stability of pure aluminium and are believed to produce beneficial effect also in commercial alloys.

REFERENCES

[1] H. Yamagata, "*The science and technology of materials in automotive engines*" (2005) Woodhead Publishing, Cambridge

[2] European Aluminium Association, "*The Aluminium Automotive Manual – Power Train – Pistons*" (2011)

[3] F. Stadler, H. Antrekowitsch, W. Fragner, H. Kaufmann, P.J. Uggowitzer, "*Effect of main alloying elements on strength of Al–Si foundry alloys at elevated temperatures*", International Journal of Cast Metals Research, 25 (2012) 4, 215-224

[4] S. Manasijevic, S. Markovic, Z. Aimovic- Pavlovic, K. Raic, R. Radisa, "*Effect of heat treatment on the microstructure and mechanical properties of piston alloys*", Materials and technology, 47 (2013) 5, 585–591

[5] M. Zeren, "*The effect of heat-treatment on aluminum-based piston alloys*", Materials and Design, 28 (2007) 2511–2517

[6] S.J. Barnes, K. Lades, "*The Evolution of Aluminium Based Piston Alloys for Direct Injection Diesel Engines*", SAE Technical Paper 2002-01-0493 (2002)

[7] M. Jayamathy, R. VasanthAluminium, "*Piston Alloy to Retard Age softening Characteristics in Motorcycle Engines*", SAE Technical Paper 2006-32-0030 (2006)

[8] Mielke, Steffens, Beer, Henning, "*New Aluminum Piston Alloy with Increased Fatigue Strength at High Temperatures*", SAE Technical Paper 980687 (1998)

[9] C.Y. Jeong, "*Effect of Alloying Elements on High Temperature Mechanical Properties for Piston Alloy*", Materials Transactions, 53 (2012) 1, 234-239

[10] J.E. Hatch, "*Aluminium: Properties and Physical Metallurgy – Chapter 9: Properties of Commercial Wrought Alloys*", (1984) ASM International, Materials Park, OH

[11] American Society for Metals, "*ASM handbook. Volume 2: Properties and selection: nonferrous alloys and special-purpose materials*" (1990) ASM International, Materials Park, OH

[12] I.N.A. Oguocha, Y. Jin, S. Yannacopoulos, "*Characterization of AA2618 containing alumina particles*", Materials Science and Technology, 13 (1997) 173-181

[13] F. Novy, M. Janecek, R. Král, "*Microstructure changes in a 2618 aluminium alloy during ageing and creep*", Journal of Alloys and Compounds 487 (2009) 146–151

[14] Z.W. Du, G. J. Wang, X.L. Han, Z.H. Li, B H. Zhu, X. Fu, Y.A. Zhang, B.Q. Xiong, "*Microstructural evolution after creep in aluminum alloy 2618*", J Mater Sci, 47 (2012) 2541–2547

[15] I. Ôzbek, "*A study on the re-solution heat treatment of AA 2618 aluminum alloy*" Materials Characterization 58 (2007) 312–317

[16] P. Shen, "*The effects of heat treatment on the microstructure and mechanical properties of the AA2618 DC cast plate*", Ph.D. Thesis (2012) Universite du Quebec

[17] R.N. Wilson, P.J. E. Forsyth, "Effects of Additions of 1% Iron and 1% Nickel on Age-hardening of an Aluminum-2.5%Copper-1.2%Magnesium Alloy", Journal of the Institute of Metals, 94 (1966) 8-13

[18] I.N.A. Oguocha, S. Yannacopoulos, Y. Jin, "*The structure of AlxFeNi phase in Al-Cu-Mg-Fe-Ni alloy (AA2618)*", Journal of Materials Science, 31 (1996) 5615-5621

[19] E.D. Moreau, I.W. Donaldson, R.L. Hexemer, Jr. and D.P. Paul Bishop, "*Effects of Fe and Ni additions on PM alloy. Part 2-Influence of elevated temperature exposure*", Canadian Metallurgical Quarterly 52 (2013) 4, 380-390

[20] American Society for Metals, "*ASM handbook. Volume 4: Heat Treating - Heat treating of aluminium alloys*" (1991) ASM International, Materials Park, OH

[21] M. Tiryakioglu, R. T. Shuey, "*Quench sensitivity of 2219-T87 aluminum alloy plate*" Materials Science and Engineering, A 527 (2010) 5033-5037

[22] I.N.A. Oguocha, M. Radjabi, S. Yannacopoulos, "*The effect of cooling rate on the quench sensitivity of 2618 Al/Al2O3 MMC*", Journal of Materials Science 35 (2000) 5629 – 5634

[23] H.K. Hardy, "*The Ageing Characteristics of Binary Aluminium-Copper Alloys*", Journal of the Institute of Metals, 79 (1951) 321-3[48]

[24] S.P. Ringer, K. Hono, "*Microstructural Evolution and Age Hardening in Aluminium Alloys: Atom Probe Field-Ion Microscopy and Transmission Electron Microscopy Studies*", Materials Characterization, 44 (2000) 101–131

[25] Y.A. Bagaryatsky, "*Structural changes on ageing Al-Cu-Mg alloys*", Dokl. Akad. Nauk SSSR, 87 (1952) 397-401

[26] J. M. Silcock, "*The Structural Ageing Characteristics of Al-Cu-Mg Alloys with Copper-Magnesium Weight Ratios of 7-1 and 2.2-1*", Journal of the institute of metals, 89 (1961) 203-210

[27] S.C. Wang, M.J. Starink, N. Gao, "Precipitation hardening in Al–Cu–Mg alloys revisited", Scripta Materialia, 54 (2006) 287-291

[28] H.C. Shih, N.J. Ho, J.C. Huang, "Precipitation Behaviors in Al-Cu-Mg and 2024 Aluminum Alloys", Metallurgical and Materials Transactions A, 27A (1996) 2479-2494

[29] H. Perlitz, A. Westgren, "*The crystal structure of* Al_2CuMg" Ark. Kemi. Mineral. Geol., 16 B (1943) 1

[30] D.G. Eskin, "Decomposition of supersaturated solid solutions in Al–Cu–Mg–Si alloys", Journal of Materials Science 38 (2003) 279-290

[31] J. Wang, D. Yi, X. Su, F. Yin, "Influence of deformation ageing treatment on microstructure and properties of aluminum alloy 2618", Materials Characterization, 59 (2008) 965-968

[32] H. Lu, P. Kadolkar, K. Nakazawa, T. Ando, and C.A. Blue, "*Precipitation Behavior of AA2618*", Metallurgical and Materials Transaction A, 38A (2007) 2379-2388

[33] P. Shen, E.M. Elgallad, X.-G. Chen, "*ON THE AGEING BEHAVIOR OF AA2618 DC CAST ALLOY*", TSM Light Metals (2013) 373-377

[34] E.M. Elgallad, P. Shen, Z. Zhang, X.-G. Chen, "*Effects of heat treatment on the microstructure and mechanical properties of AA2618 DC cast alloy*", Materials and Design 61 (2014) 133–140

[35] J. Majimel, G. Molenat , M.J. Casanove, D. Schuster, A. Denquin, G. Lapasset, "*Investigation of the evolution of hardening precipitates during thermal exposure or creep of a 2650 aluminium alloy*", Scripta Materialia, 46 (2002) 113–119

[36] K.E. Knipling, D.C. Dunand, D.N. Seidman, "*Criteria for developing castable, creep-resistant aluminum-based alloys – A review*", Zeitschrift für Metallkunde, 97 (2006) 3, 246-265.

[37] Z. Ahmad, "*The Properties and Application of Scandium-Reinforced Aluminum*", JOM, 55 (2003) 2, 35-39

[38] J. Röyset, "*SCANDIUM IN ALUMINIUM ALLOYS OVERVIEW: PHYSICAL METALLURGY, PROPERTIES AND APPLICATIONS*", Metallurgical Science and Technology, 25 (2007) 2, 11-21

[39] K.E. Knipling, R.A. Karnesky, C.P. Lee, D.C. Dunand, D.N. Seidman, "*Precipitation evolution in Al–0.1Sc, Al–0.1Zr and Al–0.1Sc–0.1Zr (at.%) alloys during isochronal aging*", Acta Materialia 58 (2010) 5184–5195

[40] K.E. Knipling, D.C. Dunand, D.N. Seidman, "*Nucleation and Precipitation Strengthening in Dilute Al-Ti and Al-Zr Alloys*", Metallurgical and Material Transactions A, 38A (2007) 2552-2563

[41] K.E. Knipling, D.C. Dunand, D.N. Seidman, “*Precipitation evolution in Al–Zr and Al–Zr–Ti alloys during isothermal aging at 375-425 °C*”, Acta Materialia 56 (2008) 114–127

[42] K.E. Knipling, D.C. Dunand, D.N. Seidman, “Precipitation evolution in Al–Zr and Al–Zr–Ti alloys during aging at 450–600 °C”, Acta Materialia 56 (2008) 1182–1195

[43] E. Nes, “*PRECIPITATION OF THE METASTABLE CUBIC* Al_3Zr*-PHASE IN SUBPERITECTIC Al-Zr ALLOYS*”, Acta Metallurgica, 20 (1974) 4, 499-506

[44] J.D. Robson, P.B. Prangnell, “*Modelling Al3Zr dispersoid precipitation in multicomponent aluminium alloys*”, Materials Science and Engineering A, 352 (2003) 240-250

[45] Z. Yin, Q. Pan, Y. Zhang, F. Jiang, “*Effect of minor Sc and Zr on the microstructure and mechanical properties of Al–Mg based alloys*”, Materials Science and Engineering, A280 (2000) 151-155

[46] J.S. Robinson, T.Y. Liu, A.K. Khan, M.J. Pomeroy, “*Influence of processing on the properties of the aluminium alloy 2025 with a zirconium addition*”, Journal of Materials Processing Technology, 209 (2009) 30[48]–3078

[47] K.M.C. Wong, A.R. Daud, A. Jalar, “*Microhardness and Tensile Properties of a 6XXX Alloy Through Minor Additions of Zr*”, Journal of Materials Engineering and Performance, 18 (2009) 1, 62-65

[48] L. Zeng, Z. Li, R. Che, T. Shikama, S. Yoshihara, T. Aiura, H. Noguchi, “*Mesoscopic analysis of fatigue strength property of a modified 2618 aluminum alloy*”, International Journal of Fatigue, 59 (2014) 215-223

[49] A.D. Kotov, A.V. Mikhaylovskaya, I.S. Golovin, V.K. Portnoy, “Fine-grained structure and superplasticity of Al-Cu-Mg-Fe-Ni alloys”, Superplasticity in Advanced Materials - ICSAM (2012) 55-61

[50] J.H. Wang, D.Q. Yi, “*Effect of melt over-heating and zirconium alloying on the morphology of* Al_9FeNi *phase and mechanical properties of 2618 alloy*”, Acta Metallurgica Sinica (English Letters), 15 (2002) 6, 525-430

[51] N. Jaukovic, M. Lalovic, “*Effect of Zirconium and Lanthanides on the Recovery in 2618 Base Aluminium Alloy*”, ISIJ International, 45 (2005) 3, 405-407

[52] N. Jaukovic, D. Perovic, “*Influence of Zirconium on the Recovery Process in Heat-resistant Al Alloys*”, ISIJ International, 44 (2004) 7, 1238-1242

[53] Y.C. Chen, M.E. Fine, J.R. Weertman, R. E. Lewis, “*Coarsening Behaviour of* $L1_2$ *Structured* $Al_3(Zr_xV_{1-x})$ *Precipitates in Rapidly Solidified Al-Zr-V Alloy*”, Scripta Metallurgica, 21, (1987) 1003-1008

[54] Y.C. Chen, M.E. Fine, J.R. Weertman, "*MICROSTRUCTURAL EVOLUTION AND MECHANICAL PROPERTIES OF RAPIDLY SOLIDIFIED A1-Zr-V ALLOYS AT HIGH TEMPERATURES*", Acta metal. mater., 38 (1990) 5, 771-780

[55] M.S. Zedalis, M.E. Fine, "*Precipitation and Ostwald Ripening in Dilute AI Base-Zr-V Alloys*", Metallurgical Transactions A, 17A (1986) 2187-2198

[56] W.W. Park, "*Alloy designing and characterization of rapidly solidified Al-Zr(-V) base alloys*", Material & Design, 17 (1996) 2, 85-88

[57] Z. Jia, J.P. Couzinie, N. Cherdoui, I. Guillot, L. Arnberg, P. Åsholt, S. Brusethaug, B. Barlas, D. Massinon, "*Precipitation behaviour of* Al_3Zr *precipitate in Al-Cu-Zr and Al-Cu-Zr-Ti-V alloys*", Trans. Nonferrous Met. Soc. China, 22 (2012) 1860−1865

[58] E.M. Elgallad, A.M. Samuel, F.H. Samuel, H.W. Doty, "*Effects on the Microstructure and Tensile Properties of a new Al-Cu Based Alloy Intended for Automotive Castings*", AFS Transactions (2010) 39-56

[59] W. Kasprzak, B.S. Amirkhiz, M. Niewczas, "*Structure and properties of cast Al–Si based alloy with Zr–V–Ti additions and its evaluation of high temperature performance*", Journal of Alloys and Compounds 595 (2014) 67–79

[60] W. Kasprzak, D. Emadi, M. Sahoo, M. Aniolek, "*Development of Aluminium Alloys for High Temperature Applications in Diesel Engines*", Material Science Forum, 618-619 (2009) 595-600

CHAPTER 2

Experimental

INTRODUCTION

In this chapter are described the experimental material, procedures and equipments used for the experimental work.

The experimental work is ideally divided into two parts: the first one dealt with unmodified AA 2618 alloy and was carried out at the University of Bologna, while the second one dealt with chemical modification of AA 2618 and was carried out at NTNU. In this chapters, the two parts of the experimental work are reported separately.

2.1 UNMODIFIED AA2618

2.1.1 Material

The first part of the experimental work was concerned with the study of unmodified AA 2618 alloy. The samples used for this study were extracted from 6 forged pistons with the chemical composition reported in Table 2.1.

Chemical composition of AA 2618 [wt%]												
Cu	Mg	Ni	Fe	Si	Ti	Mn	Zn	Cr	Pb	Zr	Sn	Al
2.6	1.5	1.2	1.1	0.23	0.03	0.11	0.04	0.0003	0.002	0.12	0.004	balance

Tab. 2.1 – Chemical composition of the AA 2618 alloy used to produce samples for microstructural investigation of the effects of over-aging.

Normally, this alloy is T6 heat-treated (solutionized, quenched and peak-aged). The industrial treatment on these components includes a solution heat treatment consisting of three consecutive phases:

- Heating from 200 to 495 °C in 1.5 hours;
- Maintenance at 507 °C for 3 hours;
- Maintenance at 525 °C for 15.5 hours.

Heating from 495 °C to 507 °C and from 507 °C to 525 °C is quite fast. The two intermediate holding time at 495 °C and 507 °C are needed in order to dissolve low-melting eutectics, that otherwise would cause an incipient melting. After solutionizing, the samples are quenched in hot water (60 - 90 °C) and peak-aged (maintenance at 200 °C for 20 h).

2.1.2 DSC analysis

Differential scanning calorimetry (DSC) analyses was carried out on two samples, extracted from two different pistons, called 92/E990 and 148/E989, in the as-forged state (without heat treatment). The two pistons are nominally equivalent, so similar DSC results are expected for the two samples. Moreover, DSC was carried out on a sample extracted from piston 92/E990 after applying solution heat treatment, as described in § 2.1.1. The weight of the DSC samples was approximately 26-27 mg for the two as-forged samples and 45 mg for the solutionized sample. The heating rate was fixed at 10 °C/min with temperatures ranging from room temperature to 700 °C. A protective gas atmosphere of Ar was applied.

2.1.3 Optimization of heat treatment

For the optimization of heat treatment, some parallelepipeds (6x5x3 mm) were cut from the received material, ground to obtain a suitable surface finishing for Brinell hardness tests, solutionized and quenched as described in § 2.1.1. These samples were then exposed to different temperature, from room temperature to 220 °C and for each temperature, various holding times were analysed, form half an hour to 50 hour. To determine the effect of heat treatment, Brinell hardness tests HB10 (62.5 kg load and spherical indenter with 2.5 mm diameter) were carried out according to the standard ASTM E 10–08, after cleaning the surface to remove oxides due to high temperature. For each temperature, at least 2 samples were used, and at least 3 hardness test were carried out on each test, in order to have an hardness measurement as an average on 6 tests. Table 2.2 summarize holding times for each temperature.

Temperature [°C]	Time [h]
25	1 – 9 – 25 – 33 – 50
50	1 – 5 – 9 – 25 – 34 – 50
75	1 – 5 – 9 – 25 – 34 – 50
100	1 – 10 – 25 – 37 – 50
165	1 – 5 – 17 – 25 – 37 – 50
190	1 – 2 – 5 – 10 – 17 – 25 – 32 – 40 – 49
200	0.5 – 1 – 2 – 5.5 – 10 – 20 – 25 – 49
210	0.5 – 1 – 2 – 5 – 10 – 14.5 – 20 – 25 – 34 – 40 – 49
220	0.5 – 1 – 2 – 3 – 5 – 10 – 14.5 – 20 – 25 – 34 – 49

Tab. 2.2 – Holding times and temperatures used to obtain ageing curves.

2.1.4 Study of thermal stability

For the study of thermal stability of T6 heat-treated AA 2618, some parallelepipeds (12x4x6 mm) were cut from the received material, solutionized, quenched and peak-aged (200 °C for 20 h) as described in § 2.1.1. These samples were then exposed to different temperature, from 200 °C to 305 °C with temperature intervals of 15 °C, and for each temperature, various holding times were analysed, from 5 minutes to 1 week. To determine the effect of thermal exposure, Brinell hardness tests HB10 (62.5 kg load and spherical indenter with 2.5 mm diameter) were carried out according to the standard ASTM E 10–08, after cleaning the surface to remove oxides that may appear due to high temperature. At least 3 hardness test were carried out on each sample. Collecting all these data, it was possible to obtain degradation curves for T6 AA 2618 alloy. It was possible as well to deduce time-temperature curves characterized by the same hardness (hardness-time-temperature curves).

2.1.5 Tensile tests

47 flat tensile specimens were cut from the heads of 5 forged pistons in AA 2618, with the geometry reported in Figure 2.1 (a). The samples were extracted in two different ways from the piston heads: three pistons were cut as in Figure 2.1 (b), with a thickness of 10 mm, obtaining 12 suitable samples from each piston, while the other two pistons were cut as in Figure 2.1 (c), with a thickness of 4 mm, obtaining the other 11 samples. Samples were numbered as shown in Figure 2.1 (b) and (c), and the two samples on the extremities of each piston were not used because they were too short to respect the standard. The different extraction method is due to the fact that from some piston samples for study of ageing and thermal stability had already been extracted. However, no distinction will be made when presenting the results between sample extracted with the two methods.

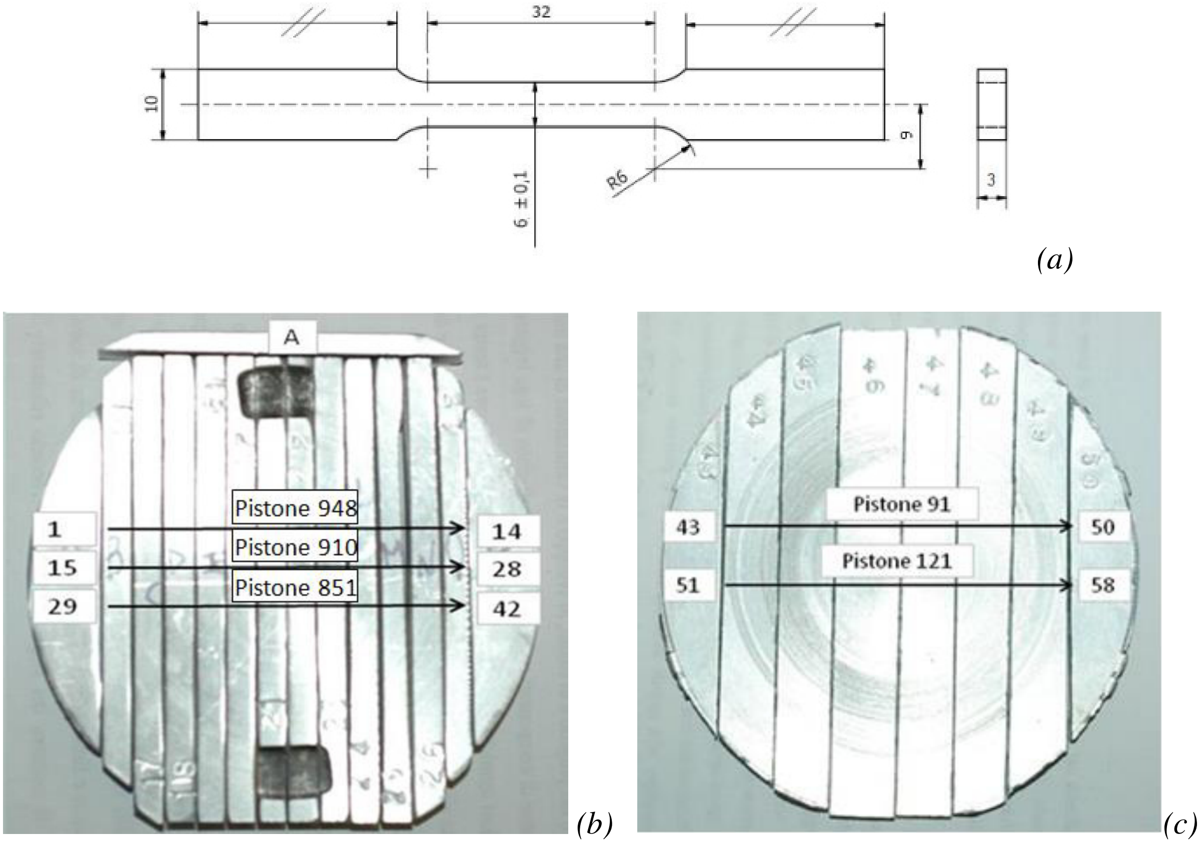

(a)

(b)

(c)

Fig. 2.1 – Dimensions of flat specimens used for tensile tests (a) and two different method used to extract the specimens from piston heads (b), (c). In Figure (b) and (c), the numbers represent the numeration of tensile specimens.

In order to examine thermal stability of T6 heat-treated material, the 47 tensile specimens were divided in 8 classes, each of which contains at least 5 specimens. All the specimens were subjected to the T6 heat treatment described in §2.1.1, and, after that, to a high temperature exposure cycle, different for each class. The classes were designed to obtain predetermined HB10 values, and holding times and temperatures were chosen on the basis of hardness-time-temperature curves previously obtained (§2.1.2). The class with a target Brinell hardness of 100 HB10 was divided into 2 classes (one consisting of 3 samples, and the other of 4), with different high temperature exposure cycles, in order to verify that mechanical properties of overaged materials do not depend on particular overaging conditions, but only on residual hardness. Target Brinell hardness, thermal exposure parameters (time and temperature), and number of samples of each class is summarized in Table 2.3.

Target hardness	Temperaure, time	no. samples
Peak-hardness	no exposure	5
130 HB10	200 °C, 24 h	5
115 HB10	230 °C, 10 h	5
100 HB10	230 °C, 5 days	4
100* HB10	275 °C, 3 h	3
90 HB10	290 °C, 3.5 h	5
80 HB10	305 °C, 8.5 h	5
75 HB10	305 °C, 16 h	5
70 HB10	305 °C, 30 h	5

Tab. 2.3 – Target hardness HB10, time and temperature parameters and number of samples for each class in which tensile samples are divided.

Before performing the tensile tests, on each specimen six Brinell hardness test HB10 (62.5 kg load and spherical indenter with 2.5 mm diameter) were carried out according to the standard ASTM E 10–08.

Tensile tests were carried out at room temperature on samples with rectangular cross-section and 30 mm long gauge length, according to standard UNI EN 10002-1:2004. A double-screw tensile machine was used, and a strain rate of $3.3 \cdot 10^{-3}$ s^{-1} was applied. From tensile tests some mechanical properties were evaluated: yield strength (YS), ultimate tensile strength (UTS), elongation to failure (E), as well as strength index (K) and strain hardening exponent (n) of Hollomon’s equation.

2.1.6 Fracture surfaces

Some fracture surfaces were observed with scanning electron microscope (SEM), equipped with energy dispersive spectroscopy. The fracture surfaces extracted from the tensile specimens were placed for 15 minutes in an ultrasonic cleaner using acetone as solvent in order to remove all the impurities from the surface, washed with ethanol and rapidly dried before observation.

2.1.7 Optical microscopy (grain size)

Grain size was measured on every tensile sample, to check if mechanical properties could be affected by large inhomogeneity in this parameter between samples extracted from different areas of the piston head, or between different pistons. Microstructural samples were extracted from the tensile specimen cross-section after the tensile tests, from the area next to the section where failure occurred. Samples were cold embedded in resin, in cylindrical mould, and then a hole was performed in the resin to make the electrochemical etching possible. After that, sample were grinded with silicon carbide papers (180 and 2000 grit) and polished with monocrystalline diamond suspensions (grain size 3 μm) and lubricant. Samples were then electrochemically etched applying a 12 V tension and using a solution of 5% HBF_4 in water, according to ASTM E 407 standard, for 30-45 s. Acetone was used to clean the etched samples.

Grain size was measured with optical microscope, using polarized light. For each cross section, 6 micrographs were taken, and grain size was measured drawing a line with the software Image Pro-Plus, and dividing its length by the number of intercepted grain boundaries.

2.1.8 Microstructural modifications due to overaging

FEG-SEM was used to characterize the microstructure of 7 of the samples used for grain size measurements. The 7 samples were chosen from 7 different hardness classes. Table 2.4 shows the overaging conditions (exposure time and temperature) applied to each sample and the consequently attained hardness value HB10. The class, indicating the target hardness, of each sample is also given in Table 2.4.

Sample No.	Over-aging conditions	Hardness [HB10]	Class
39	-	145	peak-hardness
2	200 °C, 24 h	125	130 HB10
22	230 °C, 10 h	115	115 HB10
31	230 °C, 5 days	105	100 HB10
35	305 °C, 8.5 h	90	80 HB10
33	305 °C, 30 h	80	70 HB10
40	290 °C, 3.5 h	70	90 HB10

Tab. 2.4 – Overaging conditions (temperature and time) and consequently attained hardness values (HB10), for each of the 7 samples of AA 2618 supplied by University of Bologna. The class indicates the target residual hardness that should have been reached. Note that sample no. 39 is peak-aged (T6 heat treated), while all the other samples are overaged to different hardness levels.

For the study of microstructural modification during overaging, etching is not needed, so the samples were ground and polished again in order to remove the etched surface. Grinding was done with a manual Knuth Rotor grinding machine and silicon carbide paper discs (FEPA grit sizes P-800, P-1200 and P-2000); water was used as lubricant. Polishing was carried out on a manual DP-U3 machine, with magnetic discs drenched with monocrystalline diamond suspensions (grain size 3 and 1 μm) and lubricant. The samples were then placed for 1-2 minutes in an ultrasonic cleaner using ethanol as solvent in order to remove all the impurities from the polished surface, washed with ethanol and rapidly dried.

After the preparation, the samples were examined with a Zeiss Supra 55 VP LV FE-SEM equipped with an energy dispersive spectrometer (EDS), in order to study the modification of intermetallic phases and precipitates due to different levels of over-aging. The analysis was carried out both with secondary electrons (acceleration voltage 10 kV, aperture size 30 μm, working distance 10 mm) and back scattered electrons (acceleration voltage 15 kV, aperture size 120 μm, working distance 10 mm). EDS (acceleration voltage 15 kV, aperture size 120 μm, working distance 10 mm, counting time 1 minute) of selected points was used to verify the nature of the particles observed with both secondary and back scattered electrons.

2.2 EFFECT OF Zr AND V ADDITIONS ON AA 2618

2.2.1 Calculation of the additions

The second and main part of the study is concerned with the modification of AA 2618 alloy through the addition of small amounts of transition metals, in order to achieve an enhanced heat resistance. The base material (AA 2618 aluminium alloy) was supplied by Duraldur S.p.A, an Italian company specialized in the production of pistons. The material was received in form of extruded bar (diameter 130 mm). The result of the chemical analysis carried out by Duraldur S.p.A on the supplied material is shown in Table 2.5 :

Chemical composition of AA 2618 [wt%]											
Cu	**Mg**	**Ni**	**Fe**	**Si**	**Ti**	**Mn**	**Zn**	**Cr**	**Pb**	**Zr**	**Al**
2.5	1.6	1.2	1.1	0.16	0.11	0.01	0.05	0.01	0.01	0.13	balance

Tab. 2.5 – Chemical composition (wt.%) of the aluminium alloy AA 2618 supplied by Duraldur S.p.A. and used for the study of the effect of Zr and V additions. Note that a small amount of Zr (0.13 wt.%) is present in AA2618 alloy, used as base material.

The elements (and their amounts) to be added in order to produce modified alloys with improved heat resistance were defined after reviewing the scientific literature about modification of aluminium alloys through the addition of transition metals, and in particular the addition of Sc and Zr. Generally, Sc seems to bring very good results when added to this kind of alloys, especially if added together with Zr. Nevertheless, it was chosen not to use Sc because of its very high cost, that would significantly increase the cost of the alloy.

From the study of the literature appeared that also Zr seems to have a positive effect on heat resistance of Al alloys, when added in small percentages (0.15 – 0.4 wt%). Some elements such as Ti and V also seem to improve the benefits brought by Zr.

Taking into account these considerations, it was decided to produce 3 alloys with different chemical compositions:

- AA 2618 base material, as a reference;
- AA 2618 with level of Zr increased to 0.25 wt %;
- AA 2618 with level of Zr increased to 0.25 wt% and addition of 0.1 wt% V.

Note that, as reported in Tab. 3, the base alloy AA 2618 received by Duraldur S.p.A. contained an amount of Zr equal to 0.13 wt %, thus in order to attain an amount of Zr equal to 0.25 wt % in the modified alloys it was necessary to add only 0.12 wt % of Zr.

A casting was performed to produce each of the 3 different alloy compositions. The material for each casting was calculated in order to produce 2 kg of alloy. Zr and V were added to the base material through Al-10Zr and Al-10V master alloys, respectively. In order to obtain a homogeneous alloy composition after the casting, the base material was cut into cubes with sides about 3 cm long, while master alloys were cut into pieces of about 10 grams.

The equations used to calculate the amount of master alloys to add to the base material, in the desired compositions, are shown below.

For the first modified alloy (with addition of Zr) the following equation was used:

$$(1000 - x) \cdot 0.13 + x \cdot 10 = 1000 \cdot 0.25$$

where x is the amount (in grams) of the master alloy Al-10Zr to add to (1000-x) g of base material in order to obtain 1 kg of modified alloy with 0.25 wt % of Zr. In the equation, 0.13 is the percentage of Zr in the base material, while 10 is the percentage of Zr in the master alloy and 0.25 is the targeted percentage of Zr in the modified alloy. The solution of this equation gives:

$$x = 12.1580\ g$$

$$(1000 - x) = 987.84\ g$$

where x represents the grams of master alloy and (1000-x) the grams of base material needed in order to obtain 1 kg of modified alloy. In order to produce 2 kg of modified alloy, the amounts to be used are as follows:

- 24.3161 g of master alloy Al-10Zr
- 1975.68 g of base material AA 2618

For the second modified alloy (with addition of both Zr and V) the following equations were used:

$$(1000 - x - y) \cdot 0.13 + x \cdot 10 = 1000 \cdot 0.25$$

$$y \cdot 10 = 1000 \cdot 0.1$$

where x, y and (1000-x-y) stand for the amount in grams of respectively master alloy Al-10Zr, master alloy Al-10V and base material needed in order to obtain 1 kg of modified alloy, with 0.25 wt % of Zr and 0.1 wt % of V. In the equations, 0.13 represents the percentage of Zr contained in the base material, 10 is the percentage of Zr and V contained in the two master alloys, while 0.25 and 0.1 are the targeted percentages of Zr and V, respectively.

The solution of the two equations gives:

$$x = 12.2898\ g$$

$$y = 10.0000\ g$$

$$(1000 - x - y) = 977.71\ g$$

where x represents the grams of master alloy Al-10Zr, y the grams of master alloy Al-10V and (1000-x-y) the grams of base material required in order to obtain 1 kg of modified alloy. In order to produce 2 kg of modified alloy, the amounts to be used are as follows:

- 24.5795 grams of master alloy Al-10Zr
- 20.0000 grams of master alloy Al-10 V
- 1955.42 grams of base material AA 2618

The base material was weighed with a scale with 2 decimal digits, while master alloys with a scale with 4 decimal digits. The pieces of base material and master alloys were ground with a silicon carbide paper (FEPA grit sizes P-320) until an adequately accurate weigh was reached.

For the Zr modified alloy, the real amounts of base material and master alloy used were:

- 24.3102 grams of Al-10Zr
- 1975.67 grams of AA 2618

These amounts give a theoretical percentage of Zr in the modified alloy equal to 0.24997 wt.%, that is very close to the target percentage of 0.25 wt.%.

For the Zr-V modified alloy, the real amounts of base material and master alloys used were:

- 24.5750 grams of Al-10Zr
- 19.9970 grams of Al-10V
- 1955.42 grams of AA 2618

These amounts give a theoretical percentage of Zr and V in the modified alloy equal to 0.24998 wt.% and 0.09999 wt.% respectively, that are very close to the target percentage of 0.25 wt.% Zr and 0.1 wt.% V.

2.2.2 Casting

Each of the three castings (one for each level of addition) was made with the following procedure. A boron nitride-coated clay graphite crucible was placed into a furnace and pre-heated at a temperature of 750 °C. The right amounts of base material and master alloys, cut into pieces as previously described, were placed into the crucible and heated at 750 °C. A graphite stick was used to manually stir the melt, in order to guarantee a homogeneous distribution of the added elements into the base material. The molten material was kept at 750 °C for at least 1 h.

During melting, oxides and impurities tend to accumulate on the surface of the liquid alloy. Therefore, before casting the molten material, the surface layer was removed with the help of a graphite stick. The material was then poured in a rectangular copper mould (115 mm long x 75 mm wide x 30 mm thick) and in a cylindrical copper mould (inner diameter 73 mm and height 180 mm). From each of the two modified alloys a smaller sample was also produced, to be used for chemical analysis in order to verify the level of additions. All the castings were solidified in ambient air.

2.2.3 Chemical analyses

Chemical analyses were carried out both in Bologna and in Trondheim, on specimens extracted from the various moulds in order to verify the homogeneity of the material. For the chemical analyses carried out in Bologna a Spectrolab S n. 3590-91 quantometer was used, while in Trondheim glow discharge mass spectrometry (GDMS) technic was used (Thermo Fisher Scientific Element GD machine).

2.2.4 Thermal analyses during solidification and DSC

Before casting the material, thermal analyses were performed in order to detect possible changes in the cooling curves due to the presence of Zr and V.

First, the thermocouple used for the thermal analysis needed to be calibrated and for this purpose, high purity aluminium was used. Small samples of molten material were taken with a conical steel crucible (upper outer diameter 32 mm, lower outer diameter 23 mm, height 32 mm, thickness 1.75 mm). Before each test, the crucible was sprayed with boron nitride, dried in a furnace (700 °C) and preheated by placing it on the top of the melt (750 °C), from which the surface oxides and impurities had previously been removed. After temperature equilibrium between melt and crucible had been established, the crucible was filled by submerging it into the melt, and then placed on an insulating support. A boron nitride-coated thermocouple was then placed centrally into the melt, at a constant distance of 10 mm from the bottom of the crucible. Another insulating board was then placed on the top of the crucible and the melt was cooled at room temperature in air. Initially, 10 tests were performed in order to verify the calibration and stability of the thermocouple. Between the second and the third casting, another calibration was needed due to poor stability of the thermocouple. Therefore, other 16 tests were carried out on high purity aluminium. Furthermore, 5 tests were performed both before and after the thermal analysis on each casting, in order to record any temperature drift that might take place. Note that for pure aluminium, a melting temperature of 660.3 °C was used as reference for the thermocouple calibration.

The same procedure illustrated for the calibration of the thermocouple was used for the thermal analysis carried out on the 3 different alloy compositions. Data were acquired in the range from 700 °C to 400 °C. For each composition, at least 3 tests were performed.

The cooling curves (both from calibration tests and thermal analysis measurements) were recorded with a Campbell Instruments data logger at a rate of 50 Hz. The collected data were then analysed with Microsoft Excel and with Alutron's Thermal Analyzer TAW32 software, which can filter the data and plot the solidification curve and its derivative dT/dt.

In particular, Alutron's Thermal Analyzer TAW32 software was used to find the solidification temperature from each calibration test. To increase the precision, the solidification temperature was determined considering the derivative dT/dt: solidification begins when the derivative starts to increase sharply. With TAW32 is possible to find the temperature corresponding to the time when the derivative dT/dt begins to increase, which is the solidification temperature.

The average solidification temperature of the tests performed both before and after the thermal analyses on each casting was calculated. This average solidification temperature was then compared to the exact solidification temperature of pure aluminium (660.3 °C) and the difference between the two was subtracted to the data obtained from the thermal analysis measurements.

Similarly, TAW32 was used to analyse the data from the thermal analysis measurements. First, the corrected data were filtered, and then the derivative dT/dt was used to find the temperature corresponding to the critical points (every critical point is associated to a peak in the derivative). TAW32 was also used to plot the baseline, calculated by fitting user-defined interval of the dT/dt curve before and after solidification. The baseline was used to calculate the fraction solid in points corresponding to peaks of the dT/dt derivative. Analysing the data with TAW32, it was also possible to calculate the cooling rate before the starting of the solidification, and it turned out to be approximately 1.4 – 1.6 °C/s.

Differential scanning calorimetry (DSC) analyses was carried out in Bologna, on the same material used for chemical analyses, with a NETZSCH DSC 404F3 instrument. The weight of the DSC samples was approximately 28-32 mg, and the heating and cooling rate were fixed at 10 °C/min with temperature ranging from room temperature to 650 °C. A protective gas atmosphere of Ar was applied.

2.2.5 Hot rolling

Al-Cu pistons are usually produced by forging. The forging parameters supplied by Duraldur S.p.A. are given in Table 2.6.

T billet	380-420 °C
max P	125-130 bar
no. of steps	4
Reduction x direction	2%
Reduction y direction	48%
Speed max. (first step)	2.75 mm/s
Total time	14 s

Tab. 2.6 – Forging parameters for the production of pistons in AA 2618 aluminium alloy

Hot rolling was performed to mimic the effect of the forging process on the material. In order to obtain specimens for the hot rolling, each casting obtained from the rectangular copper mould (one for each composition) was cut in 6 parts (approximately 50 mm long, 20 mm wide and 25-30 mm thick). In order to analyse the effect of different reduction ratios, the 6 specimens from each composition were divided as follows:

- 1 sample not deformed (as cast)
- 1 sample hot rolled to a reduction of ~16%
- 1 sample hot rolled to a reduction of ~33%
- 3 samples hot rolled to a reduction of ~50%

In the following study, one sample from each condition was analysed.

The parameters used for the hot rolling are reported in Table 2.7:

Hot rolling parameters for analysed samples			
Alloy	**2618**	**2618 + Zr**	**2618+Zr+V**
Initial thickness	~ 24 mm	~ 29 mm	~ 31 mm
Furnace temperature	400 °C	400 °C	400 °C
t heating before first step	30 min	30 min	30 min
Thickness reduction for each step	~ 2 mm	~ 2.5 mm	~ 2.5 mm
Heating between consecutive steps	3 min	3 min	3 min
Thickness reduction speed	12.5 mm/s	14.0 mm/s	14.0 mm/s

Sample "16%"	Deformation ratio	~16 %	~16 %	~16 %
	Total reduction y direction	4 mm	5 mm	5 mm
	no. steps	2	2	2
Sample "33%"	Deformation ratio	~33 %	~33 %	~33 %
	Total reduction y direction	8 mm	10 mm	10 mm
	no. steps	4	4	4
Sample "50%"	Deformation ratio	~50 %	~50 %	~50 %
	Total reduction y direction	12 mm	15 mm	15 mm
	no. steps	6	6	6

Tab. 2.7 – Parameters for hot rolling used to process microstructural and hardness samples. Total reduction change between 12-15 mm in relation to the initial thickness of the sample.

As reported in Table 2.7, the samples were heated at 400 °C for 30 minutes. In order to obtain a total reduction of approximately 50%, 6 passes were needed. The average thickness of the AA 2618 samples was 24 mm, so each pass was set to produce a reduction of 2 mm, to obtain a total reduction of 12 mm. For the other two casting the average thickness was 30 mm, so each pass was set to produce a reduction of 2.5 mm, to obtain a total reduction of 15 mm. Between two consecutive passes, the samples were heated for 3 minutes in the furnace at 400 °C. The thickness reduction speed was calculated with simple geometrical consideration, reported in Figure 2.2. After hot rolling, the sample were quenched in cold water to avoid modification of the deformed microstructure.

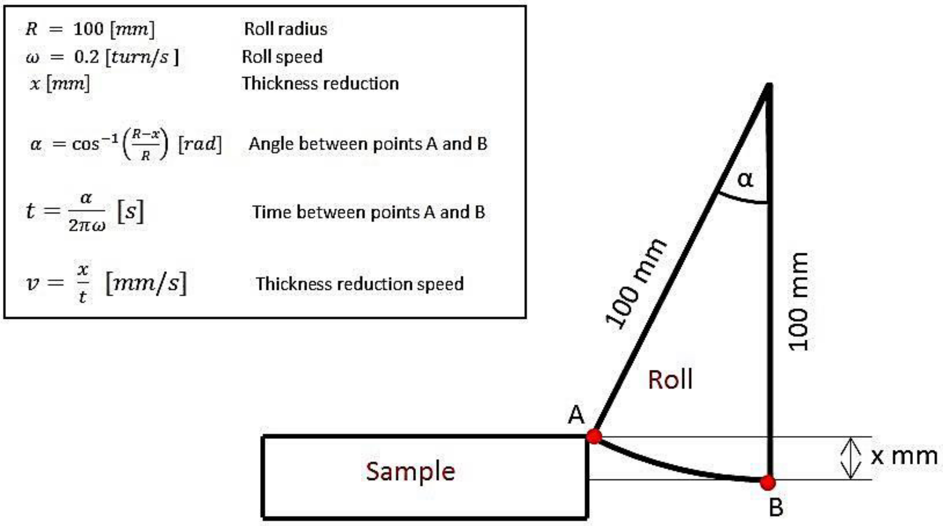

Fig. 2.2 – Scheme and equations used for the calculation of the thickness reduction speed during hot rolling

Since the samples of alloy modified with Zr and V were heavily cracked for deformation higher than 33%, it was chosen to hot roll two samples of the Zr-modified alloy with smaller thickness reduction for each steps. These specimens were hot rolled to a reduction of ~60% with 12 steps of ~1 mm. All the other parameters used for the hot rolling of these specimens were the same showed in Table 2.7. However, these samples were not used in the following analyses.

In order to understand what caused the cracks, other samples were cut from the cylindrical casting and hot rolled with different parameters. Two samples for each composition (AA 2618, AA 2618 with addition of Zr and AA 2618 with addition of Zr and V) and one sample from the extruded bar received by Duraldur (extracted in the transverse direction) were hot rolled. The dimensions of the samples are given in Table 2.8, together with the other rolling parameters:

Hot rolling parameters (second test)	
Sample dimention	50 x 20 x 10 mm
T furnace	400 °C
t heating before first step	1.5 h
Total reduction y direction	~ 50% (5 mm)
no. steps	2 (each 1 mm reduction) + 6 (each 0.5 mm reduction)
Heating between consecutive steps	10 min
Thickness reduction speed	8.9 mm/s (1 mm reduction) 6.3 mm/s (0.5 mm reduction)

Tab. 2.8 – Hot rolling parameters used for the second hot rolling test to try to avoid cracks during deformation. Two samples for each chemical composition and an additional sample of AA 2618 extracted from the extruded bar were hot rolled with this parameters.

As reported in Table 2.8, the samples were heated at 400 °C for 1.5 hours. The average thickness of the samples was approximately 10 mm. In order to obtain a total reduction of approximately 50%, 8 passes were used. The first two passed were set to produce a reduction of 1 mm, while the other 6 passes were set to produce a reduction of 0.5 mm each, to a total of 5 mm. The thickness reduction speed was calculated to be 8.9 mm/s for the steps with 1 mm reduction and 6.3 mm/s for the steps with 0.5 mm reduction. Between two consecutive passes, the samples were heated for 10 minutes in the furnace at 400 °C. After hot rolling, the sample were quenched in cold water to avoid modification of the deformed microstructure.

2.2.6 Microstructural analysis

For each chemical composition and for each of the 4 different deformation ratios, 2 microstructural samples were extracted, one on the longitudinal direction and the other on the transverse direction. The microstructural samples were extracted cutting the material in four parts, as showed in Figure 2.3.

Overall, 24 microstructural samples were extracted, each defined by 3 parameters:

- Chemical composition: AA 2618, AA 2618 + Zr or AA 2618 + Zr + V
- Level of deformation after hot rolling: as cast, 16 %, 33 % or 50%
- Direction of the surface in relation to the hot rolling direction: longitudinal or transverse

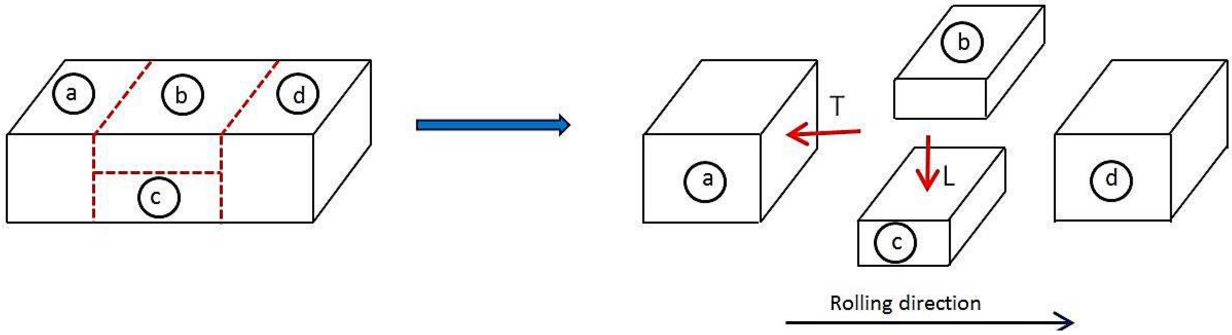

Fig. 2.3 – The diagram shows how the samples for microstructural investigation were extracted. The surfaces observed during the microstructural analysis are pointed out with red arrows: T indicates the surface in the transverse direction, while L indicates the surface in the longitudinal direction (in relation to the hot rolling direction).

Each of the 24 samples was cold embedded with Epofix resin. The mixture was prepared with 25 parts by weigh of resin and 3 parts of hardener, poured over the specimens in plastic moulds (diameter 40 mm) and let harden for at least 12 hours.

Thereafter, they were ground with an automatic Struers Rotoforce machine. Silicon carbide paper discs of FEPA grit sizes P-320, P-500, P-1200 and P-2000 were used as abrasive means, and water as lubricant. Each grinding step lasted 3 minutes; the speed and the force on each sample were set at 150 rpm and 20 N, respectively. After grinding, the sample were polished with an automatic Struers Tegraforce machine. The polishing was carried out in two steps, using monocrystalline diamond suspension with grain size of 3 µm and 1 µm, respectively. As for the grinding, each step lasted 3 minutes and the speed and the force on each sample were set at 150 rpm and 20 N, respectively. Oxide polishing (OP-S) was also necessary to attain a suitable surface finishing. The oxide polishing was performed on a Struers TegraForce automatic machine; the samples were polished for 1 minute, with a load of 10 N at a speed of 150 rpm, according to the parameters recommended by Struers. As abrasive and lubricating means, colloidal silica (grain size 0.4 mµ) with addition of chemical agents to increase the chemical activity for chemical-mechanical polishing was used.

The samples were then placed for 1-2 minutes in an ultrasonic cleaner using ethanol as solvent in order to remove all the impurities from the polished surface, washed with ethanol and rapidly dried.

The samples were then observed with both optical (LEICA MEF4M) and electron (Zeiss Supra 55 VP LV FE-SEM equipped with EDS) microscope. The analysis on the electron microscope was carried out with secondary electrons (acceleration voltage 10 kV, aperture size 30 µm, working distance 10 mm). EDS (acceleration voltage 15 kV, aperture size 120 µm, working distance 10 mm, counting time 30 s) of selected points was used to verify the nature of the particles observed. Line scan EDS was used to verify the distribution of Zr inside the dendrites and at the boundary.

As stated above, modified alloys specimens after rolling at high deformation show extensive cracks. The fracture surfaces of these cracks were analysed with electron Zeiss Supra 55 VP LV FE-SEM equipped with EDS microscope. Before observation, samples were placed for 10 minutes in an ultrasonic cleaner using ethanol as solvent in order to remove all the impurities from the surface, washed with ethanol and rapidly dried.

Specimens extracted from the material hot rolled with the optimized parameters were also prepared as described above for samples from the first hot rolling and analysed with optical LEICA MEF4M microscope.

The microstructure of the extruded bar received by Duraldur S.p.A. was also analysed with optical microscope (LEICA MEF4M) and scanning electron microscope (Zeiss Supra 55 VP LV FE-SEM equipped with ESD). Two samples were extracted from approximately the half of the cylinder radius: one was analysed along the axial direction and the other along the cross section. The samples were cold embedded and then ground and polished to 0.04 μm (same preparation as the hot rolled samples for microstructural analysis).

2.2.7 SDAS measurements

SDAS measurements were performed on the as-cast and hot rolled samples in order to evaluate the cooling rate during solidification and possible modification during hot rolling. On the optical microscope images were drawn lines which intercept at least three dendrite secondary arms. The line were then measured and the length of each line was divided for the number of intercepted secondary arms in order to obtain SDAS values. Images were taken with optical microscope LEICA MEF4 and analysed with image analysis software Progres CapturePro 2.8.8. For each sample the SDAS value was calculate as the average of 15 measurements. Figure 3.35 is reported as an example of the method used to measure SDAS.

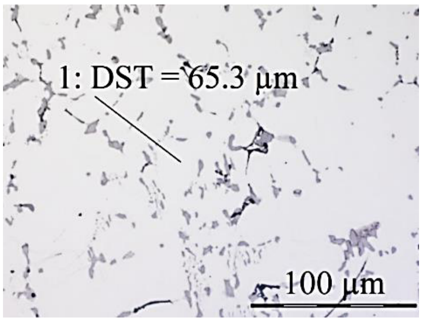

Fug. 2.4 – Example of SDAS measurement: the line in figure intercepts 3 secondary arms, therefore its length is divided by 3 to find the SDAS value.

2.2.8 EPMA analysis

In order to check the distribution on Zr and V across the dendrite arms, EPMA analyses were carried out on samples extracted from the as-cast specimens. These analyses were carried out on lines intercepting three or four secondary dendrite arms.

2.2.9 Brinell and Vickers hardness tests

Brinell hardness tests were performed on one sample of each material (the base alloy and the 2 modified alloys) and of each deformation level (as cast and 16%, 33% and 50% reduction). Samples for Brinell hardness tests were extracted from the longitudinal direction, and were manually grinded using a Knut-Rotor grinding machine and silicon carbide paper discs (FEPA grit sizes P-500, P-1000 and P-2000); water was used as lubricant.

Brinell hardness tests were done with a Struers Duramin – A2500 hardness test machine. Standard Brinell test HB10 were performing using a spherical steel indenter with 2.5 mm diameter and a 62.5 kgf load, applied for 15 s.

The indentation diameters were measured with optical microscope LEICA MEF4M, and HB10 values were calculated with the following equation:

$$HB10 = \frac{2 \cdot F}{\pi \cdot D(D - \sqrt{D^2 - d^2})}$$

Where *F* is the applied load, *D* is the diameter of the indenter and *d* is the diameter of the indentation.

On each sample at least three HB10 tests were performed to ensure statistical reliability.

Vickers microhardness measurements were done for each composition on samples as-cast and deformed to 16 % and 50 % reduction, extracted from the longitudinal direction, to evaluate the hardness of the α-Al phase. For these test, the same samples prepared for microstructural analysis were used. Vickers microhardness tests were carried out using a 15 g load ($HV_{0.015}$) applied for 15 s on a LEICA VMHT MOT tester. A 15 g load was chosen because with a bigger load (25 g) the hardness indentations are too big and involve also second phases, while with a smaller load (10 g) the indentations turn out to be too small to have a suitable standard deviation. For each sample the hardness was evaluated as an average of 3 measurements.

CHAPTER 3

Results and Discussion

INTRODUCTION

In this chapter, the results obtained from the experimental work are reported and discussed.

The first part of the chapter deals with unmodified AA 2618. In particular, the high temperature resistance and the degradation due to high temperature exposure were investigated.

The second part of the chapter deals with chemical modifications of AA 2618, by small additions of Zr and V, in order to enhance the mechanical properties at elevated temperatures. A preliminary study investigating the possibility of modify AA 2618 is presented.

3.1 UNMODIFIED AA 2618

The results of the experimental work carried out on the AA 2618 alloy are reported in this section. In particular, the experimental work is concerned with optimization of heat treatment of forged pistons and effect of thermal exposure on mechanical properties and microstructure of T6 AA 2618.

3.1.1 DSC analyses

DSC analysis analyses was were carried out on two samples extracted from two as-forged pistons, in order to detect the presence of possible low-melting phases that could melt during heat treatment, and in particular during solutionizing. In fact, if solution treatment is carried out at temperatures higher than the melting temperature of the lower-melting phases, undesired incipient melting will occur in the material, with dramatic consequences on mechanical properties of the component. DSC was carried out on two samples extracted from two different pistons, nominally equal, to verify if the material is homogeneous and the forging process is reproducible. On one of the two pistons, solution treatment reported in §2.1.1 was applied, and then DSC analysis was carried out again.

The results of the DSC analyses are reported in Figure 3.1 (a), where the red and blue curves are related to the two as-forged samples, while the green curve is related to the solutionized sample (after the three steps: heating from 200 to 495 °C in 1.5 h, maintenance at 507 °C for 3 h and maintenance at 525 °C for 15.5 h). In Figure 3.1 (a), it is possible to distinguish an endothermic peak in the red and blue curves, highlighted by the red rectangle, just before melting of the alloy. Figure 3.1 (b) shows the enlargement of the area where the peak is detected.

The curves related to the two as-forged samples (Figure 3.1 a) are similar, as expected, confirming that the material is homogeneous and the process reproducible. Figure 3.1 (b) shows that the peak detected in the as-forged samples starts at temperatures higher than 540 °C. This represents the higher temperature that must not be exceeded during solution treatment. Having said that, the maximum temperature of the industrial solution treatment, equal to 525 °C, seems to be quite conservative.

After solutionizing (green curve in Figure 3.1), the peak resulted much reduced, almost disappeared, indicating that the low-melting phase had been dissolved during solution heat treatment.

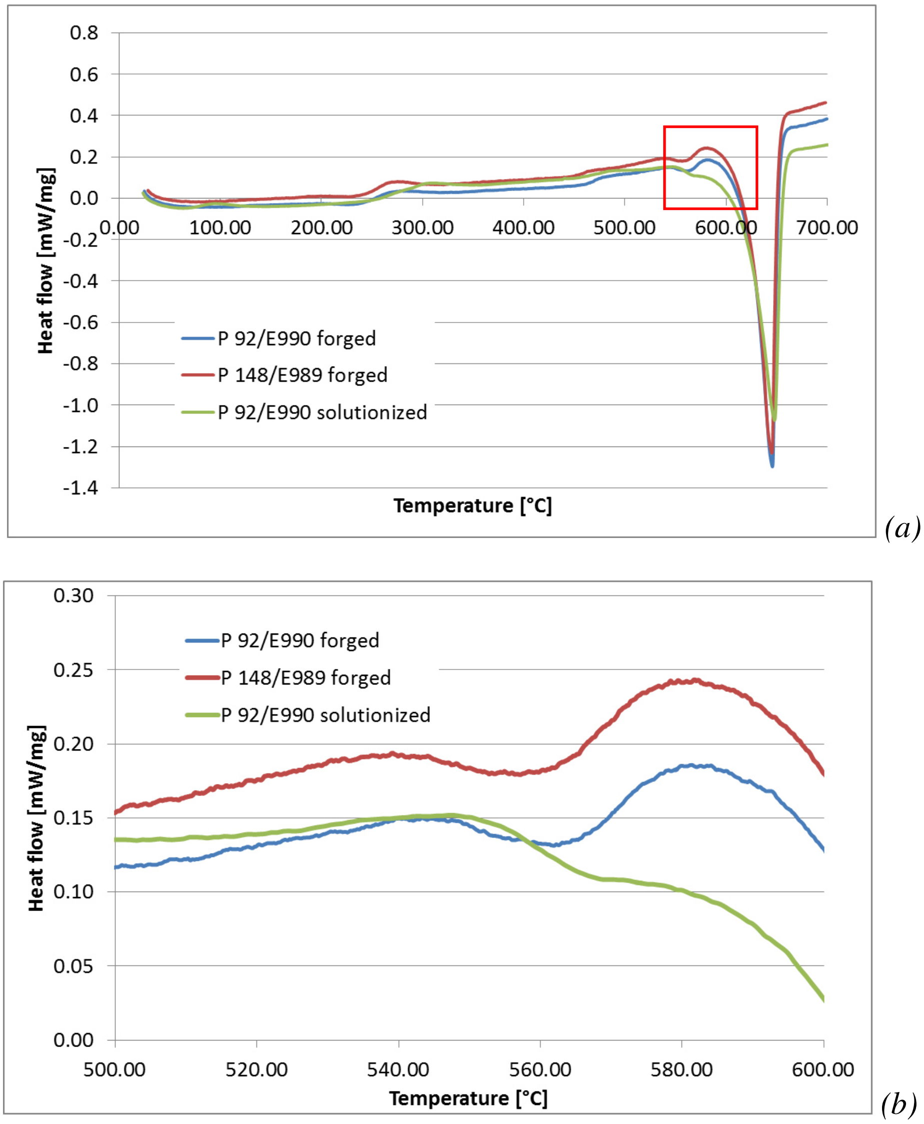

Fig. 3.1 – DSC heating curves from room temperature to 700 °C (a) and enlargement of the area between 500 and 600 °C. The red rectangle in (a) highlights the enlarged area. Red and blue curves are related to as-forged samples, while the green one is obtained after solutionizing.

3.1.2 Optimization of ageing heat treatment

After verifying that the maximum temperature of solutionizing is compatible with DSC results, the optimization of ageing treatment was carried out. Solutionising and quenching were carried out as described in §2.1.1. In order to study the ageing response, samples in the as-quenched condition were aged at temperature ranging from 25 °C (corresponding to natural ageing) to 220 °C for durations ranging from 0.5 to 50 hours. The ageing effect was evaluated with Brinell hardness tests (HB10). The hardness value corresponding to the material in the as-quench condition resulted 81 HB10 with a standard deviation of 2 HB10, this value being bound to increase after an appropriate ageing treatment. The results are given in Figure 3.2, which shows that at room temperature (25 °C) the hardness increase is certainly slow, and after 50 hours hardness is still increasing. At higher aging temperatures (50 to 165 °C), hardness increases much faster than at room temperature during the early hours of thermal exposure. Anyway, the highest hardness value (115-125 HB10 depending on temperature) is reached after few hours, and this value will not change considerably prolonging thermal exposure up to 50 hours. Further increasing the aging temperature results in a change in hardness trend. In fact, for temperature from 190 to 220 °C, hardness value reach a peak at a defined time, and further prolonging the exposure will cause a decrease in hardness. Raising the temperature in the range 190-220 °C, decreases the time to reach peak hardness, but at the same time decreases also peak-hardness value. Moreover, for higher temperatures the loss in hardness caused by thermal exposure after time-to-peak is much faster. According to the graph, the highest hardness value (145 HB10) is reached at 190 °C after a 40 hours thermal exposure. Anyway, this time could be quite long for industrial treatment. The graph shows that at 200 °C a slight lower hardness (140 HB10) is reached after just 20-25 hours. Further increasing the temperature results in very short times to peak hardness, but quite lower peak hardness values (138 HB10 after 5 hours at 210 °C and 136 HB10 after 3 hours at 220 °C). This study led to the choice of the best aging parameters: after considerations about peak hardness and treatment time, 20 h at 200 °C was identified as the optimum, in agreement with the industrial treatment.

Wang *et al.* [1] found peak hardness condition after 20 h at 200 °C for AA 2618 homogenized, hot rolled (450 °C) and solutionized at 535 °C. Kadolkar *et al.* [3] studied the ageing behaviour of the AA 2618 extruded, hot forged (425 °C) and solutionized at 530 °C for 1 hour, and found peak hardness for 48 hours at 180 °C, 20 h at 200 °C, or 2 hours at 230 °C. Comparing these results to the present study, it can be seen that they seem in good agreement. In contrast, Novy *et al.* [3] studied an AA 2618 forged disc, solution treated for 8 h at 530 °C and quenched in cold water, and found peak hardness after 10 hours at 190 °C. Elgallad *et al.* [4] and Shen *et al.* [5] found that peak hardness is reached in a DC cast ingot solutionized at 530 °C for 5 h, after 36 h at 175 °C or 10 h at 195 °C. Novy *et al.* [3] don’t specify the forging temperature, while in the study presented in [4] and [5] the material is not deformed. This can be the cause of the different aging behaviour found by these authors. However, the trend of the curves found by Elgallad *et al.* [4] and Shen *et al.* [5] is similar to that found in the present study, as can be seen comparing Figures 3.2 and 3.3.

It is interesting to note, for both aging conditions at 190 and 200 °C, that the hardness of the AA 2618 alloy tend to decrease very slowly after reaching peak hardness contrary to the Al-Cu binary alloys. This observation indicates that AA2618 alloy is not very susceptible to overaging, compared to other aluminium alloys, which may be due to the low coarsening tendency of its main strengthening phase, S-Al_2CuMg [6]. Aging at 210 or 220 °C further shortened the time to peak hardness but prolonged aging at these temperatures seems to lead to a rapid hardness decrease as compared to aging conditions at 190 and 200 °C.

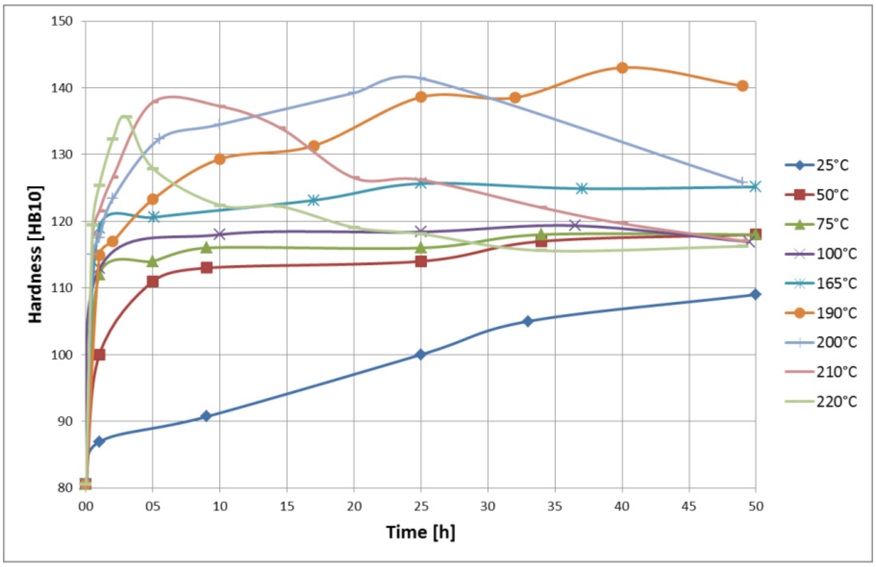

Fig. 3.2 – Experimental aging curves hardness-exposure time for AA 2618 at different temperatures (from room temperature to 220 °C) after forging, solutionising and quenching found in the present study.

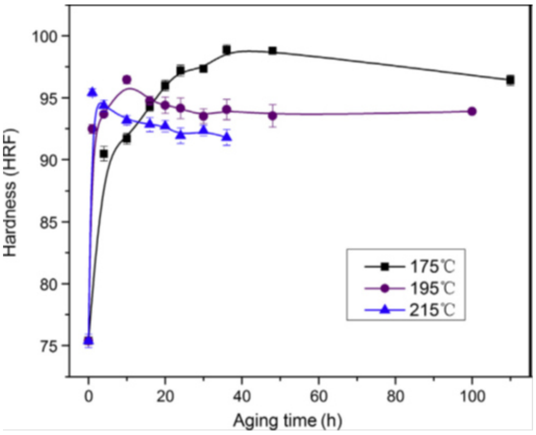

Fig. 3.3 - Experimental ageing curves presented in [4] and [5] for AA 2618 DC cast alloy, reported as comparison.

3.1.3 Study of thermal stability

It is well known that prolonged soaking at temperatures higher than that of peak aging can lead to overaging of aluminium alloy with significant hardness decrease. An investigation of degradation was therefore also carried out, exposing peak-aged samples (aged for 20 h at 200 °C) at higher temperatures. The aim of this part of the research was to evaluate the loss in hardness (and consequently in other mechanical properties) as a function of exposure temperature and time. Peak-aged samples were exposed to temperature ranging from 200 °C (corresponding to the ageing temperature) to 305 °C for times up to a week. The results are shown in Figure 3.4 (a). It is clear that temperatures higher than 200 °C cause a rapid degradation in the investigated AA 2618 alloy, the higher the temperature, the faster the loss in hardness. Figure 3.4 (b) is a detail from figure 3.4 (a), showing the first minutes of thermal exposure.

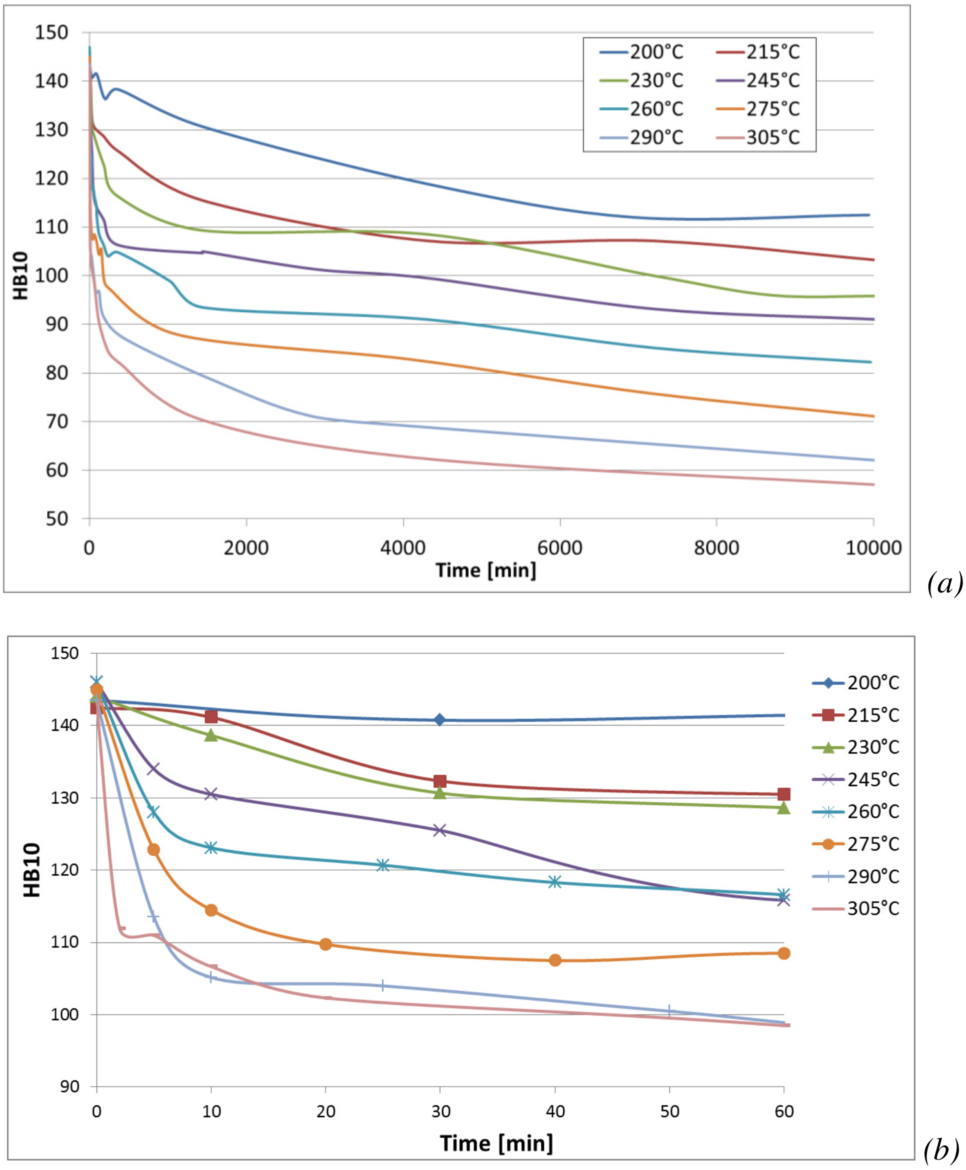

(a)

(b)

Fig. 3.4 – Hardness-time curves for AA 2618 peak-aged (aged for 20 h at 200 °C) after thermal exposure at 200 - 305 °C: effects of thermal exposure up to 1 week (a) and detail of the first hour of thermal exposure (b).

In agreement with what observed during the study of ageing treatment, the results in Figure 3.4 show that during thermal exposure of peak-aged AA 2618 alloy at 200 °C the loss in hardness is quite slow. In particular, no loss in hardness is detected during the first hour of thermal exposure, while an exposure of a week cause a loss of about 30 HB10. In contrast, for temperatures higher than 230 °C, the loss of hardness in the first minutes of exposure is really rapid: 20 minutes at 290 or 305 °C cause a loss of around 40 HB10. Minimum hardness value, found after a week at high temperature (290 and 305 °C), is about 60 HB10.

Elaborating the data reported in the graph in Figure 3.4 (a), it was possible to obtain the hardness-time-temperature curves reported in Figure 3.5. This is just another means to present the data in Figure 3.4 (a), but it is useful since it makes it possible to forecast the residual hardness after a thermal exposure of defined time and temperature. Moreover, with this graph it is possible to find the temperature at which a component had been exposed during in-service conditions, just knowing the exposure time and measuring the residual hardness. This method can be particularly useful to find the working temperature of engine components.

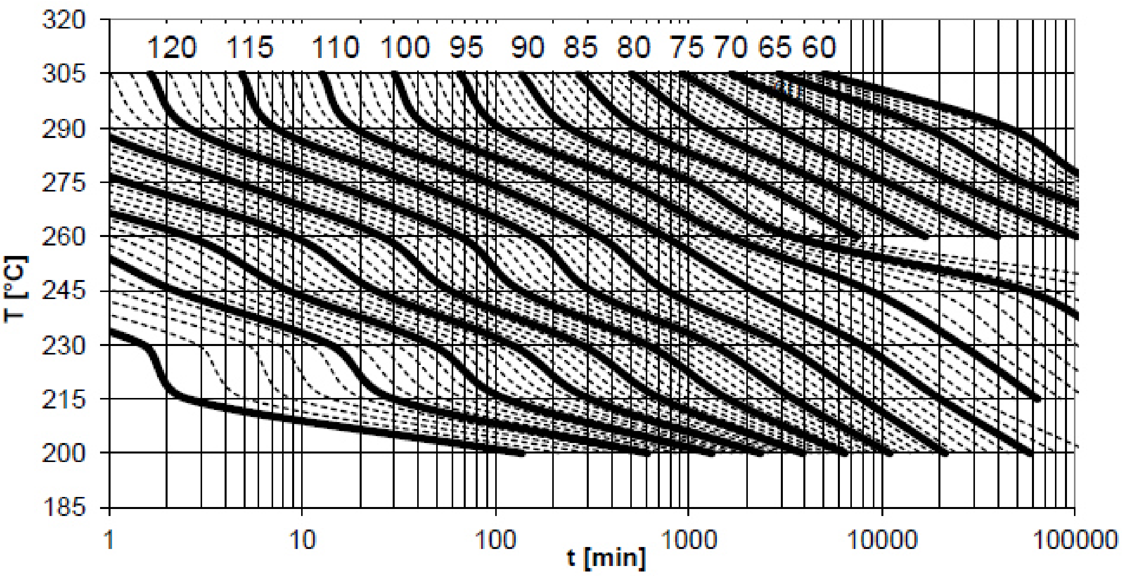

Fig. 3.5 – Hardness-time-temperature curves for T6 AA 2618 alloy.

3.1.4 Tensile tests

Tensile specimens were divided in eight classes, with different level of overaging. The hardness level of each class was decided, and the time and temperature of thermal exposure were chosen with the help of hardness-time-temperature curves reported in Figure 3.5. Hardness was measured on tensile samples before the test, to verify that the desired hardness had been reached, and to subsequently find correlations between hardness and tensile parameters. These measurements are reported in Table 3.1, together with the mechanical properties measured with the tensile tests, and it can be seen that measured hardness display a certain discrepancy with the target values, indicated by the experimental hardness-time temperature curves. This discrepancy is also evident in Figure 3.6, which shows the experimental degradation curves reported in Figure 3.4, with superimposed points representing hardness measurements on tensile samples after thermal exposure. Labels indicates the nominal class, while colours indicates the exposure temperature. Some points are quite far from the relative curve, which means there is discrepancy between the nominal and real values. However, this discrepancy is not constant for all the hardness levels, and is generally conservative.

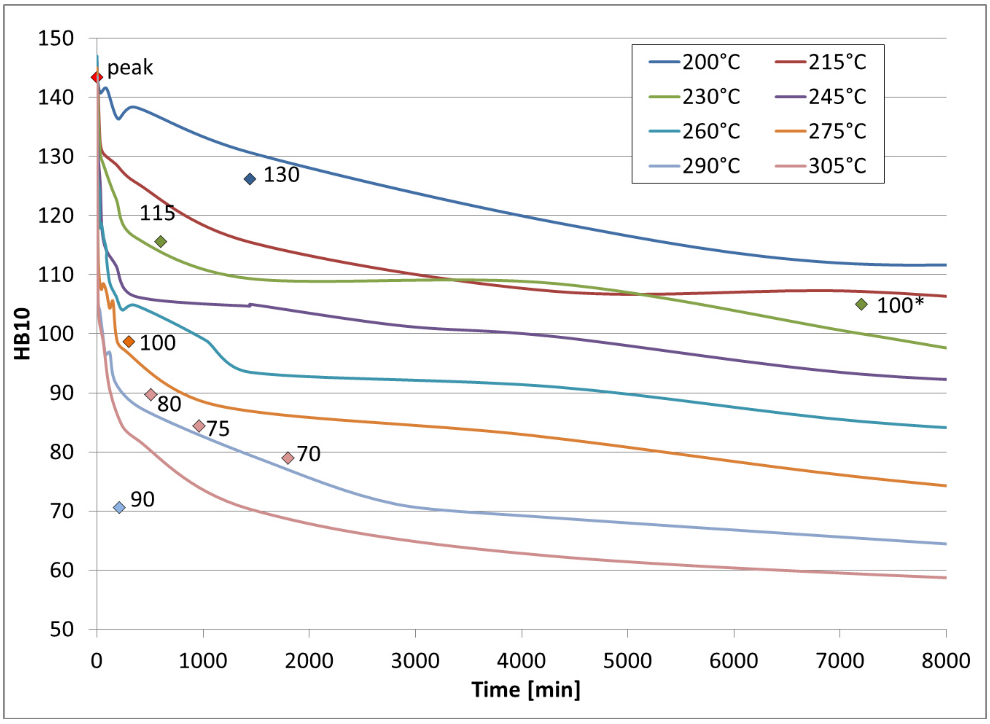

Fig. 3.6 – Experimental overaging curves of T6 AA 2618 with superimposed points representative of hardness level obtained in tensile specimens after thermal exposure. Labels indicate the nominal class, while colours indicate the exposure temperature.

Class	HB10	YS [MPa]	UTS [MPa]	E %	K [MPa]	n
Peak-aged	139	372	422	3.6	578.8	0.0841
	141	343	415	4.4	580.6	0.0937
	143	377	426	4.5	570.3	0.0792
	146	366	430	4.0	582.6	0.0822
	148	341	437	6.1	604.6	0.0909
130HB	125	313	384	5.5	577.9	0.1179
	125	315	382	5.5	568.8	0.1144
	127	315	381	5.3	573.2	0.1164
	127	322	388	5.9	572.6	0.1109
	127	322	385	6.8	563.4	0.1084
115HB	115	263	351	6.3	589.7	0.1523
	115	274	359	5.6	591.2	0.1452
	115	271	353	7.6	580.0	0.1478
	116	256	348	6.3	576.7	0.1496
	117	271	352	7.0	580.7	0.1490
100HB	100	201	310	7.2	593.3	0.1962
	104	223	317	5.0	602.6	0.1907
	104	225	330	7.9	597.3	0.1802
	105	216	323	6.2	604.7	0.1884
	106	223	325	6.5	592.7	0.1823
90HB	69	107	230	9.3	542.8	0.2811
	70	103	226	10.4	533.4	0.2828
	71	106	231	10.6	541.8	0.2797
	71	109	235	11.1	534.3	0.2712
	72	110	235	12.2	536.5	0.2762
80HB	89	159	271	6.4	578.9	0.2359
	89	163	275	8.2	561.9	0.2251
	90	164	280	7.8	576.3	0.2257
	91	168	282	8.2	583.6	0.2300
	92	174	285	8.2	580.3	0.2215
75HB	83	132	253	10.4	539.1	0.2474
	83	132	258	8.9	553.6	0.2514
	85	122	261	8.0	648.2	0.2877
	85	147	269	10.6	571.9	0.2440
	86	145	267	8.9	567.0	0.2414
70HB	78	118	244	10.7	541.5	0.2651
	79	118	246	10.1	543.5	0.2628
	79	122	245	10.4	545.6	0.2649
	80	124	246	9.6	535.3	0.2569

Tab. 3.1 – Data from AA 2618 tensile specimens after thermal exposure, divided for nominal hardness level: Brinell hardness (HB10), yield strength (YS), ultimate tensile strength (UTS), elongation to failure (E), and strength index (K) and strain hardening exponent (n) of Hollomon's equation.

Data obtained from tensile tests, reported in Table 3.1, are represented against residual hardness in the graphs in Figures 3.7 and 3.8. It should be mentioned that two samples showed very low values of elongation to failure (less than 1%) and therefore the data related to these samples are not reported in Table 3.1 and Figures 3.6 and 3.7; the fracture surfaces of these samples are analysed in §3.1.5. Moreover, the data related to the two classes with 100 HB10 nominal hardness did not show appreciable differences, as expected, and therefore in Table 3.1 are classified in the same group.

As it can be clearly seen from the graphs in Figure 3.7 and 3.8, yield strength (YS), ultimate tensile strength (UTS), strength index (K) and strain hardening exponent (n) appeared to be a linear function of residual hardness, while a logarithmic function was found to be the most suitable to fit the data for the elongation to failure (E). As expected, it was found that strength decreases with decreasing residual hardness, while elongation to failure increases; that means that increasing the level of overaging, the material becomes less resistant but more ductile. The empirical functions of residual hardness found for yield strength (YS), ultimate tensile strength (UTS), elongation to failure (E), strength index (K) and strain hardening exponent (n) are reported on the relative graphs and in equations (1) – (5), together with the relative coefficients of determination.

$$YS = 3.75 \cdot HB - 169.89 \qquad R^2 = 0.983 \qquad (1)$$

$$UTS = 2.75 \cdot HB + 32.4 \qquad R^2 = 0.995 \qquad (2)$$

$$E = -8.84 \cdot \ln(HB) + 48.29 \qquad R^2 = 0.832 \qquad (3)$$

$$K = 0.56 \cdot HB + 512.08 \qquad R^2 = 0.382 \qquad (4)$$

$$n = -0.0029 \cdot HB + 0.485 \qquad R^2 = 0.991 \qquad (5)$$

Having obtained the strength index (K) and strain hardening exponent (n) of Hollomon's law, it was possible to determine the equation of true stress-true strain as a function of residual hardness, reported in (6).

$$\sigma_r = (0.56 \cdot HB + 512) \cdot {\varepsilon_r}^{(-0.0029 \cdot HB + 0.485)} \qquad (6)$$

This model was implemented and compared with some experimental true stress-true strain curves. The result is displayed in Figure 3.9, where the experimental curves are indicated with solid line, while the curves obtained applying equation (6) are indicated with dashed line at different levels of residual hardness. The results evidence that the agreement between the model and the experimental data is quite good. However, the model is more suitable to describe the behaviour of the material with lower residual hardness, while when it comes to peak-aged material, important gaps are found between the experimental and the model. This can be basically ascribed to the simplicity of Hollomon's law, which becomes increasingly unsuitable to describe the behaviour of plastic deformation when the material is less ductile, that is, when the material is close to the peak-ageing condition.

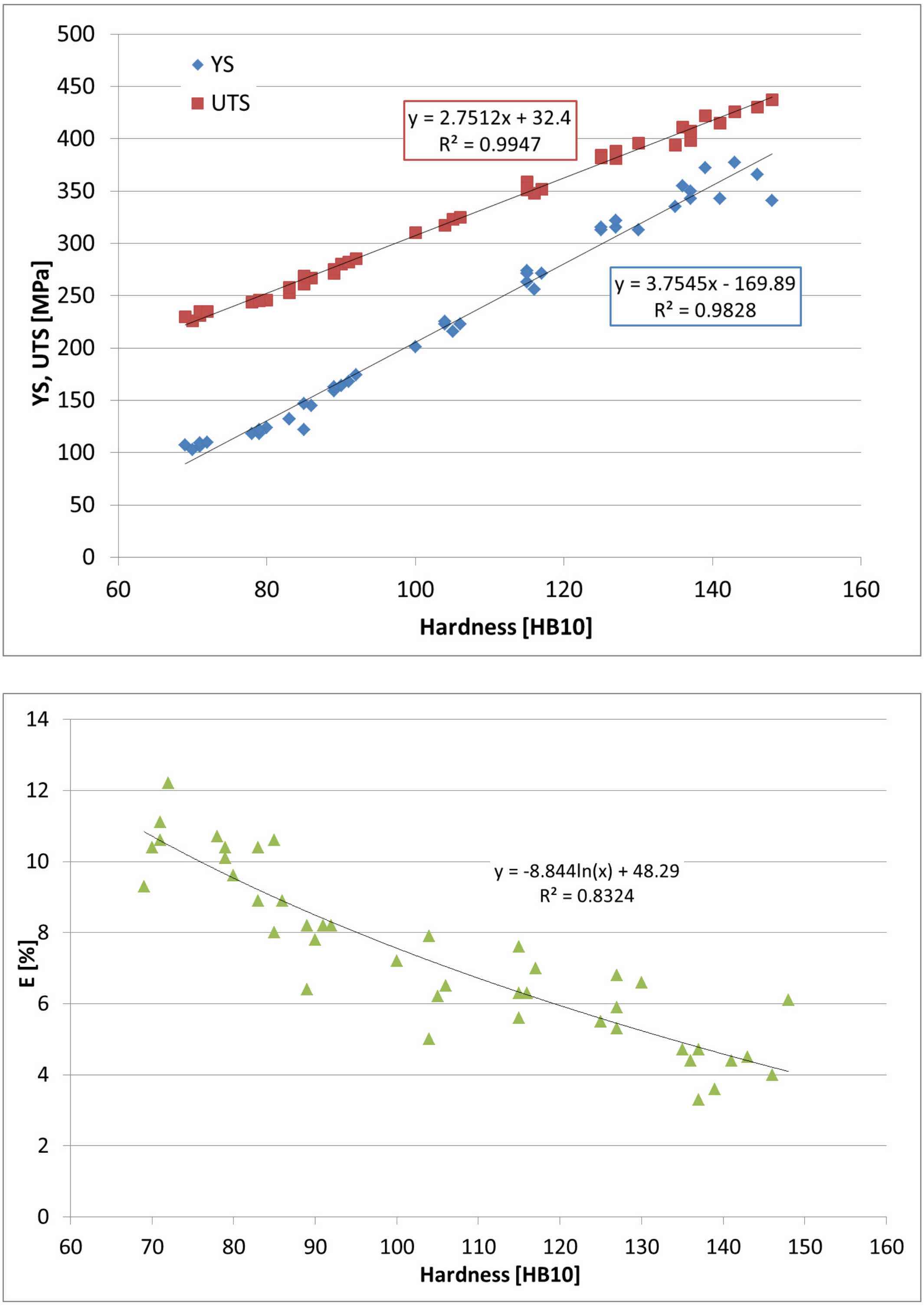

(a)

(b)

Fig. 3.7 – Relation between residual hardness and: yield strength and ultimate tensile strength (a), and elongation to failure (b) for AA 2618-T6 alloy after thermal exposure.

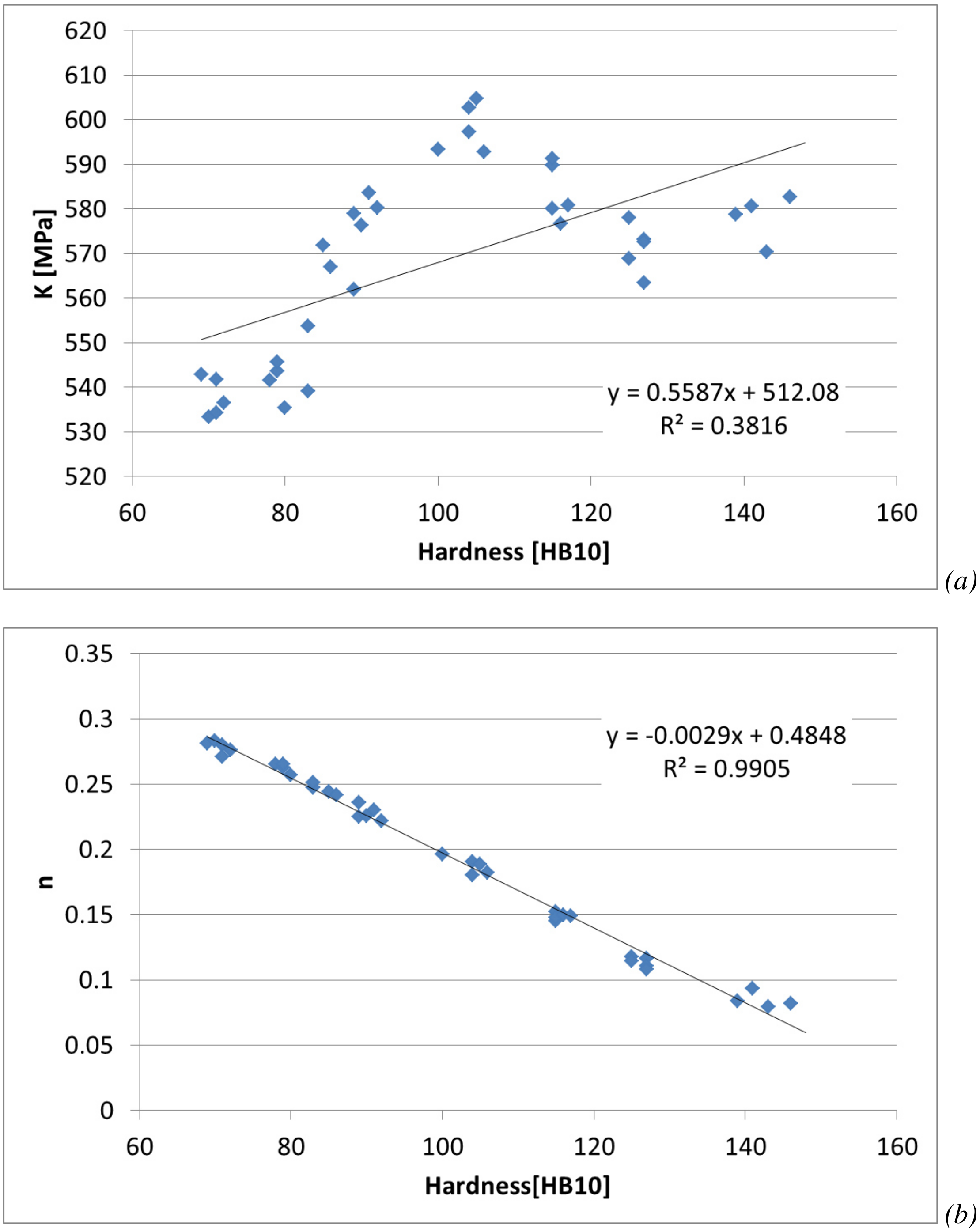

Fig. 3.8 - Relation between residual hardness and: strength index (a) and strain hardening exponent (b) for AA 2618-T6 alloy after thermal exposure.

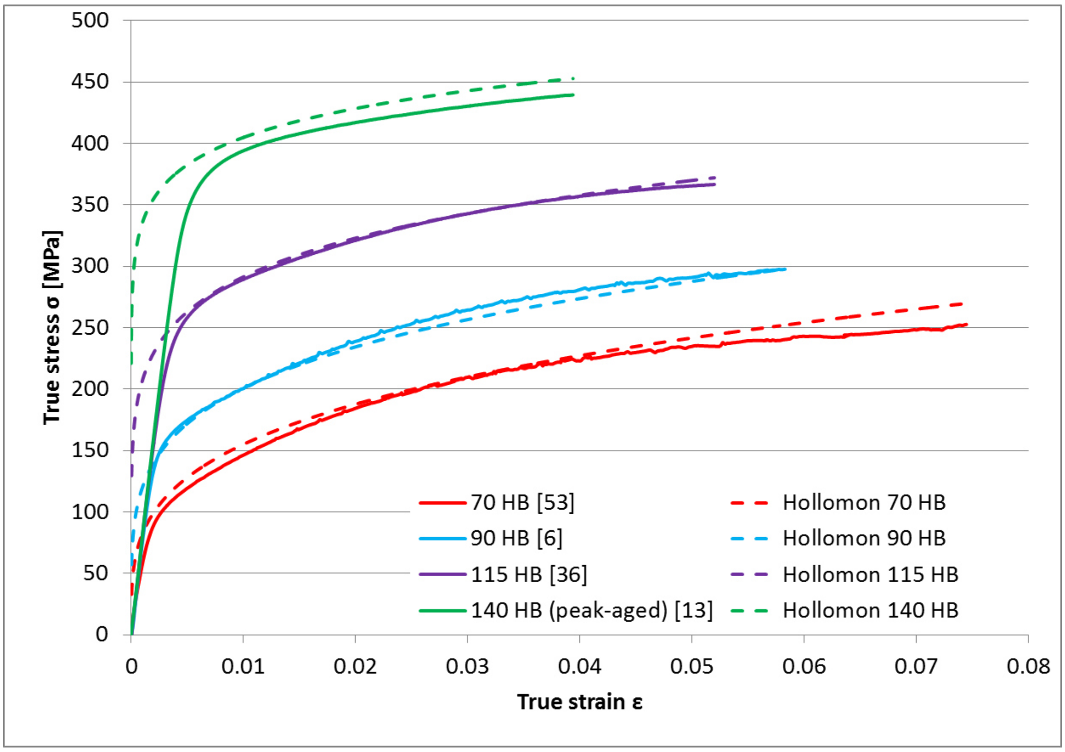

Fig. 3.9 – True stress-true strain curves at various values of residual hardness: comparison between experimental data (solid lines) and Hollomon's model (dashed lines). The numbers in square brackets are the designations of the samples used to obtain the experimental data.

3.1.5 Fracture surfaces

The results of the SEM investigations for the two samples with very short elongation to failure (<1%) revealed abundant presence of oxides, which evidently made the material more brittle; these oxides are probably due to the presence of an air bubble during forging process. The two samples were extracted from adjacent areas on the same piston, therefore the oxide zone was the same for the two samples. Figure 3.10 (a) shows a low magnification SEM micrograph of an oxidised zone on the fracture surface of one of these samples, while Figure 3.10 (b) and (c) show the EDS spectrum and the EDS quantitative results related to the area called Spectrum 1 in Figure 3.10 (a). Oxygen is the most abundant element, followed by aluminium and magnesium. On the basis of atomic percentages of these three elements, is likely that the area highlighted by the purple rectangle in Figure 3.10 (a) contains spinel ($MgAl_2O_4$), an Al-Mg mixed oxide. These oxides changed the material behaviour from ductile to brittle, in fact, in this zone the fracture appear to be completely brittle, with a flat undeformed surface. This can explain the discrepancy in the tensile behaviour of these two sample compared to the other ones.

The tensile results obtained from the oxidised samples are considered not significant and therefore are not reported in Table 3.1 and in Figure 3.7 and 3.8.

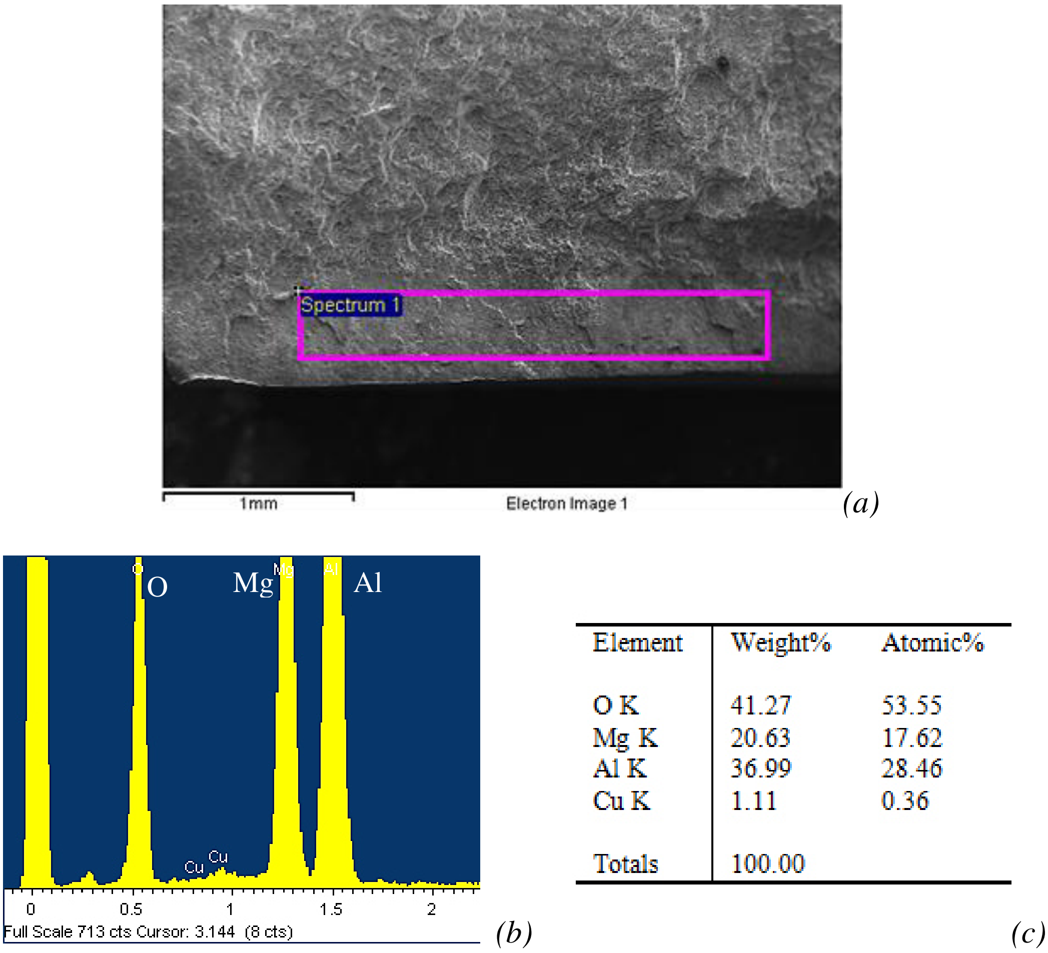

Element	Weight%	Atomic%
O K	41.27	53.55
Mg K	20.63	17.62
Al K	36.99	28.46
Cu K	1.11	0.36
Totals	100.00	

Fig. 3.10 – Low magnification SEM micrograph of a fracture surface showing a highly oxidised area (highlighted by the purple rectangle) which caused a brittle fracture (a), EDS spectra (b) and quantitative results (c) related to the area called Spectrum 1.

The other samples, characterized by larger elongations to failure, exhibited ductile fracture surfaces, as can be seen in Figures 3.11 and 3.12. At low magnification (Figure 3.11), the fracture surface presents different depth levels, in contrast with the oxidised surface, which appears flat (Figure 3.10 (a)); while at higher magnification (Figure 3.12) it is possible to recognize the presence of equiaxed dimples. Both of these features are characteristic of ductile fractures, confirming the ductile behaviour of the material. However, even if large oxidised areas were not detected, at higher magnification it was possible to recognise the presence of small oxidised fragments scattered in the matrix, as showed in Figure 3.13.

It is worth noticing that grains and strengthening phases (mainly containing Fe and Ni), are aligned on a preferential direction, as can be seen in the low magnification micrograph in

Figure 3.11. This directionality, also observed in the optical micrographs (§3.1.6), was clearly induced by the forging process.

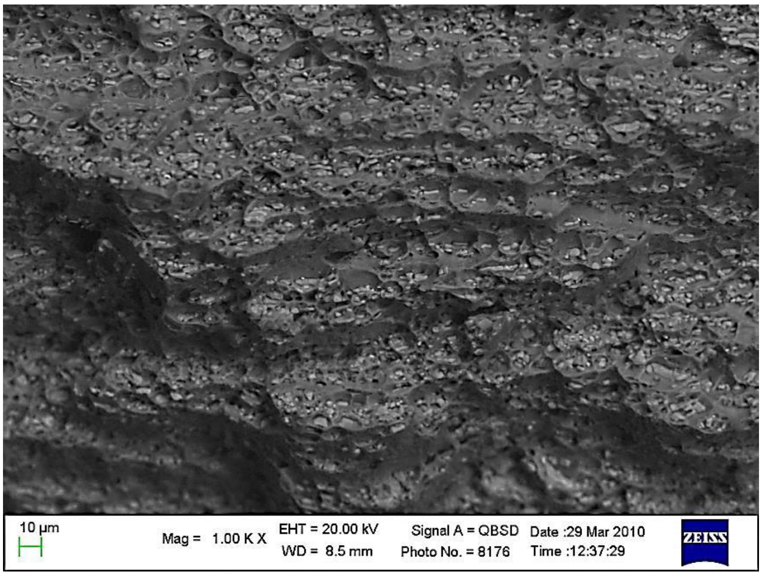

Fig. 3.11 – Low magnification SEM micrograph of a fracture surface showing ductile characteristics and preferential alignment of both grains and intermetallic compounds.

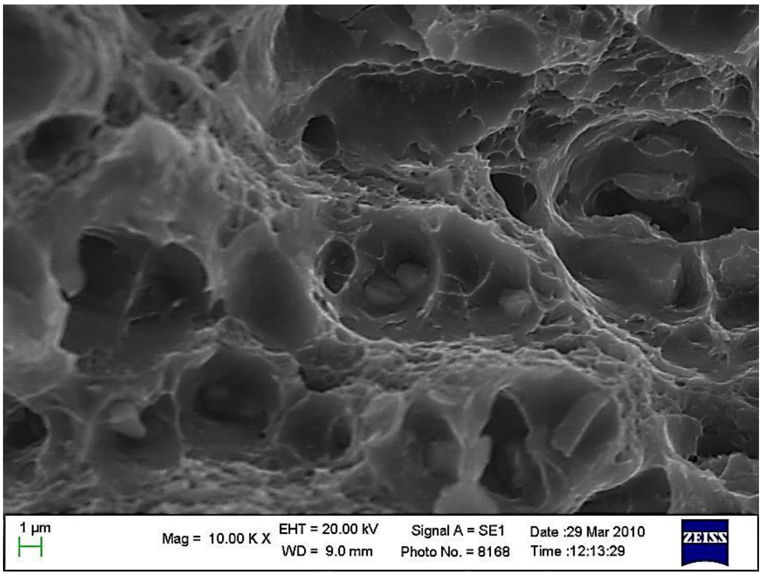

Fig. 3.12 – High magnification SEM micrograph showing equiaxed dimples typical of ductile failures.

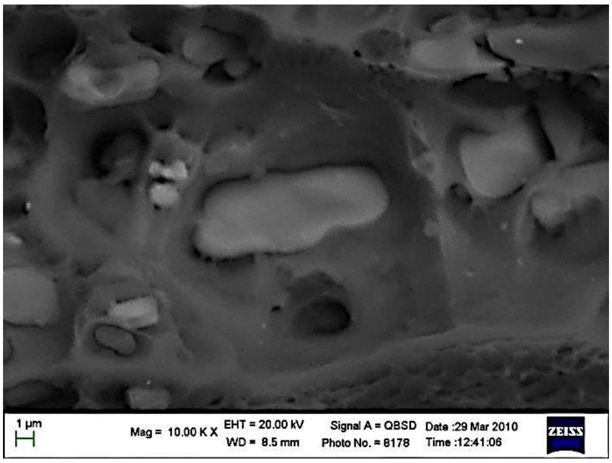

Fig. 3.13 – High magnification SEM micrograph showing the presence of oxide fragments in the matrix.

3.1.6 Grain size

Optical microscope with polarized light was used to measure grain size on etched samples extracted from tensile specimens. It was found a certain inhomogeneity in the distribution of grain size, typical of forged components. Micrographs of two areas characterized by different grain size are reported in Figure 3.14. Micrographs in Figure 3.14 also confirm the presence of a preferential direction in the grain distribution, as already observed with SEM.

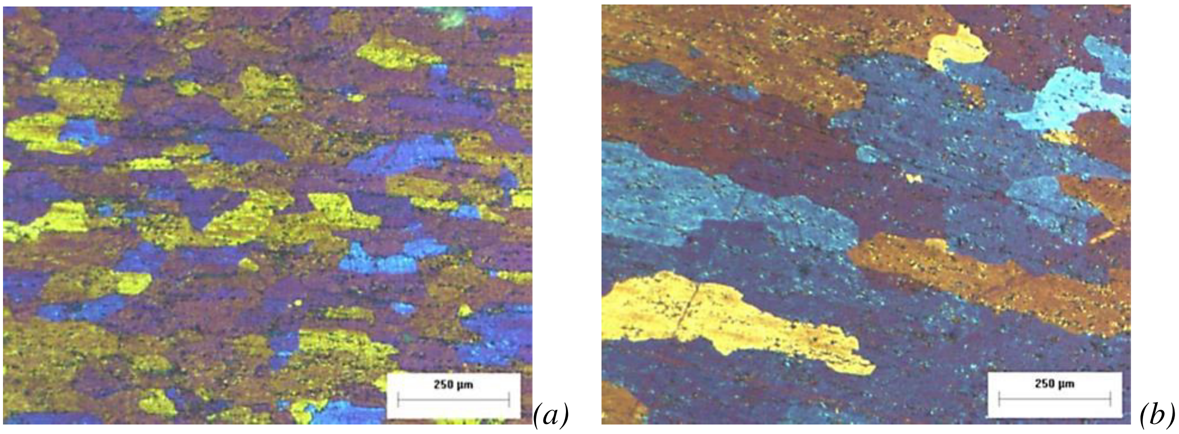

Fig. 3.14 – Optical micrographs showing areas of the material characterized by fine (a) and coarse (b) grain size.

Grain size was measured on tensile samples extracted from the pistons as shown in Figure 2.1 (b), that is, with the width of the samples parallel to the piston axis. Measuring grain size on different samples it was possible to analyse how it changes with the distance from the piston axis. Moreover, grain size was measured in three different areas of each sample, to analyse the relationship between this parameter and the distance from the piston top; depths of

3 mm, 5 mm and 7 mm from the top were chosen. The average values of measurements carried out on samples extracted from three different pistons were calculated, and the results are reported in the graph in Figure 3.15. This graph shows that grain is finer (100-200 µm) in the central area of the piston (near the piston axis) than in the outer areas (200-300 µm). Moreover, grain size decreases with increasing distance from the piston top. However, grain size results generally quite coarse, ranging approximately from 100 µm to 300µm. The variation in grain size is considerable, but it does not appear highly significative if compared to the average value (approximately 180 µm). That means that the observed variation in grain size throughout the piston head is not so important to affect mechanical properties. Concerning tensile test results, there is no need to take into account grain size fluctuation.

No correlation between grain size and residual hardness was found, as clearly seen in the graph in Figure 3.16. That means that there is no effect of overaging on grain size, that is, thermal exposure of T6 heat-treated material does not result in grain coarsening.

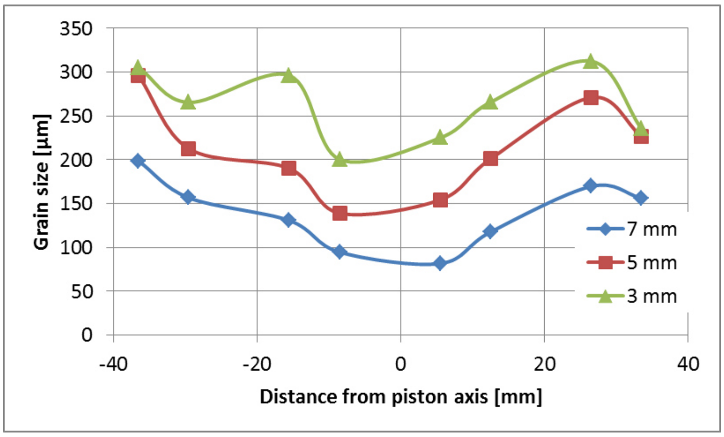

Fig. 3.15 – Grain size as a function of the distance from the piston axis. Different curves are related to different distances from the piston top (3, 5 and 7 mm depth).

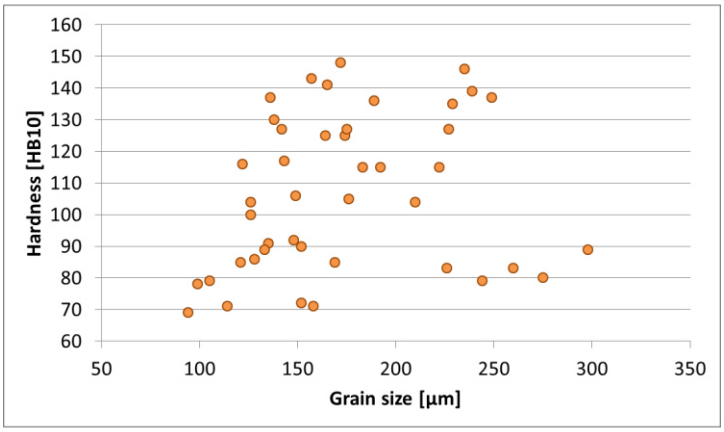

Fig. 3.16 – Graph showing grain size against hardness: no relation was found between the two parameters.

3.1.7 Microstructural modifications due to overaging

The degradation of mechanical properties, described in §3.1.3 and §3.1.4 evaluated with hardness measurements and tensile tests, has its origin in changes that take place in the microstructure, at the level of the strengthening precipitates, during thermal exposure. To better understand this phenomenon, the microstructure of 7 samples, overaged to different hardness values, was analysed with a FEG-SEM electron microscope equipped with EDS. The samples were peak-aged (20 h at 200 °C) and then exposed to different temperatures and times. In Figure 3.6, points represent the samples used for microstructural investigation: the tags indicate the hardness of the samples, and the colour indicates the overaging temperature. It can be seen that generally there is not good agreement between the experimental curves and the points, as already observed in §3.1.4. It is worth highlighting that the idea on which this study was based is that combination of time and temperature that leads to the same hardness, also leads to very similar microstructures. Therefore, when discussing the results of microstructural investigation on these samples, it will be linked only with residual hardness and not with exposure temperature and time. In Table 3.2 are reported samples number and related hardness value. Sample no. 39 is peak-aged (145 HB10) and sample no. 40 (70 HB10) is a little higher than the minimum hardness value observed in this alloy (60 HB10). That means that in this condition most of the microstructural transformation had already taken place.

Sample No.	Hardness [HB10]
39	145 (peak)
2	125
22	115
31	105
35	90
33	80
40	70

Tab. 3.2 - Samples analysed and their hardness HB10 values.

Figure 3.17 shows pictures taken with FEG-SEM microscope at lower magnification (1000 x) for samples with hardness 145, 115, 90 and 70 HB10. It can be seen that at low magnification, the microstructures of different samples, as expected, do not show relevant differences. At 1000 x is possible to see the presence of quite big (order of magnitude of some microns) intermetallics, all oriented in the same direction. This orientation is due to the hot working the material underwent before heat treatment. The intermetallics were distributed within the matrix, at grain boundaries, or sometimes, adjacent to each other in the specimens examined, and they were not uniformly shaped but generally oblong with curved ends. This result is in good agreement with Oguocha *et al*. [7], reporting that the observed intermetallics are aluminide particles rich in Ni and Fe. These intermetallics are reported by some authors [8,9] to have a composition that comply to the formula Al_9FeNi, but Oguocha [7,10] showed that they transform or are modified during solution heat treatment or fabrication. In particular, the aluminium content seems to vary while atomic ratio of iron to nickel remains consistent at about 1:1, therefore Al_xFeNi is suggested as formula for these intermetallics.

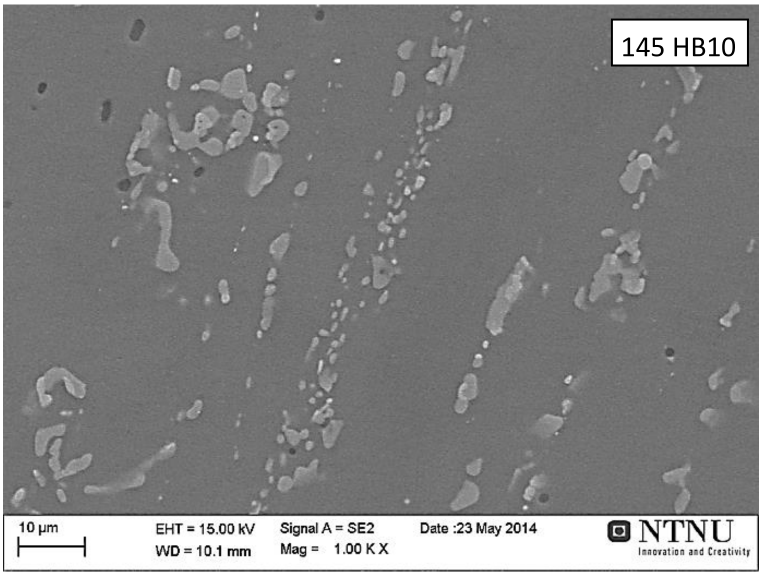

(a)

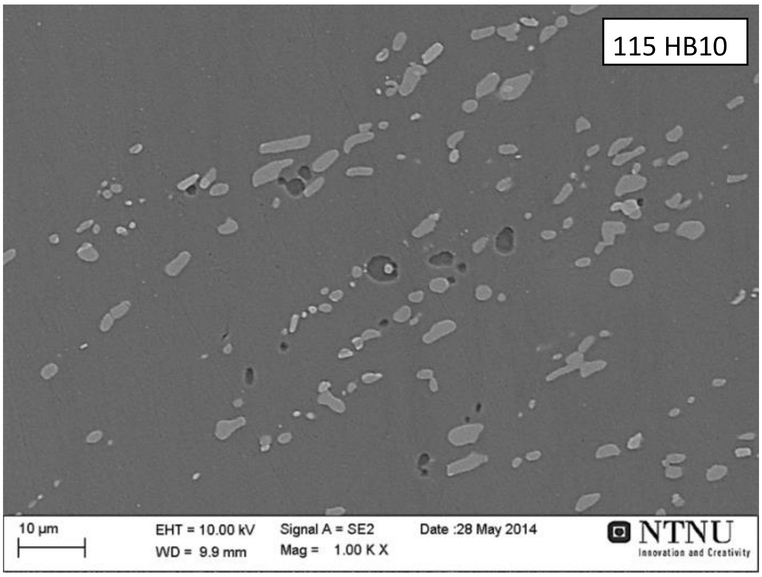

(b)

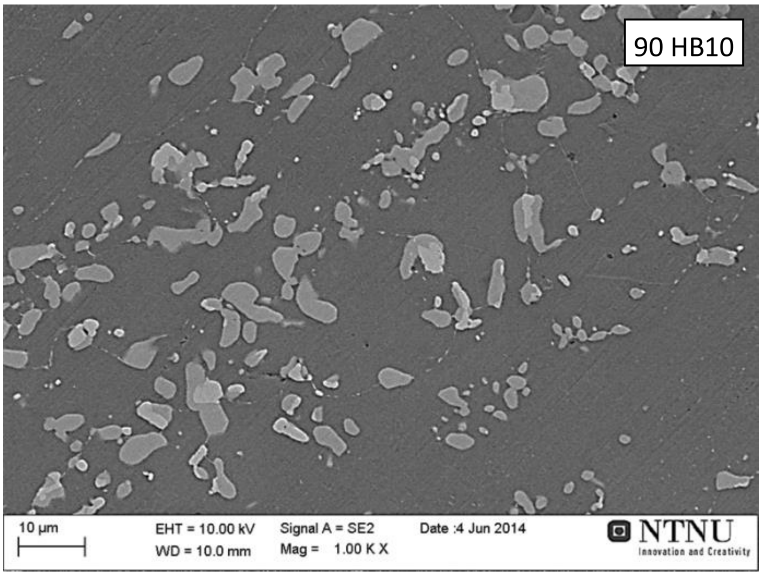

(c)

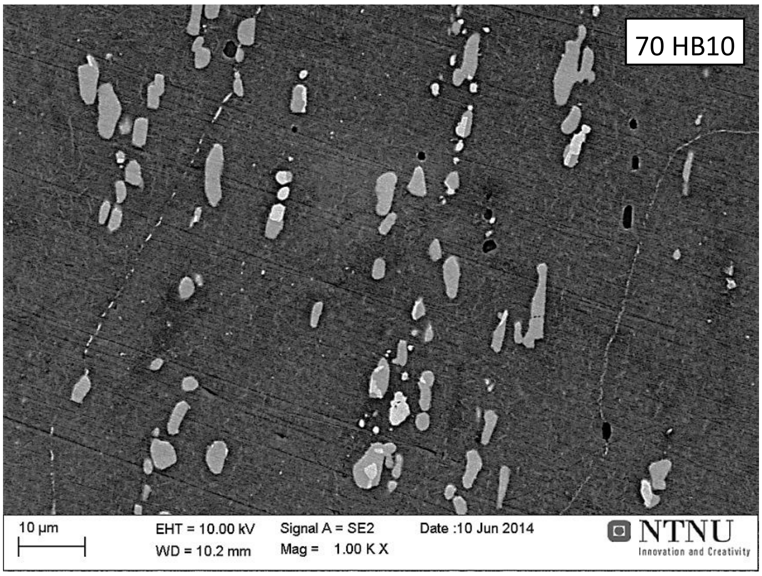

(d)

Fig. 3.17 – Low magnification FEG-SEM images taken with secondary electrons of samples with hardness: 145 (a), 115 (b), 90 (c) and 70 (d) HB10

In contrast to what reported by Oguocha [7], a more careful look at the images in Figure 3.17 reveals that different kind of intermetallics are present: in particular, it is possible to recognize a dark and a light grey phase which form bigger intermetallics, and also smaller white particles. The white particles are often associated to the light grey phase. This can be seen more clearly in Figure 3.18, which shows FEG-SEM images at higher magnification. The light grey phase form the absolute majority of the intermetallics volume fraction.

With the help of EDS analyses, it was found that:

- matrix contain Al, Mg and Cu

- light grey phase contain Al, Fe and Ni
- dark grey phase contain Mg and Si
- white precipitates contain Cu and are of two different kinds: one containing both Ni and Fe, and the other containing just Ni.

To identify the detected phases, data from EDS were compared to data obtained from literature. Oguocha et al. [7,10] reported only the presence of Al_xFeNi as insoluble phase in AA 2618 alloy. On the contrary, Novy *et al.* [3] in peck-aged AA 2618 detected also oval particle of Mg_2Si and exceptionally particles of AlCuNi and Al_7Cu_2Fe. Anyway, the authors calculated that Al9FeNi constitute the 99% of all intermetallic phases observed. Other authors [4,5] observed a solutionized AA 2618 alloy and identified three intermetallic phases: Al9FeNi, Al7CuNi and Al7Cu2(Fe,Ni). Since these phases were found to be little affected by solutionising treatment [4,5], it seem reasonable that they are not affect from aging treatment and subsequent degradation. In conclusion, if these phases are present in the solutionized material they will be present also after thermal exposure.

Comparing the results of the EDS analyses with what reported by Novy *et al.* [3], Elgallad *et al.* [4] and Shen *et al.* [5], the intermetallics were identified as follow:

- light grey: Al_xFeNi
- dark grey: Mg_2Si
- white: $Al_7Cu2(Fe,Ni)$ and Al_7CuNi.

The average EDS results, showed in Table 3.3, are not in very good agreement with the proposed formulae. This anyway can be due to the influence of the matrix composition, since the intermetallics could be too small for an EDS spot analysis. In the case of $Al_7Cu(Fe,Ni)$ intermetallics, they are often found in combination with Al_xFeNi, so the EDS spectra can be influenced by the presence of these intermetallics. Figure 3.19 shows the EDS spectra related to the four different intermetallic phases detected.

Shape, size and composition of intermetallic phases seem not affected by thermal exposure.

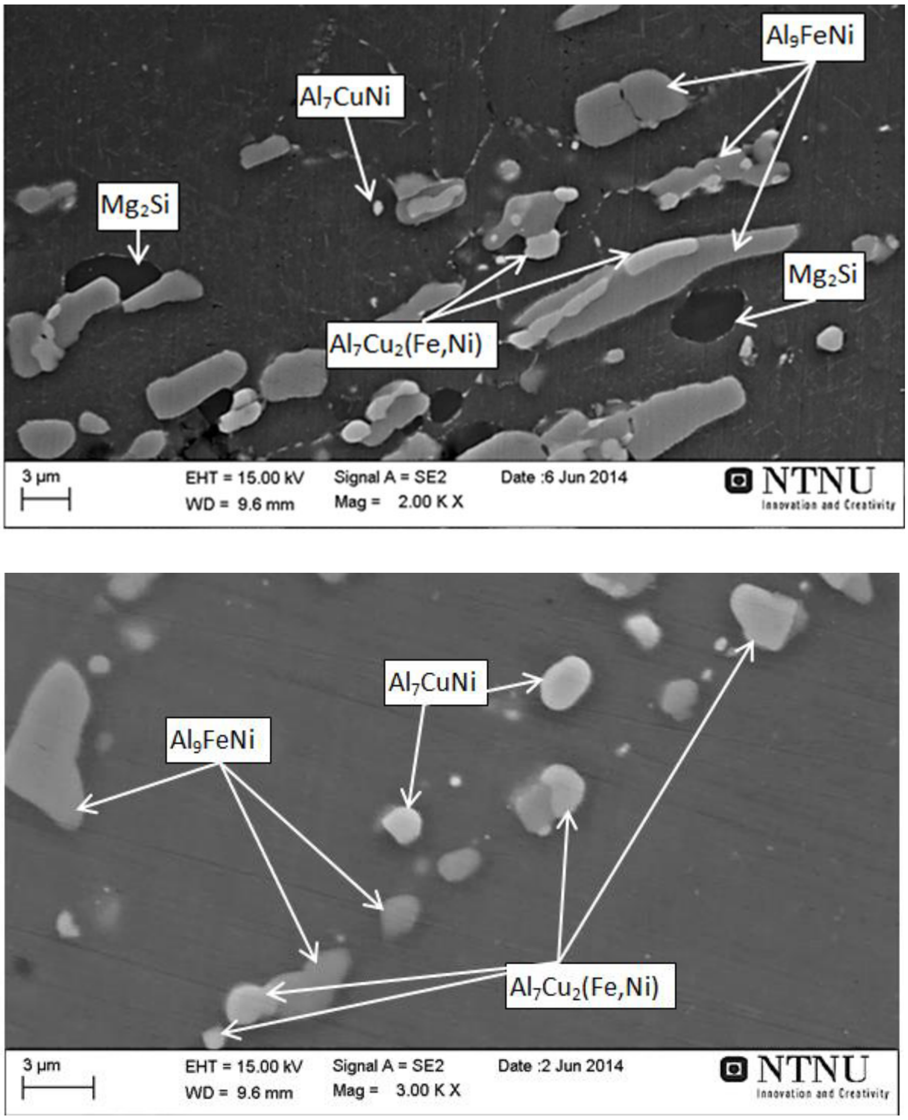

Fig. 3.18 – FEG-SEM secondary electrons images at higher magnification, showing different kinds of intermetallics.

Phase	**Elements [at %]**						**Suggested formula**
	Al	**Fe**	**Ni**	**Cu**	**Mg**	**Si**	
-	96.66	-	-	1.01	2.15	-	Matrix
Light grey	84.08	7.12	7.36	1.82	1.02	-	Al$_9$FeNi
Dark grey	30.20	-	-	-	44.17	25.63	Mg$_2$Si
White	76.08	5.94	3.62	13.73	0.89	-	Al$_7$Cu$_2$(Fe,Ni)
White	75.28	-	10.76	12.03	1.68	-	Al$_7$CuNi

Tab. 3.3 – Average compositions in at.% of matrix and intermetallic phases detected with EDS spot analyses in peak-aged and overaged samples.

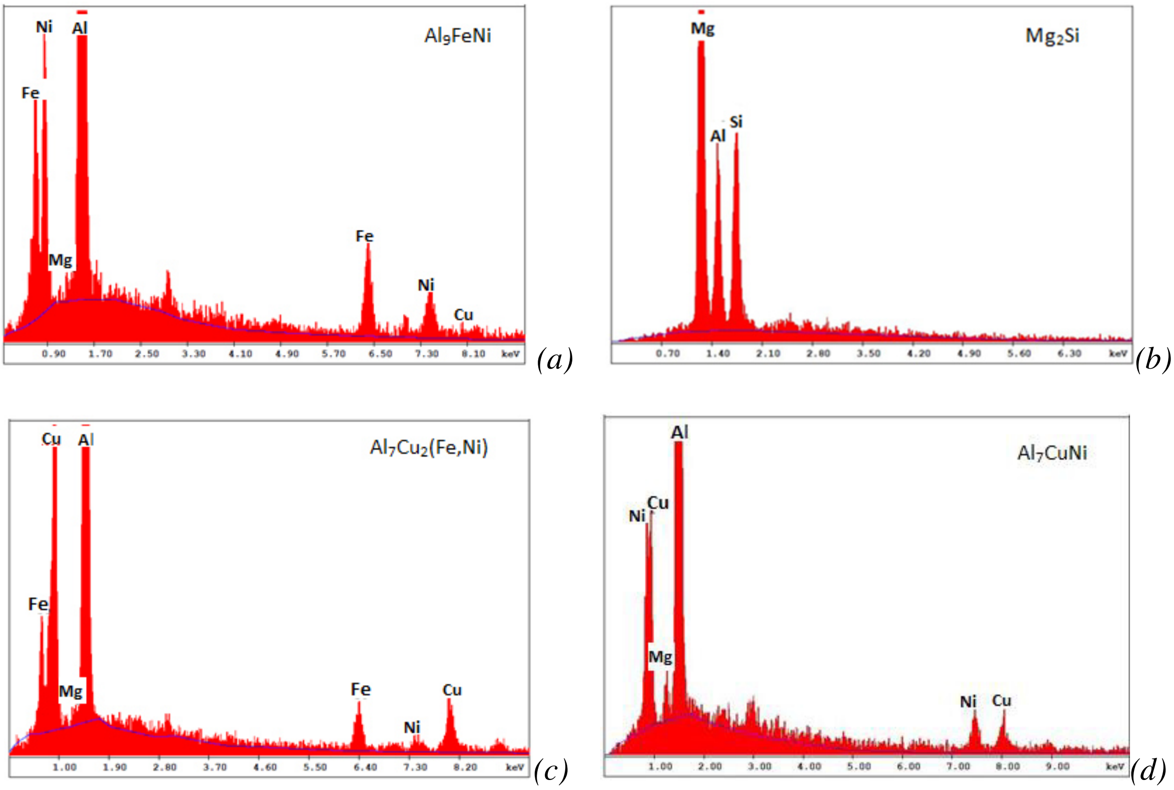

Fig. 3.19 – EDS spectra associated to the four different intermetallic phases detected: Al_9FeNi (a), Mg_2Si (b), $Al_7Cu_2(Fe,Ni)$ (c) and Al_7CuNi (d).

To investigate the effect of thermal exposure on strengthening precipitates, it is necessary to increase the magnification. Back-scattered electrons were used, because it is possible to get a better contrast with the matrix. The images taken with FEG-SEM at a magnification of 2000x for the 7 samples analysed are shown in Figure 3.20.

The peak-aged sample (Figure 3.20 (a)) shows quite large (~ 0.5 µm), round-shaped precipitates. Unfortunately, they are too small to allow an EDS point analysis; however, it is likely that they are Cu-based, because of the light colour. These particles results quite heterogeneously distributed, with some area presenting a higher concentration. Since their size is quite coarse, it is unlikely that they are the coherent or semicoherent strengthening phases. On the basis of literature data, the strengthening precipitates in fact are nanometer in size. The sample overaged to a residual hardness of 125 HB10 (Figure 3.20 (b)) results quite similar to the peak-aged sample, when a magnification of 2000x is used. Not outstanding differences are highlighted after an overaging that causes the reduction in hardness of 20 HB10, at least when a micrometrical order of magnitude is considered.

When hardness is reduced to 115 HB10 (figure 3.20 c), it becomes clear the appearance of small precipitates on the grain boundaries. These precipitates appear round-shaped and their dimension is smaller than 1 µm. They form continuous networks on the grain boundaries, as indicated with the arrows in Figure 3.20 (c). The precipitates heterogeneously scattered in the matrix are still present and they don't seem to undergo substantial changes in shape or dimension.

Figure 3.20 (d) represents the microstructure of the sample with a residual hardness of 105 HB10. At this level of over-aging other changes in the microstructure take place. Firstly, it becomes possible to resolve a pattern of fine, elongated precipitates (Figure 3.20 (d)). As the round shaped precipitates observed before, also the elongated precipitates appear to be inhomogeneously distributed in the matrix. Secondly, it can be seen that precipitation becomes much more significant on grain boundaries, causing clusters of small precipitates that are 1-2 µm in thickness. This precipitates are indicated with the arrow in Figure 3.20 (d).

Further increase in over-aging does not result in new microstructural features, but the previously described features become more evident. For example, Figure 3.20 (e), representing the microstructure of the samples with 90 HB10, shows that the elongated precipitates observed before become coarser and grow in number. It is possible to see that the elongated precipitates are not homogeneously distributed, but areas in which these precipitates are almost absent can be clearly seen. Moreover, the arrow indicates a quite broad cluster of precipitates with size ~1 µm, probably on grain boundary.

Figure 3.20 (f), related to the 80 HB10 sample, shows the same features of Figure 3.20 (e), but the elongate precipitates result coarser, particularly in some areas. Their length is about 1-2 µm; on the grain boundaries, the precipitates appear elongated. Note the presence of precipitates free area, in particular next to the grain boundaries (indicated with the arrow).

The microstructure of the 70 HB10 sample, showed in Figure 3.20 (g), is similar to the microstructure of the 80 HB10 sample (Figure 3.20 (f)). In Figure 3.20 (g) is possible to notice the presence of bigger precipitates on the grain boundaries (~2 µm), indicated with the arrow.

The elongated precipitates, detected in the over-aged specimens, are shown at higher magnification in Figure 3.21, for the 80 HB10 sample. From this figure, it can be seen that these precipitates seem elongated on two orthogonal directions. Moreover, they are not homogeneously distributed, and in some areas they result coarser than in other areas.

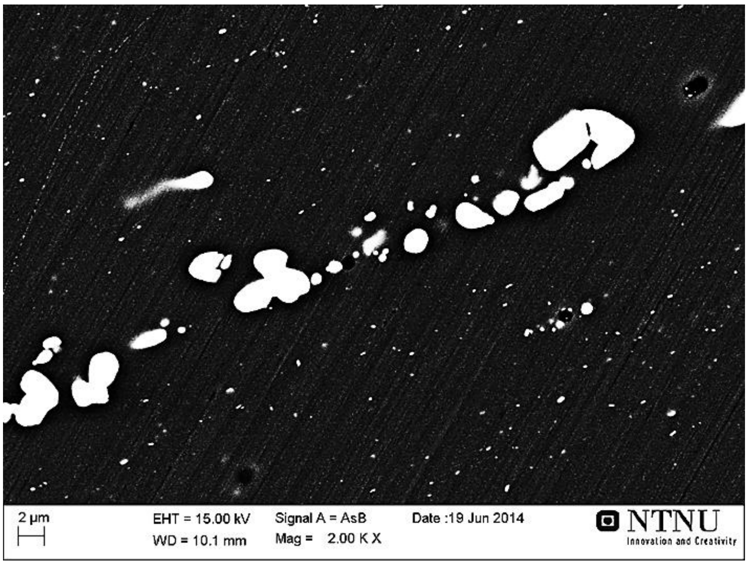
2 µm
EHT = 15.00 kV
WD = 10.1 mm
Signal A = AsB
Mag = 2.00 K X
Date :19 Jun 2014
NTNU
Innovation and Creativity

(a)

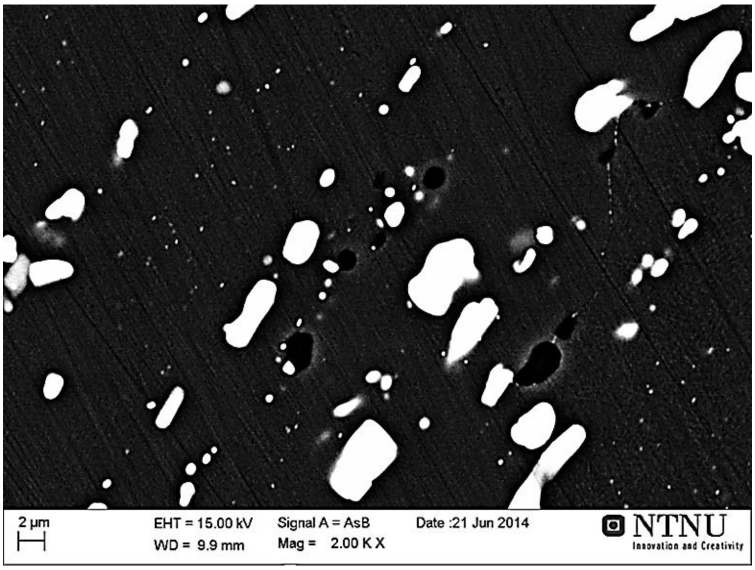
2 µm
EHT = 15.00 kV
WD = 9.9 mm
Signal A = AsB
Mag = 2.00 K X
Date :21 Jun 2014
NTNU
Innovation and Creativity

(b)

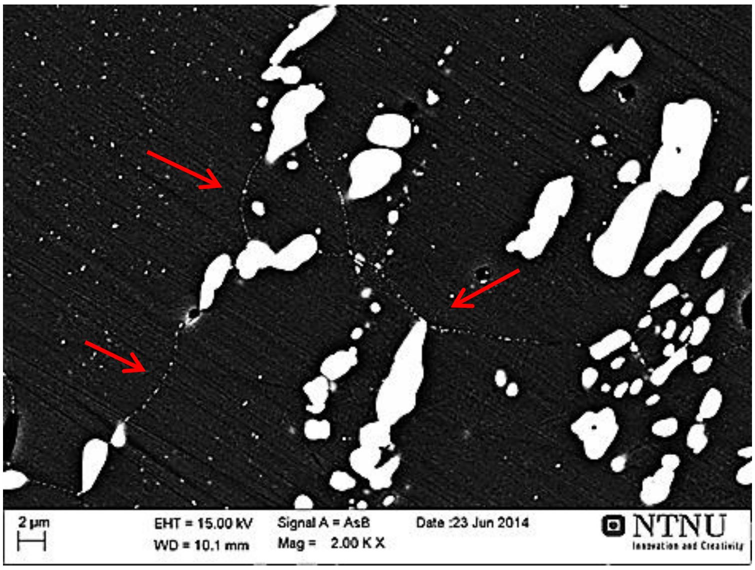
2 µm
EHT = 15.00 kV
WD = 10.1 mm
Signal A = AsB
Mag = 2.00 K X
Date :23 Jun 2014
NTNU
Innovation and Creativity

(c)

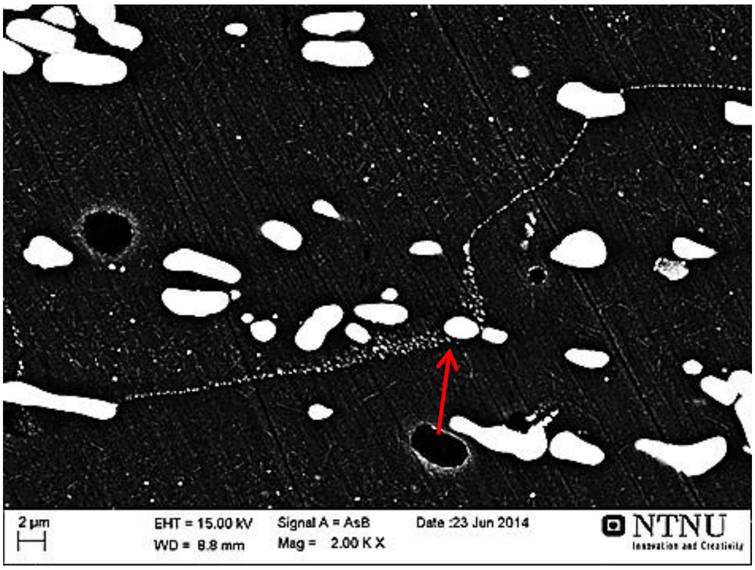
2 µm
EHT = 15.00 kV
WD = 8.8 mm
Signal A = AsB
Mag = 2.00 K X
Date :23 Jun 2014
NTNU
Innovation and Creativity

(d)

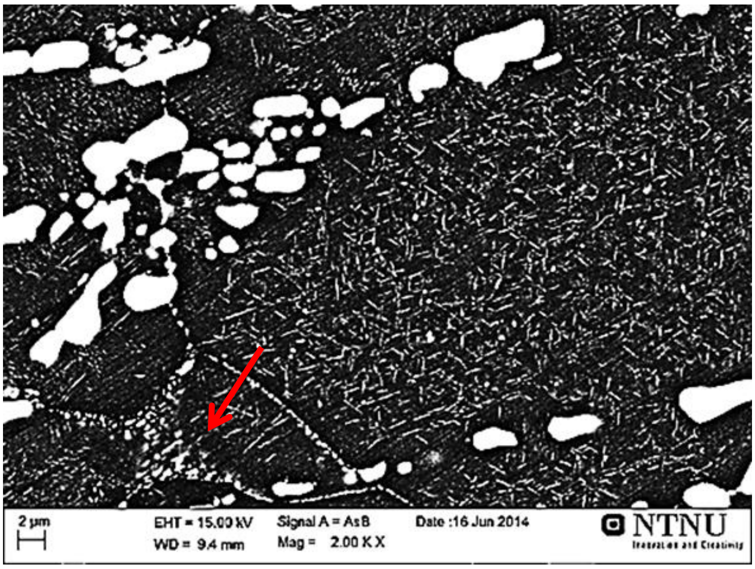
2 µm
EHT = 15.00 kV
WD = 9.4 mm
Signal A = AsB
Mag = 2.00 K X
Date :16 Jun 2014
NTNU
Innovation and Creativity

(e)

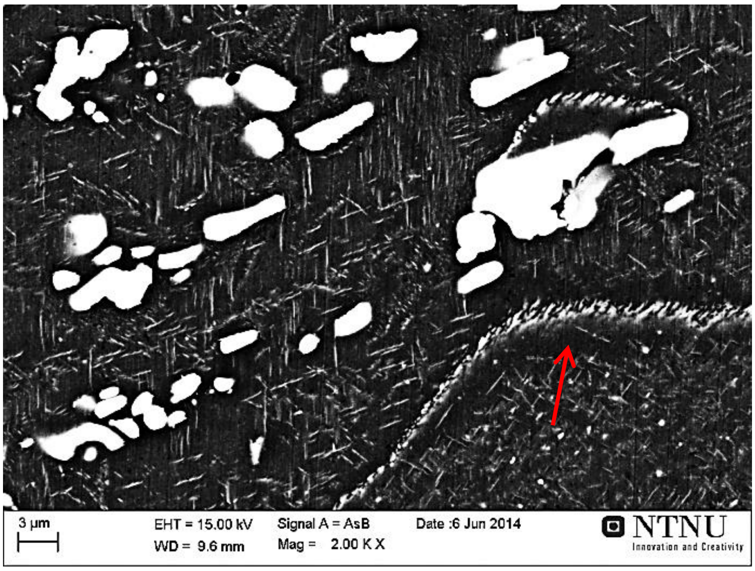
3 µm
EHT = 15.00 kV
WD = 9.6 mm
Signal A = AsB
Mag = 2.00 K X
Date :6 Jun 2014
NTNU
Innovation and Creativity

(f)

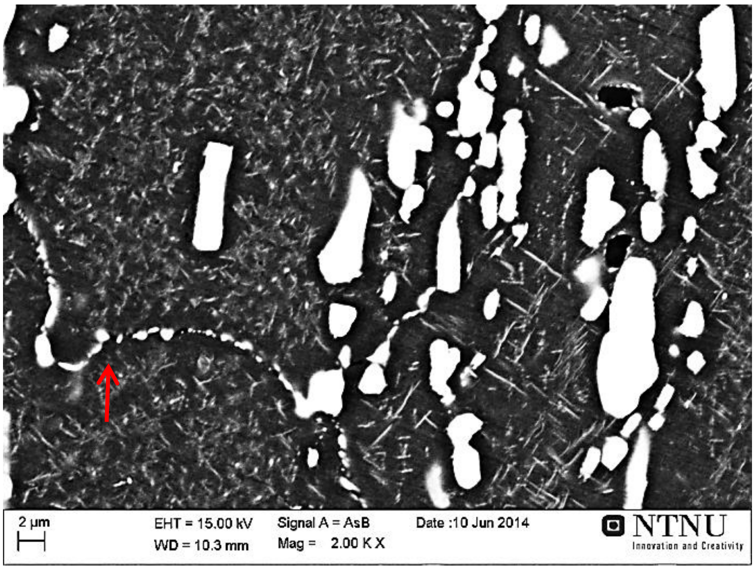

(g)

Fig. 3.20 – Images at higher magnification (2000x) of the 7 samples investigated taken with FEG-SEM using backscattered electrons: 145 HB10 (a), 125 HB10 (b), 115 HB10 (c), 105 HB10 (d), 90 HB10 (e), 80 HB10 (f), 70 HB10 (g). The red arrows indicate the formation of coarse particles on the grain boundaries.

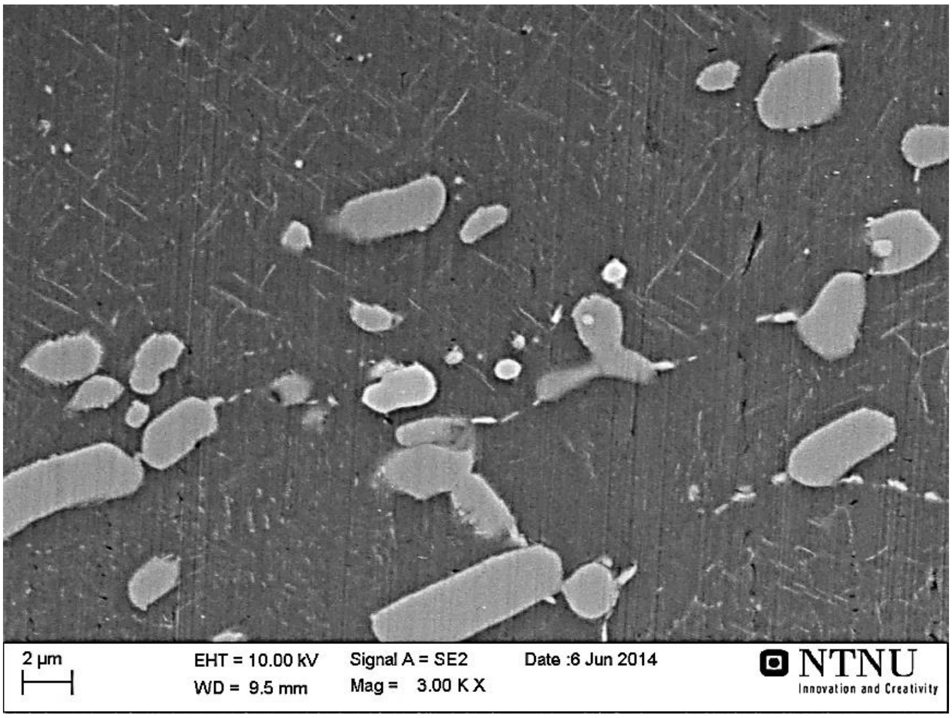

Fig. 3.21 – Image at higher magnification representing the elongated precipitates in the samples with 80 HB10 hardness value. These precipitates appear due to thermal exposure and seem to be elongated on two orthogonal directions.

On the basis of literature data, the main strengthening precipitates formed during the heat treatment of alloy AA 2618 is the S-Al_2CuMg and its precursors [3]. It is well known that in the peak-aged and in the slightly over-aged samples these precipitates are too fine to be resolved with a scanning electron microscope. Increasing exposure time and/or temperature results in the coarsening of S-phase precipitates. The coarsening in turn results in a loss of coherence of the precipitates with the aluminium matrix, and in the deterioration of mechanical properties. Unfortunately, the dimension and shape of the detected precipitates do not allow an EDS analysis to verify their chemical composition.

The obtained results were compared to previous studies from the literature, to confirm our findings.

Moreau *et al.* [9] studied an Al-4.4Cu-1.5Mg-0.2Sn-1.0Fe-1.0Ni wt.% alloy in peak-aged conditions and after thermal exposure. They found that the microstructures observed in the material treated at 120 °C for 1000 hours were similar to those of the material before thermal exposure, showing no obvious signs of precipitate formation detectable via SEM imaging [9]. In contrast, after exposure at 280 °C, regular arrays of what appeared to be lathe-like precipitates, identified as S-precipitates, were clearly present. These results are shown in Figure 3.22 (a) for the material exposed to 120 °C and (b) for the material exposed to 280 °C. It can be seen that the microstructure in Figure 3.22 (b) [9] for the Al-4.4Cu-1.5Mg-0.2Sn-1.0Fe-1.0Ni wt.% alloy exposed to 280 °C for 1000 h is similar to the microstructure in Figure 3.7 for the AA 2618 alloy exposed to 305 °C for 8.5 h, suggesting that the precipitates observed in the over-aged samples could be the S-phase.

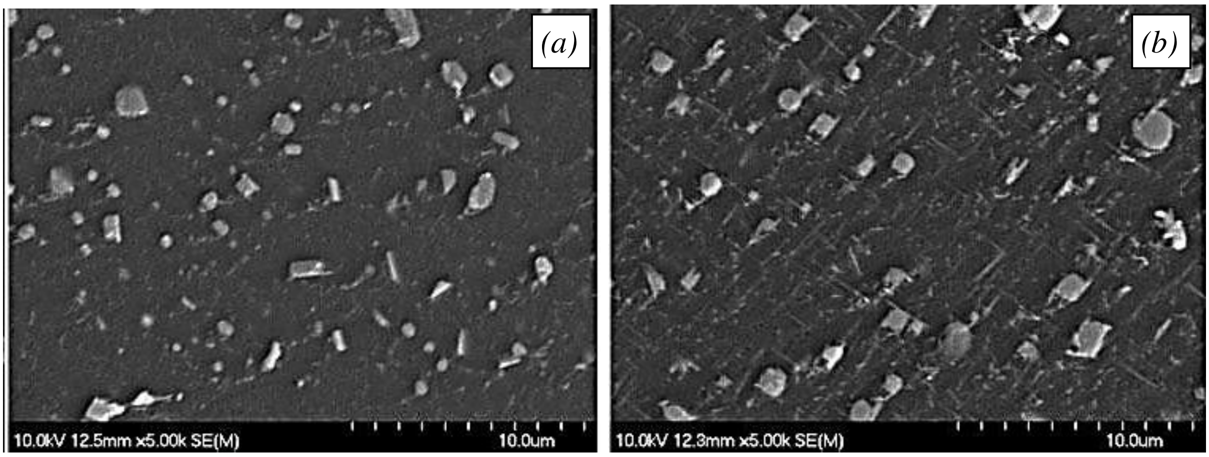

Fig. 3.22 – SEM images of microstructures reported in [11] for an Al-4.4Cu-1.5Mg-0.2Sn-1.0Fe-1.0Ni wt.% alloy peak-aged and exposed to high temperature: after exposure at 120 °C for 1000 h (a), and after exposure at 280 °C for 1000 h (b).

Majimel *et al.* [11] studied a AA 2650 alloy (Al-2.68Cu-1.86Mg-0.21Si-0.21Fe-0.24Ni), which presents a composition similar to the AA 2618, but with a lower content of Fe and Ni. In the peak-aged material the authors [11] detected a heterogeneous precipitation of S and S' phases which form strings of precipitates, together with a homogeneous precipitation of S' phase and fine needle-like GPB/GPB2 zones or S'' phase.

During thermal exposure at 150 °C, the disappearance of the needle-like precipitates (GPB zones) was observed, presumably because they are consumed by the formation of S precipitates; the combined effects of ageing and plastic deformation during creep were found to accelerate this disappearance. This process is recognized to be responsible for the softening of the 2650 alloy, and since the chemical composition of this alloy is similar to that of AA 2618 alloy, the same consideration can apply to the present study.

Du *et al.* [12] confirmed that S phase and S''/GPB2 precipitates co-exist in a peak-aged AA 2618 alloy. After 100 h creep test at 180 °C, S'' was found to transform to rod or lath-shaped S phase, with obvious increase in the dimension of precipitates. Increasing the temperature test to 240 °C resulted in the almost complete transformation of all precipitates into the equilibrium S-phase, with just a few of GPB zones and S'' phase still present in the microstructure.

In contrast, Novy *et al.* [3] observed that in peak-aged AA 2618 alloy the strengthening phase was present just in the form of GPB2 zones, uniformly distributed tiny plate-like precipitates of the size of several tens of nanometres. These precipitates are far too fine to be resolved with SEM, and this can explain why no precipitates were detected in the peak-aged specimen, in the present study.

After 24 hours of creep test at 270 °C with a load of 140 MPa, the microstructure analysed by Novy *et al.* [3] presented intergranular and intragranular partially coherent needle-like S' precipitates, while increasing the test duration or the temperature to 300 °C caused the transformation of the S' phase into the equilibrium S phase. The stable S-phase was detected mainly along grain boundaries, and was found to exist in two morphologies: as plate-like precipitates, and/or irregular precipitates. According to this study, the elongated precipitates observed in the matrix could be S' phase, while the coarser precipitated observed on the grain boundaries could be S-phase. However, it was shown that the difference between the two phases is slight, and some author doesn't make a distinction between the two phases.

In the present study, the microstructural investigations revealed the existence of some areas were the precipitates were absent in the heavily over-aged samples. Denuded precipitation-free zones were also observed by Novy *et al.* [3] after 24 h creep test at 240 °C on T6 AA 2618. The denuded PFZs were found to be of 0.5–1 μm wide and to form along grain boundaries. They are formed due to the growth and coarsening of the S-phase: this process consumes a great amount of solute elements, resulting in the depletion of solutes in the matrix near the growing S-phase boundary. An example of the denuded PFZs detected by Novy *et al*. [3] is reported in Figure 3.23. These zones are reported to have a detrimental effect on the mechanical properties of the alloy.

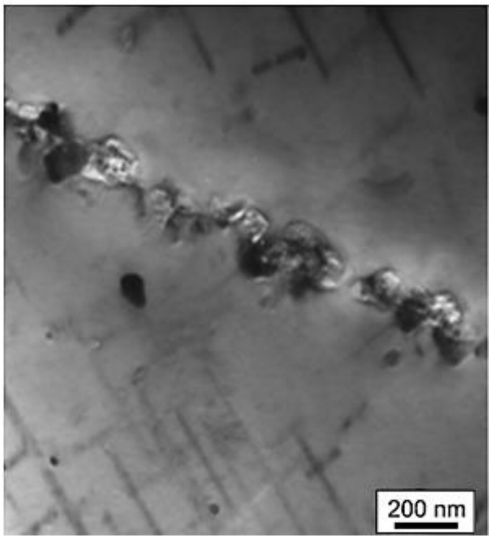

Fig. 3.23 – Example of PFZ detected by Novy et al. [3] in T6 AA 2618 after 24 h creep test at 270 °C (140 MPa load)

3.2 EFFECT OF Zr AND V ADDITIONS ON AA 2618

Zr and V were added to AA 2618 aluminium alloy, according to the procedure explained in §2.2.1 and §2.2.2. The base material (AA 2618) used in this study exhibits the chemical composition reported in Table 2.3. As explained in §2.2.1, the two modified alloys were designed to have a target composition containing 0.25 wt.% Zr and 0.25 wt.% Zr plus 0.1 wt.% V, respectively. All the results from the study of the base and modified alloys are reported below.

3.2.1 Chemical analyses

The chemical analyses results are reported below. Table 3.4 (a) shows the result of the quantometer analysis carried out in Bologna on samples extracted both from the small and cylindrical castings for the modified alloys, and from the cylindrical casting for the base material. Table 3.4 (b) shows the results of the GDMS analysis carried out at NTNU on samples extracted from both the rectangular and cylindrical castings of the two modified alloys.

	Quantometer analysis results - Element wt. %												
	Cu	**Mg**	**Si**	**Ni**	**Fe**	**Zr**	**V**	**Mn**	**Cr**	**Zn**	**Ti**	**Ga**	**Al**
2618	2.39	1.30	0.18	1.11	1.05	0.12	0.014	0.05	0.011	0.04	0.099	0.006	93.65
2618+Zr	2.33	1.29	0.18	1.10	1.05	0.15	0.014	0.06	0.011	0.04	0.077	0.006	93.73
2618+Zr+V	2.35	1.30	0.18	1.10	1.06	0.16	0.055	0.10	0.011	0.05	0.078	0.006	93.54
2618+Zr cylindrical	2.36	1.32	0.18	1.07	1.05	0.15	0.013	0.00	0.010	0.05	0.088	0.006	93.69
2618+Zr+V cylindrical	2.39	1.32	0.18	1.07	1.03	0.17	0.060	0.14	0.011	0.05	0.094	0.006	93.47

(a)

		GDMS results - Element wt. %						
		Cu	**Mg**	**Si**	**Fe**	**Ni**	**Zr**	**V**
2618+Zr rectangular	Average	1.58	1.11	0.154	0.75	0.96	0.138	0.010
	SD	0.11	0.02	0.004	0.37	0.33	0.002	0.000
2618+Zr cylindrical	Average	2.01	1.22	0.160	1.10	1.03	0.183	0.012
	SD	0.10	0.02	0.004	0.03	0.20	0.007	0.000
2618+Zr+V rectangular	Average	1.85	1.23	0.160	1.18	0.95	0.228	0.070
	SD	0.10	0.04	0.003	0.05	0.04	0.008	0.003
2618+Zr+V cylindrical	Average	1.90	1.14	0.147	1.11	0.90	0.353	0.066
	SD	0.03	0.01	0.002	0.06	0.02	0.010	0.001

(b)

Tab. 3.4 – Chemical analyses results (mass percentage): quantometer analysis carried out on samples extracted from both the small and cylindrical castings for the modified alloys and from the cylindrical casting for the base material AA 2618 (a); GDMS analysis carried out on samples extracted from both the rectangular and cylindrical castings for the modified alloys (b). Note that the data highlighted by the red circles were obtained from the same samples.

The quantometer analysis results reported in Table 3.4 (a) clearly show that the amounts of Zr and V added to the base material are lower than expected, but they seem to be quite constant in sample extracted from different castings. On the other hand, the GDMS results reported in Table 3.4 (b) show that Zr content presents quite strong variations with values from 0.14 to 0.35 wt. %. It is worth noticing that the same samples extracted from the cylindrical castings were examined with quantometer and GDMS. The detected amounts of Zr are quite different for the two techniques (highlighted by red circles in Table 3.4). The results concerning the amounts of V are more consistent; however V amount is lower than expected. These results must be taken into account when comparing the different samples and interpreting the data.

Since holding temperature (750-800 °C) and time (1-2 h) of the melt should be sufficient to completely dissolve the master alloys, it is still to be understood why the amount of Zr and V revealed by chemical analyses is lower than expected. The most probable hypotheses are that i) the composition of the master alloys was different from the nominal ones, or that ii) Zr and V were concentrated in some areas of the melt due to poor stirring. The second hypothesis could explain the GDMS results that show different contents of Zr in different areas of the same sample. Anyway, the GDMS results are not in agreement with the quantometer results obtained from the same samples, which could mean that GDMS results are not very precise or that the material is very inhomogeneous.

Additional experiments will be carried out in order to understand the reason for the lower concentration of Zr and V in the modified alloys. The results presented in the following sections will be discussed taking into account the chemical analyses reported in Table 3.4.

3.2.2 Thermal analysis

Table 3.5 shows the results of thermocouple calibration tests, carried out measuring pure aluminium solidification temperature. The first calibration reported in Table 3.5 (a) was carried out before the measurements on the first casting, to check the thermal stability of the thermocouple, while the second calibration reported in Table 3.4 (b) was carried out between the second and third casting, since a shift in the measured temperature was detected during the measurements on the second casting, and another calibration was carried out. The correction represents the value to be added to the measured temperature and it was calculated using the solidification temperature of pure aluminium (660.3 °C) as reference. It is evident that a temperature shift occurred between the two calibrations.

Table 3.6 shows the results of the thermocouple calibration before and after the measurements on each of the three castings. It seems that during the second casting (AA 2618 with Zr addition), a shift in the measured temperature took place during the thermal analysis tests. The data in Table 3.5 (b) indicate a large difference between the pure aluminium solidification temperature measured before and after the tests on the modified alloy. This in turns causes the standard deviation value to be quite high. It is clear that the correction resulted to be quite different in the three castings, i.e. the thermocouple stability was quite poor; however this should not affect the thermal analysis results.

Calibration 1 [°C]	
Average	665.3
SD	0.60
Correction	**-5.0**

(a)

Calibration 2 [°C]	
Average	662.7
SD	0.49
Correction	**-2.4**

(b)

Tab. 3.5 – Average value and standard deviation of the measured solidification temperature for pure aluminium, and the corresponding correction, found during the first (a) and the second (b) calibration carried out on the thermocouple used for thermal analysis measurements.

Calibration AA 2618 [°C]		
Before tests	Average	665.6
	SD	0.10
After tests	Average	665.7
	SD	0.51
Total	Average	665.6
	SD	0.33
Correction		***-5.3***

(a)

Calibration AA 2618+Zr [°C]		
Before tests	Average	665.2
	SD	0.62
After tests	Average	661.6
	SD	0.38
Total	Average	663.4
	SD	1.96
Correction		***-3.1***

(b)

Calibration AA 2618+Zr+V [°C]		
Before tests	Average	660.8
	SD	0.19
After tests	Average	660.7
	SD	0.27
Total	Average	660.8
	SD	0.23
Correction		***-0.5***

(c)

Tab. 3.6 – Average value and standard deviation of solidification temperature for pure aluminium measured before and after thermal analysis tests on the three casting, and for all the tests (total) and corresponding correction: data related to AA 2618 (a), AA 2618 modified with Zr (b) and AA 2618 modified with Zr and V (c).

The corrections reported in Table 3.6 were algebraically added to the temperatures measured during the thermal analysis tests, i.e. a translation in the y direction was applied to the temperature-time (T-t) curves. From the analysis of these curves, the cooling rate before the starting of solidification was calculated to be about 1.4 – 1.6 °C/s.

No relevant differences were detected between the T-t curves for the base material and the modified alloys. Figure 3.24 shows a T-t (blue) and the related first derivative dT/dt (light blue) curves, representative for all the materials. The grey curve in Figure 3.24 represents the fraction solid, calculated with TAW32.

The first derivative dT/dt (Figure 3.24) presents four peaks, highlighted by red arrows, each of which corresponds to a decrease in the slope of the T-t curve. Each peak represents the solidification of one or more phases. The enlargements of the areas relative to the peaks from Figure 3.24 are shown in Figure 3.25.

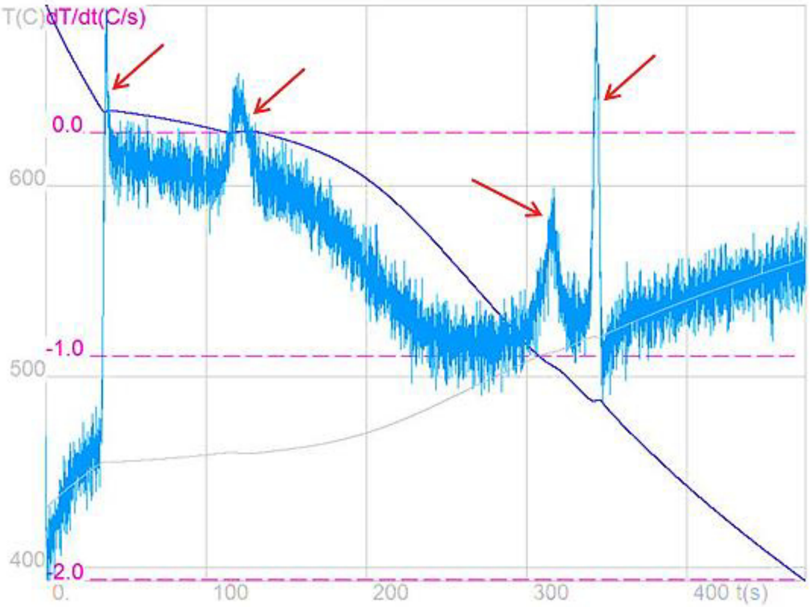

Fig. 3.24 – Example of thermal analysis results: T-t curve (blue), first derivative dT/dt (light blue) and fraction solid (grey). The red arrows indicate four peaks.

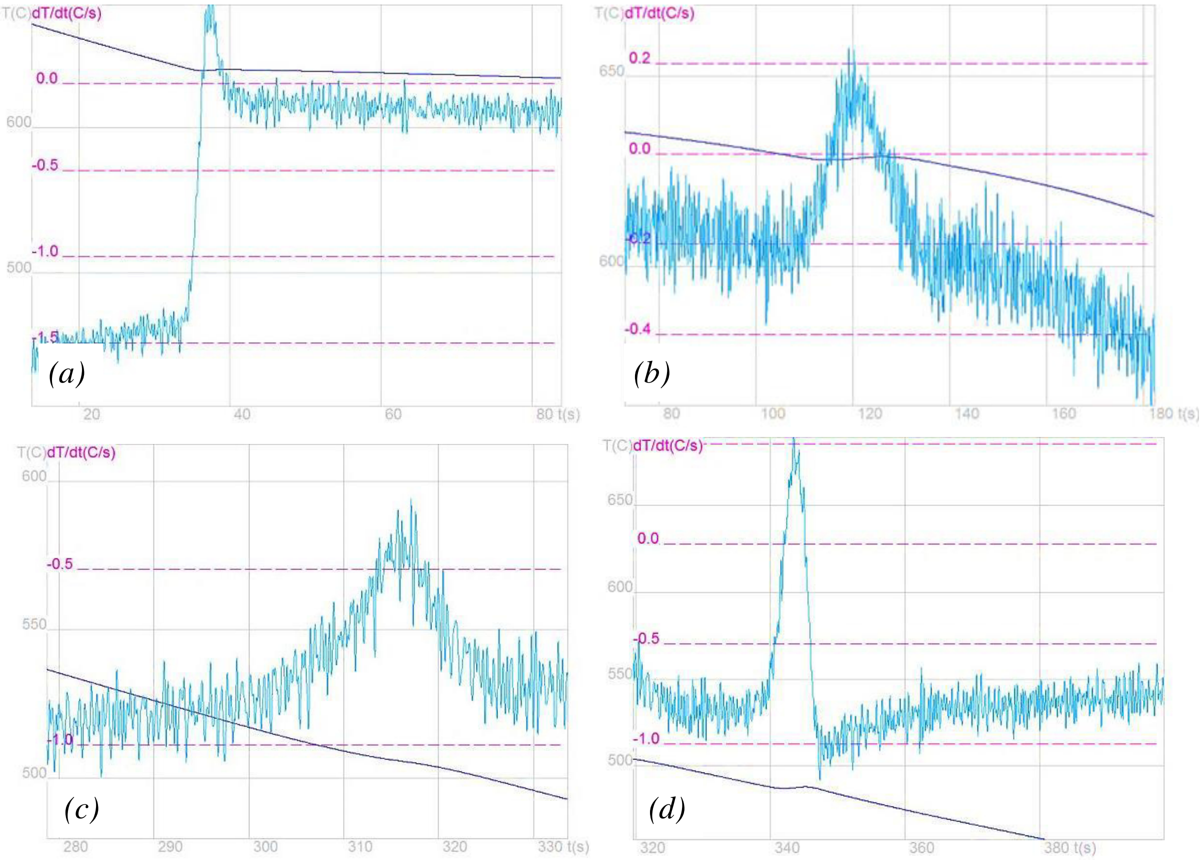

Fig. 3.25 – Enlargement of the four peaks detected in the dT/dt curve: in order of decreasing temperature first (a), second (b), third (c) and fourth (d) peak. Each peak corresponds to a solidification reaction.

Figure 3.26 shows the enlargement of the curves T-t in the areas relative to the peaks of the first derivative. All the tests carried out on the three different alloys are reported, and it is possible to see that the differences between the curves of alloys with different compositions are not very large if compared to the differences between the curves relative to the same composition.

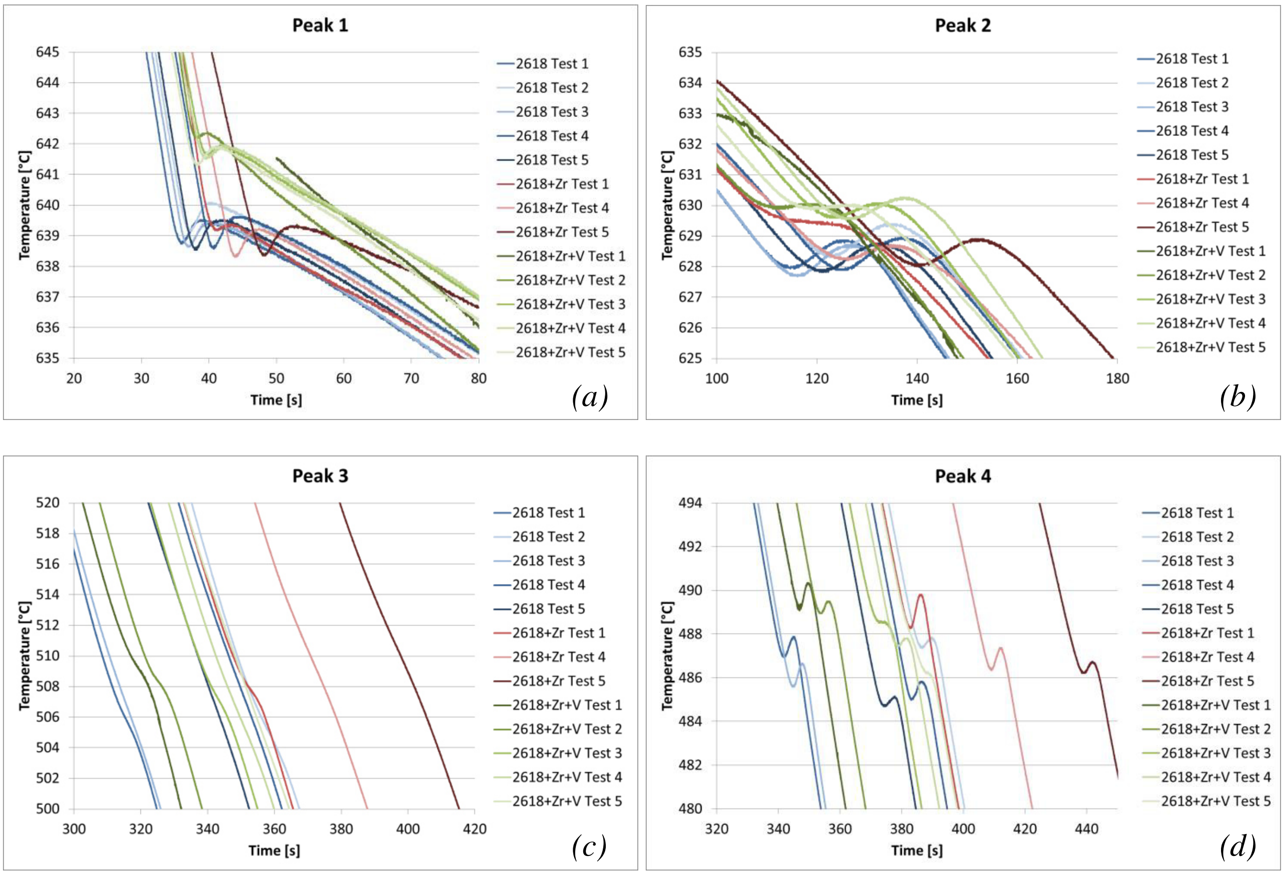

Fig. 3.26 – Enlargements of areas of the T-t curves relative to the first derivative peaks: area related to first (a), second (b), third (c) and fourth (d) peaks. All the test carried out on the three different alloys are reported in the graphs.

The temperatures relative to the beginning and end of each peak were measured with TAW32, and the average values and standard deviations are reported in Table 3.7 for each composition. The graph in Figure 3.27 shows the data reported in Table 3.7: the bar chart shows the temperatures for the beginning and the end of each peak for the three different compositions; the black bars represent the standard deviations. It can be seen that the differences in the peak temperatures between the three different compositions are quite small, and the standard deviation value generally results moderate, which means that the tests have a good repeatability. The additions of Zr and Zr + V do not seem to affect the thermal analysis result, at least when these elements are added in such small quantities. In fact, the shape of the T-t curves and the temperatures of dT/dt peaks are similar for the three different alloys.

Temperature of dT/dt peaks [°C]									
Peak no.		1		2		3		4	
2618	Average	640	640	628	629	515	500	487	485
	SD	0.4	0.3	0.2	0.4	4.9	1.4	1.3	1.7
2618+Zr	Average	640	639	629	629	514	505	488	487
	SD	1.1	0.1	0.9	0.6	3.3	0.8	0.9	1.8
2618+Zr+V	Average	643	642	631	630	514	503	489	487
	SD	0.3	0.2	1.3	1.2	2.3	3.5	1.6	1.7

Tab. 3.7 – Temperatures relative to the beginning and end of the four peaks identified in the dT/dt curves. Average values and standard deviations are reported for the three different compositions.

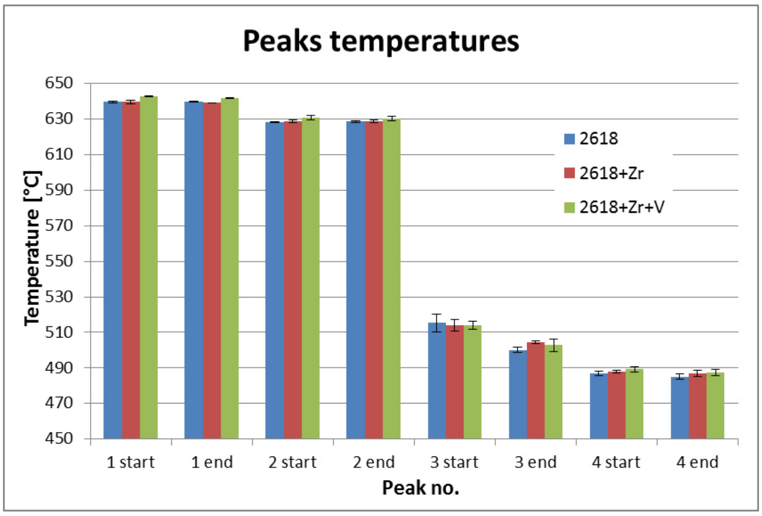

Fig. 3.27 – The bar chart shows the average values of the temperatures relative to the beginning end the end of the four peaks identified in the dT/dt curves for the three different compositions. The black bars represent standard deviations. Data shown from Table 3.7.

As explained before, each peak is related to a reaction taking place during solidification. Peak number 1 represents the start of the solidification and is related to the formation of α-Al dendritic network. The temperature identified for this reaction (~640 °C) is a little higher than the value reported in [13] (637 – 633 °C) for the AA 2024 alloy (Al-4.44Cu-1.56Mg-0.55Mn-0.23Fe-0.21Si). On the basis of the microstructural analysis reported below, and comparing the experimental data with data reported in [5] and [13], the second and third peaks are believed to be associated with the solidification of Al-Fe-Ni and Al-Cu-Ni-(Fe) phases. The fourth peak (~487 °C) correspond to the end of the solidification (solidus temperature), and is probably related to the solidification of Al_2Cu, Al_2CuMg and Mg_2Si phases [13]. The interpretation of peaks reactions is summarized below:

First reaction: liq. → Al (dendritic network) ~ 640 °C

Second reaction: liq. → Al + Al_9FeNi ~ 629 °C

Third reaction: liq. → Al + Al-Cu-Ni-(Fe) ~ 515 – 500 °C

Fourth reaction: liq. → Al + Al_2Cu + Mg_2Si + Al_2CuMg ~ 487 °C

It is important to note that the interpretation of reactions reported above is elaborated on the basis of the microstructural investigation presented below, data on solidification of AA 2024 alloy [13] and DSC analysis of AA 2618 alloy [5], since no data on solidification reactions of the AA 2618 alloy were found in literature. Data reported in [5] and [13] are not coherent with the temperatures reported in Table 3.6, but this can be due to the fact that data reported in [13] are referred to a different alloy, while data reported in [5] were found with a DSC analysis on a DC cast AA 2618 during heating. Nevertheless, the sequence in the melting temperatures reported in [5] was used to identify the sequence of reactions found in the present study.

Elaborating the data with TAW32, it was also possible to find the fraction solid associated to peaks number 2, 3 and 4, that is, the percentage of material already solidified when reactions number 2, 3 and 4 took place. Table 3.8 reports the result and shows that there is no considerable difference between the three alloys.

Fraction solid				
Peak no.		**2**	**3**	**4**
2618	Average	*0.28*	*0.95*	*0.98*
	SD	0.013	0.005	0.000
2618+Zr	Average	*0.23*	*0.95*	*0.98*
	SD	0.020	0.000	0.000
2618+Zr+V	Average	*0.25*	*0.94*	*0.98*
	SD	0.029	0.010	0.000

Tab. 3.8 – Average values and standard deviations of the fraction solid before starting of reaction 2, 3 and 4 for the three different alloy compositions.

It is possible to see that reaction number 2 starts when approximately 25% of the material has already solidified, and therefore there is still much liquid left, while reaction 3 and 4 start when 95% and 98% of material has solidified, respectively. That means that phases formed during reaction 3 and 4 have a low volume fraction, since there is little liquid left, while the phase formed with reaction 2 could have a higher volume fraction. This consideration, together with the results from the microstructural study presented below, confirms the fact that peak 2 from the thermal analysis can be associated with the solidification of Al_9FeNi intermetallic phase.

3.2.3 DSC analyses

The DSC analysis was carried out in Bologna on the as-cast materials, both during heating and cooling with a rate of 10 °C/min. The results did not point out relevant distinction due to the addition of Zr or Zr and V. Figure 3.28 shows, as an example, the curves heat flow-temperature related to the base material AA 2618: the blue curves were obtained during heating while the black ones during cooling. The curves reported on the right represent the enlargement of the areas in the red rectangles on the left.

The curves in Figure 3.28 (b) and (d) show two peaks related to the melting/solidification of two phases. The temperatures at which these two peaks are detected, both during heating and cooling, in the three different alloys are listed in Table 3.9. The peaks are designed 1 and 2, at lower and higher temperature, respectively.

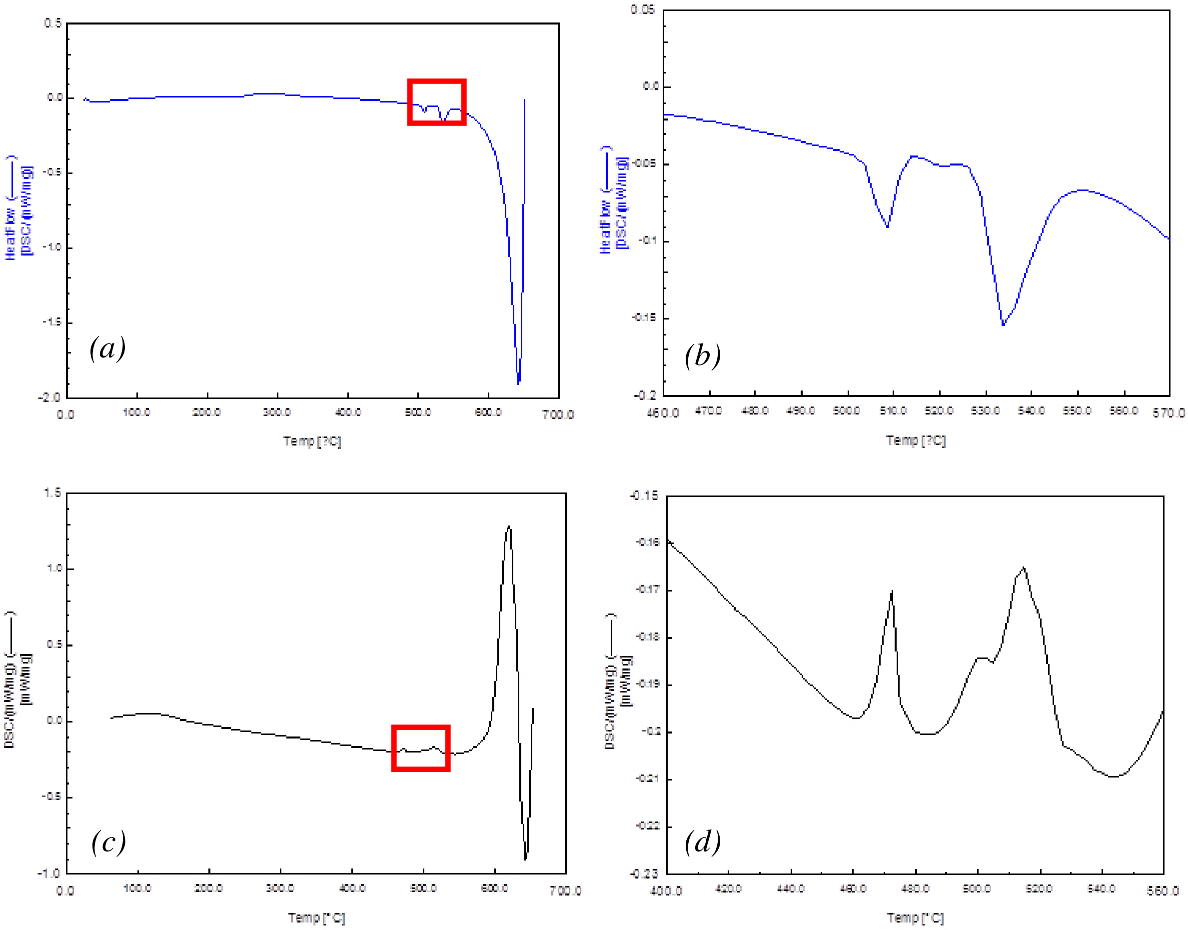

Fig. 3.28 – Heat flow-temperature curves obtained from the DSC analysis of as-cast AA 2618 aluminium alloy during heating (a), (b) and cooling (c), (d). Figures (b) and (d) represent the enlargement of the area highlighted by the red rectangle in figures (a) and (c), respectively, and clearly show the presence of two peaks.

	DSC results [°C]			
	Heating		Cooling	
	Peak 1	Peak 2	Peak 1	Peak 2
2618	503.2	528.0	480.2	526.7
2618+Zr	503.3	528.0	474.0	524.5
2618+Zr+V	501.7	528.4	476.7	526.6

Tab. 3.9 – Temperatures related to DSC peaks detected during heating and cooling of the three as-cast alloys. The peaks were designated 1 (the peak at lower temperature) and 2 (the peak at higher temperature).

Table 3.9 shows that the peaks temperatures are not strongly influenced by the addition of Zr and/or V to AA 2618 aluminium alloy. It is also possible to see that temperature relative to peak 2 is quite constant during heating and cooling, while temperature relative to peak 1 is much higher during heating than during cooling.

The DSC results presented in Table 3.9 were compared to data collected from the literature in order to verify their soundness and interpret the peaks. In particular, Shen *et al.* [5] and Wang *et al.* [14] carried out DSC during heating of a DC cast and a semi-continuous cast AA 2618 aluminium alloy, respectively. Wang *et al.* [14] reported the presence of 2 endothermic peaks at temperature lower than 600 °C, as in the present study, while Shen *et al.* [5] identified 6 endothermic peaks from room temperature up to 650 °C. The 2 peaks identified by Wang *et al.* [14] and the first 2 peaks identified by Shen *et al.* [5] correspond to the peaks identified in the present study; their temperatures are compared in Table 3.10. It can be noted that the temperatures reported in [5] and [14] for the first peak are higher, while the temperatures for peak 2 are somewhat lower than that found in the present study. However, these differences are not really considerable and it is possible to affirm that the data reported in Table 3.8 are in good agreement with data from the literature.

	DSC [°C]	
	Peak 1	Peak 2
Present study	502.7	528.1
Shen *et al.* [5]	508.3	539.9
Wang *et al.* [14]	511.4	535.1

Tab. 3.10 – Comparison of the temperatures corresponding to DSC peaks detected in the present study with data from the literature. The temperatures reported in table were recorded during heating of as-cast AA 2618 aluminium alloy.

On the basis of what is reported in [5] and [14], it is possible to assert that peak 1 and 2 represent the melting point (or solidification temperature, if the cooling curve is considered) of Al/Al_2CuMg and Al/Al_2Cu eutectic phases, respectively:

Peak 1: melting of Al/Al_2CuMg ~503 °C

Peak 2: melting of Al/Al_2Cu ~528 °C

These temperatures are of particular importance when designing an heat treatment; in fact, it is necessary to avoid the melting of these low-melting phases during solutionizing.

Note that the peak detected with the thermal analysis associated to these reactions is peak 4, at a temperature of ~487 °C, while DSC during cooling revealed the first peak at ~477 °C, and the second at ~526 °C. It is possible to conclude that the peak at lowest temperature, corresponding to the solidus temperature, appears at similar temperatures in DSC and thermal analysis and therefore the agreement between the two different techniques is quite good. The difference in the other peaks can be justified with the fact that cooling rates are quite dissimilar (1.5 °C/s, corresponding to 90 °C/min, for thermal analysis and 10 °C/min for DSC).

3.2.4 Hot rolling

As-cast samples were hot rolled as explained in detail in §2.2.5. Hot-rolled samples of the base material (AA 2618), Zr-modified and Zr- and V-modified alloys are pictured in Figures 3.29, 3.30 and 3.31, respectively. The samples highlighted by the red circle in Figure 3.30 were hot rolled using different parameters, reported in §2.2.5.

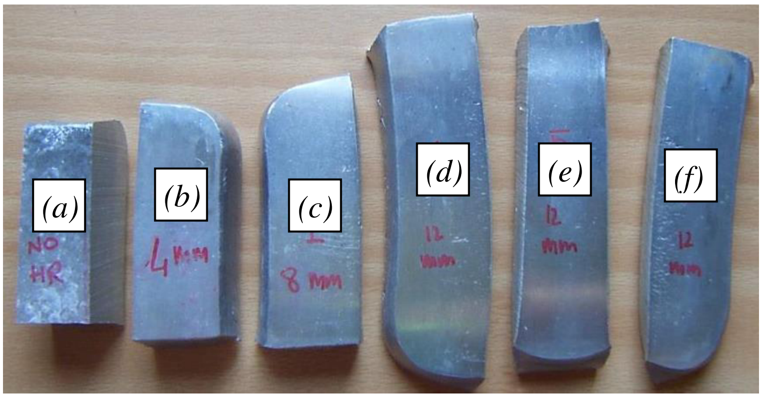

Fig. 3.29 – Hot rolled samples of AA 2618: as-cast sample (a), and 16% (b), 33% (c), 50% (d), (e), (f) deformed samples.

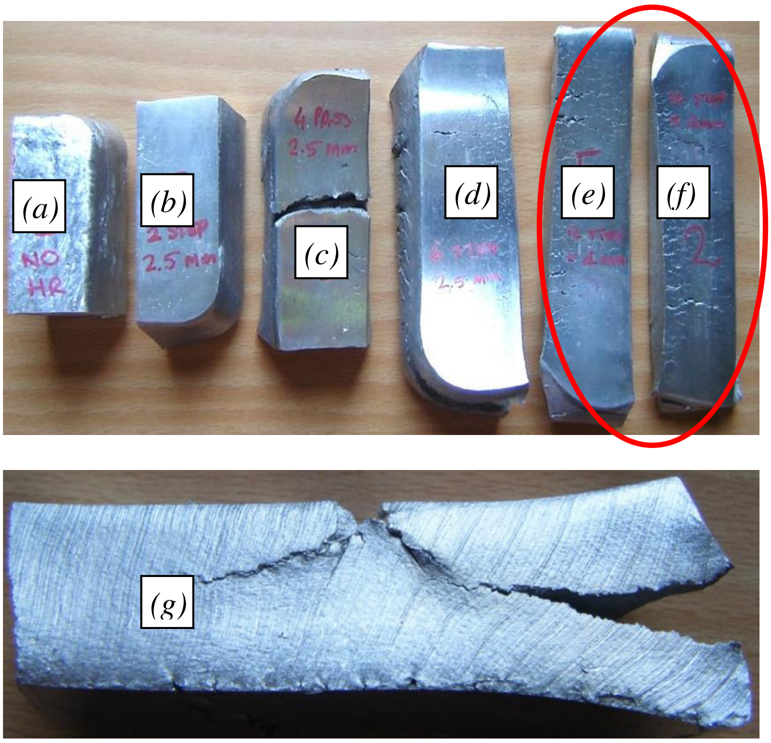

Fig. 3.30 – Hot rolled samples of Zr-modified AA 2618: as-cast sample (a), 16% (b), 33% (c), 50% (d), (e), (f) deformed samples, and enlargement of a 50% deformed sample (g). As explained in paragraph 2.2.5, samples (e) and (f), highlighted by the red circle, were hot rolled using different parameters from the other samples.

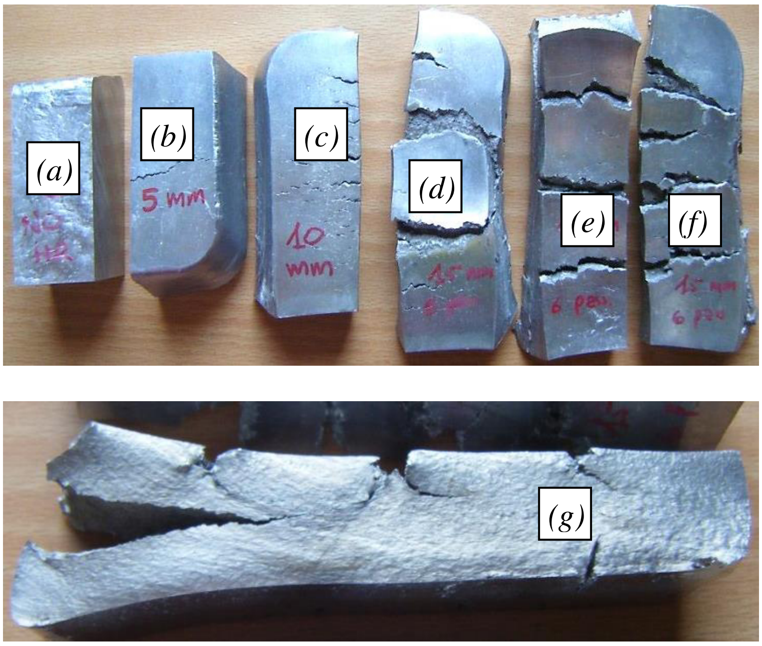

Fig. 3.31 – Hot rolled samples of Zr- and V-modified AA 2618: as-cast sample (a), 16% (b), 33% (c), 50% (d), (e), (f) deformed samples, and enlargement of a 50% deformed sample (g).

As it is possible to see in Figure 3.30 (c), (d), (g) and in Figure 3.31 (d)-(g), the modified alloys deformed to high deformation ratios presented extensive cracks, while the base material did not (Figure 3.29). This was initially believed to be due to the Zr and V additions, however, the chemical analysis indicated no significant differences. Therefore, it is the most likely that the fractures in modified alloys are due to the slightly different hot rolling parameters from the ones used for the base material, in particular the thickness reduction for each hot rolling step. This parameter was set to 2 mm for base material and 2.5 mm for modified alloys, due to the fact that the as-cast thickness was higher for modified alloys than for base material. In order to verify this hypothesis, 2 samples of the Zr-modified alloy were hot rolled with a thickness reduction for each step equal to 1 mm (samples (e) and (f) in Figure 3.30, highlighted by the red circle). The result shows that changing the hot rolling parameters can avoid the appearance of important cracks, so it seems that hot rolling parameters have a more important role in cracks formation than Zr and V additions.

To further support this theory, it should be noted that cracks pictured in Figure 3.30 (g) and 3.31 (g) represent a typical rolling defect [15], called alligator defect, caused by deformation conditions. These fractures tend to occur at the end of the slab after appreciable amounts of reduction, and to extend in a plane that is essentially parallel to the rolled surfaces and centrally located between such surfaces; on exit, the top and bottom parts follow the rotation of their respective rolls. Such fracturing, or alligatoring, is caused by the internal stress state of the slab which results from the non-uniformity of deformations that take place in the rolling passes [16]. If deformation is higher in the centre than in the surface, tensile stresses are originated in the surface, while compressive stresses are originated in the centre. If these stresses are high enough, and together with the presence of defects such as inclusions, the fracture occurs [15]. In the present case, not uniform deformation could also be caused by a thermal gradient in the samples, due to the fact that the surface of the samples were in contact with the cold rolls, and therefore at a lower temperature than the centre. This distribution of temperatures can result in a distribution of stresses, with traction on the surface and compression on the centre, due to thermal expansion.

To solve this problem, another rolling was done with modified parameters (§2.2.5). In particular, the thickness reduction for each step was dramatically decreased, and the holding time at high temperature was increased since, as it will be explained below, the microstructure of samples from the first rolling did not appear hot deformed. A sample of the extruded bar received from Duraldur S.p.A. was also rolled, in order to compare the response of the extruded material with that of the as-cast material. The hot rolled sample are pictured in Figure 3.32; it can be seen that samples do not show fractures of extensive cracks, therefore the rolling parameters were responsible for the fractures detected after the first hot rolling.

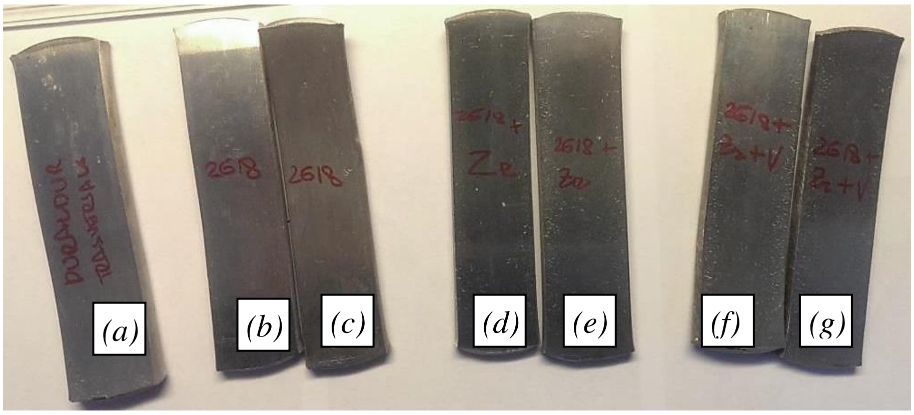

Fig. 3.32 – Samples obtained after the second hot rolling with a thickness reduction of 50 %: extruded material received from Duraldur (a); unmodified AA 2618 (b) ,(c); Zr-modified AA 2618 (d), (e); Zr- and V-modified AA 2618 (f), (g).

3.2.5 First hot rolling: optical microscopy

As-cast microstructure

The micrographs shown in Figure 3.33 display as-cast microstructures of base material and modified alloys, taken with optical microscope at a magnification of 5x. As-cast microstructure appears uniform throughout the examined samples, and consists of equiaxed primary dendrites of aluminium-rich solid solution and an interdendritic network of intermetallic compounds around the primary grains. It can be seen that the grain boundaries are decorated by large, irregular eutectic phases and intermetallic particles that have a detrimental effect on mechanical properties, making heat treatment necessary. The same microstructure for as-cast AA 2618 was reported by various authors in [4], [5] and [14]. Moreover, typical casting defects can be identified, such as shrinkage defects and gas porosity.

At low magnification, microstructures of base material and modified alloys do not present considerable differences. However, a careful examination of micrographs in Figure 3.33 suggests that the distribution of interdendritic phases in AA 2618 is coarser than in modified alloys.

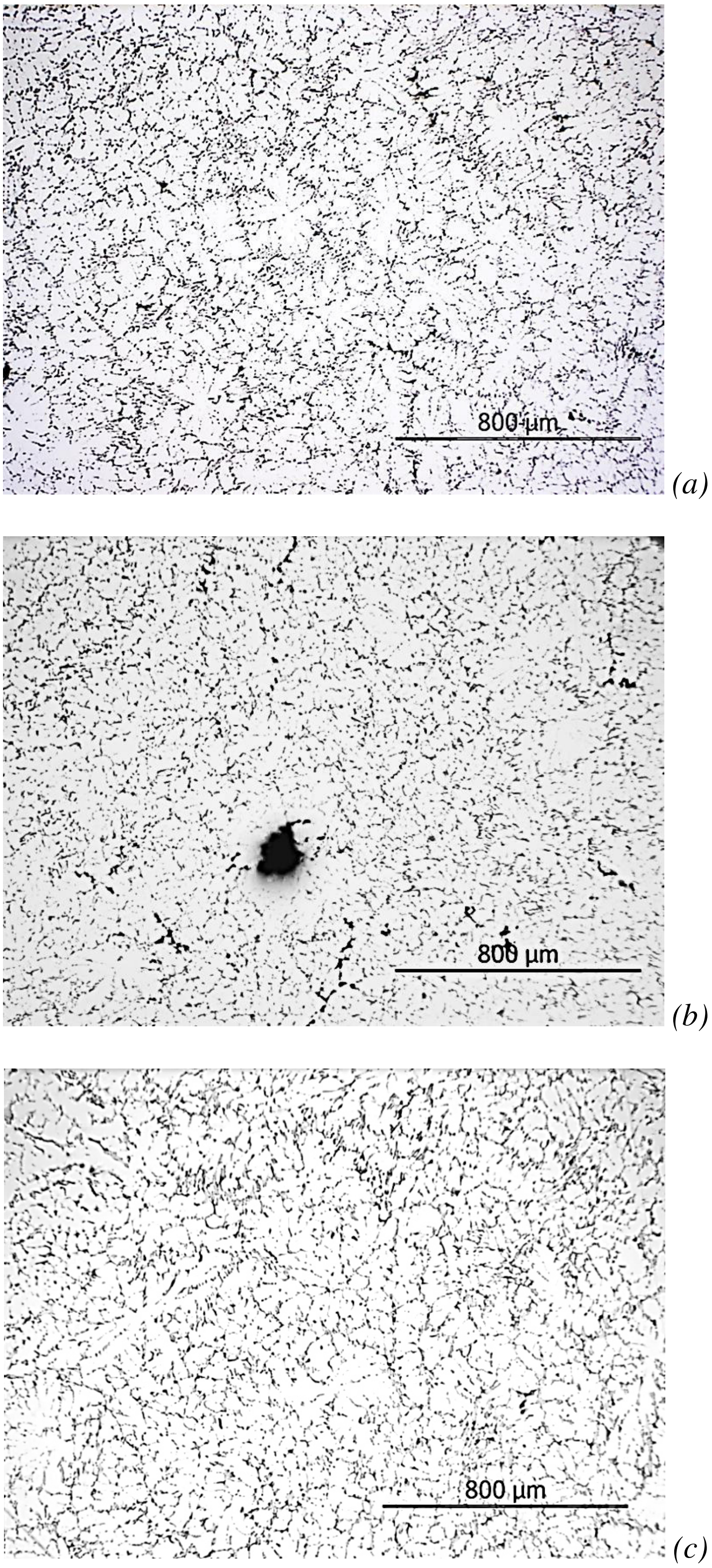

Fig. 3.33 – Optical micrographs of as-cast samples at 5x magnification: AA 2618 (a), Zr-modified AA 2618 (b), Zr- and V-modified AA 2618 (c). OP-S polished and not-etched samples. The microstructure consists of equiaxed α-Al dendrites and interdendritic compounds.

Figure 3.34 shows the microstructure of the three as-cast alloys taken with optical microscope at higher magnification (100x). At higher magnification, different intermetallic phases can be clearly observed. In fact, it can be seen that the second phases on the grain boundaries present various shapes and colours. According to the morphology and light contrast of the phases, in the OM micrographs it is possible to recognize the presence of four different types of the secondary phases labelled 1 (lamellar eutectic structure), 2 (needle-like black phase), 3 (light grey phase) and 4 (dark grey feather-like, lath-like or irregular phases) in Figure 3.20 (a), as an example. The chemical composition of the different phases will be discussed in the following paragraph, concerning SEM and EDS observations. The observations concerning as-cast optical microstructures are in agreement with the observation of Shen [6] and Wang *et al.* [17] on AA 2618 and on an Al-Cu-Mg-Fe-Ni alloy, respectively.

In high magnification optical micrographs of Zr- and V-modified alloy, it was possible to observe the presence of fine, elongated particles dispersed in the matrix next to the secondary phases at the grain boundaries. An example of these particles is given in Figure 3.34 (d) and (e), which show enlargements of the areas highlighted by the red rectangles in Figure 3.34 (c). It was not possible to observe these particles in the as-cast optical microstructure of the other two alloys, but unexpectedly they were not even observed in the SEM micrographs of as-cast Zr- and V-modified alloy. Therefore, it is not possible to certainly identify the nature of these particle, but due to their shape and size, they could be S-phase particles (Al_2CuMg), like the dispersed phase detected in AA 2618 overaged samples (§3.1.7).

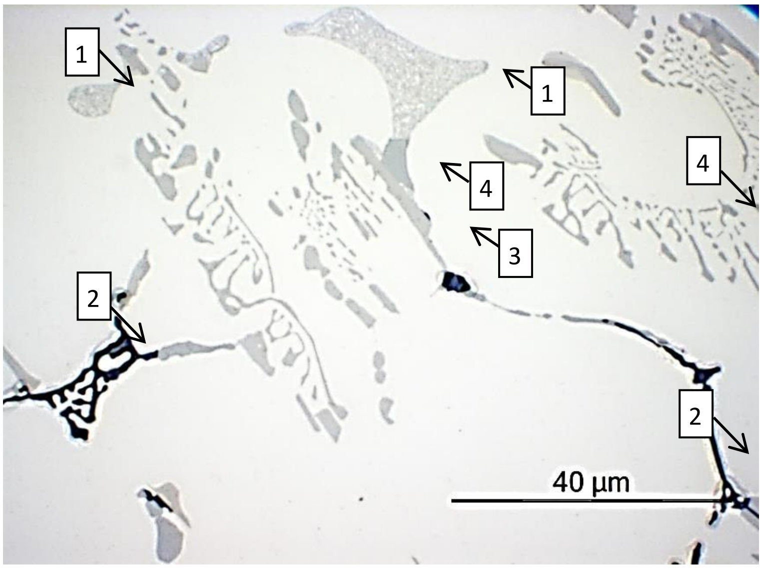

(a)

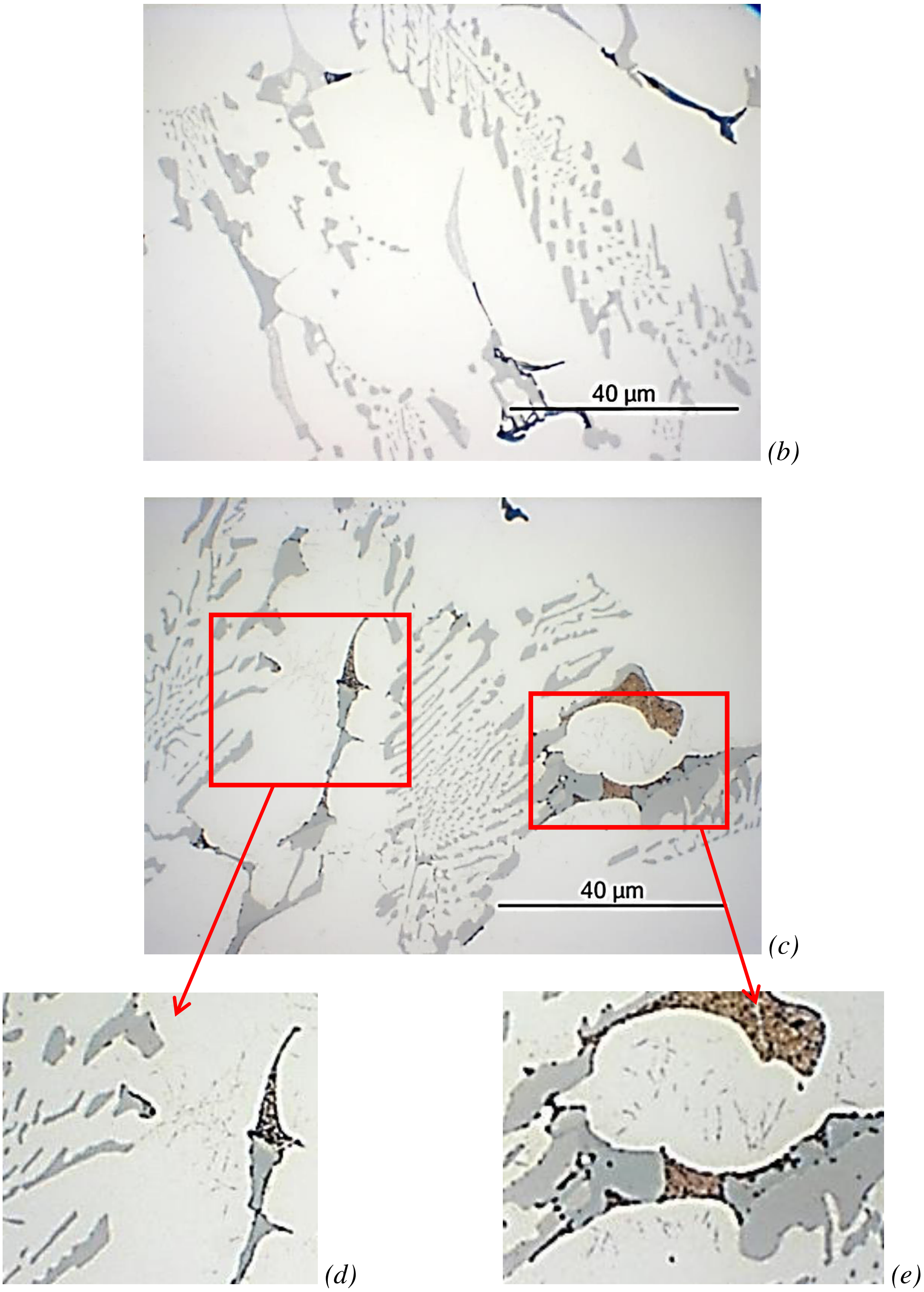

Fig. 3.34 – Optical micrographs at 100x magnification: AA 2618 (a), Zr-modified AA 2618 (b), Zr- and V-modified AA 2618 (c), enlargement of areas in the red rectangles, which show a fine phase dispersed in the matrix (d) and (e). In Figure 3.20 (a) the different types of phases detected are indicated: lamellar eutectic structure (1), needle-like black phase (2), light grey phase (3) and dark grey feather-like, lath-like or irregular phases(4). OP-S polished and not-etched samples.

Secondary dendrite arms spacing (SDAS) was measured on as-cast samples extracted from the material cast in the rectangular mould; the results are reported in Table 3.11. The SDAS average value is about 30 µm, and no relevant differences in this value are detected between the different alloy compositions. Thus was expected, since SDAS value mainly depends on cooling rate during solidification and should be little affect by slight chemical modification. The resulting value is typical for die cast aluminium alloys, proving that the copper mould can provide a quite high cooling rate during solidification, that should prevent primary precipitation of Zr-containing phase.

	SDAS [µm]		
	2618	**2618 + Zr**	**2618 + Zr + V**
Average	*28*	*28*	*33*
SD	4.2	5.2	4.7

Tab. 3.11 – Results of SDAS measurement on as-cast sample of the three different alloys; average value and standard deviations are reported.

Deformed microstructure

Figure 3.36 pictures the optical microstructure at low magnification (5x) of samples of the three alloys deformed to 50% of initial thickness, along the longitudinal and transverse directions. Since the changes in the microstructure due to deformation are not very significant, the microstructures obtained after 16% and 33% reductions are not reported.

Despite the substantial deformation carried out at high temperature (400 °C), the microstructures in Figure 3.35 do not show noticeable signs of hot deformation, such as a strong directionality in the microstructure, or the alignment of intermetallic phases with the plastic flow. On the contrary, it is still possible to recognize a dendritic microstructure with intermetallic phases located in the interdendric region. Moreover, α-Al dendrites do not appear heavily deformed. These features, as said before, are not typical of hot deformation, despite the material was hot rolled at 400 °C.

It is possible that the holding time at high temperature before rolling (30 min) and especially between two consecutive steps (3 min) was not long enough to heat up the sample to the desired temperature. Another hot rolling, described in §3.2.11, was carried out in order to study the effect of longer times at high temperature on deformed microstructure. However, it must be remembered that during hot rolling, the rolls were at room temperature, and since they are much larger than the samples are, it is possible that the samples cool down extremely rapidly when in contact with the rolls.

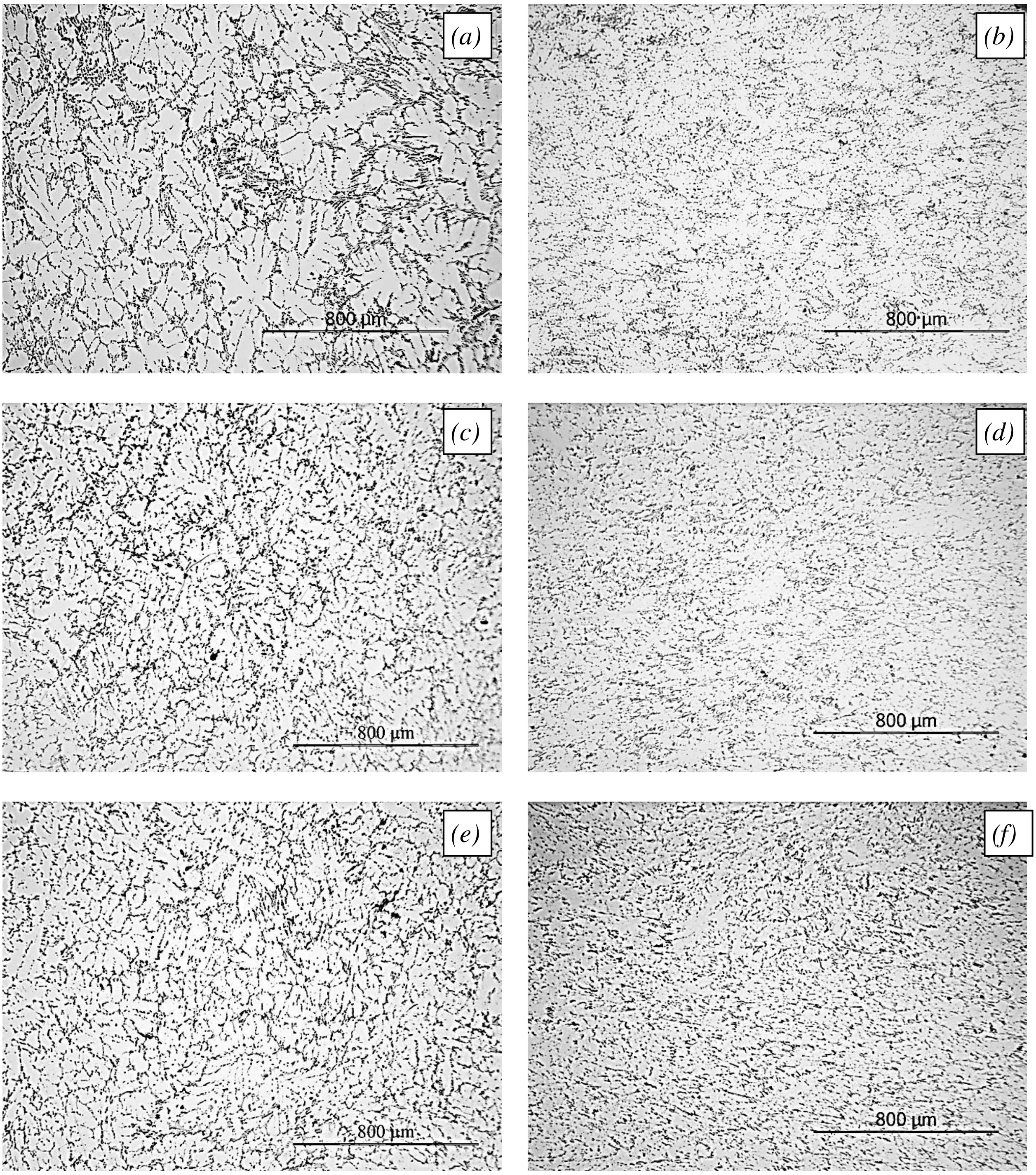

Fig. 3.35 – Optical micrographs at low magnification (5x) of samples hot-rolled to 50% of the initial thickness: AA 2618 along the longitudinal (a) and transverse (b) direction, Zr-modified alloy along the longitudinal (c) and transverse (d) direction, Zr- and V-modified alloy along the longitudinal (e) and transverse (f) direction. OP-S polished and not etched samples.

Higher magnification (20x) optical micrographs of 50% deformed samples, taken along the longitudinal direction, are shown in Figure 3.22. Once again, these micrographs show that there is not a strong directionality in the microstructure. Moreover, the intermetallic phases at the grain boundaries appear to be finer distributed in the modified alloys than in the base AA 2618: in fact, in Figure 3.36 (a) the intermetallics seem to form coarser clusters at the grain boundaries than in Figure 3.36 (b) and (c).

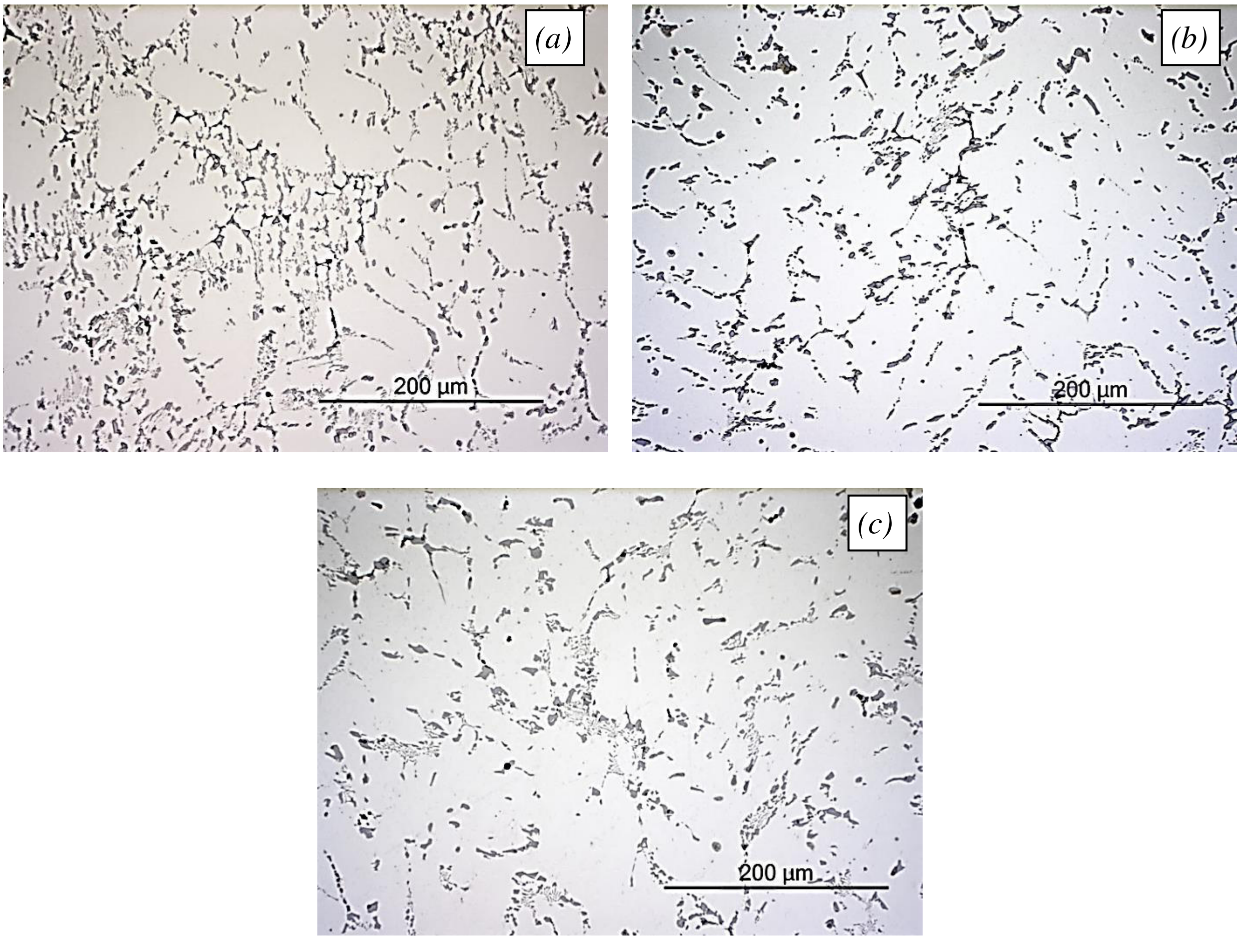

Fig. 3.36 – Optical micrographs at higher magnification (20x) of samples hot-rolled to 50% of the initial thickness, along the longitudinal direction: AA 2618 (a), Zr-modified alloy(b), Zr- and V-modified alloy (c). OP-S polished and not etched samples.

Secondary dendrite arms spacing (SDAS) was measured on the as-cast and deformed samples of the three alloys, to verify if deformation can affect dendrites dimensions. The results are displayed in Table 3.12 and Figure 3.37. The average values range between 27 µm and 35 µm, with standard deviations between 4 µm and 7 µm. Thus, the differences in the average values are not significant if compared with standard deviations, and it is not possible to identify a trend of SDAS value with deformation or chemical composition. This is confirmed by the graph in Figure 3.37, which clearly shows that standard deviation (represented by the black bars) is quite high compared to SDAS variations. In conclusion, SDAS is not affected by chemical composition or hot deformation.

		SDAS [µm]		
		2618	**2618+Zr**	**2618+Zr+V**
AC	Average	*28*	*28*	*33*
	SD	4	5	5
16%	Average	*29*	*30*	*28*
	SD	5	7	6
33%	Average	*31*	*28*	*27*
	SD	6	5	4
50%	Average	*35*	*32*	*27*
	SD	6	6	6

Tab. 3.12 – Average values and standard deviations of SDAS for the three alloys, in as-cast and different deformed conditions.

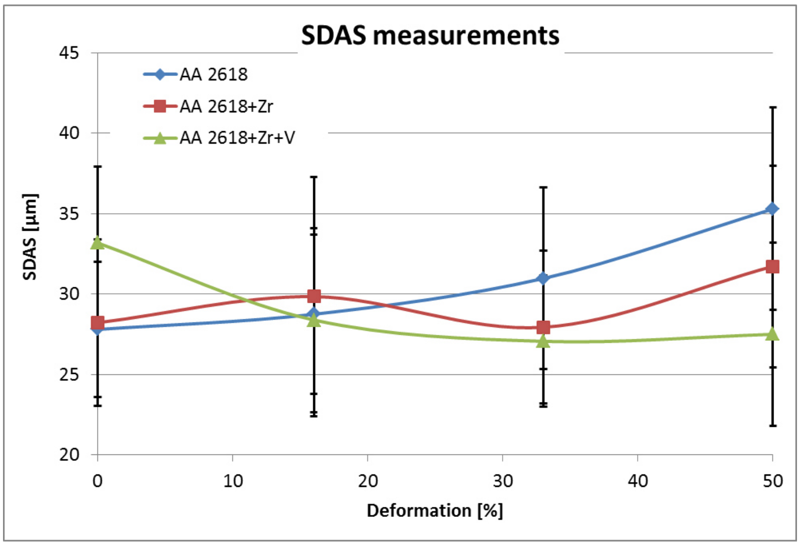

Fig. 3.37 – SDAS-deformation graph for the three alloys; the black bars represent standard deviation.

3.2.6 Electron microscopy

As-cast microstructure

Figure 3.38 shows FEG-SEM micrographs of as-cast samples of the three alloys, at high magnification (2000x and 5000x). It is not possible to recognize peculiar characteristics of the three different alloys: the microstructure does not appear to be modified by the addition of Zr or Zr and V in such small amounts. In particular, it was not possible to detect primary precipitates containing Zr and/or V, that were expected given the nominal composition of the modified alloys. However, taking into account the chemical analyses results (§3.2.1), which show that Zr and V amounts are significantly lower than expected, and SDAS measurements (§3.2.5), which indicate that the cooling rate during solidification was quite high, it seems coherent that primary precipitation was avoided during solidification, and therefore non detected with FEG-SEM. This is an interesting point, since primary precipitation is deleterious for mechanical properties, since it consumes elements (Zr and V in the present case), that should form fine precipitates during heat treatment.

In the FEG-SEM micrographs it is possible to discern different phases, that appear to be complexly overlapping and interconnected. On colour and shape basis, it is easy to discern 4 phase, as in the optical micrographs (§3.2.5), but the ESD analysis presented below indicates that at least 6 phases with different chemical compositions are present.

From micrographs at lower magnification (2000x), pictured in Figure 3.38 (a), (c) and (e), it is possible to see that intermetallic phases are heterogeneously distributed and present quite complex shapes, such as the one reported in Figure 3.38 (e). The matrix results featureless, without dispersed phases, and also increasing the magnification to 5000x (Figure 3.38 (b), (d) and (f)), it is not possible to clearly distinguish dispersed phases in the matrix.

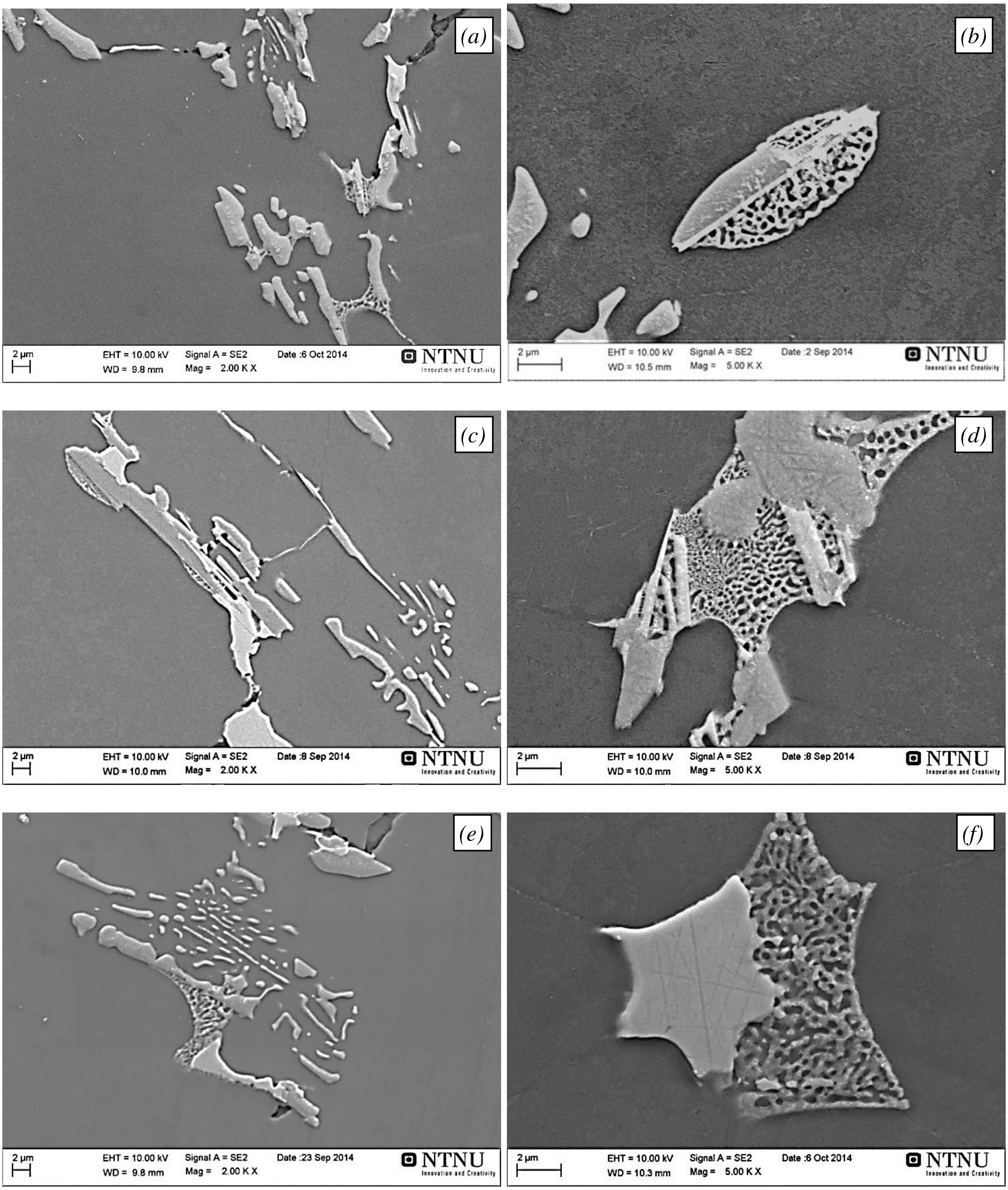

Fig. 3.38 – FEG-SEM micrographs at high magnification of as-cast samples: AA 2618 at 2000x (a) and 5000x(b), Zr-modified alloy at 2000x (c) and 5000x (d), Zr- and V-modified alloy at 2000x (e) and 5000x (f). Samples were OP-S polished and not etched.

Typical casting defects were recognized in the as-cast microstructure, such as interdendritic shrinkage and gas porosity, as shown in Figure 3.39 (a) and (b), respectively.

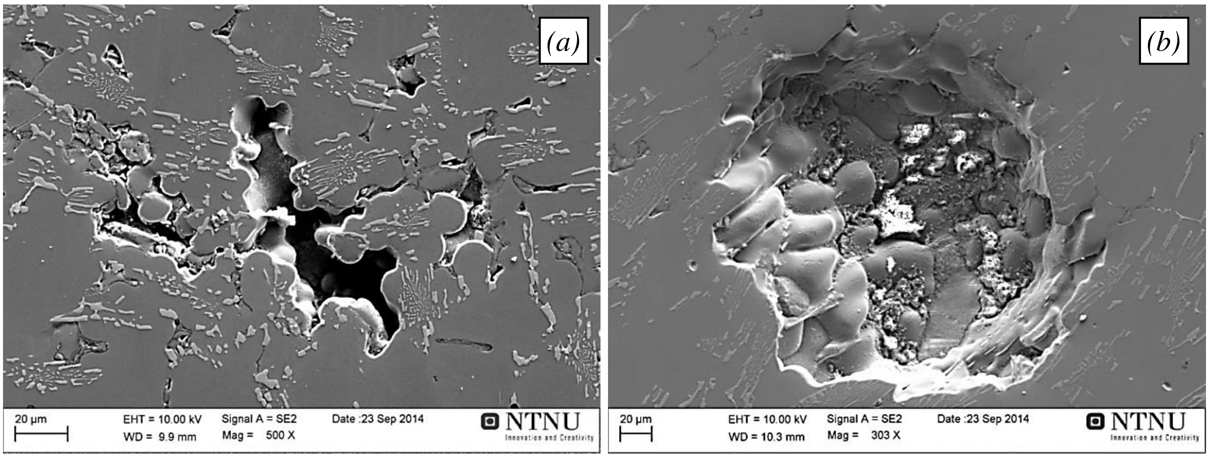

Fig. 3.39 – Example of interdendritic shrinkage (a) and gas porosity (b) in as-cast samples.

<u>*Deformed microstructure*</u>

Figure 3.40, 3.41 and 3.42 picture high magnification (5000x) FEG-SEM micrographs of samples from the three alloys deformed to thickness reductions of 16%, 33% and 50%, respectively. As it will be explain more extensively below, no appreciable differences were detected in the chemical composition, distribution and shape of intermetallic and eutectic phases as a result of hot rolling. Both microstructures along longitudinal and transverse direction were studied, but since no significant differences were detected, just micrographs taken along the longitudinal direction are reported here.

Even if chemical composition and distribution of intermetallic and eutectic phases are unaffected by hot rolling, there are two main modifications that take place in the microstructure during deformation. The first, is the apparition of dispersed phases in the matrix. These phases, visible just at high magnification (5000x) with an electron microscope, result light in colour and elongated in shape. They are definitely too tiny to attempt an EDS analysis, so it was not possible to determine their chemical composition. However, they are similar for size, shape and colour to the phases detected in overaged AA 2618 samples (§ 3.1.7); therefore, on the basis of what explained in §3.1.7, it is likely that this is S-phase (Al_2CuMg), which precipitates or coarsen due to hot deformation.

The second modification that is worth noticing, is that large intermetallic phases crack, as the deformation becomes heavier; this is probably due to the fact that these intermetallics are brittle and cannot sustain the same amount of plastic deformation as the matrix does. This phenomenon is more evident as the deformation increases, in particular when 50% of thickness reduction is reached. The red arrows in figure 3.42 highlight some of these cracks.

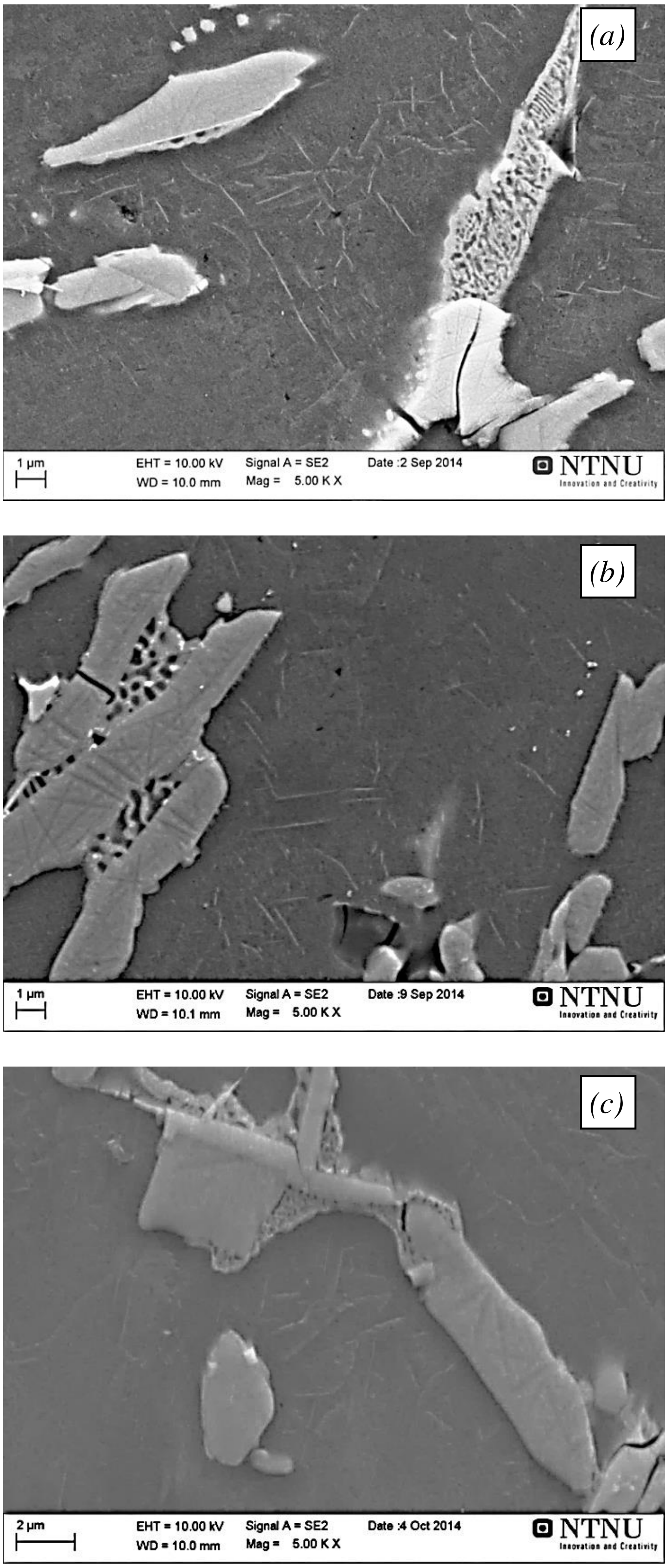

Fig. 3.40 – FEG-SEM micrographs at high magnification (5000x) of samples hot rolled to 16% thickness reduction taken along the longitudinal direction: AA 2618 (a), Zr-modified alloy (b), Zr- and V- modified alloy (c). Samples were OP-S polished and not etched.

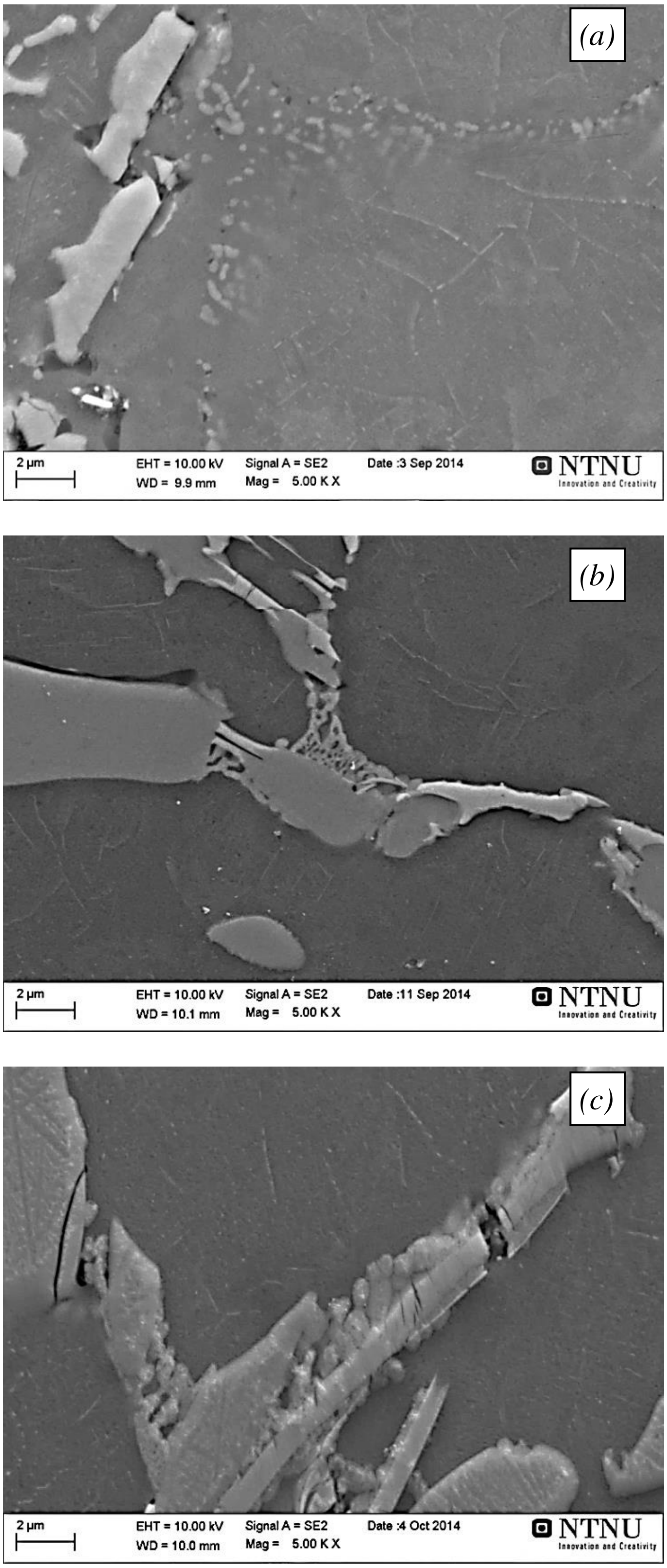

Fig. 3.41 – FEG-SEM micrographs at high magnification (5000x) of samples hot rolled to 33% thickness reduction taken along the longitudinal direction: AA 2618 (a), Zr-modified alloy (b), Zr- and V- modified alloy (c). Samples were OP-S polished and not etched.

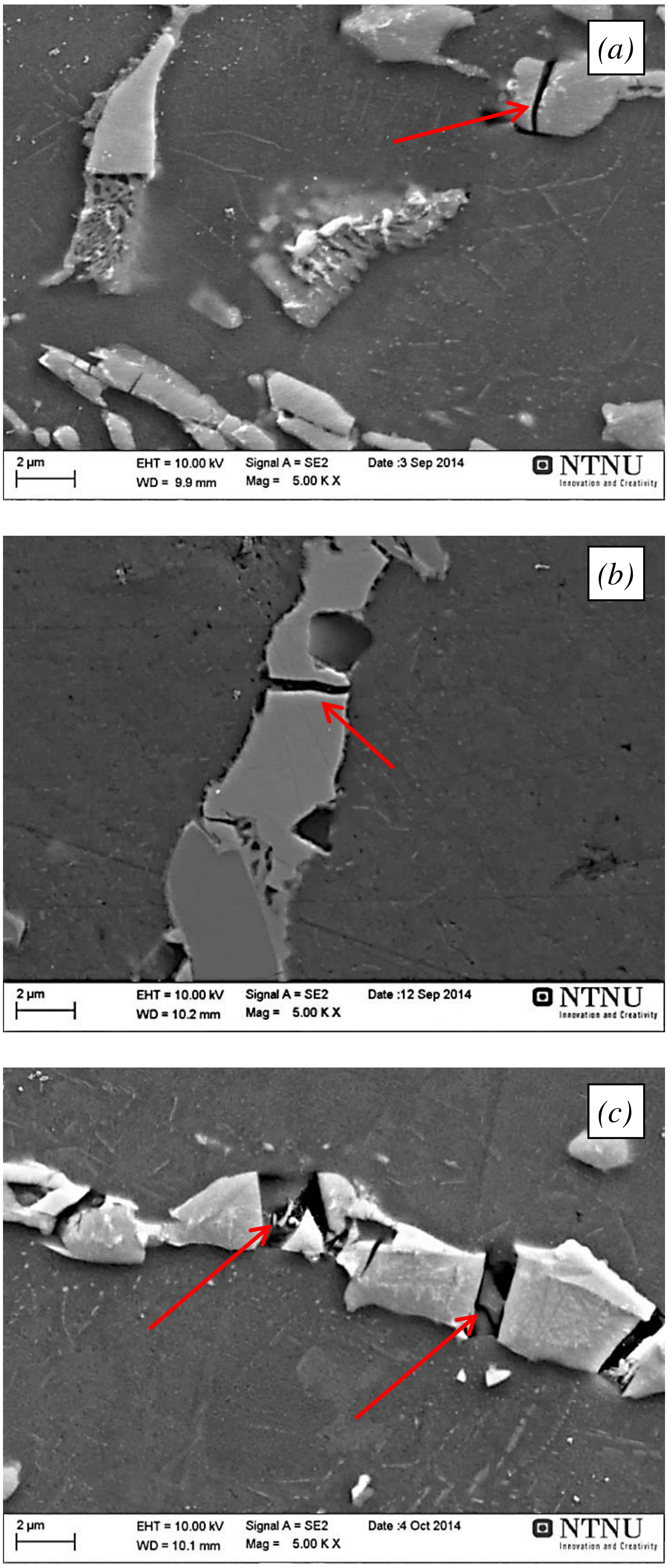

Fig. 3.42 – FEG-SEM micrographs at high magnification (5000x) of samples hot rolled to 50% thickness reduction taken along the longitudinal direction: AA 2618 (a), Zr-modified alloy (b), Zr- and V- modified alloy (c). The red arrows point cracks in large intermetallics, due to deformation process. Samples were OP-S polished and not etched.

EDS

Energy dispersion spectrometry (EDS) point analyses were carried out on many particles in order to find out which phases are present. As said before, with both optical and electron microscope it was possible to distinguish 4 different phases, but EDS analyses showed that the number of different phases was higher. On the basis of EDS results, and of what reported by Elgallad *et al.* [4], Shen *et al.* [5] and Wang e*t al.* [14, 16], it was possible to identify 6 different phase, listed in Table 3.13. For each phase, colour or shape are reported, together with its average chemical composition (at.%) as identified with EDS, and the suggested formula.

Three phases are very easy to identify: Al_9FeNi appears grey; it's the most abundant phase present in the examined alloys and can occur in a feather-like, lath-like or irregular shape. Its composition, measured with EDS, results in quite good agreement with the commonly accepted formula. Mg_2Si, on the other hand, appears dark grey, almost black, with a needle-like shape, and is present with a low volume fraction. It was not possible to measure its composition with EDS, since much Si oxide was present, probably due to OP-S polishing. The third phase is Al_2CuMg, which results light-coloured and lamellar. From EDS analysis, it appear to contain also a small amount of Ni and Fe.

Other three phases were identified, but they are hard to recognize since all of them appear very light in colour, with an irregular or lath-like shape. The most abundant of these three phases is Al_7Cu_4Ni; very small amounts of $Al_7Cu_2(Fe,Ni)$ and Al_2Cu were also detected. As it can be seen in Table 3.13, the compositions measured with EDS for these phases do not correspond exactly to the proposed formulae: in particular, Al_7Cu_4Ni and $Al_7Cu_2(Fe,Ni)$ appear to contain also a certain amount of Mg, and Al_2Cu appears to contain significant amounts of Mg and Ni. However, EDS is not a very precise technique, and the obtained results can be influenced by the matrix or by near phases, particularly if the examined phase is small.

It is worth noticing that the presence of the two phases highlighted by the red circle in Table 2.13 (Al_2Cu and Al_2CuMg), is deleterious since Cu and Mg are supposed to form very fine precipitates during heat treatment. Therefore, solutionizing is necessary to dissolve them, in order to obtain suitable properties after heat treatment. Also Al_7Cu_4Ni and $Al_7Cu_2(Fe,Ni)$ are not desirable, since they consume Cu, but Özbek [18] showed that these phases can be only partially dissolved with solution treatment. It would be better to avid the formation of these intermetallics during solidification; however, these phases are present in very small amount in the analysed alloys.

Figure 3.43 shows representative examples of EDS spectra for the matrix and the 6 phases listed in Table 3.13.

Phase	Elements [at %]					Suggested formula
	Al	Cu	Mg	Fe	Ni	
-	97.2	0.6	2.1	-	-	**Matrix**
Grey	85.1	-	-	7.6	7.3	**Al_9FeNi**
Dark grey	Presence of oxide. Imposible to determine.					**Mg_2Si**
Light grey	67.0	26.4	1.3	0.6	5.6	**Al_7Cu_4Ni**
Light grey	74.6	15.8	2.1	4.1	3.7	**$Al_7Cu_2(Fe,Ni)$**
White	70.1	21.2	4.1	0.7	4.0	**Al_2Cu**
Lamellar	70.0	15.5	13.5	0.3	0.9	**Al_2CuMg**

Tab. 3.13 – EDS results: average compositions (at. %) of the matrix and the phases detected in as-cast and deformed alloys, and the corresponding suggested formulae. The phases highlighted by the red circle should be dissolved with solution treatment.

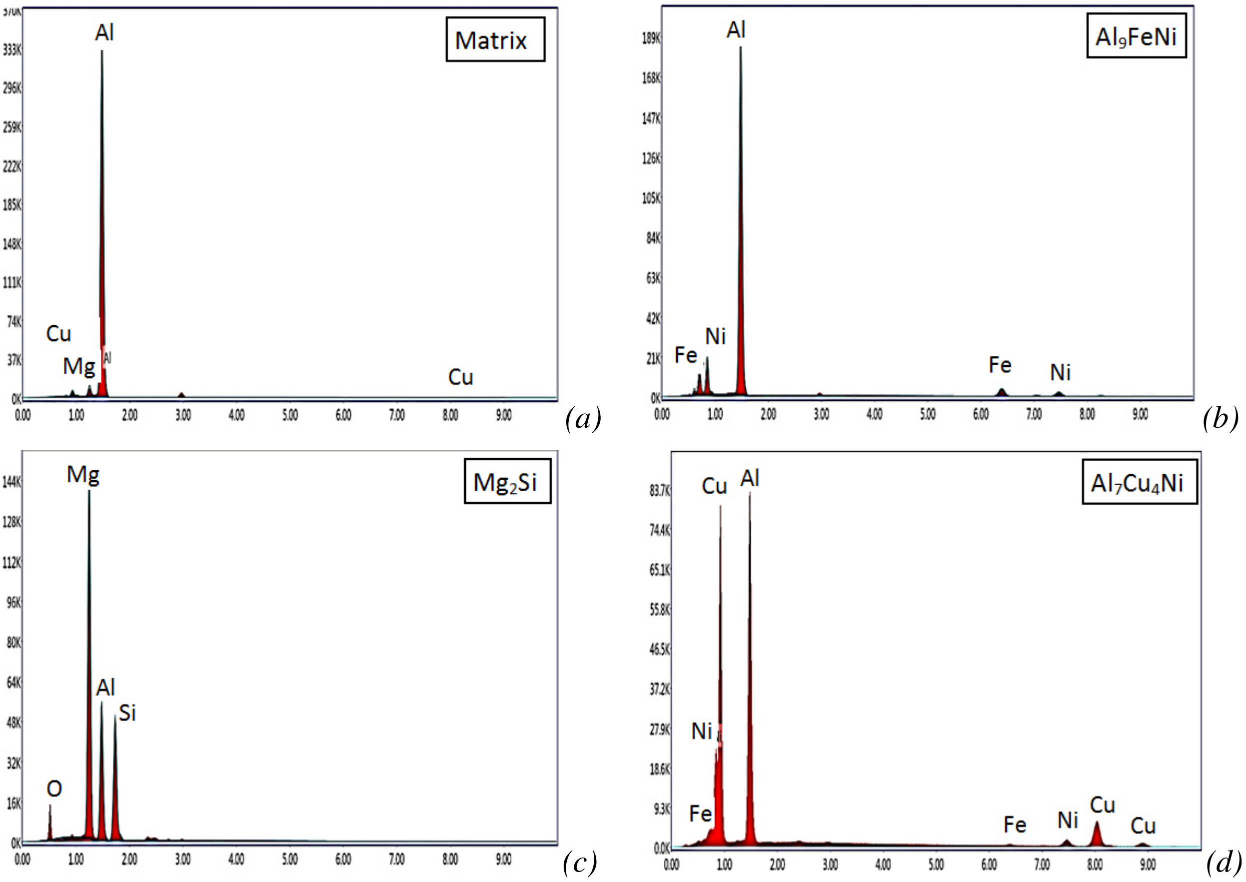

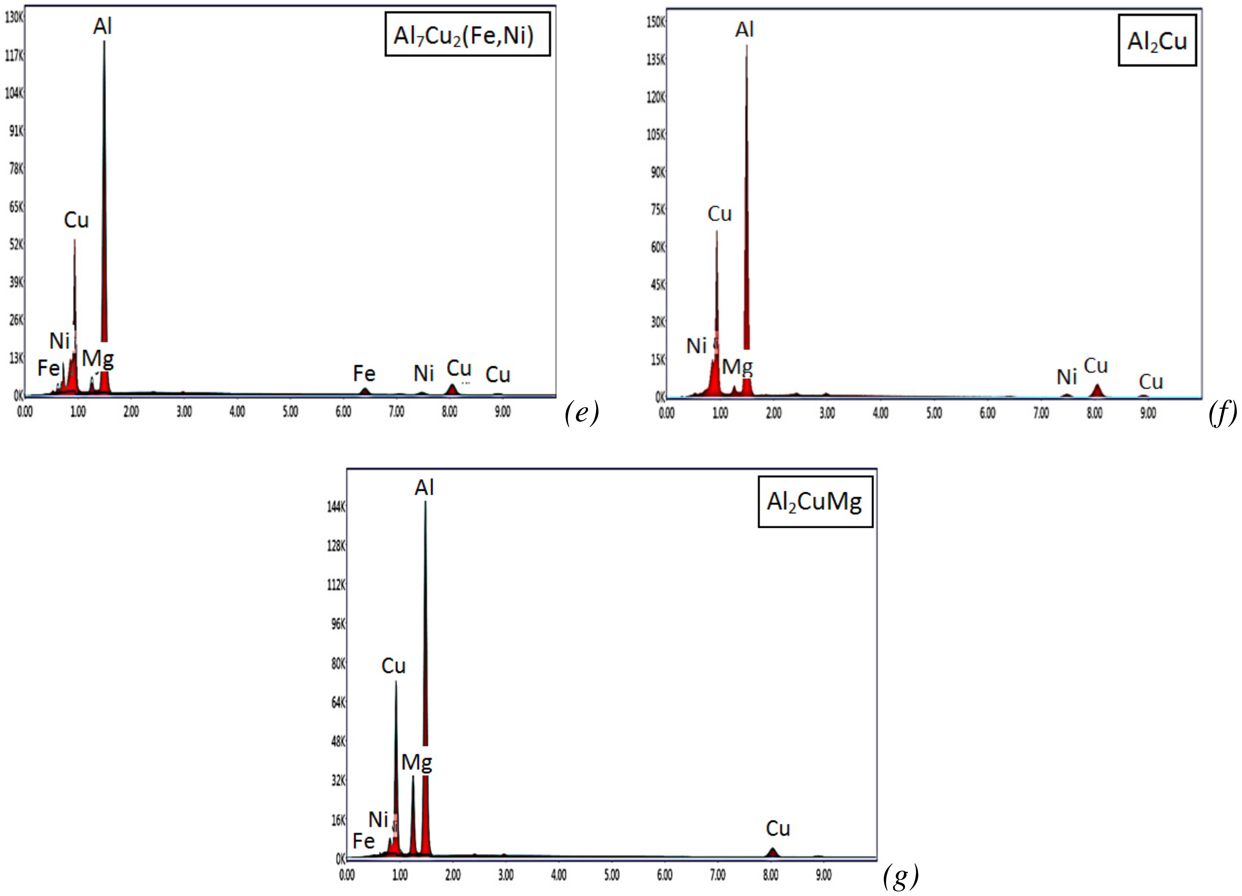

(e) (f) (g)

Fig. 3.43 – Representative EDS spectra of the matrix and the 6 phases detected and listed in Table 3.13: EDS spectrum of matrix (a), light grey phase Al_9FeNi (b), black phase Mg_2Si (c), light phases Al_7Cu_4Ni (d), $Al_7Cu_2(Fe,Ni)$ (e), Al_2Cu (f), lamellar phase Al_2CuMg (g).

No differences were detected in chemical composition or shape of detected phases, due to different chemical composition of the alloys or plastic deformation at high temperature (400 °C). It is likely that Zr and V remain in solid solution or form very fine precipitates, since no phases containing these elements were found, not even in the modified alloys. However, the micrographs in Figure 3.17, related to the base AA 2618 alloy hot extruded, hot forged, heat-treated and degraded, show a completely different microstructure, characterized by rounded intermetallics. That means that hot deformation processes and/or solution treatment have an effect on the shape of insoluble intermetallics. The effect of solution treatment on fragmentation and spheroidization of insoluble phases is confirmed by Elgallad *et al.* [4].

In Figure 3.44 are given some examples of the different types of phases that were detected, highlighted by arrows and identified by tags. Since, as said before, no differences in the phases were found due to chemical composition or deformation degree, a series of representative micrographs was chosen, taken from different alloys and deformation conditions.

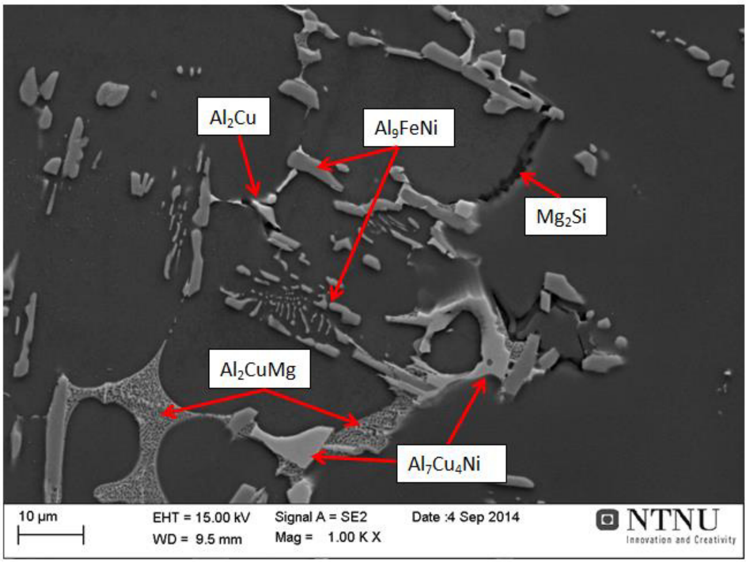
Al_2Cu
Al_9FeNi
Mg_2Si
Al_2CuMg
Al_7Cu_4Ni
10 µm
EHT = 15.00 kV
WD = 9.5 mm
Signal A = SE2
Mag = 1.00 K X
Date :4 Sep 2014
NTNU
Innovation and Creativity

(a)

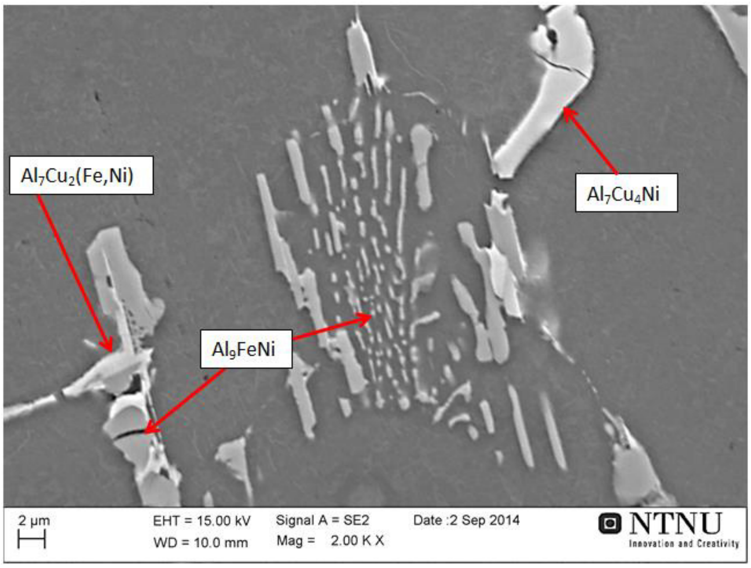
$Al_7Cu_2(Fe,Ni)$
Al_7Cu_4Ni
Al_9FeNi
2 µm
EHT = 15.00 kV
WD = 10.0 mm
Signal A = SE2
Mag = 2.00 K X
Date :2 Sep 2014
NTNU
Innovation and Creativity

(b)

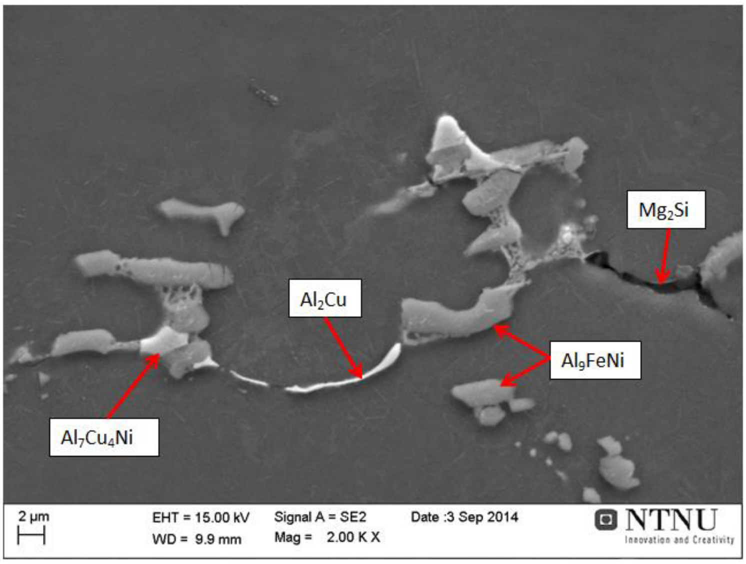
Mg_2Si
Al_2Cu
Al_9FeNi
Al_7Cu_4Ni
2 µm
EHT = 15.00 kV
WD = 9.9 mm
Signal A = SE2
Mag = 2.00 K X
Date :3 Sep 2014
NTNU
Innovation and Creativity

(c)

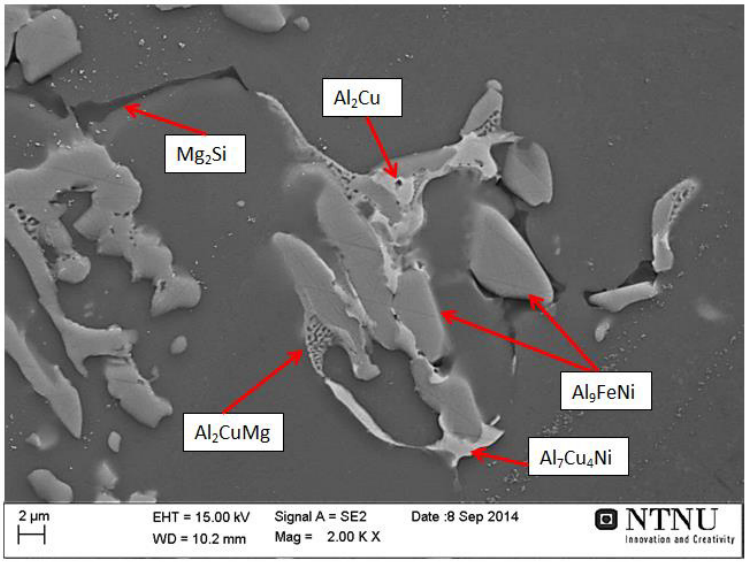
Al2Cu
Mg2Si
Al9FeNi
Al2CuMg
Al7Cu4Ni
2 µm
EHT = 15.00 kV
WD = 10.2 mm
Signal A = SE2
Mag = 2.00 K X
Date :8 Sep 2014
NTNU
Innovation and Creativity

(d)

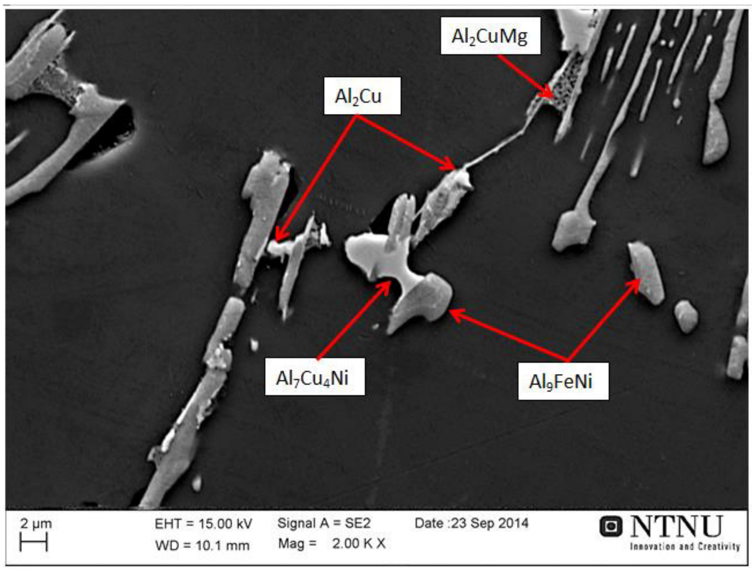
Al2CuMg
Al2Cu
Al7Cu4Ni
Al9FeNi
2 µm
EHT = 15.00 kV
WD = 10.1 mm
Signal A = SE2
Mag = 2.00 K X
Date :23 Sep 2014
NTNU
Innovation and Creativity

(e)

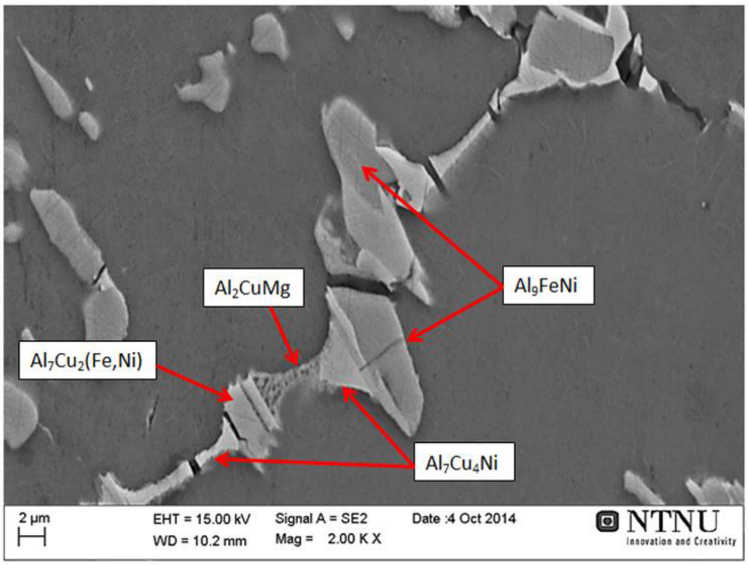
Al9FeNi
Al2CuMg
Al7Cu2(Fe,Ni)
Al7Cu4Ni
2 µm
EHT = 15.00 kV
WD = 10.2 mm
Signal A = SE2
Mag = 2.00 K X
Date :4 Oct 2014
NTNU
Innovation and Creativity

(f)

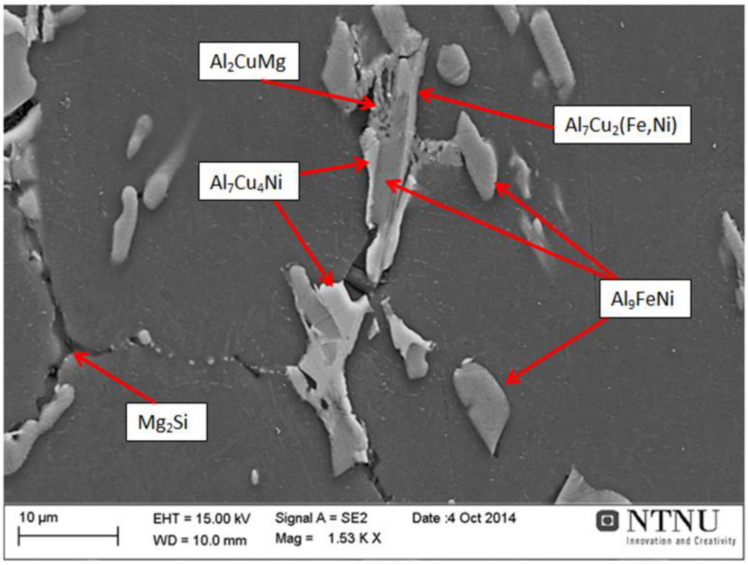

(g)

Fig 3.44 – FEG-SEM micrographs showing the typical features of the 6 phases detected with EDS analysis: AA 2618 as-cast at 1000x (a), AA 2618 with 16% deformation degree at 2000x (b), AA 2618 with 33% deformation degree at 2000x (c), Zr-modified alloy as-cast at 2000x (d), Zr- and V-modified alloy as-cast at 2000x (e), Zr- and V-modified alloy with 16% deformation degree at 2000x (f), Zr- and V-modified alloy with 33% deformation degree at 2000x (g).

3.2.7 Fracture surfaces

The surfaces of fractures caused by hot rolling were observed with FEG-SEM microscope. EDS point analyses were also carried out, in order to find out if fractures had propagated from Zr- and/or V-containing particles. However, EDS analyses did not give interesting results: no Zr- or V-containing particles were detected, but only the phases described at paragraph 3.2.6 and some oxidized particles were found. FEG-SEM micrographs of fracture surfaces in a sample of Zr-modified and Zr- and V-modified alloys are pictured in Figure 3.45 and 3.46, respectively. The analysed samples were hot rolled to 50% of thickness reduction.

Micrographs in Figure 3.45 and 3.46 do not show typical features of ductile fractures. In fact, ductile fractures are characterised by appreciable plastic deformation, and by the formation of dimples due to microvoid coalescence [19]. On the contrary, fracture surfaces represented in Figure 3.45 and 3.46 do not present evident sings of plastic deformation, and they result faceted instead of presenting dimples. On a macroscopic level, the surfaces have a bright, granular appearance and exhibit no necking. In literature [19], these features are reported to be characteristic of intergranular brittle fracture, also referred to as grain-boundary separation or decohesive rupture. Literature [19] also reports that this type of fracture is promoted by the synergistic effect of environmental conditions and sustained stresses. In the present case, the appearance of brittle intergranular fracture could have been promoted by the presence of a large volume fraction of intermetallic phases at the grain boundaries which make the material brittle, as reported in §3.2.5 and §3.2.6. It is likely that applying an heat treatment such as homogeneization or solutionizing, that can dissolve part of these intermetallics, before hot rolling, has some benefits on the deformation behaviour.

Another factor that has an effect on the type of fracture are external loading conditions: since the samples are quite thick, it is possible that a triaxial state of stresses occurred, promoting a brittle fracture.

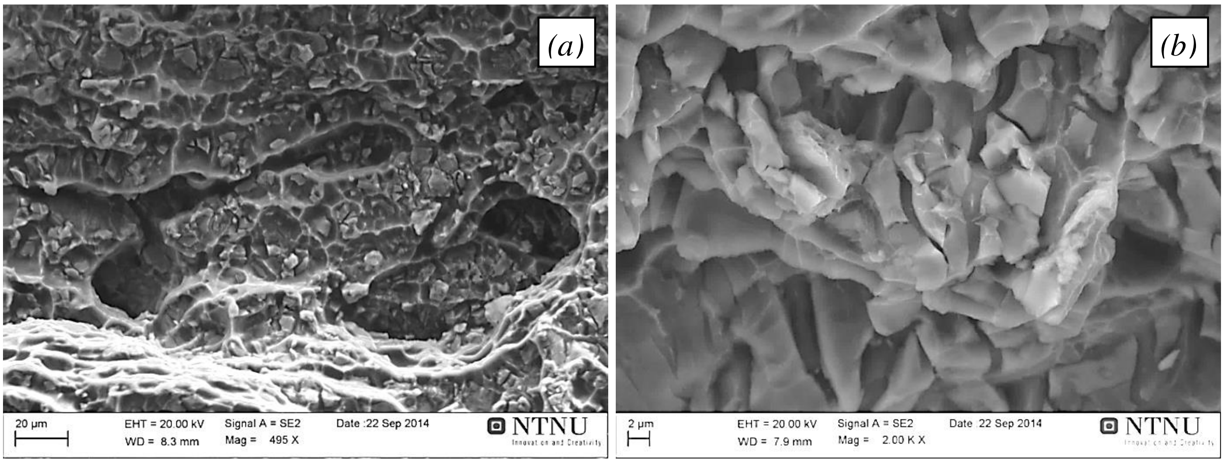

Fig. 3.45 – FEG-SEM micrographs of the fracture surface due to hot rolling in a sample of Zr-modified alloy deformed to 50% thickness reduction at magnification of 500x (a) and 2000x (b). The surface shows the features typical of a brittle intergranular fracture.

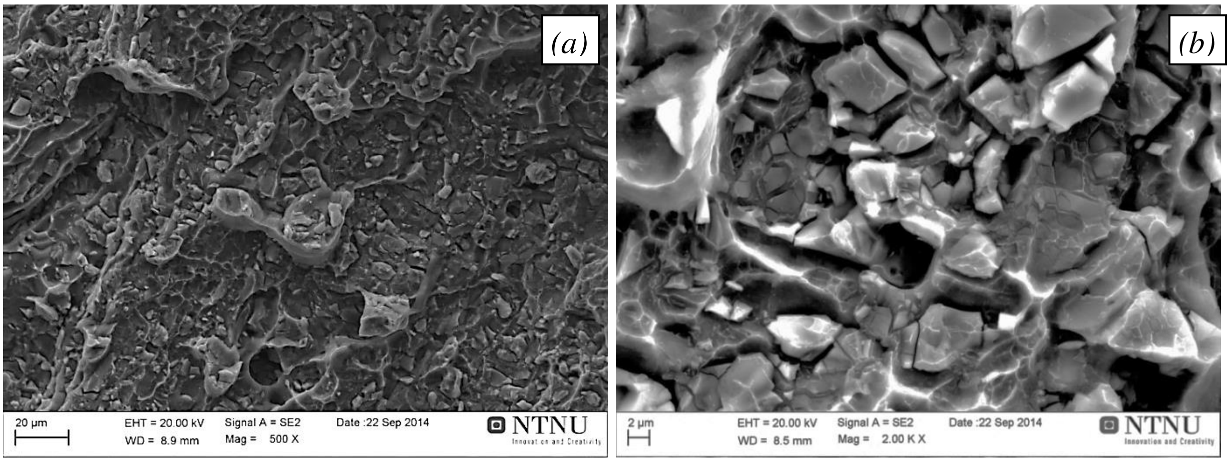

Fig. 3.46 – FEG-SEM micrographs of the fracture surface due to hot rolling in a sample of Zr- and V-modified alloy deformed to 50% thickness reduction at magnification of 500x (a) and 2000x (b). The surface shows the features typical of a brittle intergranular fracture.

It’s worth noticing that the occurring of a brittle fracture could be another sign that the samples were not at high temperature (400 °C) during deformation, since high temperatures usually promote a ductile behaviour.

3.2.8 Electron Probe Micro-Analysis (EPMA)

Since no Zr-containing phases had been found, it’s likely that Zr remains in solid solution instead of forming primary precipitates. From literature [20] it is known that Zr tends to be not uniformly distributed along grains and dendrites. This is particularly undesired because the not uniform distribution of Zr will be reflected in the distribution of Zr-containing precipitates after heat treatment, with a negative effect on mechanical properties. In order to verify the distribution of Zr in the as-cast material, three EPMA (electron probe micro-analysis) line scans across secondary dendrite arms were carried out on the Z-modified alloy. A representative quantitative result is shown in Figure 3.47: the graph plots the mass percentage of Zr against the distance taken on the red line drawn on the micrograph (from point 1 to point 90). It can be seen that Zr tends segregates at the cores of dendrite arms, and the lowest concentration of Zr is found at the dendrite boundaries. The fluctuations in Zr level across the analysed region reflect the underlying dendritic structure. Peaks correspond to measurements made close to the centres of the dendrite arms: these regions solidified first during casting and are thus enriched in Zr, while very low zirconium levels are present near the grain boundaries and interdendritic regions. The same result was found by Robson and Prangnell [20], who explained that Zr tends to segregate in the opposite direction to the major alloying elements, as expected from a consideration of the peritectic Al–Zr phase diagram.

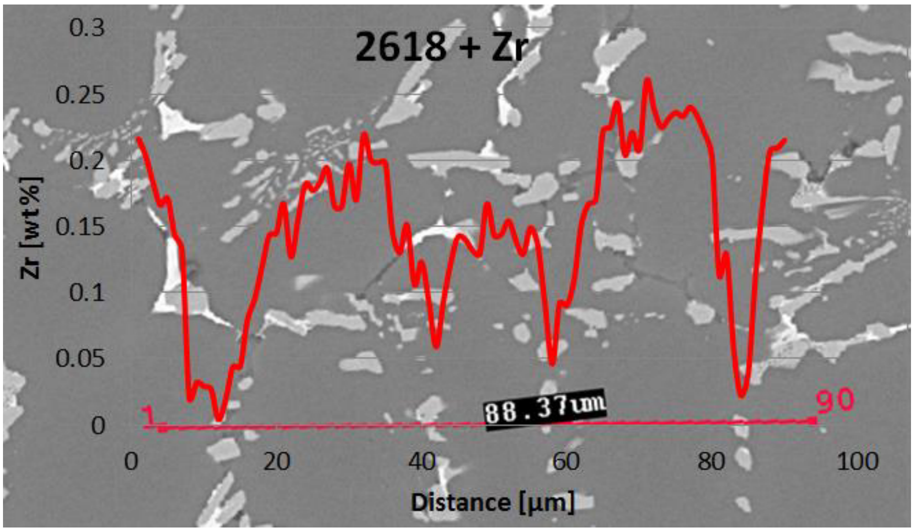

Fig. 3.47 – Typical EPMA result, showing fluctuation in Zr mass concentration (wt. %) along the red line drawn on the micrograph.

Taking into consideration quantitative measurements, EMPA shows that Zr concentration peaks, measured close to the centre of secondary dendrite arms, range from 0.2 to 0.3 wt. %, while the average value of Zr concentration in around 0.18 wt %. Once again, this measure confirms that Zr level is lower than expected, since the target Zr concentration for the modified alloy was set to 0.25 wt. %. However, EPMA analysis shows that there are significative fluctuations in Zr level around the detected average value of 0.18 wt. %: in fact, Zr level was measured to range from 0.004 wt. % to 0.31 wt. % along the considered lines.

3.2.9 Brinell hardness and Vickers micro-hardness

Brinell hardness (HB10) tests were carried out on samples of the three alloys, with different deformation conditions, on surfaces along rolling longitudinal direction. The result are reported in Table 3.14 and illustrated in Figure 3.48. The graph in Figure 3.48 shows the average Brinell hardness values for the three alloy compositions against the level of deformation, ranging from 0 (as-cast) to 50%, while the black bars represent the standard deviations from the average values. Looking at the graph, it easy to see that hardness decreases when hot rolling is applied, but its variation with the deformation level is uncertain. However, Brinell hardness in all deformed conditions is certainly lower than in as-cast condition. Taking into account the results shown in §3.2.6, the decrease in hardness after hot rolling can be explained with the coarsening of the dispersed phase detected in the matrix, identified as S-phase (Al_2CuMg). As in the case of overaged AA 2618, discussed in paragraph 3.1.7, it is likely that coarsening of S-phase is responsible for a loss in mechanical properties. This loss is less pronounced than in the case of overaging discussed before, because in the as-cast samples S-phase was quite coarse compared to peak aging condition.

In deformed condition, harness of not modified alloy seems slightly lower than that of the modified alloys, but comparing hardness variations to standard deviations it is difficult to draw some conclusions.

Brinell hardness test HB10						
Condition	**AA 2618**		**AA 2618 + Zr**		**AA 2618 + Zr + V**	
	Average HB10	**SD**	**Average HB10**	**SD**	**Average HB10**	**SD**
AC	*87*	1.3	*89*	2.0	*85*	2.7
16%	*72*	1.6	*74*	2.1	*74*	5.0
33%	*72*	1.1	*77*	1.1	*75*	1.5
50%	*70*	0.8	*70*	0.9	*77*	3.3

Tab. 3.14 – Average values and standard deviations of Brinell hardness HB10 tests on samples of the three alloys in different deformation conditions (as-cast and deformed to 16%, 33% and 50% of initial thickness), on rolling longitudinal direction.

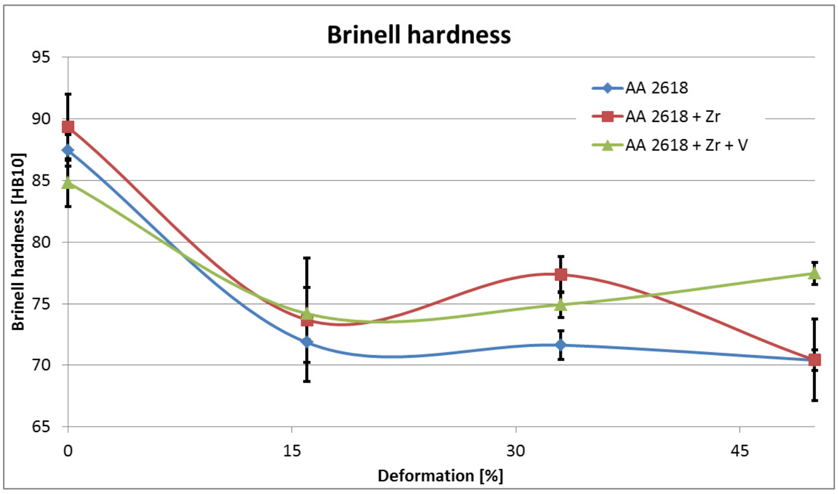

Fig. 3.48 – Brinell hardness HB10 average values (reported in Table 3.14) against deformation condition (0 corresponding to as-cast). Black bars show standard deviation.

Since it has been verified that Zr and V do not form precipitates, and therefore they probably are in solid solution, Vickers microhardness tests were carried out in order to verify if Zr and V can affect matrix hardness. The microhardness tests were carried out on the α-Al matrix, trying to avoid that the indentation concerned other phases. A load of 15 g was chosen because it was the bigger load that produce an indentation small enough to not exceed α-Al phase dimensions. The results are shown in Table 3.15, which reports both average values and standard deviations of microhardness measurements. The same results are illustrated in Figure 3.49, which provides a graph of Vickers microhardness against deformation conditions, with standard deviation represented by black bars.

Vickers microhardness tests $HV_{0.015}$						
Condition	**AA 2618**		**AA 2618 + Zr**		**AA 2618 + Zr + V**	
	Average $HV_{0.015}$	**SD**	**Average $HV_{0.015}$**	**SD**	**Average $HV_{0.015}$**	**SD**
AC	*60*	6.8	*74*	2.6	*75*	0.87
16%	*71*	6.9	*68*	2.3	*72*	2.65
33%	*76*	7.1	*70*	5.0	*68*	2.23
50%	*65*	3.8	*76*	1.3	*76*	4.71

Tab. 3.15 – Average values and standard deviations of Vickers microhardness $HV_{0.015}$ tests on α-Al matrix of the three alloy in different deformation conditions (as-cast and deformed to 16%, 33% and 50% of initial thickness), on rolling longitudinal direction.

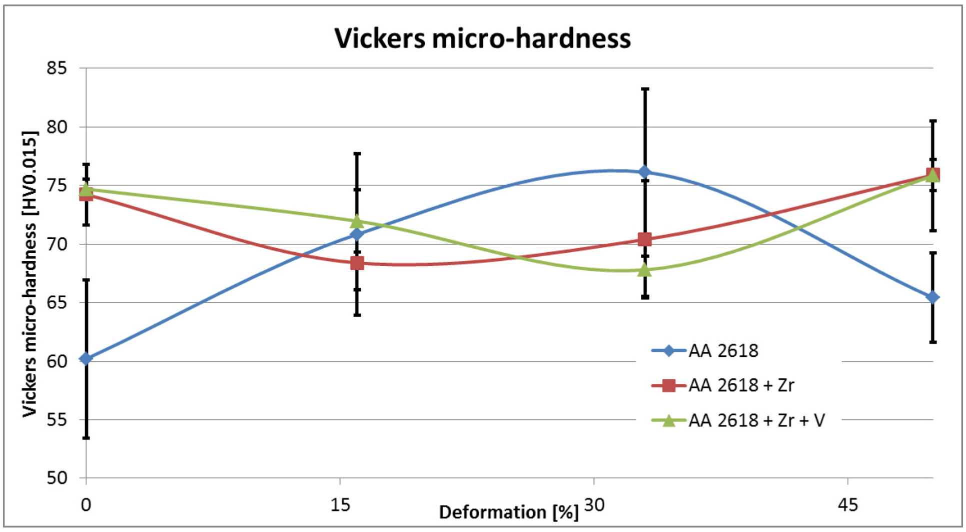

Fig. 3.49 – Vickers microhardness $HV_{0.015}$ *average values (reported in Table 3.14) against deformation condition (0 corresponding to as-cast). Black bars show standard deviation.*

On the basis of what was found for Brinell hardness, it would be expected that also matrix microhardness decreases after hot rolling. However, the graph in Figure 3.49 shows that it is not possible to identify a trend in microhardness value with deformation. Also differences between different alloy compositions are not clear. Moreover, standard deviations result quite high, making almost impossible to find significant differences among the different samples.

Standard deviation results very high, in part because the applied load is extremely low and therefore indentation measurement is less precise. Moreover, it is possible that sometimes, accidentally, indentations involve not just α-Al matrix but also some very fine phases, hardly detectable with optical microscope.

3.2.10 Material received by Duraldur S.p.A.

The material received by Duraldur S.p.A. was analysed, in order to check in which conditions AA 2618 is forged in industrial practice. The optical micrographs in Figure 3.50 confirm that the bar was hot extruded: the microstructure in Figure 3.50 (a), taken along the longitudinal direction, exhibit the typical features of hot deformation, with intermetallics that are no more at the grain boundaries, but aligned on the extrusion direction and at the centre of recrystallized grains.

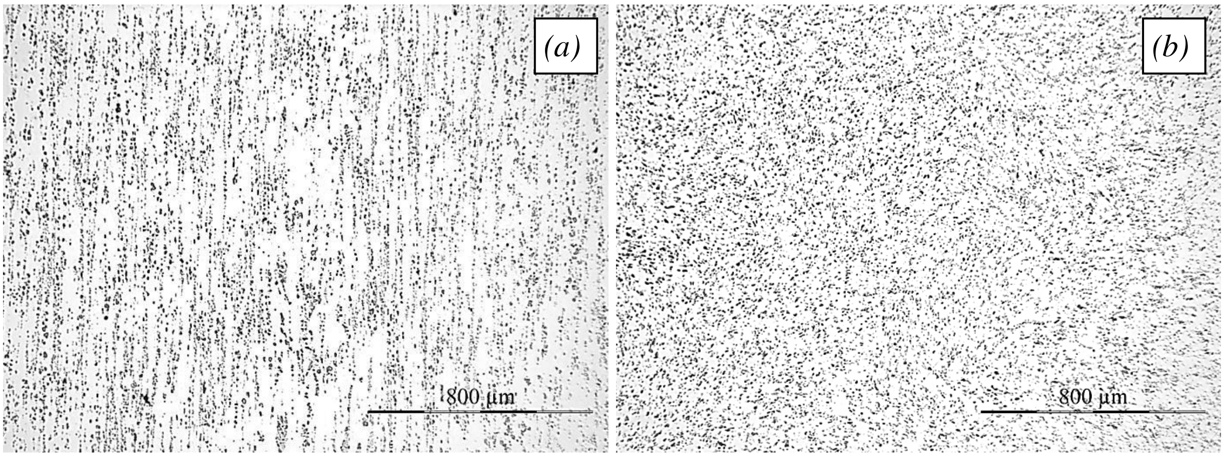

Fig. 3.50 – Optical micrographs at low magnification (5x) of AA 2618 extruded bar received by Duraldur S.p.A. along the longitudinal (a) and transverse (b) direction. Microstructure features confirm that the bar received from Duraldur S.p.A. was hot extruded.

EDS measurements were carried out on the extruded bar samples. The results showed that almost all the intermetallics present in the microstructure comply with the formula Al_9FeNi, and some are of the kind Mg_2Si. This is in agreement with the results shown in § 3.1.7 for the overaged AA 2618 and in §3.2.6 for the as-cast and deformed AA 2618 and modified alloys. In contrast with what reported in §3.2.6, however, in the extruded bar it was impossible to find Al_2Cu and Al_2CuMg phase. Moreover, almost no particles containing Cu and Ni and/or Fe were detected. That means that the as-cast material was subject to a high temperature heat treatment (homogenization or solutionizing), or that the extrusion temperature was high enough to dissolve these phases. Finally, some Ti-containing phase was found, probably with a grain-refinement function. Figures 3.51 – 3.52 show examples of the different phases and the relative EDS spectra.

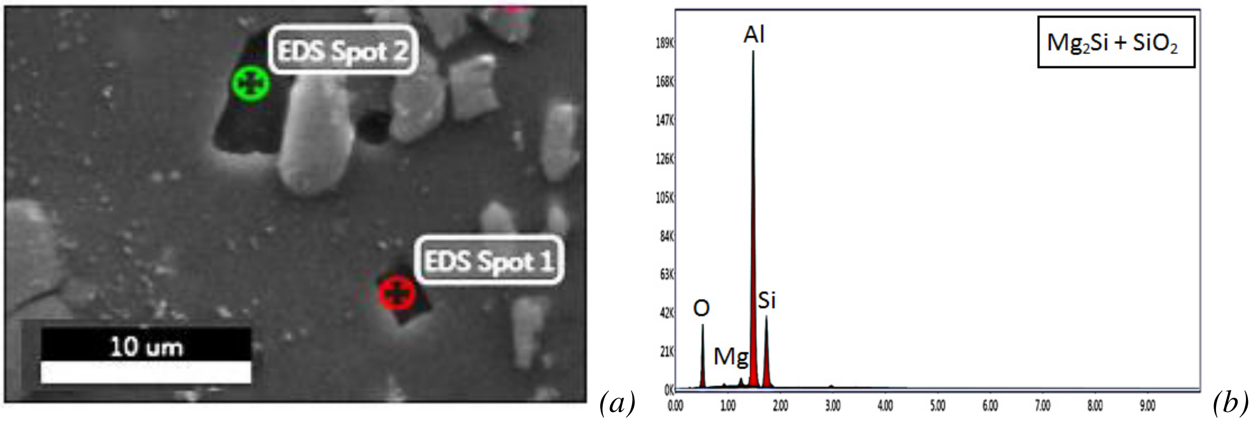

Fig. 3.51 – FEG-SEM micrograph showing Mg_2Si particles (a) and EDS spectrum relative to Spot 2. The spectrum shows a high amounts of O, which probably reacts with the Si present in Mg_2Si during last step of polishing.

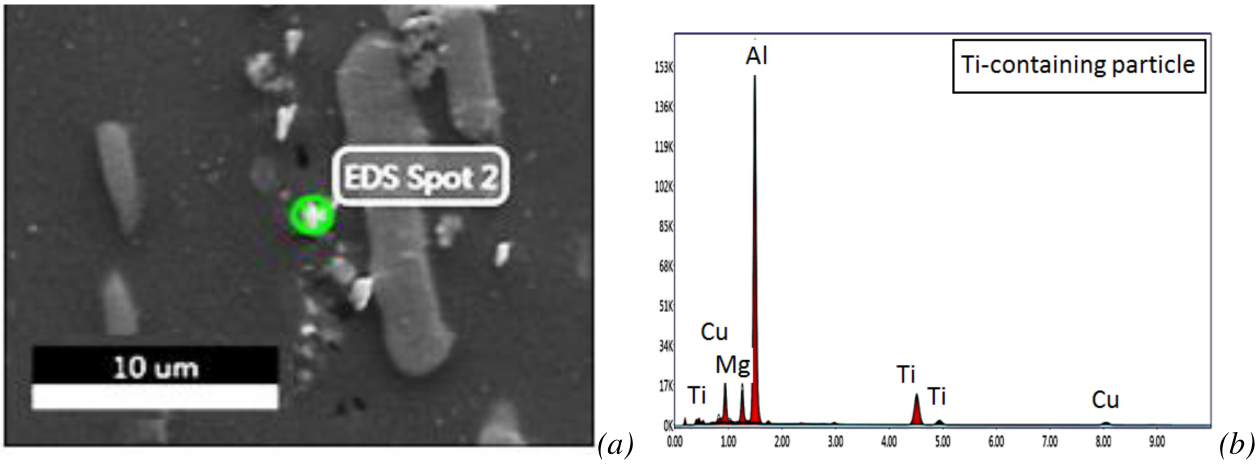

Fig. 3.52 – FEG-SEM micrograph showing Ti-rich particles (a) and EDS spectrum relative to Spot 2. The spectrum shows a high amounts of Al (70 wt%) and Ti (26 wt%), and the presence of small amounts of Cu and Mg.

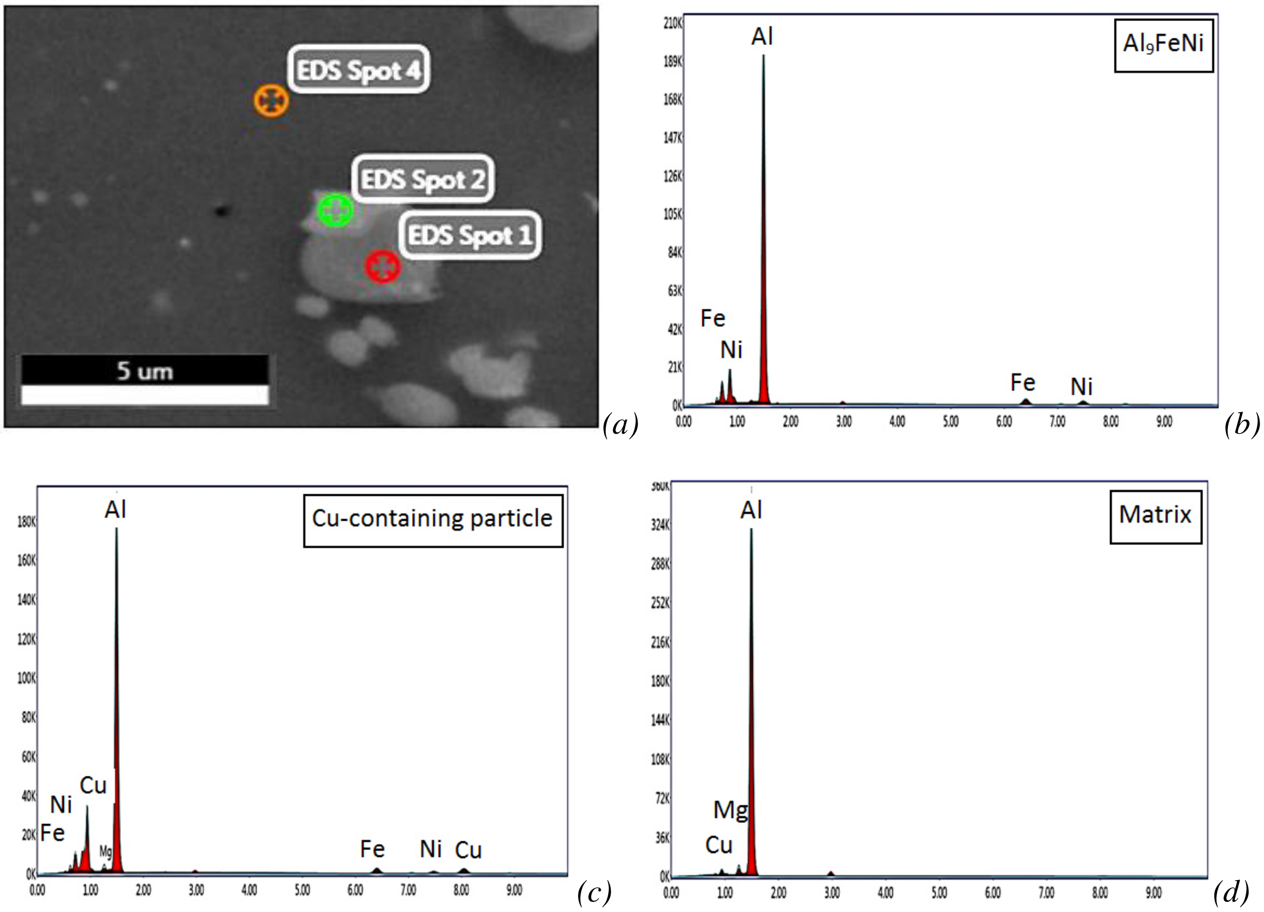

Fig. 3.53 – FEG-SEM micrograph showing Al_9FeNi (Spot 1) and Cu-rich phase (Spot 2) (a) and EDS spectrum: Spot 1 relative to Al_9FeNi (b), Spot 2 relative to Cu-rich particle (c) and Spot 4 relative to the matrix (d).

FEG-SEM micrographs at high magnification (5000x), show that Al_9FeNi phase presents white stripes, that probably are composed by a Cu-rich phase. Unfortunately, these stripes are far too tiny for EDS point analysis. An example of this is provided in Figure 3.54.

Moreover, intermetallic phases appear spherodized, opposite to what observed on as-cast samples, which shows irregular, lath-like and feather-like intermetallics. That confirms that hot extrusion is able to modify the intermetallic phases' shape.

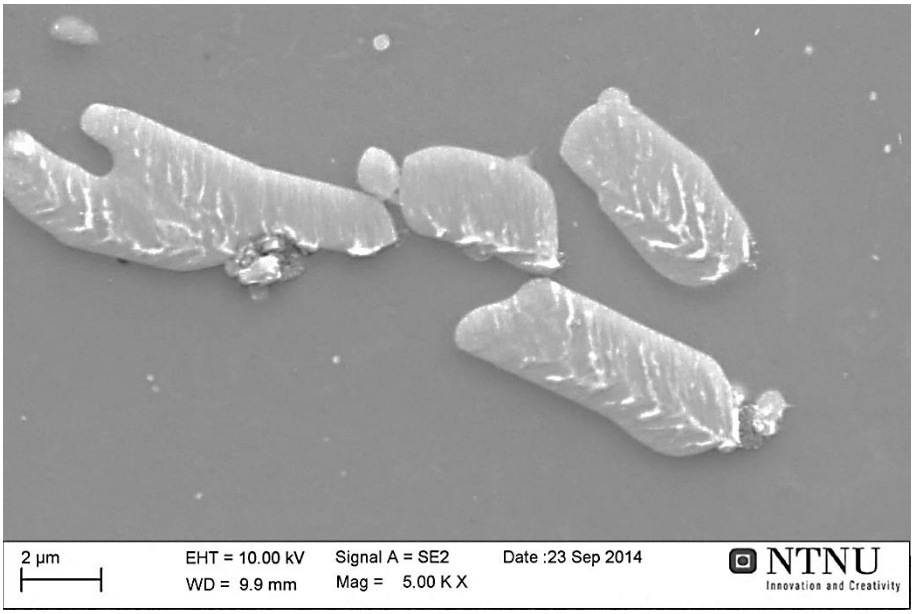

Fig. 3.54 – High magnification (5000x) FEG-SEM micrograph showing white stripes on Al_9FeNi phase in a sample of AA 2618 extracted from the extruded bar received by Duraldur S.p.A. The sample was OP-S polished.

3.2.11 Second hot rolling – OM

Figure 3.55 shows optical micrographs at low magnification (5x) of the samples hot rolled with the modified parameters, deformed to 50% of thickness reduction. Images taken both along the longitudinal and transverse directions are reported. These images show that, even if holding time at high temperature was increased, the obtained microstructures still do not exhibit the typical features of hot deformation. Therefore, it must be concluded that, during rolling, the contact between samples and the large rolls at room temperature immediately cools the samples down, with the result that the deformation probably takes place at a temperature much lower than 400 °C.

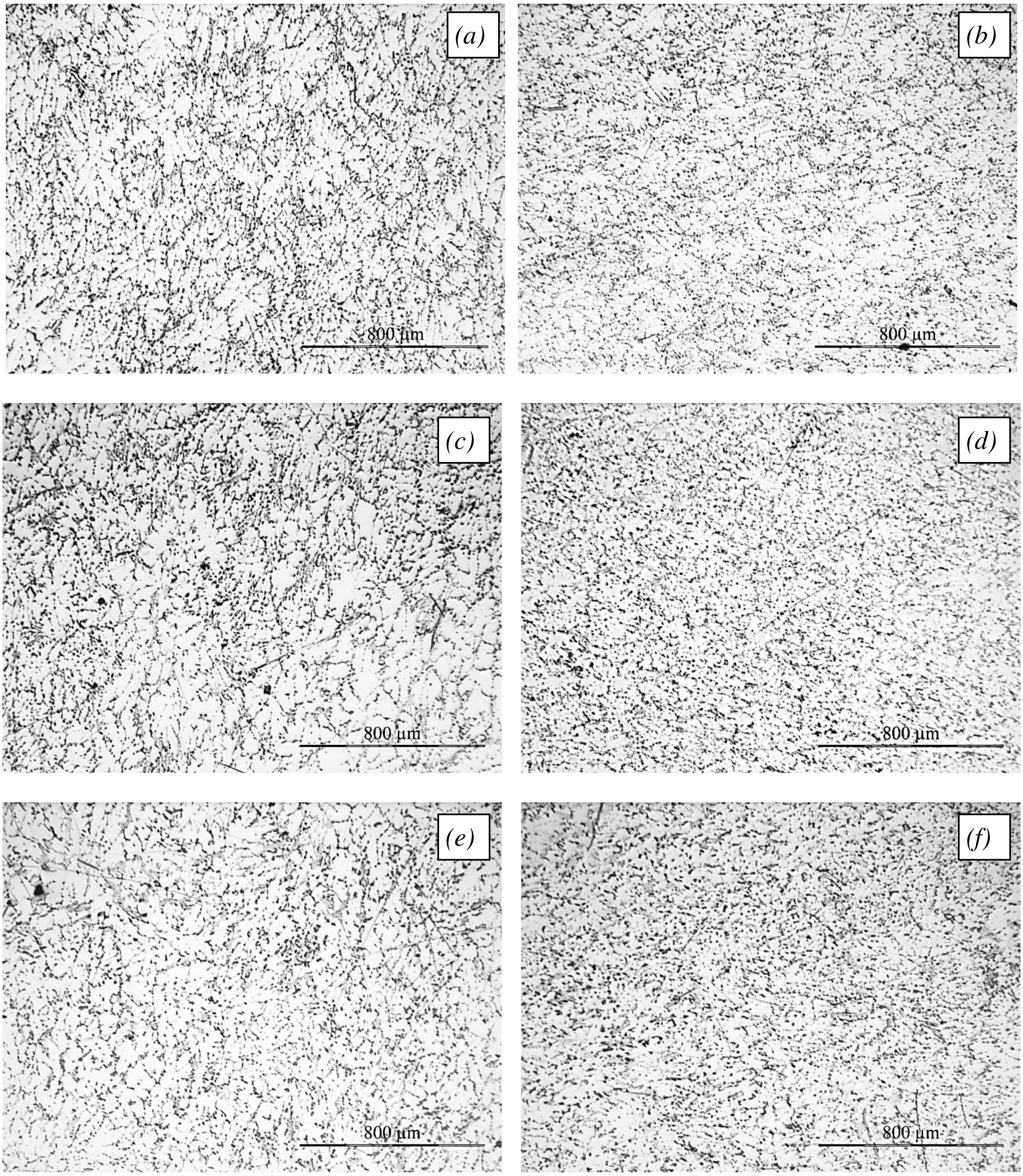
(a)
800 µm
(b)
800 µm
(c)
800 µm
(d)
800 µm
(e)
800 µm
(f)
800 µm

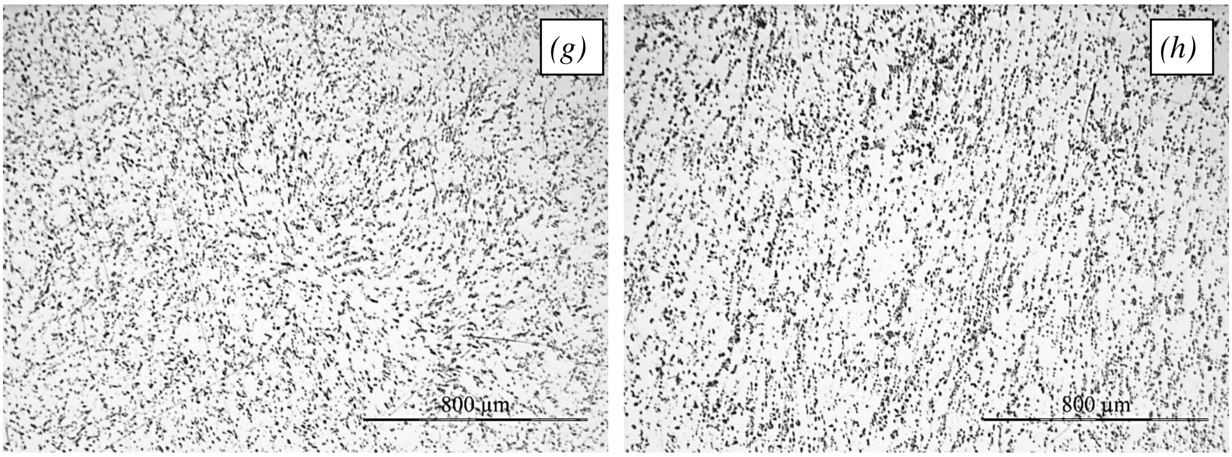

Fig. 3.55 – Optical micrographs at 5x of samples after second hot rolling, deformed to 50% of thickness reduction: AA 2618 along longitudinal (a) and transverse (b) directions, Zr-modified alloy along longitudinal (c) and transverse (d) directions, Zr- and V-modified alloy along longitudinal (e) and transverse (f) directions, previously hot extruded AA 2618 received by Duraldur S.p.A. along longitudinal (g) and transverse (h) directions.

3.2.12 Second hot rolling: Brinell hardness

Brinell hardness HB10 tests were carried out on samples subjected to hot rolling with modified parameters, deformed to 50% of initial thickness. The results are reported in Table 3.16.

Brinell hardness test HB10				
	AA 2618	**AA 2618+Zr**	**AA 2618+Zr+V**	**Duraldur**
Average	*73*	*75*	*75*	*76*
SD	0.7	1.2	1.2	0.8

Table 3.16 – Average values and standard deviations of Brinell hardness HB10 tests on sample of the three alloys and on extruded AA 2618 received by Duraldur S.p.A. after hot rolling with the modified parameters. Samples were deformed to 50% of initial thickness, and hardness tests were carried out on the longitudinal rolling direction.

The Brinell hardness measured on samples deformed with the modified rolling parameters was compared to the Brinell hardness measured on samples deformed to 50% of initial thickness with the first rolling. As explained in §3.2.4, the main differences between the first and second hot rolling parameters are that the holding time at 400 °C was increased and the thickness reduction for each step was dramatically decreased. The Brinell hardness measured on the two sets of samples after hot rolling is shown in the bar chart in Figure 3.56, where the first three bars represent the hardness of samples after the first hot rolling, while the other four bars represent the hardness of samples after the second hot rolling (with modified parameters). As in the other graphs, the black bars represent the standard deviations from the average values. In general, Brinell hardness after hot rolling with modified parameters appear higher, the only exception being represented by Zr- and V-modified alloy, which shows a higher hardness after deformation with the first hot rolling parameters. In this case, however, standard deviation appear to be much higher than in the other cases (5 HB10 instead of 1-2 HB10), so there is the possibility that this measure is not really accurate. In conclusion, it is possible to affirm the new hot rolling parameter produce higher hardness in samples deformed to 50% of thickness reduction.

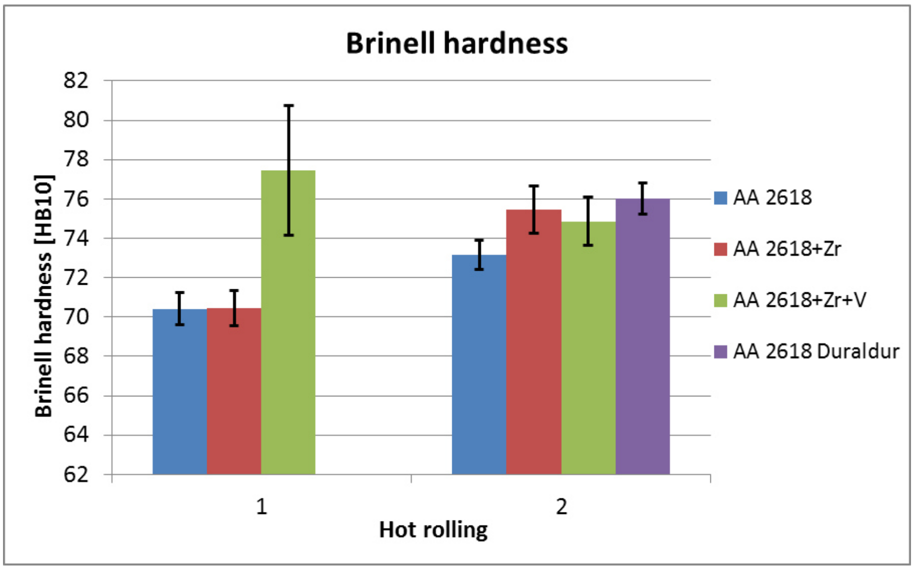

Fig. 3.56 – Brinell hardness HB10 and samples hot rolled to 50% of initial thickness with the first hot rolling parameters (1) and the modified rolling parameters or second hot rolling (2). Black bars represent standard deviation.

REFERENCES

[1] J. Wang, D. Yib, X. Sua, F. Yina, "*Influence of deformation ageing treatment on microstructure*
and properties of aluminum alloy 2618", Materials Characterization, 59 (2008) 965-968

[2] H. Lu, P. Kadolkar, K. Nakazawa, T. Ando, and C.A. Blue, "*Precipitation Behavior of AA2618*", Metallurgical and Materials Transactions A, 38A (2007) 2379-2388

[3] F. Novy, M. Janecekb, R. Král, "*Microstructure changes in a 2618 aluminium alloy during ageing and creep*", Journal of Alloys and Compounds, 487 (2009) 146–151

[4] E.M. Elgallad, P. Shen, Z. Zhang, X.-G. Chen, "*Effects of heat treatment on the microstructure and mechanical properties of AA2618 DC cast alloy*", Materials and Design, 61 (2014) 133–140

[5] P. Shen, E.M. Elgallad, X.-G. Chen, "*On the aging Behavior of AA2618 DC cast alloy*", TMS Light Metals, Light Metals 2013 - At the TMS 2013 Annual Meeting and Exhibition, p 373-377

[6] P. Shen, "*The effects of heat treatment on the microstructure and mechanical properties of the AA2618 DC cast plate*", Ph.(2012) Universite du Quebec

[7] I. N. A. Oguocha, Y. Jin, and S. Yannacopoulos, "*Characterisation of AA2618 containing alumina particles*", Materials Science and Technology, 13 (1997) 173-181

[8] R. N. Wilson, P. J. E. Forsyth, "*Effects of Additions of 1% Iron and 1% Nickel on Age-hardening of an Aluminum-2.5%Copper-1.2%Magnesium Alloy*", Journal of the Institute of Metals 94 (1966) 8-12

[9] E. D. Moreau, I. W. Donaldson, R. L. Hexemer, Jr and D. P. Paul Bishop, "*Effects of Fe and Ni additions on emerging Al-4.5Cu-1.5Mg powder metallurgy alloy. Part 2 – Influence of elevated temperature exposure*", Canadian Metallurgical Quarterly, vol. 52 no. 4 (2013) 380-390

[10] I. N. A. Oguocha, Y. Jin, and S. Yannacopoulos, " *The structure of* Al_xFeNi *in Al-Cu-Mg-Fe-Ni alloy (AA2618)*" Journal of Materials Science, 31 (1996) 5615-5621

[11] J. Majimel, G. Molenat, M.J. Casanove, D. Schuster, A. Denquin, G. Lapasset, "*Investigation of the evolution of hardening precipitates during thermal exposure or creep of a 2650 aluminium alloy*", Scripta Materialia, 46 (2002) 113–119

[12] Z. W. Du, G. J. Wang, X. L. Han, Z. H. Li, B. H. Zhu, X. Fu, Y. A. Zhang, B. Q. Xiong, "*Microstructural evolution after creep in aluminum alloy 2618*", J Mater Sci, 47 (2012) 2541-2547

[13] L. Backert, "*Solidification Characteristics of Aluminum Alloys, Vol. 1: Wrought Alloys*" (1986) Skan Aluminium

[14] G. Wang, B. Xiong, Y. Zhang, Z. Li , P. Li, "*Microstructural characterization of as-cast and homogenized 2D70 aluminum alloy*", International Journal of Minerals, Metallurgy and Materials, 16 (2009) 427-431

[15] A. Morri, "*Lavorazioni per deformazione plastica – Laminazione*", slides from lectures at University of Bologna

[16] M. Predeleanu S.K. Ghosh, "*Material Processing Defects*" (1995) Elsevier

[17] F. Wang, B. Xiong, Y. Zhang, Z. Li , P. Li, "Microstructural characterization of an Al-Cu-Mg alloy containing Fe and Ni", Journal of Alloys and Compounds 487 (2009) 445-449

[18] I. Özbek, "*A study on the re-solution heat treatment of AA 2618 aluminum alloy*", Materials Characterization 58 (2007) 312–317

[19] American Society for Metals, "*ASM Handbook. Volume 12: Fractography*" (1987) ASM International

[20] J. D. Robson, P. B. Prangnell, "*Dispersoid precipitation and process modelling in Zirconium containing commercial aluminium alloys*" Acta mater. 49 (2001) 599–613

CONCLUSIONS

UNMODIFIED AA 2618

Heat treatment, thermal stability, degradation of mechanical properties and microstructural modifications due to thermal exposure were studied in an Al-Cu-Mg-Si-Fe-Ni alloy (AA 2618). The following results were obtained:

- Precipitation hardening heat treatment was optimized for the AA 2618 alloy. DSC analysis confirmed that the maximum temperature used for solutionizing (525 °C) does not lead to incipient melting, which begins for temperatures higher than 540 °C. The optimum ageing treatment was identified, taking into consideration peak hardness and treating time, as 200 °C for 20 h. In this condition (T6), AA 2618 reached a hardness value of almost 140 HB10.

- The high temperature resistance of T6 heat treated AA 2618 alloy was studied for a wide range of soaking temperatures (from 200 to 305 °C), and for soaking times up to 7 days. Experimental data, collected in hardness-time curves, show that AA 2618 exhibit a good thermal stability for temperatures up to 230 °C, while for higher temperatures the loss of hardness in the first minutes of exposure is really rapid. However, these results confirm that AA 2618 has a higher thermal stability than most of the other aluminium alloys.

- Experimental data on the thermal stability of T6 AA 2618 were used to build hardness-time-temperature curves, which can be used to forecast the hardness of the alloy after a thermal exposure at a given temperature and time. Moreover, they can be used to find the working temperature of a component which operated for a given time, simply measuring the residual hardness.

- Tensile tests on overaged specimens showed that UTS and YS are a liner function of residual hardness, while E% is best fitted by a logarithmic function; that means that increasing the level of overaging, the material becomes less resistant but more ductile.

- Strength index (K) and strain hardening exponent (n) of the Hollomon's law were evaluated from the tensile tests, and they appeared to be a linear function of residual hardness. The agreement between Hollomon's model and experimental data was found to be quite good, particularly for the material with lower residual hardness. In contrast, important gaps were found between the experimental data and the model for the peak-aged material.

- The fracture surfaces of two tensile specimens presented important amounts of oxides, containing Al and Mg. These oxides lead to fracture surfaces typical of a brittle material, and elongation to failure during tensile test <1%. The fracture surfaces of the other samples, however, showed a very limited amount of oxides and typical features of ductile fractures.

- The grain size in the pistons used for extracting the tensile specimens varies with the distance from the piston axis and the depth (distance from the piston top). However, these variations are in the range 100-300 µm, which is not significant compared to the average value (180 µm). Therefore, variations in grain size are believed to have no important effects on mechanical properties.

- No relation was found between grain size and residual hardness, indicating that thermal exposure in the range 200-305 °C does not lead to grain coarsening.

- At low magnification (1000x) the microstructures of samples overaged to different residual hardness are similar. Four intermetallic phases are identified, but Al_9FeNi is the most abundant while the others present low volume fractions. Thermal exposure has no effect on size, shape and distribution of intermetallics.

- Thermal exposure of AA 2618 T6 alloy results in the coarsening of precipitates at the GB. Increasing the exposure time and/or temperature (that is, decreasing the residual hardness) results also in the coarsening of elongated precipitates in the matrix. These precipitates are elongated on two orthogonal directions, and are not homogeneously distributed. On the basis of literature review, they are believed to be S-type phase. The growth and coarsening of these precipitates result in the formation of PFZ. These modification in the microstructure are responsible for the hardness decrease in overaged material.

EFFECTS OF ZR AND V ADDITIONS TO AA 2618

A preliminary investigation concerning the modification of AA 2618 with small additions of Zr and Zr/V was carried out. Here are summarized the obtained results.

- AA 2618 was modified with small additions of Zr and V, but the amounts of Zr and V in the modified alloy were less than expected. It is necessary to take into account the real amounts of Zr and V in the modified alloy to discuss the experimental results

- Thermal analyses during solidification showed the presence of 4 peaks in the first derivative dT/dt. Each peak corresponds to a reaction taking place in the molten material. The temperatures at which the peaks are identified are not affected by Zr/V additions.

- DSC analyses showed the presence of two low-melting eutectics. The results of DSC are not in good agreement with the results of thermal analyses, but it could be due to the different cooling rate.

- Optical micrograph of as-cast samples showed that as-cast microstructure consist of equiaxed primary dendrites of aluminium-rich solid solution and an interdendritic network of intermetallic compounds around the primary grains. Microstructural analysis does not show significant differences between base material and modified alloys. However, optical micrographs suggest that the distribution of interdendritic phases in AA 2618 is coarser than in modified alloys. Typical casting defects were present, such as gas porosity and interdendritic shrinkage.

- Six different phases were identified by EDS analysis. The most abundant was confirmed to be Al_9FeNi; in addition, small volume fraction of Mg_2Si and Al-Cu-Ni(-Fe) intermetallics were detected. Moreover, the eutectic phases Al_2Cu and Al_2CuMg were present in the as-cast microstructure. It's very important to dissolve these eutectics, in order to obtain a suitable precipitation strengthening. No Zr and/or V-containing particles were detected, due to the low Zr and V content and to the high cooling rate during solidification.

- There are no significant differences in SDAS average values for the base and modified alloys. SDAS is about 30 μm, that is a typical value for die casted aluminium alloys, indicating a quite high cooling rate during solidification.

- Modified alloys after hot rolling presented extensive cracks, but when thickness reduction for each step is decreased the cracks were not formed anymore. Therefore, it is believed that cracks during hot rolling depend on hot rolling parameters and not on the modification of chemical composition.

- Optical micrographs of hot rolled material did not show a hot deformed microstructure. This is likely due to the contact between the specimens, which are at high temperature (400 °C), and the large cold rolls at room temperature. Since the rolls are much bigger than the specimens, the short contact time is enough to cool down the specimens during the deformation.

- The fracture surfaces of the cracks appeared during rolling showed features typical of brittle fractures, probably due to the presence of large intermetallics.

- SEM images showed that during hot rolling fine elongated precipitates are formed (or coarsen). They probably are the same S-type phase found in the overaged material.

- Shape, size, distribution and chemical composition of intermetallic phases appeared to be not affected by hot rolling. However, SEM micrographs showed that large intermetallic phases crack as the deformation becomes heavier; this is probably due to the fact that these intermetallics are brittle.

- No Zr- and/or V-containing precipitates were found in the modified alloys, after hot rolling. Probably the hot rolling temperature (400 °C) ant soaking time (30 min) are too low to form Zr and V precipitates, or they are too fine to be detected with SEM.

- EPMA line scans across secondary dendrite arms showed that Zr tends segregates at the cores of dendrite arms, and the lowest concentration of Zr is found at the dendrite boundaries, in agreement with the peritectic nature of the Al-Zr system.

- Brinell hardness did not evidenced differences among the base and modified alloys. However, Brinell hardness was found to decrease from the as-cast to the hot deformed conditions. This is believed to be due to the coarsening of the elongated phase detected in the matrix with SEM. When the samples were hot rolled with lower thickness reduction for each step and longer soaking times, Brinell hardness in deformed materials resulted generally somewhat higher.

- Unexpectedly, Vickers microhardness did not show the same trend of Brinell hardness. In fact, it was not possible to identify a trend in Vickers microhardness with deformation, or differences due to chemical compositions. However, standard deviations resulted quite high, and this could be the reason why Vickers microhardness did not showed a clear trend.

FUTURE WORK

An extensive experimental work has been carried out on precipitation hardening heat treatment and thermal stability of AA 2618 alloy.

However, the study of chemical modification of this commercial alloy in order to enhance its high-temperature mechanical properties is just at its beginning, and still a lot of experimental work has to be carried out before obtaining significative results. In particular, the first steps should be the following:

- Produce new alloys with higher content of Zr and V, since probably the small amounts added in the investigated alloys is not enough to produce considerable effects. Melting temperatures and time must provide a complete dissolution of the master alloys.
- Find an alternative technique to hot deform the material, since the hot rolling used in the present work did not result in a hot deformed microstructure of the rolled sample. Moreover, it could be convenient to use a deformation process that can better reproduce the effects of hot forging, since this is the process used in industrial practice.
- It is necessary to use a casting method, which can provide a cooling rate during solidification high enough to avoid the undesired primary precipitation of Zr- and/or V-containing phases.
- Find optimum parameters for heat treatment of modified alloys. This is a very important point, since due to the addition of Zr and V, the optimum parameter for heat treatment are probably modified. In fact, the optimum precipitation temperature for Zr is much higher than the optimum precipitation temperature for commercial AA 2618. That leads to the impossibility of precipitate all the strengthening phases during the same ageing treatment, and to the possibility that Zr-containing phase precipitate during homogenization or solutionizing. An experimental study is required to define the new optimum parameters for heat treatment of the modified alloys.
- Verify the thermal stability of the modified alloys in T6 condition, for thermal exposures in the range 200-305 °C. This data will be compared to the data presented in this work about AA 2618 alloy.

- Verify the mechanical properties of modified alloys after thermal exposure and at elevated temperature. In this respect, tensile test is particularly useful. Even creep test could be interesting.

ACKNOWLEDGEMENTS

In the first place, I would like to thank Prof. Lorella Ceschini for the opportunity to carry out part of the experimental work at the Norwegian University of Science and Technology (NTNU) and for the time she dedicated to “my” project before, during, and after my staying in Norway. My sincere thanks go also to Prof. Alessandro Morri, who passionately followed the development of the experimental work from Bologna during my staying in Norway, giving useful advices, and to Andrea Morri, for being always willing to help me.

I am also very thankful to Professor Marisa Di Sabatino and Professor Lars Arnberg, who hosted my stay at the Norwegian University of Science and Technology (NTNU) in Trondheim. I sincerely appreciated the opportunity to live this experience abroad, to work with people from all over the world and to be part of the Solidification and Casting Group. Many thanks to all the people from NTNU who helped me with the experimental work, and in particular to Chiara, Pål, Torstein, Trygve and Yingda.

I would also like to acknowledge Duraldur S.p.A for providing the material used during the experimental work.

Thanks to all the friends I met in Trondheim. Ginevra, Martyna, Serena, Valerio, Emma, Eleonora, Szymon, Piotr, Florian, Holger, Luis, Arnaud, thank you for all the time spent together, which made my summer in Norway amazing. Special thanks to Emma and Eleonora, my “colleagues”, for making much happier the endless hours spent together in our “office”.

At the end of my academic studies, I would like to thank the friends who shared with me all these long years at the University: Elisa, Paolo, Simone, Marco and Matteo, thanks for the time spent together during the lectures, the projects we did together, and the beers in Via Zamboni.

The last, but maybe the most important thanks to my parents, because without them I would have never been what I am now.